Influences of deep convective cloud systems on tropospheric trace gases and photochemistry over the tropical West Pacific: A modeling case study

Dissertation
zur Erlangung des Grades
"Doktor der Naturwissenschaften"
am Fachbereich Physik
der Johannes Gutenberg-Universität
in Mainz

Marc Salzmann
geboren in Bad Hersfeld

Mainz, 2005

Tag der mündlichen Prüfung: 31. Januar 2006

D77 Mainzer Dissertation

Abstract

A numerical model for studying the influences of deep convective cloud systems on photochemistry was developed based on a non-hydrostatic meteorological model and chemistry from a global chemistry transport model. The transport of trace gases, the scavenging of soluble trace gases, and the influences of lightning produced nitrogen oxides (NO_x=NO+NO_2) on the local ozone-related photochemistry were investigated in a multi-day case study for an oceanic region located in the tropical western Pacific. Model runs considering influences of large scale flows, previously neglected in multi-day cloud resolving and single column model studies of tracer transport, yielded that the influence of the mesoscale subsidence (between clouds) on trace gas transport was considerably overestimated in these studies. The simulated vertical transport and scavenging of highly soluble tracers were found to depend on the initial profiles, reconciling contrasting results from two previous studies. Influences of the modeled uptake of trace gases by hydrometeors in the liquid and the ice phase were studied in some detail for a small number of atmospheric trace gases and novel aspects concerning the role of the retention coefficient (i.e. the fraction of a dissolved trace gas that is retained in the ice phase upon freezing) on the vertical transport of highly soluble gases were illuminated. Including lightning NO_x production inside a 500 km 2-D model domain was found to be important for the NO_x budget and caused small to moderate changes in the domain averaged ozone concentrations. A number of sensitivity studies yielded that the fraction of lightning associated NO_x which was lost through photochemical reactions in the vicinity of the lightning source was considerable, but strongly depended on assumptions about the magnitude and the altitude of the lightning NO_x source. In contrast to a suggestion from an earlier study, it was argued that the near zero upper tropospheric ozone mixing ratios which were observed close to the study region were most probably not caused by the formation of NO associated with lightning. Instead, it was argued in agreement with suggestions from other studies that the deep convective transport of ozone-poor air masses from the relatively unpolluted marine boundary layer, which have most likely been advected horizontally over relatively large distances (both before and after encountering deep convection) probably played a role. In particular, it was suggested that the ozone profiles observed during CEPEX (Central Equatorial Pacific Experiment) were strongly influenced by the deep convection and the larger scale flow which are associated with the intra-seasonal oscillation.

Zusammenfassung

Ein numerisches Modell zur Untersuchung der Einflüsse hochreichender Konvektion auf die Photochemie in der Troposphäre wurde auf Grundlage eines nichthydrostatischen meteorologischen Modells und eines globalen Chemie-Transport-Modells entwickelt. Der Transport von Spurengasen, das Auswaschen löslicher Spurengase, sowie die Einflüsse der Stickoxidproduktion durch Blitze auf die lokale Ozonchemie wurden anhand einer Fallstudie untersucht. Hierbei wurde ein begrenztes Gebiet im tropischen westlichen Pazifik über einen Zeitraum von mehreren Tagen betrachtet. In den meisten Modellläufen wurden Einflüsse großräumiger Strömungen berücksichtigt, die bisher in einigen ähnlichen Modellstudien bezüglich des Transports unreaktiver und unlöslicher Spurengase mit willkürlich vorgegebenen Anfangsprofilen vernachlässigt wurden. Dabei ergab sich, dass der Einfluss des mesoskaligen Absinkens (zwischen den Wolken) auf den Spurenstofftransport in diesen ähnlichen Studien stark überschätzt wurde. Der simulierte Vertikaltransport und das Auswaschen hochlöslicher Spurengase hingen stark von den vorgegebenen Anfangsprofilen ab. Hierdurch lassen sich widersprüchliche Folgerungen aus zwei früheren Studien erklären. Einflüsse der Aufnahme durch flüssige und gefrorene Hydrometeore wurden für einige wenige atmosphärische Spurengase detailliert untersucht und neue Erkenntnisse bezüglich der Rolle des Retentionskoeffizienten (Anteil eines gelösten Gases, der beim Gefrieren durch die Eisphase beibehalten wird und nicht an die Umgebungsluft abgegeben wird) gewonnen. Die Berücksichtigung der Produktion von Stickoxiden (NO_x=NO + NO_2) durch Blitze innerhalb eines 500 km langen zweidimensionalen Modellgebiets veränderte das NO_x–Budget beträchtlich und verursachte moderate Änderungen der Ozonkonzentrationen. Sensitivitätsläufe ergaben, dass ein bedeutender Anteil des durch Blitze produzierten NO_x durch chemische Reaktionen in der Umgebung der Gewitter umgewandelt wird. Dieser Anteil variiert in Abhängigkeit von Annahmen bezüglich der durch Blitze produzierten NO_x–Menge und bezüglich der Höhe, in der die NO_x–Produktion stattfindet. Im Gegensatz zu einem Vorschlag aus einer vorangegangenen Studie wurde argumentiert, dass extrem niedrige Ozon–Mischungsverhältnisse, deren Auftreten in der Nähe des Modellgebiets beobachtet wurde, sehr wahrscheinlich nicht durch die Stickoxidproduktion in Gewittern verursacht wurden. Stattdessen wurde im Einklang mit den Ergebnissen anderer früherer Studien vorgeschlagen, dass diese beobachteten, extrem niedrigen, Ozonwerte in der oberen Troposphäre auf den vertikalen Transport ozonarmer Luftmassen aus der maritimen Grenzschicht zurückzuführen sind. Diese Luftmassen wurden vermutlich horizontal über weite Strecken transportiert, sowohl vor als auch nach dem Aufwärtstransport in Kumulonimbuswolken. Insbesondere wurde vorgeschlagen, dass die während dem Central Equatorial Pacific Experiment (CEPEX) beobachteten Ozonprofile durch die großräumigere Strömung, die mit der 30–60 Tage (Madden-Julian) Oszillation in den Tropen verbunden ist, beeinflusst wurden.

First day of summer

I laid in the park. The sun was shining
when I saw you with your silver lining.

I had eyes only for you
(since the rest of the sky was blue).

At first you looked to me like a deer,
then like a huge glass of Bavarian beer.

Finally, you took the form
of a severe thunderstorm.

You brought lightning, thunder, and storm,
and the silver lining was gone.

You fed rivers, trees, and other plants,
but soaked me to my underpants.

Strong variation of a theme by E A. Poe.

Contents

Chapter 1

Introduction

The anthropogenic pollution of the atmosphere has a number of consequences such as acid rain, the ozone hole, increasing greenhouse warming, and photosmog. These consequences arise from often complex interactions of physical and chemical processes in the atmosphere, in many cases coupled to processes in the bio- and the oceanosphere. In some cases, processes and/or their interactions are not yet fully understood, making predictions for the future difficult. For example, probably the greatest uncertainty in future projections of climate arises from clouds (both optically thin and thick) and their interaction with radiation (IPCC, 2001). Another example in which clouds play a role which is in in many regards still uncertain is for ozone and its precursors in the troposphere.

This study focuses on the influence of deep convective cloud systems on trace gases including ozone. The vertical transport of trace gases, the scavenging of soluble trace gases, and the influence of lightning produced nitrogen oxide on the local tropospheric photochemistry were studied in a model case study with a cloud resolving model for an oceanic region located in the tropical western Pacific centered at 2°S, 156°E.

Ozone, nitrogen oxides, and free radicals are key species in tropospheric chemistry. Together, they play determining roles in the reaction chains which lead to the oxidation of many reactive trace gases including carbon monoxide (CO) and methane. Methane is a more efficient (per molecule), albeit less abundant greenhouse gas than carbon dioxide (e.g. IPCC, 2001). Furthermore, tropospheric ozone is an effective greenhouse gas (e.g. Fishman *et al.*, 1979; Brasseur *et al.*, 1998). The effects of tropospheric photochemistry on ozone and on the lifetime of methane are both important for climate warming (e.g. Lelieveld and Crutzen, 1992; IPCC, 2001). At high concentrations near the surface, ozone is harmful to human health and vegetation (U. S. Environmental Protection Agency, 1996; WHO, 2000). In recent years, concerns have been growing about rapidly increasing emissions in Asia leading to higher background ozone levels in the United States (e.g. Jacob *et al.*, 1999; Yienger *et al.*, 2000), and globally (Berntsen *et al.*, 1996; Lelieveld and Dentener, 2000; National Research Council, 2001). Based on climate change scenarios, tropospheric ozone levels are projected to rise, threatening the attainment of air quality standards

and compromising forest and crop productivity (IPCC, 2001). While tropospheric ozone in the southern Atlantic shows clear upwards trends (Lelieveld *et al.*, 2004), a number of studies did not find significant trends for the Pacific (Oltmans *et al.*, 1998; Logan *et al.*, 1999; Davis *et al.*, 2003), where the observational coverage is scarce.

Ozone is formed in the troposphere during the oxidation of CO, methane, and numerous hydrocarbons. These oxidation sequences are catalyzed by nitrogen oxides (NO_x = nitrogen monoxide + nitrogen dioxide) and involve free radicals, mainly hydroxyl (OH) and hydroperoxy (HO_2) radicals (Crutzen, 1972, 1973, 1974; Chameides and Walker, 1973). The photolysis of ozone in the presence of water vapor leads to the formation of OH radicals, which oxidize CO and methane (Levy II, 1971, 1972), forming HO_2 radicals. HO_2 radicals can oxidize nitrogen monoxide (NO) to form nitrogen dioxide (NO_2), and to regenerate OH. Under conditions of very low NO_x concentrations, the reaction of HO_2 with ozone can instead become important, leading to a net loss of ozone. Otherwise, if enough NO_x is available, the photolysis of NO_2 dominates, leading to the formation of NO and ozone (in the presence of molecular oxygen). The OH molecules formed during the oxidation of NO can again oxidize CO or methane, amplifying the production of ozone. In this case, ozone formation takes place while NO and NO_2 as well as OH and HO_2 are inter-converted. Some details, as well as the reactions which terminate these reaction chains, are discussed in Section 1.2. Whether ozone is on the whole formed or lost depends strongly on the availability the nitrogen oxides. Net photochemical ozone loss takes place in the remote tropical marine boundary layer, where in most places NO_x levels are still relatively low and the formation of OH radicals is favored by high photolysis rates and by high water vapor abundances.

Nitrogen oxides are emitted from fossil fuel combustion and from biomass burning, released from soils and formed during lightning (e.g. Brasseur *et al.*, 1999). In remote regions, the long range transport and subsequent chemical decomposition of NO_x reservoir gases, in particular of peracetyl nitrate (PAN), which can be formed e.g. in association with biomass burning emissions, can be another important source of nitrogen oxides (e.g. Singh and Hanst, 1981; Schultz *et al.*, 1999; Wild *et al.*, 2004). The main tropospheric source of hydroxyl radicals on a global bases is the photolysis of ozone in the presence of water vapor (Crutzen *et al.*, 1999). In the upper troposphere where water vapor mixing ratios are low, the injection of peroxides and acetone due to vertical trace gas transport in deep convective clouds is another important source of OH radicals (e.g. Chatfield and Crutzen, 1984; Singh *et al.*, 1995; Prather and Jacob, 1997; Jaeglé *et al.*, 1997, 2000). The deep convective injection of HO_x(=HO_2 + OH) reservoir gases into the upper troposphere can act to increase net ozone formation at these altitudes.

Deep convection can rapidly transport trace gases from the lower to the upper troposphere (e.g. Isaac and Joe, 1983; Gidel, 1983; Chatfield and Crutzen, 1984; Dickerson *et al.*, 1987; Pickering *et al.*, 1990) where in many cases their chemical lifetimes are longer and, especially at mid-latitudes, horizontal winds are often stronger. Thus, deep convection can play an important role for the long range trans-

port of reactive trace gases with sources close to the Earth's surface such as NO_x (and its reservoirs), CO, and hydrocarbons (e.g. Dickerson *et al.*, 1987; Pickering *et al.*, 1996; Jonquieres and Marenco, 1998; Mühle *et al.*, 2002; Ridley *et al.*, 2004). Pickering *et al.* (1990) found that outflow from deep convection can cause enhanced ozone production in the upper troposphere hundreds of kilometers downstream from the clouds. Deep convection may also play a role in diluting large scale pollutant plumes, for example in the Southern Pacific Convergence Zone (Raper *et al.*, 2001). Furthermore, descent associated with deep convection can efficiently transport tracers downward. Both upwards as well as downwards transport associated with deep convection were found to influence global budgets of tropospheric ozone (Lelieveld and Crutzen, 1994; Lawrence *et al.*, 2003a). Lelieveld and Crutzen (1994) found in a global model study that the transport of ozone and NO_x towards the Earth's surface where these gases are more efficiently removed causes an overall reduction of total tropospheric ozone by 20%, outweighing the effect of the upwards transport of its precursors. On the other hand, Lawrence *et al.* (2003a) found deep convection acting to increase the tropospheric ozone burden in a study using a more recent global chemistry transport model (GCTM). A very recent model study, which is still under discussion, has indicated that deep convection on the whole acts to decrease the tropospheric ozone burden (Doherty *et al.*, 2005), suggesting that the influence of deep convection on global ozone chemistry needs further study.

GCTMs have become valuable tools for helping to understand the influences of meteorological processes on tropospheric chemistry. Furthermore, many key features found in atmospheric measurements of a number of important trace gases can be re-produced in GCTM simulations (e.g. Bey *et al.*, 2001b; von Kuhlmann *et al.*, 2003a; Horowitz *et al.*, 2003; Lawrence *et al.*, 2003b). One of the uncertainties in GCTM studies arises from the difficulty of parameterizing deep convective transport. Currently deep convection has to be parameterized in GCTMs because of limitations in today's computer resources. Unfortunately, the modeled deep convective transport is known to be highly sensitive to the deep convective parameterization applied (Mahowald *et al.*, 1995) and even to the treatment of transport based on the mass fluxes provided by individual parameterization schemes (Lawrence and Rasch, 2005). Attempts to improve these parameterizations and to better evaluate the existing parameterizations require knowledge about relevant processes and parameters on the cloud scale, which are often difficult to estimate solely based on observations. Other important uncertainties in GCTMs include uncertainties in emission inventories, in the estimates of nitrogen oxide production due to lightning, and in the amount of stratospheric ozone entering the troposphere.

In recent years cloud resolving models (CRMs), have been used by numerous investigators to study the vertical transport of insoluble (sometimes idealized) trace gases (e.g. Scala *et al.*, 1990; Wang and Chang, 1993a; Lu *et al.*, 2000; Skamarock *et al.*, 2000; Wang and Prinn, 2000; Pickering *et al.*, 2001). CRMs were also used to study the distribution of lightning NO_x in thunderstorms in combination with aircraft observations (Pickering *et al.*, 1998; DeCaria *et al.*, 2000; Fehr *et al.*, 2004; DeCaria *et al.*, 2005). Early CRM studies of the scavenging and transport of trace

gases focused mainly on sulfur dioxide (e.g. Trembley and Leighton, 1986; Trembley, 1987; Wang and Crutzen, 1995). More recently, several authors (Wang and Chang, 1993b; Barth *et al.*, 2001; Yin *et al.*, 2002) studied influences of the ice phase on convective transport on idealized trace gases using CRMs; Yin *et al.* (2001) using an axis-symmetric model. Ekman *et al.* (2004) used a CRM to study the influence of aerosols on cloud dynamics and found high sensitivities to assumptions in their aerosol-microphysics parameterizations. The sensitivity of cloud microphysics and radiation fluxes to sulfate loading was studied by Andronache *et al.* (1999) using a CRM in a semi-prognostic setup (compare Section 3.2). High resolution limited area models were also used to study the vertical distribution of biomass burning emissions from wildfires (Trentmann *et al.*, 2002), and the injection of aerosols into the stratosphere by vigorous deep convection which can be associated with these fires (Trentmann *et al.*, 2005). A CRM study of small scale cross tropopause transport due to breaking gravity waves excited by modeled mid-latitude deep convection was presented by Wang (2003). Recently, results of this study were found to be in-line with observations (Hegglin *et al.*, 2004).

The number of CRM studies including photochemical processes is still limited. Wang and Prinn (2000) studied the influences of lightning NO_x production on the local photochemistry for a storm which was observed during CEPEX (Central Equatorial Pacific Experiment, Kley *et al.*, 1996, 1997). CEPEX was conducted subsequent to the TOGA COARE IOP (Tropical Ocean Global Atmospheres/Coupled Ocean Atmosphere Response Experiment, Intensive Observing Period, Webster and Lukas, 1992) in the western Pacific. Recently, DeCaria *et al.* (2005) studied a Colorado thunderstorm using a cloud resolving model including photochemistry.

The advantage of CRMs is that they can explicitly resolve an important part of the cloud system dynamics, and their major disadvantage lies in being restricted to a limited area, again because of today's limited computer resources. With the exception of Lu *et al.* (2000), who presented the first multi-day 2-D model study of the transport of idealized tracers by deep convective cloud systems, in previous CRM studies of cumulus transport, the evolution of an isolated deep convective storm was simulated. Similar setups as the one used by Lu *et al.* (2000) were used in single column model and CRM setups (Rasch *et al.*, 2003; Bechtold *et al.*, 2005). In the study by Lu *et al.* (2000), the influences of the large scale circulation on the horizontal advection of trace gases were not taken into account. Furthermore, the influence of the non-zero mean vertical velocity on trace gas transport, which is not reproduced by these models, was neglected. Lu *et al.* (2000) applied periodic lateral boundary conditions and observed large-scale advection terms for water vapor and potential temperature, but neglected the corresponding terms for tracers. In Chapter 3, a setup is suggested in which specified lateral boundary conditions for tracers (SLBC) are used in a CRM study. In this setup, the influence of the mean ascent on the vertical advection of trace gases is taken into account based on observed mean vertical velocities. The corresponding term was named "vertical large scale advection tendency for tracers (VLSAT)". Results from sensitivity studies for the transport of idealized tracers are discussed in Chapter 4.

While insoluble trace gases are rapidly transported to the upper troposphere, highly soluble trace gases are effectively scavenged in deep convective clouds (e.g. Rodhe, 1983; Crutzen and Lawrence, 2000). Furthermore, a fraction of trace gases that are formed in the upper troposphere and taken up by ice particles can be scavenged by deep convective clouds. Crutzen and Lawrence (2000) studied the vertical transport of idealized soluble gases with different Henry's Law constants H in a global chemistry transport model. They found a large decrease of the amount transported upwards between H=10^4 mol l^{-1} atm^{-1} and 10^5 mol l^{-1} atm^{-1} (SI Unit: 1 mol l^{-1} atm^{-1} = 101.325 mol m^{-3} Pa^{-1}). Based on results from a CRM study, Barth *et al.* (2001) argued that Crutzen and Lawrence (2000) may have largely overestimated the effect of scavenging of highly soluble trace gases. The reason for this apparent discrepancy is investigated in Chapter 6. In later chapters, the vertical transport of a number of soluble trace gases, some of which can be taken up by ice is discussed.

In order to study the influence of deep convection on reactive trace gases, lateral boundary values for the cloud resolving chemistry transport model (CRCTM) used in this study were derived from the global Model of Atmospheric Transport and Chemistry – Max Planck Institute for Chemistry Version (MATCH-MPIC). The cloud resolving model was run for a seven day episode during the TOGA COARE IOP. Based on the model simulation of a storm during CEPEX, Wang and Prinn (2000) found that the fraction of NO_x which is chemically transformed in the vicinity of the lightning source of NO can be considerable. Furthermore, in contrast to results from earlier studies, they argued that the near zero ozone values which were observed during the CEPEX campaign, may have been caused by the formation of NO associated with lightning. In earlier studies, it was suggested that near zero ozone values in the upper troposphere may in principle have been caused by the rapid transport of ozone-poor air by deep convective clouds from the marine boundary layer without considerable dilution (Wang *et al.*, 1995; Kley *et al.*, 1996, 1997; Lawrence *et al.*, 1999a). This issue is investigated in some detail.

The CRCTM used in this study including the photochemistry module is described in Chapter 2. The model was newly developed largely based on the Weather Research and Forecast Model (WRF) and a gas phase chemistry module from MATCH-MPIC. The setup for the TOGA COARE case is described in Chapter 3. A brief description and evaluation of the modeled meteorological conditions is found in the same chapter. In Chapter 4, the vertical transport of idealized tracers is studied. Results from this chapter were also presented by Salzmann *et al.* (2004). In Chapter 5, mass flux diagnostics used in CRM studies are investigated, and Chapter 6 deals with aspects of the scavenging of idealized, highly soluble trace gases. The lateral boundary conditions for the runs including effects of photochemistry and the large scale meteorological and chemical conditions during the TOGA COARE episode as well as selected observations in the region are discussed in Chapter 7. The modeled flash rates, the transport of NO_x associated with lightning, and the NO_x budget are discussed in Chapter 8. Chapter 9 is devoted to studying the influence of deep convection, and in particular of lightning produced NO_x on model results

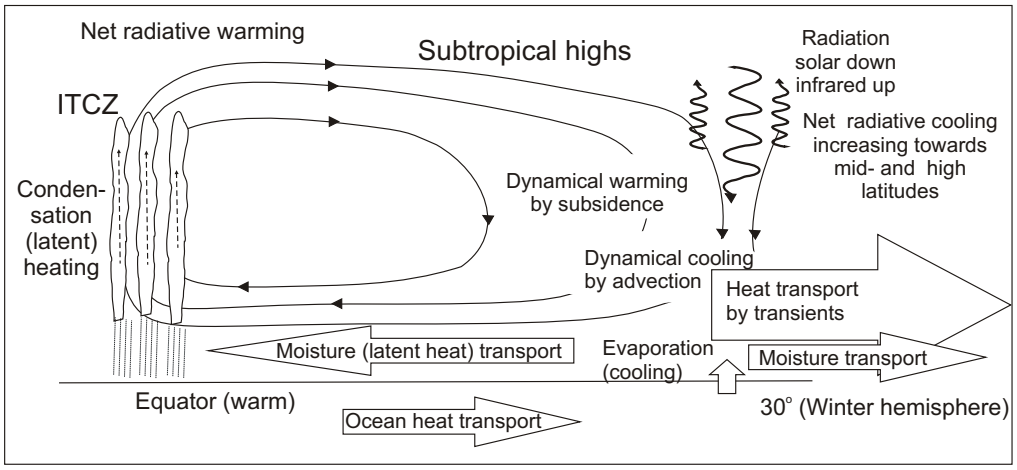

Figure 1.1: Schematic zonal mean meridional circulation (Hadley cell) and heat budget in the subtropics along with key processes (largely adapted from Trenberth and Stepaniak, 2003). The Hadley cell transfers heat from the equator towards the sub-tropics, from where it is transported further poleward by large transient and quasi-stationary disturbances (e.g. cyclones and planetary waves).

for ozone. The influence of modeled deep convection on HO_x is briefly discussed in Chapter 10. Finally, details of the scavenging of nitric acid (HNO_3), hydrogen peroxide (H_2O_2), formaldehyde (HCHO), and methyl hydroperoxide (CH_3OOH) are discussed in Chapter 11. The rest of this chapter provides an introduction to deep convection during the TOGA COARE field campaign and to "background" tropospheric photochemistry.

1.1 Tropical Moist Convection and TOGA COARE

The Earth's surface absorbs solar radiation more efficiently than the atmosphere. Surface heating as well as the evaporation of water and subsequent condensation of water vapor which acts to heat the air in cumulus clouds via the release of enthalpy are important factors for the occurence of deep convection. Furthermore, in the tropical atmosphere, where the insolation is maximum, on the whole more solar energy is being absorbed than emitted back to space as infrared radiation. While solar heating induces vertical and horizontal gradients in air density (as well as in moisture, pressure, and temperature), gravity tends to organize the atmosphere such that the less dense fluid is overlying the denser fluid, and therefore constantly tries to remove horizontal contrasts and to adjust the vertical stratification (see e.g. Gill, 1982, for an introduction to atmospheric dynamics). Deep convective clouds are often parts of larger scale phenomena, e.g. of the zonal mean meridional circulation which develops between the equator and 30° (Hadley cell). The Hadley cell is by far most pronounced in the winter hemisphere (Fig. 1.1), where net radiative cooling occurs associated with clear air in the subtropical highs (while on the annual zonal

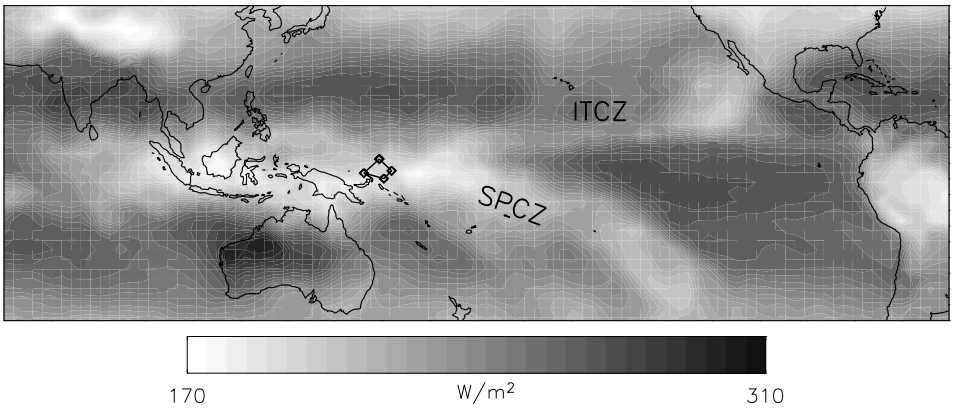

Figure 1.2: Monthly mean outgoing longwave (infrared) radiation (OLR) for December 1992. Low values (light shades) in snow free regions indicate cloudy areas. Interpolated OLR data was provided by the NOAA-CIRES Climate Diagnostics Center, Boulder, Colorado, USA, from their web site at http://www.cdc.noaa.gov. The TOGA COARE IFA (see text) is indicated by the small polygon east of Papua New Guinea.

average net heating prevails in the sub-tropics, i.e., less energy is emitted to space via infrared radiation than received via solar radiation) and where the cooling due to transient eddies (weather systems) is stronger than in the summer hemisphere. Deep convective clouds contain rapidly ascending air being heated by the release of enthalpy during condensation. Once warm and moist air starts ascending inside deep convective clouds, adiabatic cooling causes additional water vapor to condense which accounts for the heating necessary for further ascent, while a fraction of the condensed water precipitates. Ice phase processes (which amongst others play a very important role in the formation of rain) and radiative processes are other important aspects of deep convective clouds (e.g. Fu *et al.*, 1995; Krueger *et al.*, 1995; Saito *et al.*, 2001; Yin *et al.*, 2005). Next to surface heating, which can cause air at low altitudes to become buoyant and rise until water vapor starts to condense, large scale ascent associated with large scale pressure gradients causes adiabatic cooling of air which can also lead to the condensation of water vapor.

Close to the equator, low level convergence, and ascent of air are very pronounced in the Intertropical Convergence Zone (ITCZ), a narrow band of deep convective cloud systems (Fig. 1.2). The ITCZ feeds on moist air from the subtropics, where under comparatively cloud free conditions evaporation exceeds precipitation. Over the continents and the Indian Ocean the average position of the ITCZ varies strongly depending on season. Over the Atlantic and the Pacific ocean it is located close to the equator all year around. During the Asian summer monsoon for example, the ITCZ is located north of large parts of South East Asia while during the winter monsoon it is located around 5–10°S over the Indian Ocean. In the upper troposphere, air flows away from the ITCZ towards higher latitudes, where it descends. The equatorward flow at low levels is deflected westwards, resulting in the easterly direction of the trade winds. The important role of latent heat release in deep convective cloud towers for the Hadley circulation was established by Riehl and Malkus (1958).

Over the tropical Pacific Ocean, additionally a meridional mean large scale thermal direct zonal circulation, the Walker circulation (Bjerknes, 1969), is associated with large zonal sea surface temperature gradients caused by the upwelling of cold waters in the eastern Pacific and warm surface waters in the western tropical Pacific ("Pacific Warm Pool"). The Walker cell was shown to be part of a larger regime of east-west circulations in the global tropics by Krishnamurti (1971), and Krishnamurti *et al.* (1973). The strong inter-annual variability of sea surface temperatures (SSTs) over the equatorial Pacific and of the Walker cell circulation, known together as ENSO (El Niño/Southern Oscillation), has been studied intensively in recent decades (e.g. Philander, 1990; Battisti and Sarachik, 1995). The Walker circulation in general adds to the easterly direction of the trade winds over the central Pacific, but during El Niño events the trade winds weaken. The tradewinds converge with generally weaker winds in the South Pacific Convergence Zone (SPCZ), which is oriented towards the south east direction, often starting close to the Solomon islands. From satellite images, ITCZ and SPCZ are in general readily identified as narrow bands of increased amounts of deep convective clouds which meet in the western Pacific (Fig. 1.2).

In order for deep convection to occur, the vertical stratification of the ambient troposphere has to be sufficiently destabilized. Deep convection acts to stabilize the troposphere by heating the mid- and upper troposphere and by mean drying through precipitation (e.g. Yanai *et al.*, 1973; Arakawa, 1993; Johnson *et al.*, 2002). On average, the entire troposphere is driven towards the so-called radiative-convective equilibrium state (Manabe and Strickler, 1964). Locally, however, most regions are not in radiative convective equilibrium and large scale atmospheric and oceanic circulations are responsible for the meridional heat transport (e.g. Gill, 1982). The ambient temperature in environments with deep convection adjusts rapidly, i.e. at the speed of gravity waves (Bretherton and Smolarkiewicz, 1989; Nicholls *et al.*, 1991; Mapes, 1993). Moist convection is triggered by condensation which can occur due to boundary layer mixing, due to gravity waves excited by either orography or by other deep convective clouds (e.g. Mapes, 1993; Lane and Reeder, 2001; Lac *et al.*, 2002), or due to lifting of air masses. This lifting can occur for a multitude of reasons which can be associated with flows on a multitude of different scales, e.g. with flow over orography or with land breeze fronts associated with islands (Liberti *et al.*, 2001). On satellite images, convective clouds often appear as being part of larger scale phenomena, e.g. in the ITCZ or in association with synoptic systems and fronts (e.g. preceeding cold fronts).

Criteria for the static stability of the atmosphere, e.g. the increase of equivalent potential temperature (or entropy of moist air) with height, are often derived based on the highly idealized non-entraining parcel model and can be found in the standard meteorological literature. These criteria are often very useful, e.g. for diagnosing the input and output of CRMs. Another useful diagnostic quantity is the convective available potential energy (CAPE). CAPE is a measure of the amount of buoyant energy available in an unstable environment which could be converted to kinetic energy to drive the ascent of a theoretical non-entraining parcel. Typical

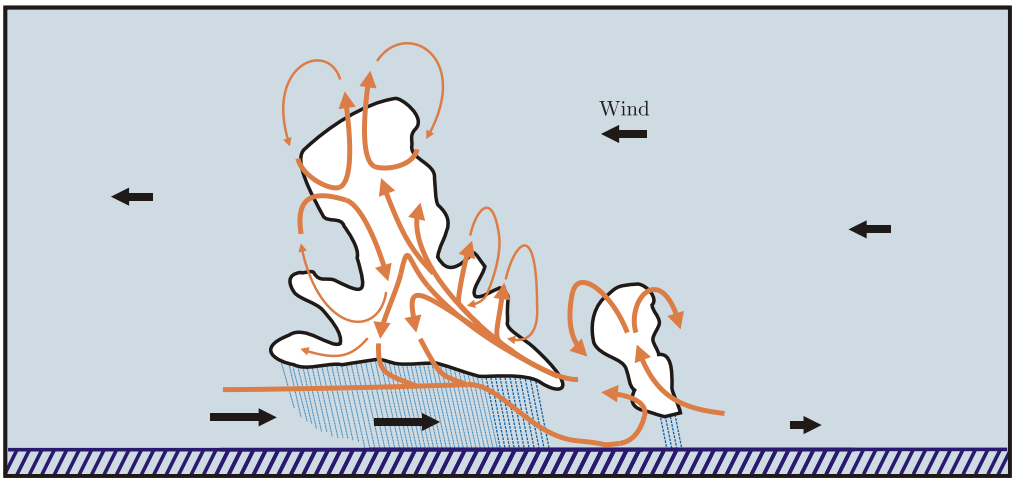

Figure 1.3: Schematic east-west cross-section of the cloud scale flow in a westward propagating mesoscale convective system (MCS). The individual storms often organize into a squall line, which here would be oriented perpendicular to the figure's plane. The cloud scale downdrafts are enforced by cooling due to the melting and the evaporation of falling hydrometeors. West of the MCS, a gust front has formed close to the Earth's surface. Lifting in the vicinity of the front triggers an arc cloud, which will later merge with the line. At the same time the MCS is decaying towards its western edge. Since the upper tropospheric winds are easterly, here the cloud is slowly moving westward. Often MCSs grow to the tropopause, where the in-cloud updrafts diverge and an anvil is formed.

values of CAPE in the tropics are smaller than the CAPE values encountered before mid-latitude thunderstorms and observed updraft velocities in the tropics are generally lower than those observed in mid-latitude thunderstorms, i.e. mid-latitude deep convection is generally more vigorous than tropical convection. Lower CAPE values in tropical marine environments reflect the fact that the lapse rate in these environments is generally close to the moist adiabatic lapse rate. Developing simple conceptual models and adequate parameterizations of deep convection have proven to be very challenging tasks (e.g. Arakawa, 2004). Parcel models can lead to physical misunderstandings about deep convection (Doswell III and Markowski, 2004) and also entraining plume models can only be viewed as a caricature of deep convection and have been criticized as being misleading and incorrect for a variety of reasons (e.g. Warner, 1970; Mapes *et al.*, 2004; Yano *et al.*, 2004).

Deep convection tends to organize into larger multi-cell or into so-called "supercell" storms and groups of storms. Often a number of storms organize in horizontal lines. These "squall lines" can stretch over 100 km or more in one direction and can propagate perpendicular to this direction over large horizontal distances. In tropical convective systems, active towers with strong vertical updrafts only take up a small fraction of the total horizontal area covered by such a system. On average, only about 10% of the rainy area in a tropical mesoscale convective systems is covered by convective rain showers (Houze, Jr., 1993). For TOGA COARE, Yuter and Houze Jr (1998) estimated that 70% of the rain during the active phase of the intra-

seasonal oscillation (ISO, see below) originated from extensive areas of stratiform clouds. Large squall lines and multi-cell storms are examples of mesoscale convective systems (MCS). In Fig. 1.3, a schematic of the flow in such a system is shown. The formation of "fresh" convective clouds is often triggered by lifting at the gust front. The newly formed cells merge with the mature part of the storm system and replace decaying cells. Rapid downward flow is associated with air in the rear inflow descending in the precipitation region (arrow through the region of heavy rainfall). Details about the evolution of MCSs have been revealed by numerous studies (see e.g. Houze, Jr., 2004). The schematic in Fig. 1.3 is largely based on model results for the TOGA COARE case from this study. The ITCZ and the SPCZ often appear as an accumulation of MCSs. It has been suggested that gravity waves excited by MCSs favor the development of additional convection beyond the area of outflow, and that thus MCSs tend to appear grouped as so-called "super-clusters" with a lifetime of several days (Mapes, 1993). Since lifting air parcels more than about a kilometer forces condensation even in air with rather low relative humidity ($< 50\%$; Lawrence, 2005), the upwards transport of air associated with the ITCZ takes place inside deep convective towers. Large scale subsidence takes place for example in the cloud free sub-tropical regions (Fig. 1.2).

Deep convection and rainfall in the tropical western Pacific show pronounced day-to-day, seasonal, and intra-seasonal variability in addition to inter-annual variability associated with ENSO. South of the equator, seasonal variations of convective activity and rainfall are generally associated with the average location and intensity of the SPCZ (e.g. Massman and Meehl, 1987) and the Australian monsoon (e.g. McBride *et al.*, 1995; Kiladis *et al.*, 1989). The ITCZ is located close to or north of the equator all year around. During northern hemispheric winter, the SPCZ is most pronounced and often associated with the Australian monsoon trough. During boreal summer, the center of convective activity is shifted towards the north west, i.e. towards South East Asia (e.g. Massman and Meehl, 1987). Lower tropospheric westerly winds prevail south of the equator in the western Pacific during the Australian monsoon instead of easterly trade winds. Sometimes long episodes of westerly winds ("westerly wind bursts") are interrupted by long episodes of easterly winds (e.g. Kiladis *et al.*, 1994; Lin and Johnson, 1996). These episodes are associated with the intra-seasonal oscillation (ISO) and can last from a few days to several weeks. In association with westerly wind bursts, low level cross equatorial flow occurs across the Indonesian Archipelago (e.g. Yanai *et al.*, 2000; McBride *et al.*, 1995). Westerly wind bursts are generally related to maxima of deep convective activity in the region (e.g. Rui and Wang, 1990; Yanai *et al.*, 2000). The large scale conditions (compare wind vectors in Fig. 7.3) and evolution (compare Fig. 7.5) related to westerly wind bursts are further discussed in Chapter 7. The ISO was first recognized by Madden and Julian (1972) and has ever since intensively been studied (see Madden and Julian, 1994; Zhang, 2005, for reviews). It is a broadband large scale phenomenon with a 30–60 day period stretching from the Indian Ocean to the central Pacific. The ISO is associated with variability in convection and a number of smaller scale phenomena.

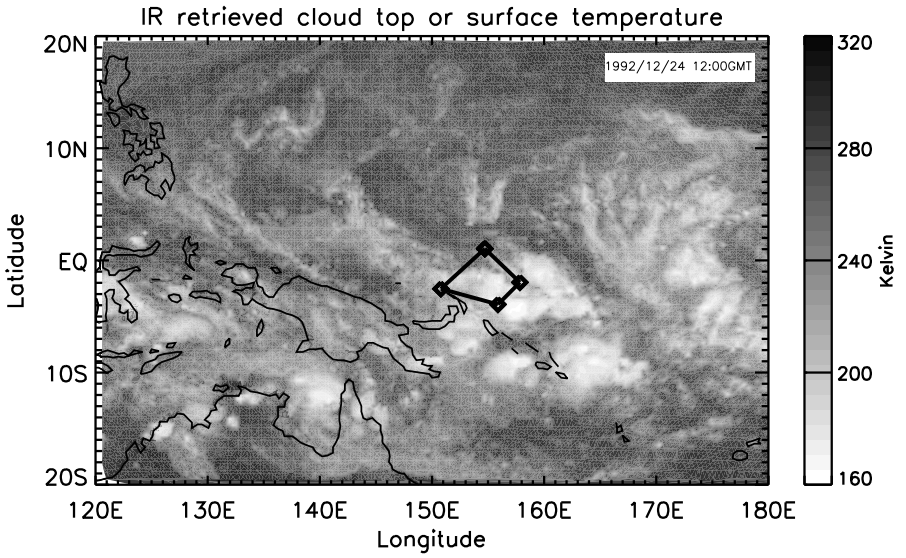

Figure 1.4: IR retrieved cloud top or surface temperatures from the ISCCP (International Satellite Cloud Climatology Project) DX dataset (Rossow and Schiffer, 1999). Low values indicate high cloud tops.

The TOGA COARE experiment (Webster and Lukas, 1992) was designed to study the variability of the coupled ocean-atmosphere system in the equatorial western Pacific and comprised a vast number of meteorological and oceanic observations from a large number of different platforms: 10 research vessels, 7 research aircraft, 35 island based priority ground stations, a number of buoys, and 4 satellites. A very large number of publications have used data from this experiment, and new ones are still being added. The TOGA COARE Intensive Observing Period (IOP) lasted from 1 November 1992 to 28 February 1993. The location of the TOGA COARE Intensive Flux Array (IFA) is indicated in Fig. 1.4. Furthermore, Fig. 1.4 shows satellite infrared retrieved temperatures for 24 December 1992.

The TOGA COARE IOP was conducted during a long lasting warm episode in the western tropical Pacific (Gutzler *et al.*, 1994). A recent example which is similar to 1992 is the year 2001 (e.g. McPhaden, 2004, or the SST plots at the NOAA El Niño theme page www.pmel.noaa.gov/tao/elnino/el-nino-story.html). During La Niña cold events of the ENSO, convective activity is minimum over the western tropical Pacific and shifts to the west, i.e. increases over the eastern Indian Ocean (Chen and Houze, 1997). The meteorological conditions during the TOGA COARE episode are described in more detail in Section 3.1. The large scale conditions are discussed in Chapter 7.

1.2 Photochemistry in the Remote Troposphere

A large number of reactive trace gases including CO, methane, and NO are emitted into the troposphere. In many cases the gases or their chemical products are

sufficiently stable to undergo long-range transport. The oxidation of many of these gases including CO, methane, and various hydrocarbons is primarily initiated by OH radicals. OH radicals are formed when ozone is photolyzed in the presence of water vapor, producing ground state oxygen ($O(^3P)$, here simply O) or excited singlet oxygen ($O(^1D)$). In the presence of water vapor a small fraction of the $O(^1D)$ reacts to produce the hydroxyl radical:

$$O_3 + h\nu \longrightarrow O(^1D) + O_2 \tag{1.1}$$
$$O(^1D) + H_2O \longrightarrow 2\,OH, \tag{1.2}$$

while most $O(^1D)$ collides with N_2 or with O_2 and is quenched to its ground state. The ground state oxygen atoms then rapidly recombine with O_2 molecules to reform ozone. The efficiency of the destruction of ozone and formation of OH in Reactions 1.1 and 1.2 decrease rapidly with height because the water vapor mixing ratio decreases rapidly with height in the troposphere.

During the oxidation of CO and methane by OH radicals, HO_2 radicals are formed. In the case of CO:

$$CO + OH \longrightarrow CO_2 + H \tag{1.3}$$
$$H + O_2 + M \longrightarrow HO_2 + M. \tag{1.4}$$

The hydrogen atom formed in Reaction 1.3 recombines quickly with O_2 so that Reaction 1.3 and Reaction 1.4 can be combined into:

$$CO + OH \xrightarrow{O_2,M} CO_2 + HO_2 \tag{1.5}$$

where M represents a third molecule, usually N_2 or O_2, that absorbs the excess internal energy and thereby stabilizes the HO_2 radical formed. HO_2 can oxidize NO to form NO_2 and OH. In the remote tropical marine boundary layer, where water vapor concentrations are high and in many places NO_x concentrations are low, the reaction of HO_2 with ozone plays a more important role:

$$O_3 + HO_2 \longrightarrow OH + 2\,O_2, \tag{1.6}$$

leading to a net loss of ozone. In the reaction chain consisting of Reactions 1.3, 1.4, and 1.6, OH and HO_2 are inter-converted, while the amount of HO_x=OH + HO_2 remains constant, i.e. the reaction chain is catalyzed by OH and HO_2:

$$CO + OH \xrightarrow{O_2,M} CO_2 + HO_2 \tag{1.5}$$
$$O_3 + HO_2 \longrightarrow OH + 2\,O_2 \tag{1.6}$$

$$\text{Net:}\quad CO + O_3 \xrightarrow{M} CO_2 + O_2$$

Ozone is formed in the troposphere mainly during daylight hours as a result of

the photolysis of NO_2 at wavelengths λ<424nm:

$$NO_2 + h\nu \longrightarrow NO + O \tag{1.7}$$
$$O + O_2 + M \longrightarrow O_3 + M. \tag{1.8}$$

Ozone can react with NO to reform NO_2:

$$O_3 + NO \longrightarrow NO_2 + O_2. \tag{1.9}$$

In extremely polluted environments, e.g. in urban centers, ozone can be titrated by NO, i.e. Reaction 1.9 can lead to large conversions of ozone to form NO_2, and consequently to lower ozone concentrations. Downwind from the sources, under sun-lit conditions, the photolysis of the NO_2 becomes more important in the balance with Reaction 1.9, and thus ozone can be formed, leading to high ozone episodes ("photosmog"). Reactions 1.7, 1.8, and 1.9 constitute a null cycle in the sense that in the entire cycle, neither NO nor NO_2 nor O_3 is formed or consumed in the net. This cycle works towards an equilibrium between NO and NO_2 during day-time:

$$NO_2\ (+O_2) \rightleftharpoons NO + O_3. \tag{1.10}$$

Ozone is formed in the troposphere, when HO_2 oxidizes NO instead of reacting with ozone. A typical reaction chain leading to ozone formation is the oxidation sequence of CO:

$$CO + OH \xrightarrow{O_2,M} CO_2 + HO_2 \tag{1.5}$$
$$HO_2 + NO \longrightarrow NO_2 + OH \tag{1.11}$$
$$NO_2 + h\nu \longrightarrow NO + O \tag{1.7}$$
$$O + O_2 + M \longrightarrow O_3 + M \tag{1.8}$$

$$\text{Net:}\quad CO + 2\,O_2 + h\nu \xrightarrow{M} CO_2 + O_3$$

In this catalytic reaction chain neither HO_2 nor OH nor NO_2 nor NO is consumed. The net formation of ozone is accomplished by the fact that NO is oxidized to NO_2 in Reaction 1.11 with the hydroperoxy (HO_2) radical (where the O_2 from 1.10 is omitted for better readability):

$$\begin{array}{ccccc} NO_2 & \rightleftharpoons & NO & + O_3. \\ \uparrow & & \downarrow & \\ & HO_2 & & \end{array}$$

If instead NO is converted to NO_2 in Reaction 1.9 with ozone, no net ozone formation results.

The entire catalytic reaction chain 1.7, 1.8, 1.5 and 1.11, can be interpreted as

two interwoven cycles, which can be written as (after Seinfeld and Pandis, 1998):

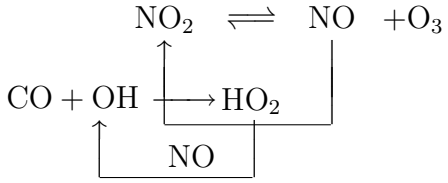

where the lower cycle is the slower one. Note, that in this annotation, the NO molecule on the lowest arrow is the same as the one on the right hand side of the highest arrow.

Another example of an oxidation chain, in which hydroxyl and hydroperoxy radicals and nitrogen oxides plays important roles is the oxidation of methane:

$$\mathrm{CH_4 + OH \xrightarrow{O_2,M} CH_3O_2 + H_2O} \tag{1.12}$$
$$\mathrm{CH_3O_2 + NO \longrightarrow CH_3O + NO_2} \tag{1.13}$$
$$\mathrm{CH_3O + O_2 \longrightarrow HCHO + HO_2} \tag{1.14}$$
$$\mathrm{HO_2 + NO \longrightarrow OH + NO_2} \tag{1.11}$$
$$\mathrm{2\,(NO_2 + } h\nu \mathrm{\longrightarrow NO + O)} \tag{from 1.7}$$
$$\mathrm{2\,(O + O_2 + M \longrightarrow O_3 + M)} \tag{from 1.8}$$

$$\text{Net:}\quad \mathrm{CH_4 + 2\,O_2 + 2}\,h\nu \mathrm{\xrightarrow{M} HCHO + 2\,O_3 + H_2O}$$

Formaldehyde, ozone, and water vapor are the first stable products of this reaction chain. Formaldehyde can be dissolved in liquid water. It is either scavenged from the atmosphere by rain or continues to react to form CO and then CO_2. Kanakidou and Crutzen (1999) and von Kuhlmann *et al.* (2004) estimated that about 90% of the methane oxidized globally contributes to the formation of CO, while this fraction was smaller for isoprene (C_5H_8) and other non-methane hydrocarbons.

In the methane oxidation chain, the hydroperoxy and also the methylperoxy (CH_3O_2) radicals oxidize NO to form NO_2. Because the rate coefficients of Reaction 1.11 and of Reaction 1.13 are much larger than the rate coefficient of Reaction 1.9, in remote settings, where peroxy radicals are competitive with O_3 in converting NO to NO_2, the equilibrium 1.10 has to be modified accordingly, even though the tropospheric mixing ratios of HO_2 and CH_3O_2 are much smaller than that of ozone (e.g. Crawford *et al.*, 1996).

If the ozone molecule resulting from the CO or the methane oxidation chain is photolyzed in the presence of water vapor, two OH radicals can eventually be formed which again can initiate the oxidation of two CO or CH_4 molecules. Unless the reaction chain is terminated, this would lead to the production of two O_3 molecules and so on until the complete depletion of the CO and CH_4. The reaction chains are terminated when one of the catalysts is removed, e.g. in one of the following

reactions:

$$HO_2 + OH \longrightarrow H_2O \quad (1.15)$$

$$HO_2 + HO_2 \xrightarrow{O_2,M} H_2O_2 + O_2 \quad (1.16)$$

$$NO_2 + OH + M \longrightarrow HNO_3 + M \quad (1.17)$$

$$HO_2 + CH_3O_2 \longrightarrow CH_3OOH + O_2 \quad (1.18)$$

Nitric acid (HNO_3) and hydrogen peroxide (H_2O_2) are highly water soluble and can be scavenged by precipitation. Methyl hydro-peroxide (CH_3OOH) is less water soluble and can be efficiently transported to the upper troposphere in deep convective clouds, where it can be photolyzed or react with OH, in both cases leading to an increase of upper tropospheric HO_x(=OH+HO_2). This addition of HO_x radicals can lead to enhanced photochemical ozone formation in the upper troposphere.

When NO_x levels are elevated, the fraction of NO_x which can be removed by Reaction 1.17 before contributing to the formation of ozone increases. The daily ozone production per unit NO_x is greater for lower NO_x levels, and increases if NO_x rich air masses are diluted during transport (Liu *et al.*, 1987). In the remote troposphere, the rate of gross ozone production increases almost linearly with NO_x concentration, while the gross loss rate varies little for a given moisture and temperature (i.e. at a certain height, see e.g. Liu *et al.*, 1992). The net in-situ photochemical ozone formation or loss rate is the difference between the gross production or formation and the gross loss rate at a certain location (net tendency = $P(O_3)$-$L(O_3)$).

A number of studies for the Pacific ocean (e.g. Liu *et al.*, 1983; Chameides *et al.*, 1987b; Crawford *et al.*, 1997b; Wang *et al.*, 2001; DiNunno *et al.*, 2003) using observations in combination with photochemical models found that in the relatively clean marine boundary layer gross ozone loss dominates over gross production, i.e. that the net tendency was negative. In the polluted marine boundary layer, on the other hand, e.g. in continental outflow from Asia, net ozone formation was found to take place (Crawford *et al.*, 1997a; DiNunno *et al.*, 2003; Kondo *et al.*, 2004b). The gross ozone loss decreases with increasing altitude, due to the strongly decreasing water vapor abundance. In the upper troposphere, net ozone formation was found in a number of campaigns over the Pacific Ocean (e.g. Chameides *et al.*, 1987a; Crawford *et al.*, 1997b; DiNunno *et al.*, 2003).

The terms contributing to the global budget of ozone are global gross photochemical formation and loss, downwards transport from the stratosphere, and dry deposition (see e.g. von Kuhlmann *et al.*, 2003a, for estimates of the tropospheric ozone budget). By far the largest terms in the budget are gross photochemical loss and production. These terms of the ozone budget are often calculated for the broader family of "odd oxygen" in order to eliminate the influence of fast null cycles (e.g. Crutzen *et al.*, 1999). Even for the remote troposphere, the average column gross production of ozone was estimated to be several times the average stratospheric intrusion flux of ozone (Bradshaw *et al.*, 2000). The magnitude of the net photochemical formation or loss term is much smaller than the magnitudes of the

gross terms. Estimates of the net global ozone formation or loss using global models differ between different models. While a majority of current global estimates yield net photochemical formation taking place in the troposphere, a number of estimates yield net photochemical ozone loss (IPCC, 2001).

An overview of some of the results from studies of photochemistry focusing on the tropical western Pacific is presented in Section 7.3. A number of aspects of the tropospheric "background" photochemistry which were not included in this introduction are highlighted in later chapters.

Chapter 2

The Cloud Resolving Chemistry Transport Model (CRCTM)

2.1 Overview

In this chapter the components of the cloud resolving chemistry transport model (CRCTM) are described. The model is based on a modified version of the Weather Research and Forecast (WRF) Model described in the next sections.

The advection of trace gases, of water vapor and of hydrometeors in the liquid and ice phase (subsequently referred to as "cloudmeteors") is calculated using the monotonic algorithm by Walcek (2000). For soluble trace gases the uptake into or onto, release from, transport together with, and mass transfer between different model categories of cloudmeteors (cloud droplets, rain, small ice particles, graupel, and snow) are calculated. A gas phase chemistry module based on the chemistry module from the Model of Atmospheric Transport and Chemistry - Max Planck Institute for Chemistry Version (MATCH-MPIC, Lawrence *et al.*, 1999b; von Kuhlmann *et al.*, 2003a, and references therein), a simple parameterization of the production of nitrogen oxide by lightning, and a dry deposition scheme have been implemented in order to study effects of the simulated cumulus cloud systems on tropospheric chemistry. The rate of change of the gas phase concentration of the i-th trace gas in the full model is calculated from its continuity equation:

$$\begin{aligned}\partial_t C_{i,g} = &- \nabla \cdot (\mathbf{v} C_{i,g}) + \partial_t C_{i,g}|_{vlsat} + \partial_t C_{i,g}|_{fixstrat} + \partial_t C_{i,g}|_{lno} \\ &+ \partial_t C_{i,g}|_{turb} + \partial_t C_{i,g}|_{solu} + \partial_t C_{i,g}|_{drydep} + \partial_t C_{i,g}|_{chem} \\ &+ \partial_t C_{i,g}|_{bc} \end{aligned} \tag{2.1}$$

where ∂_t is the partial derivative with respect to time, $\mathbf{v} = (u, v, w)$ is the three dimensional wind vector, $\partial_t C_{i,g}|_{vlsat}$ is the rate of change due to the vertical advection by the large scale vertical motion which is not reproduced by the CRM (see Sect. 3.2), $\partial_t C_{i,g}|_{fixstrat}$ is a rate implied by prescribing stratospheric concentrations of some gases as upper boundary conditions and is zero in the troposphere (see Sect. 7.2),

$\partial_t C_{i,g}|_{lno}$ is the rate of NO production by lightning (Sect. 2.6), $\partial_t C_{i,g}|_{turb}$ is the rate of change due to parameterized turbulent mixing by sub-grid scale eddies (Sect. 2.2.1), $\partial_t C_{i,g}|_{solu}$ is the uptake or release rate of soluble gases by or from cloudmeteors (Sect. 2.3), $\partial_t C_{i,g}|_{drydep}$ is the dry deposition rate (Sect. 2.5), $\partial_t C_{i,g}|_{chem}$ is the rate of change due to gas phase chemical reactions (Sect. 2.4), and $\partial_t C_{i,g}|_{bc}$ is implied by specifying trace gas concentrations at the model's lateral boundary and is zero in the interior of the domain (Sections 3.3 and 7.2).

For each water soluble tracer additional continuity equations for the trace gas concentrations (per volume of air or grid box volume) taken up by cloudmeteors are solved:

$$\partial_t C_{i,j} = - \nabla \cdot (\mathbf{v} C_{i,j}) + \partial_t C_{i,j}|_{turb} + \partial_t C_{i,j}|_{solu} + \partial_t C_{i,j}|_{bc} \tag{2.2}$$

where the index j corresponds to the five cloudmeteor categories in the model (see Sect. 2.2.2). In Equations 2.2, the tendency $\partial_t C_{i,j}|_{solu}$ comprises contributions due to the uptake from or the release to the gas phase, due to the mass transfer between different cloudmeteor categories, and due to the vertical advection of the falling cloudmeteors (see Sect. 2.3). For a trace gas that is retained in cloudmeteors upon freezing, five additional equations are solved ($j = 1, 5$), and for a trace gas that is completely degassed only two additional ($j = 1, 2$) equations corresponding to the two liquid-phase hydrometeor categories are solved. At the domain boundaries, the cloudmeteor concentrations as well as the concentrations of trace gases taken up by cloudmeteors $C_{i,j}$ are set to zero, i.e. it is assumed that no clouds are advected into the domain. This is a common assumption in CRM studies and will briefly be discussed in Section 3.5.

The continuity equations are integrated numerically using an operator splitting technique in which the concentrations are updated immediately after calculating a rate and the next rate is calculated based on this updated value. The order of the terms in Equation 2.1 is identical to the sequence of calculating the rates in the model except for the last (lateral boundary conditions) term. Equations 2.1, and 2.2 together with the WRF Equations 2.4 to 2.9 are the prognostic equations of the CRCTM. The model equations constitute a nonlinear initial-boundary value problem. Because of the term $\partial_t C_{i,g}|_{chem}$, the equations for different trace gases i in the chemistry runs are coupled. For the sake of sensitivity studies individual terms in Equations 2.1 can easily be omitted or changed.

The model is mainly coded in FORTRAN90 using a modular structure and is parallelized using MPI (Message Passing Interface). A flexible integration method is used in the chemistry module considerably simplifying the implementation of new sets of trace gases and/or reactions.

2.2 The Weather Research and Forecast (WRF) Model

2.2.1 Basic Description

The cloud resolving chemistry transport model (CRCTM) is based on a modified height coordinate 2 or 3-D prototype version of the recently developed non-hydrostatic, compressible Weather Research and Forecast (WRF) model. The basic equations of the WRF model are stated below and can be found in Skamaraock *et al.* (2001). The numerics are described in Wicker and Skamarock (2002). The WRF model is developed in a collaborative effort by the National Center for Atmospheric Research (NCAR), the National Centers for Environmental Prediction (NCEP), the Air Force Weather Agency, Oklahoma University and other university scientists. The source code can be obtained from the WRF model web site at *http://wrf-model.org*. The CRCTM used in this study was derived from a version of the WRF model used at the Geophysical Fluid Dynamics Laboratory (GFDL) in Princeton, New Jersey, where a microphysics scheme was implemented which is described below. An initial setup for the TOGA COARE case described in Section 3.1, which was modified in the framework of this thesis, was also provided by scientists at GFDL.

The prognostic model equations are formulated in terms of the density coupled variables $\mathbf{V}, U, V, W, \Theta$, and Q_i which have conservation properties:

$$\mathbf{V} = \rho\mathbf{v} = (U, V, W), \quad \Theta = \rho\theta, \quad Q_j = \rho q_j \tag{2.3}$$

where ρ is the density of dry air, $\mathbf{v}$ is the three dimensional wind vector, θ is the potential temperature, and $q_j,\ j = 0, 5$ are the mixing ratios of water vapor (q_0) and of the five cloudmeteor categories in the model. Assuming a grid with equidistant grid spacings and constant terrain height, the prognostic non-hydrostatic equations are

$$\partial_t U + \nabla \cdot (\mathbf{v}U) + \gamma R\pi\partial_x\Theta' = F_U \tag{2.4}$$
$$\partial_t V + \nabla \cdot (\mathbf{v}V) + \gamma R\pi\partial_y\Theta' = F_V \tag{2.5}$$
$$\partial_t W + \nabla \cdot (\mathbf{v}W) + \gamma R\pi\partial_z\Theta' - g\left(\frac{\overline{\rho}\pi'}{\overline{\pi}} - \rho'\right) = F_W \tag{2.6}$$
$$\partial_t\Theta + \nabla \cdot (\mathbf{v}\Theta) = F_\Theta \tag{2.7}$$
$$\partial_t\rho + \nabla \cdot \mathbf{V} = 0 \tag{2.8}$$
$$\partial_t Q_j + \nabla \cdot (\mathbf{v}Q_j) = F_{Q_j} \tag{2.9}$$

where $\pi = (p/p_0)^\kappa$, $\kappa = R/c_p$, R is the gas constant for dry air, g is the acceleration due to gravity, and $\gamma = c_p/c_v = 1.4$ is the ratio of the heat capacities for dry air. Perturbation variables are defined as deviations from a time invariant hydrostatically balanced reference state such that $p = \overline{p}(z) + p'$, and $\Theta = \overline{\rho}(z)\overline{\theta}(z) + \Theta'$. The pressure

gradient term in the momentum equations is formulated using the relation

$$\nabla p = \gamma R \pi \nabla \Theta. \tag{2.10}$$

Pressure is obtained from the diagnostic equation of state:

$$p = p_0 \left(\frac{R\Theta}{p_0} \right)^{\gamma}. \tag{2.11}$$

Thus $p \propto \Theta^{\gamma}$ and Equation 2.7 takes the place of the pressure equation commonly solved in compressible models.

The terms F_U, F_V, and F_W on the right hand side of the momentum Equations 2.4, 2.5, and 2.6 contain contributions form the sub-grid turbulence parameterization described below. Here, the transfer of horizontal momentum at the Earth's surface was parameterized using a drag law formulation (e.g. Stull, 1988) with a drag coefficient $C_D = 0.001$ for water surfaces. The Coriolis force was neglected. F_Θ in Equation 2.7, and F_{Q_j} in Equations 2.9 contain contributions from the sub-grid turbulence parameterization and from the microphysics parameterization scheme (see Section 2.2.2). The latent and the sensible heat fluxes are calculated based on the Monin-Obukhov similarity theory. In the setup for this study, sea surface temperatures were prescribed from observed values. Towards the model top, above the tropopause, artifical damping was introduced by increasing the eddy-diffusion coefficients in the turbulence parameterization. The lateral boundary conditions (see Section 3.3) were either periodic or specified. In the framework of this study, a so-called semi-prognostic model setup (see Section 3.2) was used and additional nudging and "large scale advection" terms were included in F_U, F_V, F_θ, and F_{Q_i} on the right hand side of Equations 2.4, 2.5, 2.7, and 2.9.

The advection of water vapor and of cloudmeteors was calculated using the Walcek (2000) monotonic advection scheme instead of the third order Runge-Kutta scheme which was implemented in the WRF model prototype. The Walcek (2000) scheme was derived based on the flux form of the advection equation, but uses mixing ratios and air densities as input variables and calculates mixing ratios. So-called dimensional densities are calculated inside the scheme and inserted into the advection equation. These dimensional densities are discrete solutions of the continuity equation for air. Since the continuity equation for air is solved again outside the scheme and since this solution is not necessarily consistent with the dimensional densities, mass is only conserved to a good approximation (average error estimated $<0.5\%$ day^{-1} including small errors from the sub-grid turbulence parameterization scheme). An exactly mass conserving advection scheme for the WRF model has very recently been developed at NCAR, but was not available for this study. The third order Runge-Kutta scheme was used to solve the momentum equations and the theta equation using fifth/third order spatial discretizations for horizontal/vertical advection terms. Short-wave radiation was parameterized using the Goddard short wave scheme (Chou *et al.*, 1998) and for parameterizing long-wave radiation the RRTM scheme (Mlawer *et al.*, 1997) was used in the simulations. The effects of sub-grid

scale motions were parameterized as "turbulent diffusion" applying Smagorinsky's closure scheme (e.g. Takemi and Rotunno, 2003). The Hong and Pan (1996) boundary layer parameterization scheme was adapted for the CRCTM, but was not used in the standard simulations.

2.2.2 Microphysics Parameterization

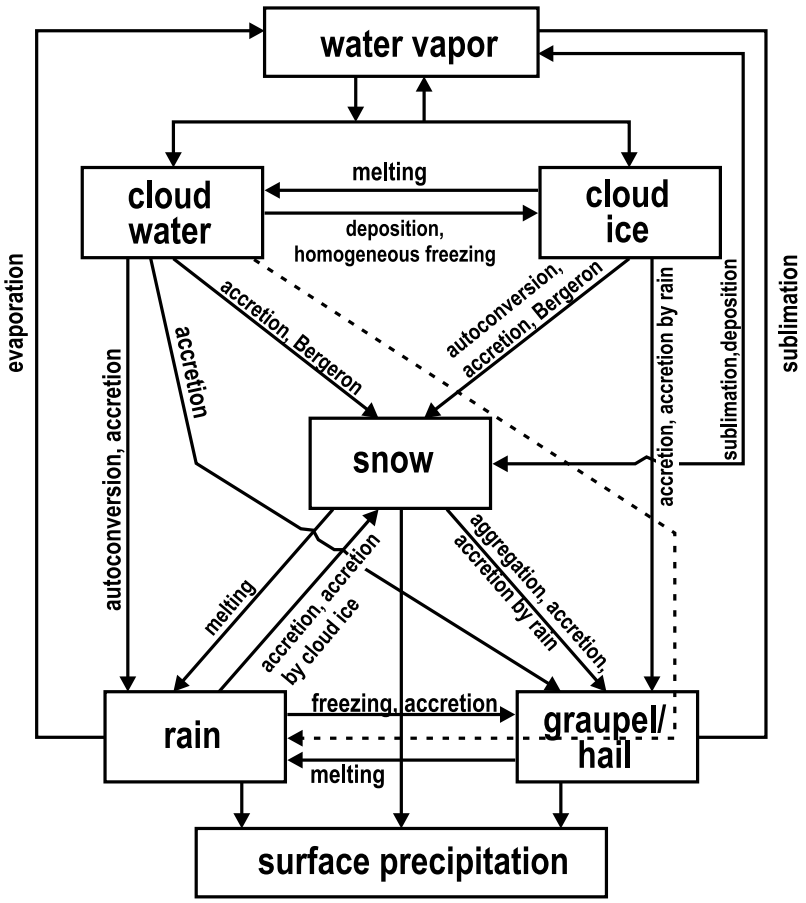

Figure 2.1: Processes simulated in the microphysics scheme. After Lin *et al.* (1983).

Two similar microphysics parameterization schemes were adapted for the CRCTM. The first scheme is described by Krueger *et al.* (1995) and based on the studies by Lord *et al.* (1984) and Lin *et al.* (1983). The second scheme (Lin *et al.*, 1983) is part of the WRF model distribution. Here, in most runs and unless otherwise stated, the first scheme was used. In both schemes a distinction is made between five cloud-meteor categories: cloud droplets (cloud water), rain, small ice particles (cloud ice), graupel, and snow. The schemes are so-called single moment or bulk schemes i.e. the gridbox average masses of cloudmeteors expressed as mixing ratios are prognostic model variables while the size-distributions of rain drops, graupel, and snow are diagnosed assuming exponential (Marshall-Palmer) size distributions. In both schemes the sedimentation of rain drops, snow, graupel, and cloud ice is considered. For cloud

ice particles, fixed diameters are prescribed. Auto-conversion concepts are used to parameterize collision-coalescence and collision-aggregation processes and a number of accretion processes are parameterized (see Figure 2.1). Here, for both schemes, the densities for cloud ice, snow, and graupel were ρ_i=917 kg m^{-3}, ρ_s=100 kg m^{-3}, and ρ_g=400 kg m^{-3}; the intercept parameters of the size distributions for rain, snow, and graupel were n_{0r}=8·10^6 m^{-4}, n_{0s}=3·10^6 m^{-4}, n_{0g}=4·10^6 m^{-4}; and the radius of the model cloud ice particles was r_i=50 μm. Differences between the schemes are due to the parameterization of the growth of cloud ice related to the Wegener-Bergeron-Findeisen process: The so-called "saturation adjustment" procedures which are used to calculate the re-distribution of mass between cloud water, cloud ice, and water vapor differ. For usage in the CRCTM, the Krueger *et al.* (1995) scheme was adjusted to guarantee mass conservation, so that water mass can only be lost due to precipitation. The Lin *et al.* (1983) scheme included in an early WRF model prototype version was adjusted to consider the heat loss during sublimation and evaporation calculated in the saturation adjustment procedure, thus reducing a known bias. This change was included into recent versions of the WRF model distribution.

2.3 Scavenging of Soluble Trace Gases

For soluble trace gases the uptake by, release from, sedimentation together with, and mass transfer between different model categories of cloudmeteors in the liquid or ice phase is parameterized. Aqueous phase reactions except for the hydrolysis of N_2O_5 discussed in Section 2.4 are not included in the CRCTM and the dissociation of HNO_3 is only considered implicitly in the calculation of effective Henry's Law constants. It is assumed that the entire mass of trace gases which are dissolved or have been taken up by ice associated with a certain cloudmeteor category is released to the gas phase upon the complete evaporation or sublimation of meteors of this category. The rate of change $\partial_t C_{i,g}|_{solu}$ of the gas phase concentration $C_{i,g}$ of a soluble gas or a gas that can be taken up by ice in Equation 2.2 is

$$\partial_t C_{i,g}|_{solu} = -\sum_{j=1}^{5} \partial_t C_{i,j}|_{mt} + \partial_t C_{i,g}|_{mp}(evap,\, sub). \tag{2.12}$$

Here $\partial_t C_{i,j}|_{mt}$ is the rate of uptake by cloudmeteors of category j (for release $\partial_t C_{i,j}|_{mt} < 0$), and $\partial_t C_{i,g}|_{mp}(evap,\, sub)$ is the source rate due to the evaporation or the sublimation of cloudmeteors. The concentrations $C_{i,j}$ are defined per grid box volume or volume of air. The rate of change of the concentration of a trace gas taken up by cloudmeteors of model category j is

$$\partial_t C_{i,j}|_{solu} = \partial_t C_{i,j}|_{mt} + \partial_t C_{i,j}|_{sed} + \partial_t C_{i,j}|_{mp} - \partial_t C_{i,g}|_{mp}(evap,\, sub), \tag{2.13}$$

where $\partial_t C_{i,g}|_{mt}$ is the rate (including sign) for the mass transfer between the meteors and the gas phase, $\partial_t C_{i,j}|_{sed}$ is the rate due to transport together with sedimenting cloudmeteors, $\partial_t C_{i,j}|_{mp}$ is the rate due to mass transfer between different hydrom-

eteor or ice-meteor categories, and $\partial_t C_{i,g}|_{mp}(evap,\, sub)$ is the tendency due to the evaporation or the sublimation of cloudmeteors. $\partial_t C_{i,g}|_{mp}(evap,\, sub)$ is zero unless cloudmeteors of a certain category entirely evaporate or sublimate during an integration timestep (compare discussion at the end of Section 2.3.1). As has been suggested by Barth *et al.* (2001), the sedimentation rate is calculated using the mass weighted mean terminal velocity $\overline{u}_{\infty j}$ of the falling cloudmeteors (all except cloud droplets, where sedimentation is neglected):

$$\partial_t C_{i,j}|_{sed} = \partial_z \left(\overline{u}_{\infty j} C_{i,j} \right). \tag{2.14}$$

The trace gas mass transfer between different cloudmeteor categories is assumed to be proportional to the mass transfer of liquid or frozen water between the different categories as calculated by the microphysics parameterization scheme (see Section 2.2.2). The rate of change due to the mass transfer between different categories can be expressed as:

$$\partial_t C_{i,j}|_{mp} = k_{ret_i} \sum_{k=1}^{5} \left(R_{k,j} \frac{C_{i,k}}{q_k} + R_{j,k} \frac{C_{i,j}}{q_j} \right) \tag{2.15}$$

where $R_{k,j} = \partial_t q_j|_{k \to j}$ is the rate of liquid or frozen water transfer from meteors of category k to meteors of category j due to a microphysical process; k_{ret} is a dimensionless retention fraction and is one for all processes except freezing. When mass is transferred from the liquid to the ice phase, absorbed trace gases are allowed to escape to the gas phase depending on the gas-specific retention fraction which is multiplied with the transfer rate (see discussion in Section 2.3.2).

2.3.1 Mass Transfer between Gas and Liquid Phase

The uptake and release of trace gases is assumed to be limited by the mass transfer across the interface of the hydrometeors and by the diffusion of the trace gas in the air surrounding the meteors and is parameterized using first-order rate coefficients (Schwartz, 1986; see also e.g. Seinfeld and Pandis, 1998) . The rate of change of the aqueous phase concentration of the ith trace gas for hydrometeor category j is

$$\partial_t C_{i,j}|_{mt} = f_{i,j} k_{i,j} L_j C_{i,g} - \frac{f_{i,j} k_{i,j}}{K_{Hi} R T} C_{i,j}, \tag{2.16}$$

where $f_{i,j}$ is the ventilation coefficient, L_j is the liquid water volume fraction of hydrometeors of category j, K_{Hi} is the temperature dependent Henry's Law constant (see Table 2.1), T is the temperature and R is the universal gas constant. Subsequently the indices i and j will be dropped. The first order rate constant k is calculated from

$$k = \left(\tau_{Dg} + \tau_{int} \right)^{-1}, \tag{2.17}$$

Table 2.1: Properties of water soluble gases: H

	Henry's Law Coefficient (1)		
	H_{298K} (mol l^{-1} atm^{-1})	$\Delta H/R$ (K)	Reference
HNO_3(2)	$2.1 \cdot 10^5$	8700	Schwartz and White (1981)
H_2O_2	$7.4 \cdot 10^4$	6615	Lind and Kok (1986)
HCHO(3)	$3.2 \cdot 10^3$	6800	Staudinger and Roberts (1996)
CH_3OOH	$3.1 \cdot 10^2$	5200	O'Sullivan *et al.* (1996)
CH_3OH	$2.2 \cdot 10^2$	5200	Snider and Dawson (1985)

(1) Temperature dependence: $H(T) = H_{298K} e^{-\Delta H/R(1/T-1/298)}$

(2) For HNO_3 the effective Henry's Law constant $H^{eff} = H(1 + K_A/[H^+])$ where $K_A = 15.1$ (Wurzler, 1995) is used for $[H^+] = 10^{-5}$ (pH=5).

(3) Diol formation is included.

where τ_{Dg} is a characteristic timescale for gas diffusion and τ_{int} is a characteristic timescale for the mass transfer across the interface of a hydrometeor:

$$\tau_{Dg} = \frac{\overline{a}^2}{3D_g}, \quad \tau_{int} = \frac{4\overline{a}}{3\nu\alpha_{acc}}, \tag{2.18}$$

where $\overline{a}$ is the mass mean radius of the hydrometeors (discussed below), D_g is the gas phase diffusivity of the trace gas, α_{acc} is the gas-dependent mass accommodation coefficient (the fraction of collisions resulting in uptake, see Table 2.2) and $\nu = \sqrt{8RT/\pi M}$ is the mean molecular velocity, where M is the molar mass of the trace gas. For the mass transfer calculations $\overline{a} = 10\,\mu$m for cloud droplets, and $\overline{a} = 2/\lambda$ for rain drops, where λ is the slope of the raindrop size distribution calculated in the microphysics scheme. The gas phase diffusivity is calculated from (Massman, 1998)

$$D_g(T,\rho) = D^0_{H_2O}\sqrt{\frac{M_{H_2O}}{M}}\left(\frac{\rho_0}{\rho}\right)\left(\frac{T}{T_0}\right)^{1.81}, \tag{2.19}$$

where the index 0 indicates values at T_0=273.15 K and p_0=1013 hPa. Typical values are of the order of 0.1 cm^2 s^{-1}. In deriving Equation 2.19 the assumption was used that the diffusivity of a particular gas with molar mass M_k can be inferred by scaling a measured diffusivity of a gas with molar mass M_u by $\sqrt{M_k/M_u}$. This assumption can lead to errors up to 23% (Massman, 1998). The ventilation coefficient is calculated from the empirical expression (Pruppacher and Klett, 1997):

$$f = 0.78 + 0.308\, N_{Sc,v}^{1/3} N_{Re}^{1/2} \tag{2.20}$$

where $N_{Sc} = \nu_a/D_g$ is the Schmidt number and $N_{Re} \approx 2\overline{u}_\infty\overline{a}/\nu_a$ is the Reynolds number, ν_a is the kinematic viscosity of air and u_∞ is the terminal velocity of the hydrometeors.

Table 2.2: Properties of water soluble gases: α_{acc}

	Mass Accomodation Coefficient [a,b]			
	α_{acc} at 273 K	ΔH_{obs} (kcal mol^{-1})	ΔS_{obs} (cal mol^{-1} K^{-1})	Reference
HNO_3	0.157	−6.6	−27.6	Jayne *et al.* (1991)
H_2O_2	0.234	−5.5	−22.5	Jayne *et al.* (1991)
HCHO	0.040	–	–	DeMore *et al.* (1997)
CH_3OOH	0.012	−6.5	−32.5	Magi *et al.* (1997)
CH_3OH	0.056	−8.0	−34.9	DeMore *et al.* (1997)

[a] Temperature dependence: $\alpha_{acc} = a/(1+a)$ where $a = exp(-\Delta G^0_{obs}/RT)$ and $\Delta G^0_{obs} = \Delta H_{obs} - \Delta S_{obs} T$).

[b] α_{acc} is assumed to be independent of drop size.

For cloud droplets in the model $f = 1$ because sedimentation is not considered. With $\alpha > 10^{-2}$, k is of the order of $10^5\,s^{-1}$ to $10^6\,s^{-1}$. Since L is of the order of 10^{-6}, the one way fractional removal rate of a trace gas into the aqueous phase, $\Lambda = fkL$ in Equation 2.16, is of the order of 10^{-1} s to 1 s. Consequently, if enough cloud droplets are present, the aqueous phase concentration $[A]$ calculated from Equation 2.16 rapidly converges towards the equilibrium ($t \to \infty$) solution:

$$[A] = K_H p_g, \tag{2.21}$$

where $p_g = C_g RT$. Equation 2.21 is Henry's Law.

For rain drops on the other hand, the trace gas exchange with the gas phase is typically limited by the gas phase diffusion in the air surrounding the drop. E.g. for a rain mixing ratio q_r=1.5g kg^{-1} and with the values from Section 2.2.2: $\overline{a} \approx$ 1mm. For α_{acc}=0.2, T=285K and ρ=0.9 kg m^{-3}: k$\approx$32 s^{-1}. Without considering the ventilation effect follows $\Lambda \approx 4.4 \cdot 10^{-5}$ and with $f \approx 12$: $\Lambda \approx 5.4 \cdot 10^{-4}\,s^{-1}$. Consequently the e-folding times for irreversible uptake are $\tau \approx$6.3 h if ventilation is not considered, and $\tau \approx$30 min if ventilation is considered. These timescales are also approximately valid for the reversible mass transfer of highly soluble gases. Model calculated fall velocities of rain drops are in the range ∼3–8 m s^{-1}. Consequently, for rain drops, the concentrations of soluble gases will generally not reach Henry's Law equilibrium. Yin *et al.* (2001) and Barth *et al.* (2001) have shown that assuming Henry's Law equilibrium in model studies of trace gas transport in deep convective clouds can lead to an over-estimation of gas scavenging. Yin *et al.* (2001) used spectrally resolved calculations of gas scavenging and Barth *et al.* (2001) used mass mean radii for the mass transfer calculations. Equation 2.18 was originally derived for a single hydrometeor radius but was subsequently used inserting either effective or mass mean radii (effective radius: third divided by second moment; mass mean radius: fourth divided by third moment of the size distribution). Barth *et al.* (2001) inserted mass mean radii into Eq. 2.18 and did not include ventilation coefficients in the mass

transfer Equation 2.16. For rain drops, this leads to a large underestimation of the fractional removal rate of a gas into the aqueous phase, but if additionally f is calculated using mass mean radii as done in this study, the fractional removal rates are closer to (overestimated by ∼30-40%) spectrally calculated fractional removal rates based on typically observed rain drop size distributions (R. von Kuhlmann, pers. comm., 2004).

Wurzler (1997) considered 2-D cloud resolving model calculations of HNO_3 scavenging by a single cloud using a detailed drop size-resolved microphysics parameterization and compared these to calculations in which she used a bulk parameterization based on the Marshall-Palmer size distribution. The rain rate was 50% lower using the bulk scheme and about 46% less HNO_3 was removed. Assuming the same rainfall rate, the wet deposition of HNO_3 using the bulk approach was 28% lower compared to when the detailed approach was used. The ventilation of falling hydrometeors was considered in the study by Wurzler (1997).

Generally, in numerical models the amount of liquid water and the size distribution of hydrometeors at a given height are sensitive to the specific parameterization scheme for both detailed and bulk parameterizations. Using either mass mean or effective radii for calculating the mass transfer between the liquid and the gas phase introduces an additional source of uncertainty in studying the influence of deep convection on water soluble trace gases. A sensitivity study testing the influence of omitting the ventilation factor is presented in Chapter 6. In the present study the CRM was operated in the so-called semi-prognostic manner (see Section 3.2). Consequently, the amount of surface precipitation was largely constrained by the model input data rather than by properties of the microphysics scheme.

The release of dissolved trace gases to the gas phase caused by changes of cloud or rain water mass related to evaporation is determined by the mass transfer equation (Eq. 2.16), unless either cloud or rain water evaporates completely, in which case trace gases are assumed to be entirely released (expressed by the tendency $\partial_t C_{i,g}|_{mp}(evap, sub)$ in Equations 2.12 and 2.13). For highly soluble trace gases, such as HNO_3, at tropospheric mixing ratios the equilibrium ratio of the concentration in the aqueous phase to that in the gas phase remains at close to 100% even at relatively low cloud water contents, and assuming the amount of tracer released from hydrometeors during evaporation to be proportional by mass, as has occasionally been done in larger-scale models, would possibly lead to an underestimate of scavenging by rain, since for large drops rapid adjustment to Henry's Law equilibrium following the release is inhibited as the uptake rate is assumed to be kinetically limited by the gas phase diffusion in the vicinity of the drops. Here, uncertainties arise due to using a bulk vs. a spectral representation and due to assuming complete release upon evaporation rather than sticking of dissolved trace gas to the condensation nucleus (Wurzler, 1995).

2.3.2 Ice Phase

Knowledge about the influence of the ice phase on trace gases has been increasing during recent years, yet a number of large uncertainties remain. The lack of a satisfactory theoretical framework for describing some of the relevant processes in cloud resolving models is another problem, which will be discussed in some detail.

For HNO_3 and H_2O_2 there is evidence of direct uptake from the gas phase. A number of laboratory studies have shown that HNO_3 is efficiently taken up by ice (e.g. Diehl *et al.*, 1995; Zondlo *et al.*, 1997; Abbatt, 1997; Hynes *et al.*, 2002). An exception is the study by Hudson *et al.* (2002). Tabazadeh *et al.* (1999) extrapolated the results of Abbatt (1997) to atmospheric HNO_3 concentrations. Assuming Langmuir (temperature dependent, reversible, monolayer) adsorption they calculated that in precipitating cirrus clouds only a small fraction of the gas phase HNO_3 is adsorbed on ice, while in clouds with higher icemeteor number densities and smaller radii and at cold temperatures this fraction is close to one. Recent in-situ studies (Popp *et al.*, 2004; Ziereis *et al.*, 2004) indicate Tabazadeh *et al.* (1999) may even have overestimated the fractional surface coverage of HNO_3 adsorbed on ice. Nevertheless, Popp *et al.* (2004) and Ziereis *et al.* (2004) found that in some cold cirrus environments with high surface areas, 100% of the total HNO_3 was partitioned on or in ice. Results of some recent in-situ measurements (Kondo *et al.*, 2003; Popp *et al.*, 2004; Ziereis *et al.*, 2004) indicate that at temperatures above ∼200–220K only a small fraction of HNO_3 is taken up by cloud ice particles; at lower temperatures the fractional ice surface coverage by HNO_3 molecules increases significantly and uptake is more efficient. In contrast, Meilinger *et al.* (1999) found, based on in-situ measurements that the uptake of HNO_3 by ice was very inefficient even at ∼196K. The number of in-situ measurements is still small and at this point any conclusions drawn should still be considered preliminary.

The uptake of H_2O_2 was studied by Conklin *et al.* (1993) in a flow tube packed with 200 μm ice-spheres. Subsequently Meier and Hendricks (2002) calculated adsorption free energies based on the results of Conklin *et al.* (1993) which were below the values for HNO_3 used by Tabazadeh *et al.* (1999) but above the adsorption enthalpy values reported by Bartels-Rausch *et al.* (2002) for HNO_3 on crystalline ice. Note that Tabazadeh *et al.* (1999) used adsorption free energy instead of adsorption enthalpy to calculate the equilibrium adsorption constant using a formula that is valid for adsorption enthalpy. Because HNO_3 was shown to be more readily adsorbed on ice than H_2O_2 (see e.g. Clegg and Abatt, 2001), the estimate by Meier and Hendricks (2002) is not used here. Instead the same adsorption enthalpy is used for H_2O_2 as was found for HNO_3 by Bartels-Rausch *et al.* (2002) in most of the simulations; ΔH_{ads}=-44kJ mol^{-1}. This results in an overestimation of the adsorption of H_2O_2. A sensitivity run completely neglecting the uptake of H_2O_2 on ice (and additionally not allowing any retention during hydrometeor freezing) was conducted in order to asses the consequences (see Section 11.3).

For the uptake on ice the same mass transfer limitations apply as for liquid hydrometeors. An equation similar to Equation 2.16 has been derived assuming

Langmuir adsorption with dissociation (see Appendix A):

$$\partial_t C_{i,j}|_{mt} = f_{i,j} k_{i,j} L_j \left(C_{i,g} - \frac{1}{K_{Li} RT} \frac{\theta_{i,j}^2}{(1-\theta_{i,j})^2} \right), \tag{2.22}$$

where K_{Li} is the equilibrium constant:

$$K_{Li} = K_{Li}^{ref} \sqrt{\frac{T_{ref}}{T}} \exp\left(\frac{\Delta H_{ads}}{R} \left(\frac{1}{T_{ref}} - \frac{1}{T} \right) \right). \tag{2.23}$$

$f_{i,j}$ and $k_{i,j}$ are as in Equation 2.16 and L_j is the ice volume fraction of ice category j. The surface coverage is calculated from (see Tabazadeh *et al.*, 1999):

$$\theta_{i,j} = \frac{\beta}{s_j \alpha \sigma} RT C_{i,j} \tag{2.24}$$

where α=0.27 is the fraction of surface sites that are assumed to be available for adsorption, σ=10^{15} is the surface site density and s_j is the ice surface area density. β=$9.6565 \cdot 10^{18} T^{-1}$ is a conversion factor.

For cloud ice and snow, s_j is parameterized using the empirical relationship from Heymsfield and McFarquhar (1996):

$$s_j = 2 \cdot 10^{-4} \ \mathrm{IWC}^{0.9} \tag{2.25}$$

where IWC is the ice content in g m^{-3}. Graupel (discussed in detail below) is assumed to have the surface area density of spheres with radius $\overline{a} = 2/\lambda$, where λ is the slope of the graupel size distribution.

Trace gases absorbed by hydrometeors are usually assumed to be well mixed inside the meteors, either due to diffusion in small droplets or due to turbulent mixing in larger drops. Because the diffusion coefficient for gases in solid ice is a few orders of magnitude smaller than that in liquid water, trace gases could theoretically be 'buried' inside (larger) icemeteors. Burial could e.g. occur during the collection of super-cooled droplets by icemeteors with subsequent freezing (riming). During riming, latent heat is released and the surface temperature of the icemeteor can be either above 0°C (wet growth riming) or below 0°C (dry growth riming). The chemical retention during dry growth riming has been investigated recently e.g. by Stuart and Jacobson (2004). In the CRCTM, currently the same gas dependent retention coefficients are applied in Equation 2.15 for the wet and the dry process and for all other freezing processes.

Burial could be considered a special case of retention. Retention could also occur as a consequence of strong adsorption on ice surfaces. Clegg and Abatt (2001) suggested that measured retention fractions of H_2O_2 may be low compared to those of strong acids (HCl, HNO_3) because of weaker adsorption on the ice surface.

Burial would lead to concentration gradients inside the icemeteors and prevent

equilibration between concentrations inside the icemeteor and the gas phase. In this case, the mass transfer between the gas and the liquid phase would be limited by diffusion inside the icemeteors and Equation 2.22 would not be applicable. If on the other hand diffusivities in ice were sufficiently large to allow equilibration, then trace gases could not be buried in ice. In this case the uptake of trace gases would depend on the mass of the ice and not the surface area. Based on the observations cited above, for cirrus particles, however, the fraction of HNO_3 taken up by ice compared to HNO_3 remaining in the gas phase appears to be determined by the surface area and not the ice mass.

The diffusion coefficient for HNO_3 in ice is still a subject of debate: e.g. Dominé and Thibert (1996, 1998) estimate D_{ice,HNO_3} to be about $10^{-10}\,cm^2\ s^{-1}$, while Sommerfeld *et al.* (1998) estimates an upper limit of $10^{-12}\,cm^2\ s^{-1}$. Furthermore, the effects of surface diffusion along crystalline boundaries are thought to be important. For comparison: a typical value for the aqueous-phase diffusion coefficient in liquid water is $D_{aq} = 10^{-5}\,cm^2\ s^{-1}$.

The solution of the diffusion equation for a spherical particle yields the following timescale (see e.g. Seinfeld and Pandis, 1998):

$$\tau_{diff} = \frac{a^2}{\pi^2 D_{diff}}. \tag{2.26}$$

For a theoretical $10\,\mu$m ice sphere with $D_{ice,HNO_3} = 10^{-10}\,cm^2\ s^{-1}$ the time scale is τ_{diff} ≈17min, which is already long compared to the time scales in Eqs. 2.18. Unfortunately, burial effects are not readily parameterized in cloud resolving models. In the present study, Equation 2.22 was applied to calculate the uptake by and release from cloud ice and snow.

In most simulations, only the burial of HNO_3 in graupel is parameterized by assuming quasi-irreversible uptake from the gas phase. This is achieved by allowing 100 monolayers of HNO_3 to exist on graupel particles and can lead to an overestimation of HNO_3 uptake from the gas phase. A sensitivity study assuming single monolayer uptake for HNO_3 on graupel was conducted in order to estimate the effect of this assumption (see Section 11.2). Currently, in the CRCTM no distinction is being made between HNO_3 enclosed in icemeteors and HNO_3 available at the surface. Furthermore, the uptake of HNO_3 on cloud ice particles and on snow is treated as a reversible process, thus in principle allowing the release of HNO_3 from the ice phase in spite of the retention coefficient being set to one. This is a problem which to the author's knowledge has not yet been solved in cloud resolving model studies. Yin *et al.* (2002), who studied the effect of the ice phase on convective transport in an axis-symmetric cloud model, assumed uptake on ice to be generally irreversible, in principle allowing ice to act as an infinite trace gas sink in the model. Barth *et al.* (2001) did not assume adsorption on ice in their CRM study of the effects of retention. One possible direction for future studies using bulk microphysics schemes to study trace gases which can be taken up by ice from the gas phase would be to include one variable for the amount of trace gas entrapped in ice and one variable for

the amount of trace gas available for reversible exchange between gas and ice phase at the surface of the icemeteors, i.e. to include two trace gas variables for each frozen hydrometeor category in the model (6 ice-phase related variables for each trace gas compound taken up by ice from the gas phase in the 5 cloudmeteor category single moment microphysics scheme). However, this approach would complicate the solution of the equation for the mass transfer between different cloudmeteor categories due to cloud microphysical processes (Equation 2.15), most likely introducing new uncertainties.

In the CRCTM, a fraction of H_2O_2 was assumed to be retained in ice upon freezing, but H_2O_2 was not assumed to be buried inside frozen hydrometeors. It can be taken up from the gas phase or lost to the gas phase via Equation 2.22.

The retention coefficient for H_2O_2 is likely to depend on the details of the freezing process. In a laboratory study Iribarne and Psyhnov (1990) found that HNO_3 and H_2O_2 were completely retained in the ice phase after cloud droplet freezing. On the other hand, Snider *et al.* (1992) and Snider and Huang (1998) found that H_2O_2 is released to the gas phase during riming. Snider and Huang (1998) determined k_{ret}=0.05 for H_2O_2. Stuart and Jacobson (2003) found in agreement with earlier studies that chemicals with high effective Henry's Law constants such as HNO_3 are likely to be retained under all non-rime and dry growth conditions. For chemicals with lower Henry's Law constants, such as H_2O_2, they argue that retention probably depends on details of the freezing process. Very recently, Stuart and Jacobson (2004) suggested the first parameterization for retention during dry growth riming, which takes into account growth conditions.

Here, in the standard simulation k_{ret}=0.05 was assumed for H_2O_2. The retention coefficients for all other soluble trace gases listed in Table 2.1 were assumed to be 0.02, except for HNO_3 for which k_{ret}=1. For CH_3OOH and HCHO these assumptions are identical to the assumptions by Mari *et al.* (2000). Large uncertainties about these estimates exist, which can have important impacts on the mixing ratios of these gases calculated to exist in the upper troposphere (see Sections 6.3). For H_2O_2 a sensitivity study in which k_{ret}=0 and the uptake on ice was turned off is discussed in Section 11.3.

The effect of a quasi liquid layer on graupel (see e.g. Conklin *et al.*, 1993; Diehl *et al.*, 1995) as well as the effect of a combination of HNO_3 molecules with H_2O molecules to form NAT (nitric acid trihydrate, $HNO_3 \cdot 3H_2O$) (see e.g. Tabazadeh and Turco, 1993; Meilinger *et al.*, 1999; Gao *et al.*, 2004) and the effect of possible multi-layer uptake at low temperatures (e.g. Hudson *et al.*, 2002) were not investigated in the present study.

So far, the number of CRM studies investigating the role of the ice phase for tracer transport is very limited. In these studies, the retention coefficients have been assumed to be gas dependent. In the future, the dependence on details of the ice process should also be investigated. It should, however, be noted that the results of these studies could in some cases depend on details of the microphysics parameterization. It will be important to study this sensitivity as well. In pre-

liminary CRCTM runs, the transport of a small number of idealized trace gases was analyzed in dependence on the retention coefficient, the uptake on ice, the two different single moment microphysics schemes described in Section 2.2.2, and two different advection schemes. For a tracer with the solubility of H_2O_2, the amount scavenged between 5 and 10 km height was found to be sensitive to the choice of the microphysics scheme. In these preliminary runs, the tracer was assumed to be taken up by ice assuming a quasi Henry's Law constant according to Conklin *et al.* (1993).

Detailed model studies about the role of the ice phase on deep convective chemistry transport are currently being planned in the framework of a future project.

2.4 Gas Phase Chemistry

The gas phase chemistry module is based on the chemistry scheme from the Model of Atmospheric Transport and Chemistry - Max Planck Institute for Chemistry (MATCH-MPIC, Lawrence *et al.*, 1999b; von Kuhlmann *et al.*, 2003a, and references therein). The scheme includes a "background" CH_4−CO−HO_x−NO_x tropospheric chemistry mechanism (reactions R1–R45). Furthermore, reactions including PAN ($CH_3C(O)O_2NO_2$, peroxy acetyl nitrate, R46-R59) and loss reactions of acetone (CH_3COCH_3, R61 and R62) are included (see discussions in Sections 8.5.1 and 10.5).

Table 2.3: Chemical Reactions

No.	Reaction[1,2]	Rate[3]	Ref.
R1	$O_3 + h\nu \rightarrow O(^1D) + O_2$	J_1	L+C98
R2	$O(^1D) + O_2 (\rightarrow O(^3P) + O_2^\star)$ $\xrightarrow{+O_2} O_3 (+O_2^\star)$	$k_2 = 3.2 \cdot 10^{-11} \exp(70/T)$	JPL97
R3	$O(^1D) + N_2 (\rightarrow O(^3P) + N_2^\star)$ $\xrightarrow{+O_2} O_3 (+N_2^\star)$	$k_3 = 1.8 \cdot 10^{-11} \exp(110/T)$	JPL97
R4	$O(^1D) + H_2O \rightarrow 2\,OH$	$k_4 = 2.2 \cdot 10^{-10}$	JPL97
R5	$O_2 + h\nu (\rightarrow 2\,O(^3P)) \xrightarrow{+2\,O_2} 2\,O_3$	J_2	L+C98
R6	$O_3 + OH \rightarrow HO_2 + O_2$	$k_6 = 1.5 \cdot 10^{-12} \exp(-880/T)$	JPL00
R7	$O_3 + HO_2 \rightarrow OH + 2\,O_2$	$k_7 = 2.0 \cdot 10^{-14} \exp(-680/T)$	JPL00
R8	$HO_2 + OH \rightarrow H_2O + O_2$	$k_8 = 4.8 \cdot 10^{-11} \exp(250/T)$	JPL00
R9	$HO_2 + HO_2 \rightarrow H_2O_2 + O_2$	$k_9 = \text{complex, f}(T, [M], [H_2O])$	JPL97
R10	$H_2O_2 + h\nu \rightarrow 2\,OH$	J_3	
R11	$H_2O_2 + OH \rightarrow HO_2 + HO_2$	$k_{11} = 2.9 \cdot 10^{-12} \exp(-160/T)$	JPL97
R12	$CO + OH \rightarrow HO_2 + CO_2$	$k_{12} = 1.5 \cdot 10^{-13} (1 + 0.6P(\text{atm}))$	JPL97
R13	$CH_4 + OH \rightarrow CH_3O_2 + H_2O$	$k_{13} = 2.8 \cdot 10^{-14} T^{0.667} \exp(-1575/T)$	JPL97
R14	$CH_3O_2 + HO_2 \rightarrow CH_3O_2H + O_2$	$k_{14} = 4.15 \cdot 10^{-13} \exp(750/T)$	Tyn01
R15	$CH_3O_2 + NO \rightarrow HCHO + HO_2 + NO_2$	$k_{15} = 2.8 \cdot 10^{-12} \exp(300/T)$	Tyn01
R16	$CH_3O_2 + CH_3O_2 \rightarrow 2HCHO + 2HO_2$	$k_{16} = 9.5 \cdot 10^{-14} \exp(390/T) /(1 + 1/(26.2\exp(-1130/T)))$	Tyn01

continued on next page

Table 2.3 continued

R17	$CH_3O_2 + CH_3O_2 \rightarrow HCHO + CH_3OH$	$k_{17}=9.5 \cdot 10^{-14}\exp(390/T)$ $/(1+26.2\exp(-1130/T))$	Tyn01
R18	$CH_3O_2 + NO_3 \rightarrow HCHO + HO_2 + NO_2$	$k_{18}=1.3 \cdot 10^{-12}$	Atk99
R19	$CH_3O_2H + h\nu \rightarrow HCHO + HO_2 + OH$	J_4	L+C98
R20	$CH_3O_2H + OH \rightarrow 0.7\,CH_3O_2 + 0.3\,HCHO + 0.3\,OH + H_2O$	$k_{20}=3.8 \cdot 10^{-12}\exp(200/T)$	JPL97
R21	$HCHO + h\nu \xrightarrow{+2\,O_2} CO + 2\,HO_2$	J_5	L+C98
R22	$HCHO + h\nu \rightarrow CO + H_2$	J_6	L+C98
R23	$HCHO + OH \rightarrow CO + HO_2 + H_2O$	$k_{23}=1.0 \cdot 10^{-11}$	JPL97
R24	$HCHO + NO_3 \rightarrow CO + HO_2 + HNO_3$	$k_{24}=3.4 \cdot 10^{-13}\exp(-1900/T)$	JPL97
R25	$NO + O_3 \rightarrow NO_2 + O_2$	$k_{25}=3.0 \cdot 10^{-12}\exp(-1500/T)$	JPL97
R26	$NO + HO_2 \rightarrow NO_2 + OH$	$k_{26}=3.5 \cdot 10^{-12}\exp(250/T)$	JPL97
R27	$NO_2 + h\nu \xrightarrow{+O_2} NO + O_3$	J_7	L+C98
R28	$NO_2 + O_3 \rightarrow NO_3$	$k_{28}=1.2 \cdot 10^{-13}\exp(-2450/T)$	JPL97
R29	$NO_2 + OH + M \rightarrow HNO_3 + M$	k_{29}=complex	Dra99
R30	$NO_2 + HO_2 + M \rightarrow HNO_4 + M$	k_{30}=complex	
R31	$HNO_3 + h\nu \rightarrow OH + NO_2$	J_8	L+C98
R32	$HNO_3 + OH + M \rightarrow NO_3 + H_2O + M$	k_{32}=complex	JPL00
R33	$NO_3 + h\nu \xrightarrow{+O_2} NO_2 + O_3$	J_9	L+C98
R34	$NO_3 + h\nu \rightarrow NO$	J_{10}	L+C98
R35	$NO_3 + NO \rightarrow 2\,NO_2$	$k_{35}=1.5 \cdot 10^{-11}\exp(170/T)$	JPL99
R36	$NO_3 + NO_2 + M \rightarrow N_2O_5 + M$	k_{36}=complex	JPL00
R37	$N_2O_5 + h\nu \rightarrow NO_3 + NO_2$	J_{11}	L+C98
R38	$NO_3 + HO_2 \rightarrow 0.8\,NO_2 + 0.8\,OH + 0.2\,HNO_3$	$k_{38}=3.5 \cdot 10^{-12}$	JPL97
R39	$N_2O_5 + M \rightarrow NO_3 + NO_2 + M$	$k_{39}=k_{36}/(3 \cdot 10^{-27}\exp(10991/T))$	JPL00
R40	$N_2O_5 + H_2O \rightarrow 2\,HNO_3$	k_{40}=complex	D+C93
R41	$N_2O_5 + H_2O \rightarrow 2\,HNO_3$	$k_{41}=2.5 \cdot 10^{-22} + 1.8 \cdot 10^{-39}[H_2O]$	Wah98
R42	$HNO_4 + h\nu \rightarrow 0.39\,NO_3 + 0.39\,OH + 0.61\,NO_2 + 0.61\,HO_2$	J_{12}	L+C98, Atk97
R43	$HNO_4 + M \rightarrow HO_2 + NO_2 + M$	$k_{43}=k_{30}/(2.1 \cdot 10^{-27}\exp(10900/T))$	JPL97
R44	$HNO_4 + OH \rightarrow NO_2 + H_2O + O_2$	$1.3 \cdot 10^{-12}\exp(380/T)$	JPL97
R45	$H_2 + OH \rightarrow HO_2 + H_2O$	$k_{45}=5.5 \cdot 10^{-12}\exp(-2000/T)$	JPL97
R46	$CH_3OH + OH \rightarrow HCHO + HO_2$	$k_{46}=6.7 \cdot 10^{-12}\exp(600/T)$	JPL97
R47	$CH_3CO_3 + HO_2 \rightarrow CH_3CO_3H$	$k_{47}=4.3 \cdot 10^{-13}\exp(1040/T)$ $(1+1/(37\exp(-660/T)))$	Tyn01
R48	$CH_3CO_3 + HO_2 \rightarrow CH_3COOH + O_3$	$k_{48}=4.3 \cdot 10^{-13}\exp(1040/T)$ $(1+37\exp(-660/T))$	Tyn01
R49	$CH_3CO_3 + NO \rightarrow CH_3O_2 + NO_2 + CO_2$	$k_{49}=8.1 \cdot 10^{-12}\exp(270/T)$	Tyn01
R50	$CH_3CO_3 + NO_2 \rightarrow PAN$	k_{50}=complex	Tyn01
R51	$CH_3CO_3 + CH_3O_2 \rightarrow HCHO + HO_2 + CH_3O_2 + CO_2$	$k_{51}=2.0 \cdot 10^{-12}\exp(500/T)/$ $(1+1/(2.2 \cdot 10^{6}\exp(3820/T)))$	Tyn01, JPL97
R52	$CH_3CO_3 + CH_3O_2 \rightarrow CH_3COOH + HCOH + CO_2$	$k_{52}=2.0 \cdot 10^{-12}\exp(500/T)/$ $(1+2.2 \cdot 10^{6}\exp(-3820/T))$	Tyn01, JPL97
R53	$CH_3CO_3 + CH_3CO_3 \rightarrow 2\,CH_3O_2 + 2\,CO_2 + O_2$	$k_{53}=2.5 \cdot 10^{-12}\exp(500/T)$	Tyn01
R54	$CH_3CO_3 + NO_3 \rightarrow CH_3O_2 + NO_2 + CO_2$	$k_{54}=4 \cdot 10^{-12}$	Tyn01

continued on next page

Table 2.3 continued

R55	$CH_3CO_3H + h\nu \rightarrow CH_3O_2 + OH$	J_{13}=0.025J_5	RvK01
R56	$CH_3CO_3H + OH \rightarrow CH_3CO_3$	k_{56}=k_{20}	
R57	$PAN + OH \rightarrow HCHO + NO_2 + CO_2$	k_{57}=$2 \cdot 10^{-14}$	JPL97[4]
R58	$PAN + h\nu \rightarrow CH_3CO_3 + NO_2$	J_{14}	RvK01, L+C98
R59	$PAN + M \rightarrow CH_3CO_3 + NO_2$	k_{59}=$k_{50}/9 \cdot 10^{-29}$ exp(−14000/T)	JPL97
R60	$CH_3COOH + OH \rightarrow CH_3O_2 + CO_2$	k_{60}=$4 \cdot 10^{-13}$exp(200/T)	JPL97
R61	$CH_3COCH_3 + h\nu \rightarrow CH_3CO_3 + CH_3O_2$	J_{15}	RvK01, L+C98
R62	$CH_3COCH_3 + OH \rightarrow CH_3COOH + CH_3O_2$	k_{62}=$1.7 \cdot 10^{-14}$exp(423/T)	Wol00
R63	$HNO_4 + h\nu \rightarrow HO_2 + NO_2$	J_{15}=$4.5 \cdot 10^{-5}J_{10}$	see text

References: JPL00 is Sander *et al.* (2000), JPL97 is DeMore *et al.* (1997), Tyn01 is Tyndall *et al.* (2001), L+C98 is Landgraf and Crutzen (1998), Atk99 is Atkinson *et al.* (1999), Atk97 is Atkinson *et al.* (1997), Dra99 is Dransfield *et al.* (1999), D+C93 is Dentener and Crutzen (1993), Wah98 is Wahner *et al.* (1998), RvK01 is von Kuhlmann (2001), Wol00 is Wollenhaupt *et al.* (2000) and Wollenhaupt and Crowley (2000).

Notes: [1] Where appropriate, several reactions have been summarized as one step.
[2] Changes of O_2, H_2O, CO_2, and H_2 concentrations due to chemical reactions are not considered in the CRCTM.
[3] For first-, second-, and third- order reactions, the units of the rate coefficients k are s^{-1}, cm^3 $molecule^{-1}$ s^{-1}, and cm^6 $molecule^{-2}$ s^{-1}. The units of the photolysis rates J are s^{-1}.
[4] One half of the maximum rate constant given in DeMore *et al.* (1997) is used.

The rate equations for the reactions in Table 2.3 form a set of coupled stiff differential equations. A three-stage Rosenbrock solver (e.g. Hairer and Wanner, 1996) was used to numerically integrate those equations forward in time. A symbolic preprocessor (KPP, Kinetic PreProcessor; Damian-Iordache, 1996; Damian *et al.*, 2002; Sander *et al.*, 2005) was coupled to the WRF-based CRCTM. KPP is a computer program that reads reactions and reaction rates from an input file provided by the user and writes the program code necessary to perform the numerical integration. The syntax of the input file is similar to the syntax used in Table 2.3. Furthermore, in WRF new variables are specified in an ASCII table and the part of the code which is responsible for memory management and in- and output (IO) is written by preprocessors. An additional preprocessor was constructed for the WRF based CRCTM which writes the interface between the WRF code and the KPP generated code. The pre-processors are automatically applied prior to the compilation of the model code. This setup considerably reduces the effort necessary to include new chemical compounds and/or reactions into the CRCTM.

The concentrations of CH_4 and of NO_y=NO+NO_2+NO_3+HNO_3 in the stratosphere above 17.5 km are specified based on data from MATCH-MPIC which was constrained by observations as described by von Kuhlmann *et al.* (2003a). The model calculated concentrations of the members of the NO_y group are scaled in

order for the concentration of NO_y to remain constant. The partitioning between the concentrations of the different members calculated by the model is not changed.

Photolysis rates are computed every 5 minutes using the computationally efficient scheme by Landgraf and Crutzen (1998). In this scheme, the rates are computed using a parameterization for a purely absorbing atmosphere at eight representative wavelengths. Then corrections for the effects of clouds, aerosols, and molecular scattering are added. Cloud water paths are calculated from modeled hydrometeor concentrations, currently treating meteors in both the ice and in the liquid phase as liquid phase meteors. For aerosols, a constant background distribution and optical properties typical of marine aerosols are assumed. Some of the photolysis rates needed in the CRCTM were not calculated in the original scheme. Von Kuhlmann (2001) extended the scheme making use of correlations between these newly added photolysis rates and photolysis rates already calculated in the original scheme. 3-D radiation effects are not considered in the scheme by Landgraf and Crutzen. The radiative transfer in the scheme by Landgraf and Crutzen is calculated using the δ-two stream model by Zdunkowski *et al.* (1982).

Aqueous phase reactions are currently not explicitly included in the CRCTM, except for the hydrolysis reaction of N_2O_5 (R40). Early studies by Lelieveld and Crutzen (1995, 1991) indicated that tropospheric ozone can be strongly affected through aqueous phase reactions. More recent studies estimated moderate (Jonson and Isaksen, 1993) to small effects on ozone (Liang and Jacob, 1997). Liang and Jacob (1997) estimated the impact of aqueous phase reactions on tropospheric ozone to be below 3%. They argued that there is little justification for including aqueous phase HO_x chemistry in regional and global models of atmospheric O_3. Walcek *et al.* (1997) found that in-cloud reactions strongly influence local O_3 production in polluted areas, but that longer-term impacts of clouds on O_3 formation would be much smaller due to compensating chemical processes in regions remote from NO_x emissions. They found ozone formation in polluted clouds to be strongly influenced by reactions involving trace metals. Barth *et al.* (2002) studied the effect of marine boundary layer clouds on tropospheric chemistry in a 20° by 10° region centered over Hawaii. After a 60 hours simulation with a regional model, they found 4.8% less domain integrated ozone when including aqueous chemistry in their model. The influences on H_2O_2, HNO_3, HCHO, CH_3OOH, and HO_2 were, however, much larger. While the net effect of including aqueous chemistry on ozone should not be expected to be large in the TOGA COARE study, large changes can be expected for other compounds. This is further discussed in Section 11.3 and in Chapters 12 and 13.

Currently, a fixed pH is assumed in the CRCTM. A simple sulfur chemistry could be implemented in the future in order to calculate the pH of the cloud droplets, which plays an important role in determining the uptake of soluble gases into the liquid phase. Reversible aqueous phase reactions are implicit in the calculations of the effective Henry's law constants in Section 2.3.1.

The photodissociation of HNO_4 in the near-IR (e.g. Roehl *et al.*, 2002, and references therein) was included in the CRCTM based on Roehl *et al.* (2002) who suggested a daytime near-IR photolysis rate of approximately $1 \cdot 10^{-5} s^{-1}$. In the

CRCTM, the clear sky photolysis rate for NO_3 (J_{10} in R34) as calculated for the first day of the TOGA COARE simulation was scaled by the factor $4.5 \cdot 10^{-5}$ to approximately yield $1 \cdot 10^{-5} s^{-1}$ (see R63). In order to assess the influence of including the near-IR photolysis of HNO_4, a sensitivity run was conducted in which R63 was omitted. The result was a somewhat larger net formation of HNO_4 in the upper troposphere (compare Sec. 8.5.3).

Additional points, such as a discussion of the treatment of PAN and acetone will be added in later sections.

2.5 Dry Deposition

Dry deposition over the ocean is parameterized using a so-called resistance formulation:

$$\partial_t C_{i,g}|_{drydep} = -\partial_z \left(V_d C_{i,g} \right) \tag{2.27}$$

where

$$V_d = \frac{1}{R_a + R_b + R_c}. \tag{2.28}$$

Here V_d is the so-called deposition velocity, R_a is the aerodynamic resistance, R_b is the quasi-laminar sub-layer resistance, and R_c is the surface resistance. The resistances are calculated based on formulations by Ganzeveld and Lelieveld (1995). For trace gases other than O_3, NO and NO_2, R_c was calculated from Henry's law constants and gas-specific reactivity coefficients using formulas by Wesely (1989) as in von Kuhlmann (2001).

2.6 Lightning NO_x Production

Lightning NO production is parameterized in five steps: First convective systems are localized, then the flash rate for each system is calculated and the flash rates are partitioned into rates for intra-cloud (IC) and cloud to ground (CG) flashes. These rates are multiplied by the number of molecules produced per IC or CG flash in order to calculate the NO production rate. Finally, the resulting amount of NO produced by each system is distributed vertically and horizontally. This calculation is currently performed every 60 s of simulated time.

Convective systems are localized fitting rectangles in the horizontal plane covering the area in which the graupel mixing ratio at any point in the model column exceeds $0.1\,\mathrm{g\,kg^{-1}}$. The flash rate F (in flashes per minute) is calculated from the following exponential dependence on the maximum vertical velocity w_{max} (in meters per second) based on a formulation used by Price and Rind (1992):

$$F = 5 \cdot 10^{-6} w_{max}^{k}. \tag{2.29}$$

Based on empirical relationships, Price and Rind (1992) derived an exponent of

k=4.54, which is somewhat less than the model study based estimate of at least 6 by Baker *et al.* (1995). Pickering *et al.* (1998) who among other convective systems studied a squall line during TOGA COARE, used different values for different model simulated storms in order obtain results comparable to observed flash rates. For the TOGA COARE case, they increased the exponent from 4.54 to 5.3. Here, sensitivity studies using different exponents were conducted.

Based on a number of different datasets and on empirical relationships (Price and Rind, 1993) found a strong dependence of the ratio z = number of IC flashes / number of GC flashes on the depth of the freezing region ΔH. ΔH is the vertical distance between the 0 °C isotherm and the cloud top. For clouds with $\Delta H > 5.5$km, Price and Rind (1993) derived the following empirical relationship:

$$P = 1/(z+1) \tag{2.30}$$

$$z = 0.021\,(\Delta H)^4 - 0.648\,(\Delta H)^3 + 7.493\,(\Delta H)^2 - 36.54\,(\Delta H) + 63.09$$

where P is the fraction of CG flashes and ΔH is in km. This relationship is implemented in the CRCTM. The cloud top is taken to be the height where the computed total icemeteor mixing ratio in the grid column in which the maximum vertical updraft velocity is located decreases to $0.01\,\mathrm{g\,kg^{-1}}$. For clouds with $\Delta H = 5.5$km the relationship yields $P \approx 0.84$ and for clouds with $\Delta H = 14$km $P \approx 0.02$. Typical climatological values for the tropics are cited in Section 8.1. For clouds with $\Delta H < 5.5$km, P is set to 0 (as in Price *et al.*, 1997a; Pickering *et al.*, 1998), based on the observation that very little lightning is produced by clouds with $\Delta H < 5.5$km and that clouds produce almost exclusively IC flashes during their growth stage before they start producing GC flashes. However, doing so implies a "jump" from the maximum value of $P = 0.84$ to $P = 0$ at $\Delta H = 5.5$km. Clouds with their tops below the -15°C isotherm are not assumed to contribute to the formation of NO due to lightning in this study. The strongest updrafts and thus by far the highest flash rates are often associated with clouds that have deep freezing regions. Assuming a constant, climatological value for the partitioning between IC and CG flashes is a possible source of uncertainty in calculating the total amount of lightning produced NO, since IC flashes are assumed to produce less NO than CG flashes.

In lightning NO production parameterizations, CG flashes are often assumed to produce either three or ten times as much NO per flash as IC flashes do (see Zhang *et al.*, 2003, for a review), based on the finding that GC flashes are more energetic than IC flashes. In contrast, Gallardo and Cooray (1996) suggested IC and CG flashes produce similar amounts of NO, which is in line with an estimate of energy dissipation in flashes by Cooray (1997). Two recent studies in which observations from field campaigns were analyzed using CRMs, also indicate the ratio $\mathrm{P}_{IC}/\mathrm{P}_{GC}$ of NO produced per IC flash to NO produced per GC flash is probably higher than previously thought. In the CRM study by DeCaria *et al.* (2000) values of $\mathrm{P}_{IC}/\mathrm{P}_{GC}$ in the range 0.5–1.0 yielded the best comparisons of model results with $\mathrm{NO_x}$ observations. Fehr *et al.* (2004) found the ratio $\mathrm{P}_{IC}/\mathrm{P}_{GC}$ to be as high as 1.4

leading to an intra-cloud contribution to the total NO_x production of up to 93%. The number of NO molecules produced per flash is rather uncertain. Estimates range from below $1 \cdot 10^{25}$ to $3 \cdot 10^{27}$ (reviews by e.g. Biazar and McNider, 1993; Lawrence *et al.*, 1995; Huntrieser *et al.*, 1998, see also Table 8.1). The values used in sensitivity studies are presented in Section 8.2.

In the CRCTM, GC flashes are placed within a one grid space wide vertical column at the location of the maximum vertical updraft (see discussion in Section 8.2.2). For IC flashes, the lightning produced NO molecules are assumed to be uniformly distributed in a vertical column three grid spaces wide (3 grid columns in a 2-D simulation) and centered at the location of the maximum vertical updraft. This horizontal distribution is comparatively easy to implement into a model designed for massive parallel computers such as the WRF based CRCTM, and a similar horizontal distribution was also used in the study by Wang and Prinn (2000). For GC flashes the column in which the NO is placed extends vertically from the Earth's surface to the model calculated -15°C isotherm. For IC flashes it extends from the height of the -15°C isotherm to the height where the computed total icemeteor mixing ratio decreases to $0.01\,\mathrm{g\,kg^{-1}}$. This vertical distribution is similar to the one used by Pickering *et al.* (1998). The -15°C isotherm was suggested to be the region of maximum negative charge by Houze, Jr. (1993).

A number of uncertainties about the lightning NO production are discussed in the later sections. Altogether, the uncertainties in parameterizing the lightning NO production are still large and the simple parameterization described here is part of one of the first attempts to estimate some effects of lightning produced NO on the chemistry of the troposphere using a CRM.

Chapter 3

Model Setup for the TOGA COARE Case Study and Meteorological Evaluation

In this chapter, the TOGA COARE study is briefly described. A model setup is suggested in which the lateral boundary conditions for wind, water vapor and trace gases are specified while for other variables periodic lateral boundary conditions (PLBCs) are applied. Since models with periodic boundary conditions for air fail to reproduce mean upwards mass fluxes in convective regions such as the SPCZ, a large scale advection tendency for tracers (VLSAT) is defined based on the mean vertical velocity derived from observations. The setups used in the later chapters and for the tracer transport sensitivity runs are described in Section 3.4.

3.1 The TOGA COARE case

A well documented seven day period from 19–26 December 1992 at the site of the TOGA COARE (Webster and Lukas, 1992) Intensive Flux Array (IFA, centered at 2°S, 156°E, see Fig 3.1) is simulated. This period overlaps with the period chosen by the GEWEX Cloud System Study (GCSS; GCSS Science Team, 1993) Working Group 4 as the second case of their first cloud-resolving model inter-comparison project (Krueger and Lazarus, 1999), and was also investigated by Su *et al.* (1999), Costa *et al.* (2001), Petch and Gray (2001), Johnson *et al.* (2002), and used in a model comparison by Gregory and Guichard (2002). During this period the IFA region was influenced by the onset of a westerly wind burst (see Fig. 3.2a) and three consecutive convection maxima developed between 20 December and 23 December and a fourth and strongest maximum with its peak on 24 December at the times of maximum large-scale ascent (Fig. 3.2c). The synoptic conditions associated with the westerly wind burst are discussed in Section 7.2.

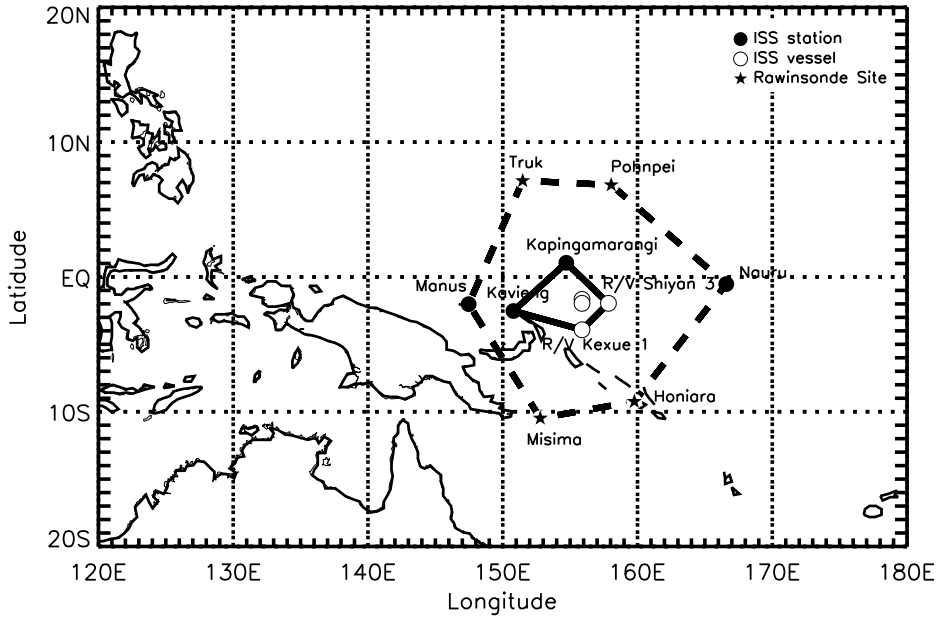

Figure 3.1: Sounding sites at the TOGA COARE region. Solid line: Intensive Flux Array (IFA), dotted line: Outer Sounding Array (OSA).

3.2 Large Scale Advection

Tropical deep convection tends to occur under conditions of large-scale low level convergence and mean tropospheric ascent, e.g. in the rising branch of the Hadley or the Walker circulation, which cannot be reproduced by a limited area CRM with the domain sizes computationally affordable today. In many studies large-scale advection (also referred to as large-scale forcing or advective forcing) tendencies for the water vapor mixing ratio q and the potential temperature θ based on observations are added to the right hand side of the prognostic CRM equations and the model is run in the so-called semi-prognostic manner first introduced by Soong and Ogura (1980). The large scale advection (LSA) tendencies can be expressed as:

$$\partial_t \overline{\theta}|_{LS} = \quad -\overline{\mathbf{v}}_h \cdot \nabla \overline{\theta} \; - \; \overline{w} \, \partial_z \overline{\theta} \tag{3.1}$$

$$\partial_t \overline{q}_v|_{LS} = -k \, \overline{\mathbf{v}}_h \cdot \nabla \overline{q}_v \; - \; \overline{w} \, \partial_z \overline{q}_v \tag{3.2}$$

where overbars denote horizontal domain averaged values. In this study, $k = 1$ when PLBCs for q are used and $k = 0$ (no horizontal LSA of q) whenever lateral boundary conditions (LBCs) for q are prescribed. $\mathbf{v}_h = (u, v)$ is the horizontal wind vector. Instead of prescribing the large-scale advection entirely from observed values it is also possible to calculate the second term on the right hand side from observed values $\overline{w}_{obs}$ together with model calculated values of $\overline{q}$ and $\overline{\theta}$ as done by Soong and Ogura (1980). Sensitivity studies testing both methods were performed yielding similar

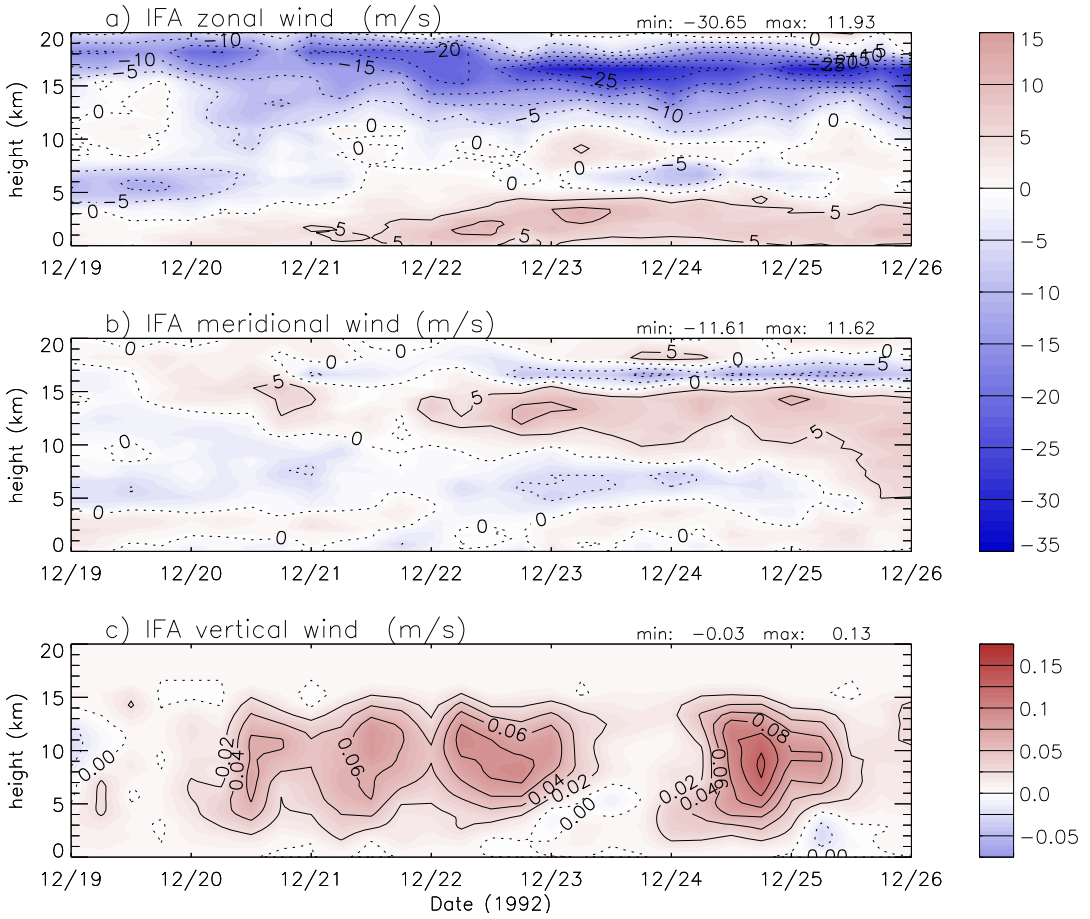

Figure 3.2: Time-height contour plots of observed **(a)** zonal **(b)** meridional and **(c)** vertical wind components. Based on data from (Ciesielski *et al.*, 2003).

results, and it was decided to use the aforementioned method of prescribing the entire right hand sides of Eqs. 3.1 and 3.2 from data based on observations (see Fig. 3.3). The effect of prescribing the LSA terms is to introduce upper tropospheric cooling and moistening tendencies. In addition to prescribing the LSA terms Soong and Ogura (1980) retained the products of domain averaged and perturbation variables in their model, while in many other studies (e.g. Xu *et al.*, 1992; Johnson *et al.*, 2002) these terms were neglected. Here q and θ were specified entirely based on observations and these products were also neglected. For q and θ, perturbations are usually small relative to their base (horizontally averaged) values, while e.g. for a trace gas with a surface source and a low tropospheric background concentration this is not the case when upwards transport of this gas in deep convective clouds sets in. The horizontal gradients of water vapor and temperature are typically much smaller than those of many trace gases. For water vapor this is a consequence of limited upwards transport due to saturation combined with the re-evaporation of hydrometeors, for temperature it is a consequence of the rapid (at the speed of

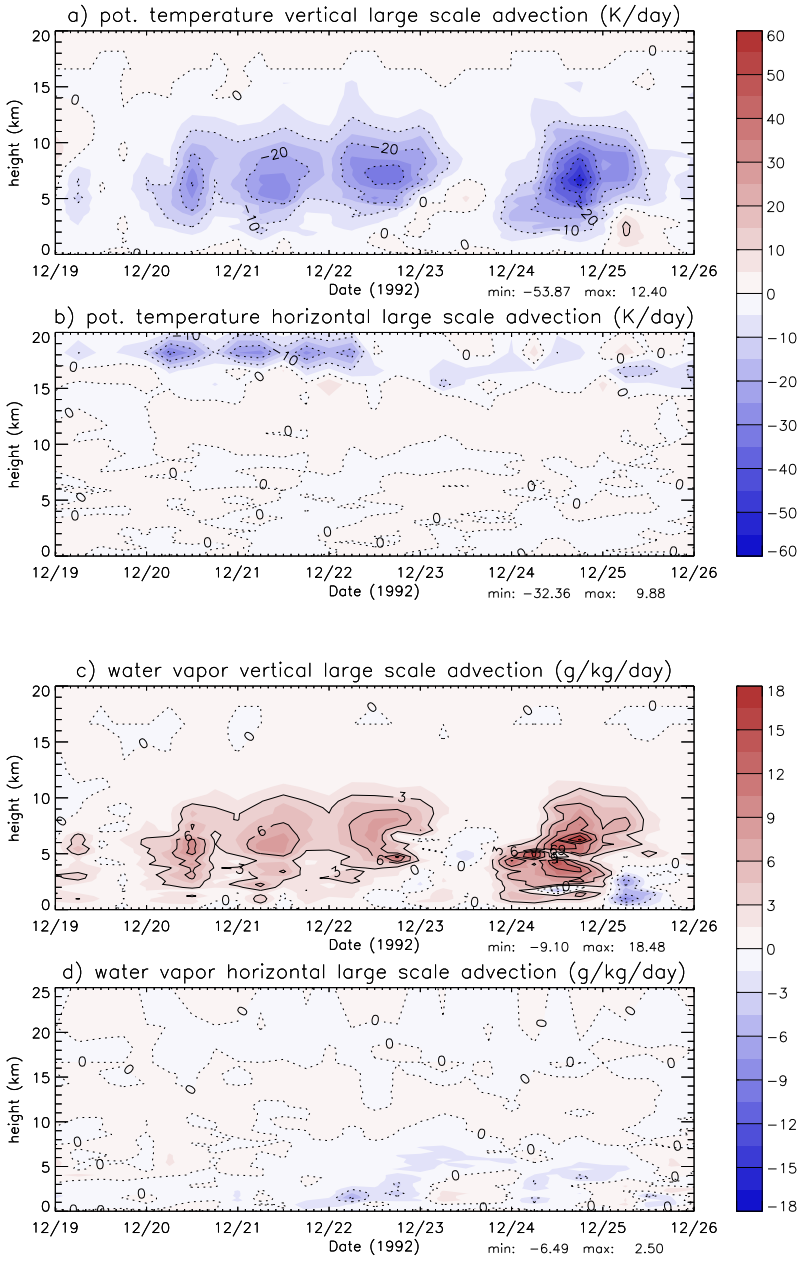

Figure 3.3: Time-height contour plots showing observed vertical and horizontal large-scale advection tendencies of potential temperature and water vapor mixing ratio. Based on data from (Ciesielski *et al.*, 2003).

gravity waves) adjustment.

For tracers a method of including large-scale transport is used which was previously used for q and θ (Xu and Randall, 1996; Xu and Krueger, 1991). The vertical advection of the tracers due to the large-scale vertical velocity $\overline{w}_{obs}$ is calculated, thus allowing horizontal inhomogeneity of the VLSAT. If the lateral boundary conditions for tracers and wind are prescribed and the average horizontal wind components are

nudged towards observed values, only the vertical advection due to $\overline{w}_{obs}$ must be considered and the VLSAT term is calculated from:

$$\partial_t \mu|_{LS} = -\overline{w}_{obs}\, \partial_z \mu \tag{3.3}$$

where μ is the modeled tracer mixing ratio and $\overline{w}_{obs}$ is depicted in Fig. 3.2c. If $\overline{\mu}$ were inserted in Eq. 3.3 instead of μ the tracer advection by $\overline{w}_{obs}$ would be non-local and the tracer would be spuriously dispersed across the entire model domain. In addition it would become necessary to apply a non-local scaling of the values in order to ensure positive definiteness and mass conservation simultaneously. In simulations of chemically reactive trace gases this would often cause significant problems. The average horizontal wind is nudged towards observed values (see Fig. 3.2, data from Ciesielski *et al.*, 2003):

$$\partial_t \overline{\mathbf{v}}_h|_{LS} = -\left(\overline{\mathbf{v}}_h - \overline{\mathbf{v}}_{h,obs}\right)/\tau_{adj} \tag{3.4}$$

where $\mathbf{v}_h = (u, v)$, as in e.g. Xu and Randall (1996) and Johnson *et al.* (2002) with an adjustment time $\tau_{adj} = 1$h.

3.3 Lateral Boundary Conditions

In semi-prognostic model studies of deep convection PLBCs are used and LSA terms for water vapor and potential temperature are prescribed, providing a means of simulating deep convection with observed mean properties. With PLBCs no fluxes into the model domain from the outside are allowed and the domain averaged net upward transport of air is zero. If instead the LSA term in Equation 3.1 were applied in a model with open or relaxation lateral boundary conditions, the strong mid-tropospheric cooling would cause subsidence and low-level divergence of air out of the model domain and have a stabilizing effect inhibiting deep convection. Alternatively, it would perhaps be possible to apply a different formulation for the large-scale forcing in such a model which would cause ascent and low level convergence. Preliminary tests using a relaxation boundary condition and a density large-scale forcing derived from $\overline{w}_{obs}$ yielded limited success and difficulties with over-estimating the model averaged ascent and low level convergence were encountered.

While for q and θ the horizontal large scale advection terms (see Fig. 3.3b and d) can be small compared to the vertical LSA terms (in Fig. 3.3a and c), this cannot be expected to be the case for moderately long lived trace gases, as will be demonstrated in this study. Thus, if no horizontal large scale advection terms are prescribed in multi-day studies of trace gas transport, PLBCs should not be used for tracers with lifetimes longer than the time $\tau_{adv} = L/\overline{v}_{max}$, where $\overline{v}_{max} = max(\overline{v}(z))$ is the maximum domain averaged horizontal wind speed and L is the horizontal domain length. Therefore, it was decided to retain PLBCs for the potential temperature and the air density but to specify LBCs for tracers and for water vapor. In this approach, periodic boundary conditions are also retained for the horizontal wind components,

but u and v are nudged towards their observed values with extremely short adjustment times (twice the model timestep dt) at the lateral boundaries. Consequently, the LBCs for u and v can be considered prescribed LBCs. The vertical velocity w and the concentrations of all hydrometeors in the liquid and the ice phase are set to zero at the lateral boundaries. The values for q and the tracer concentrations at the lateral boundaries are specified in a zone which was chosen to be 2 grid points wide. For u, v and w this width is set to three points and additionally a four point wide relaxation zone is used in which the adjustment time increases linearly in order to avoid the generation of spurious waves. The microphysics scheme is not applied in an eight points wide boundary zone in order to avoid spurious condensation. This boundary zone is not considered in the analysis of the model results and not included in the domain lengths cited below. With the choice of lateral boundary conditions presented here, tracers and water vapor are transported smoothly into the domain at the upstream lateral boundary. At the outflow boundary the same boundary conditions were applied. If a higher order advection scheme were used, spurious upwind transport would in principle be possible and a more sophisticated outflow boundary condition may become necessary. In the runs using specified lateral boundary conditions for water vapor, time-dependent water vapor boundary values were specified based on observation-derived data from the Ciesielski *et al.* (2003) dataset.

3.4 Model Setup and Sensitivity Runs with Idealized Tracers

The WRF model as described in Section 2.2.1 was run with 2 km horizontal resolution and 350 m vertical resolution up to 19 km and decreasing resolution up to the model top at nearly 24.7 km with a total of 63 grid points in the vertical direction. The timestep was 5 s and small (in the range $\pm 0.01\,\mathrm{g\,kg^{-1}}$ for 2-D runs and $\pm 0.0125\,\mathrm{g\,kg^{-1}}$ for the 3-D run) time varying random contributions were added to the water vapor mixing ratio in the sub-cloud layer during the first 2.5 h of the simulation. Time-dependent, horizontally homogeneous sea surface temperatures were prescribed based on the dataset by Ciesielski *et al.* (2003).

A number of sensitivity runs using idealized tracers were performed. The transport of ten tracers with horizontally and vertically constant initial concentrations in 1750 m thick horizontal layers was studied. For three of these tracers a detailed analysis of the model results is presented in Chapter 4. The tracers were assumed to be chemically inert, insoluble and to have no surface or tropospheric sources or sinks inside the domain.

The results from three 2-D runs using a domain length of 500 km will be discussed in detail. In the first run, PLBCs were used and the full LSA for q and θ was applied. In the second run the water vapor, the concentrations of the hydrometeors in the liquid and the ice phase, and the wind were specified at the lateral boundaries as described in Section 3.3. The full θ LSA was applied and for q only the vertical contribution of the LSA was considered. The concentrations of the idealized tracers were prescribed at the lateral boundaries and were kept constant and equal to the

Table 3.1: Sensitivity runs in Chapters 3 and 4, for abbreviations see text.

Setup	Boundary Conditions	Large Scale Advection
2-D sensitivity runs		
2-D (500 km)	PLBC	horiz. and vert. q, θ
2-D (500 km)	SLBC	vert. q, θ
2-D (500 km)[(1)]	SLBC	vert. q, θ, and VLSAT
3-D vs. 2-D sensitivity runs		
2-D (248 km)	SLBC	vert. q, θ, and VLSAT
3-D (248 km×248 km)	SLBC	vert. q, θ, and VLSAT
additional sensitivity runs		
2-D (1000 km)	SLBC	vert. q, θ, and VLSAT
2-D (500 km)[(2)]	SLBC	vert. q, θ ,and VLSAT

[(1)] In Chapters 8 to 11, the same setup is used with time-varying initial and boundary values.

[(2)] In this run, the WRF microphysics scheme by Lin *et al.* (1983) was used.

initial tracer mixing ratios. For brevity, runs with specified tracer and water vapor boundary conditions will subsequently be referred to as specified lateral boundary condition (SLBC) runs. In the third run the LBCs (and the calculated meteorology) were the same as in the second run, but additionally a VLSAT term (Equation 3.3) was added when solving the tracers' continuity equations. The same setup with different boundary values was used in Chapters 7–11.

In order to study the dependence of the model results on the domain size, two additional model runs using domain length of 248 km and 1000 km were performed. The results from these runs are not discussed in detail here. Except for the difference in domain size, the setup of these runs was identical to the setup of the third 500 km domain run, i.e. SLBCs were used and the VLSAT was considered. An additional run (see Section 3.5) was performed using the single-moment microphysics scheme by Krueger *et al.* (1995), instead of the single-moment scheme by (Lin *et al.*, 1983) implemented in the standard WRF model (see Section 2.2.2). Otherwise, the setup of this run was identical to the third 500 km domain length run. In addition to the 2-D runs described above, a 3-D run was performed. In this run, again SLBCs were applied and the VLSAT was considered. The same vertical grid configuration was used as in the 2-D runs and the horizontal domain size was 248 km×248 km. The results of the 3-D run are compared to results from the 248 km 2-D run. An overview of the different setups used in the sensitivity runs is presented in Table 3.1.

3.5 Meteorology: Results and Evaluation

The model computed precipitation rates generally compare well with the observed data (see Fig. 3.4). The total observed amount of rain for the seven day period

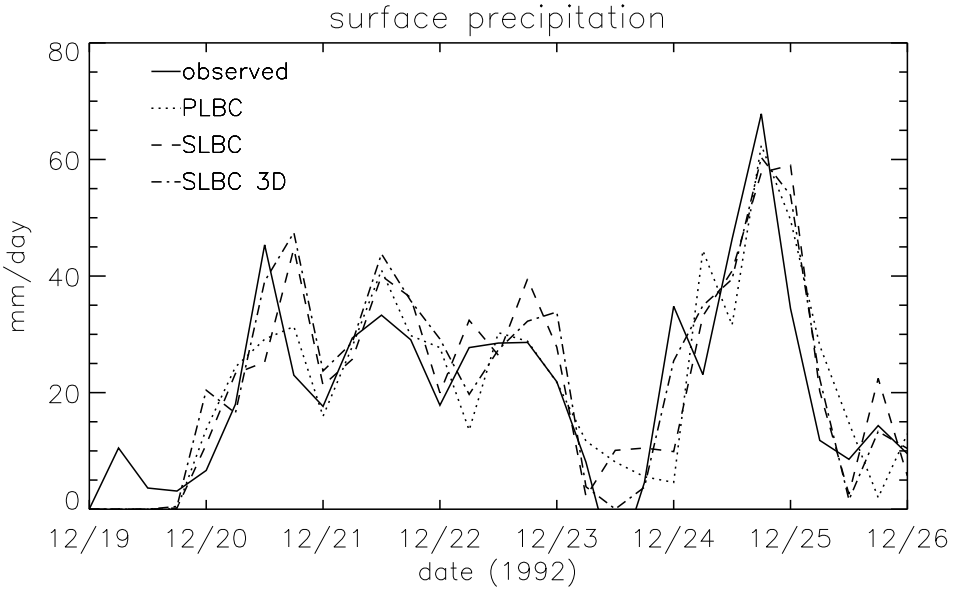

Figure 3.4: Time series of observed and modeled 6h averaged surface precipitation rates for PLBCs and for specified water vapor and wind LBCs.

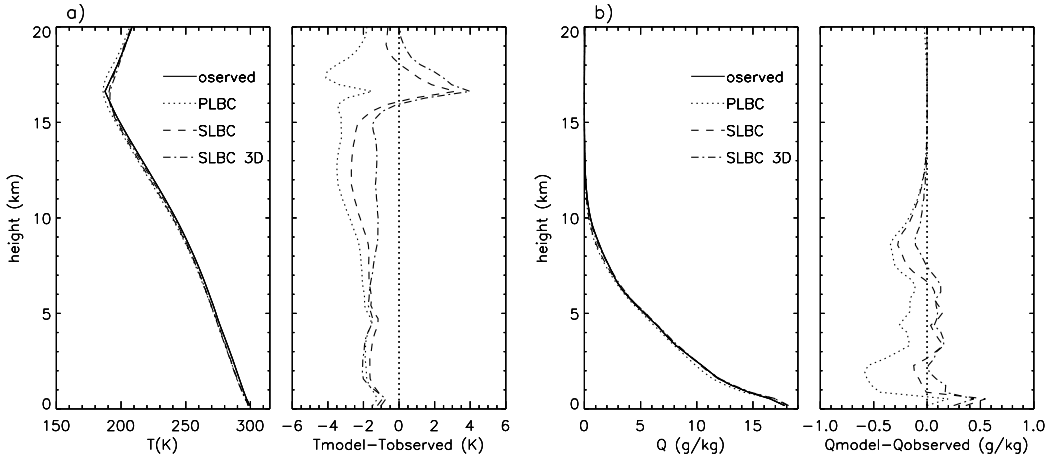

Figure 3.5: Vertical profiles of observed and modeled domain and time averaged temperatures and water vapor mixing ratios.

from 19–26 December 1992 is calculated from the Ciesielski *et al.* (2003) data to be 149.1 mm and the simulated amount is 152.2 mm for the run with PLBCs. In SLBC runs the values are 162.6 mm for the 2-D and 171.8 mm for the 3-D run and thus somewhat higher than the observed value. On the other hand, in a comparable 2-D run also using SLBCs but the single-moment scheme from WRF Lin *et al.* (1983) instead of the one described by Krueger *et al.* (1995) (see Section 2.2.2), the computed value is 143.7 mm and is thus somewhat lower than the observed value (not shown in the figure). In general, with PLBCs a large over- or underestimation is unlikely to occur in a semi-prognostic setup since the computed amount of surface precipitation is largely constrained by the input data for the water vapor LSA. In

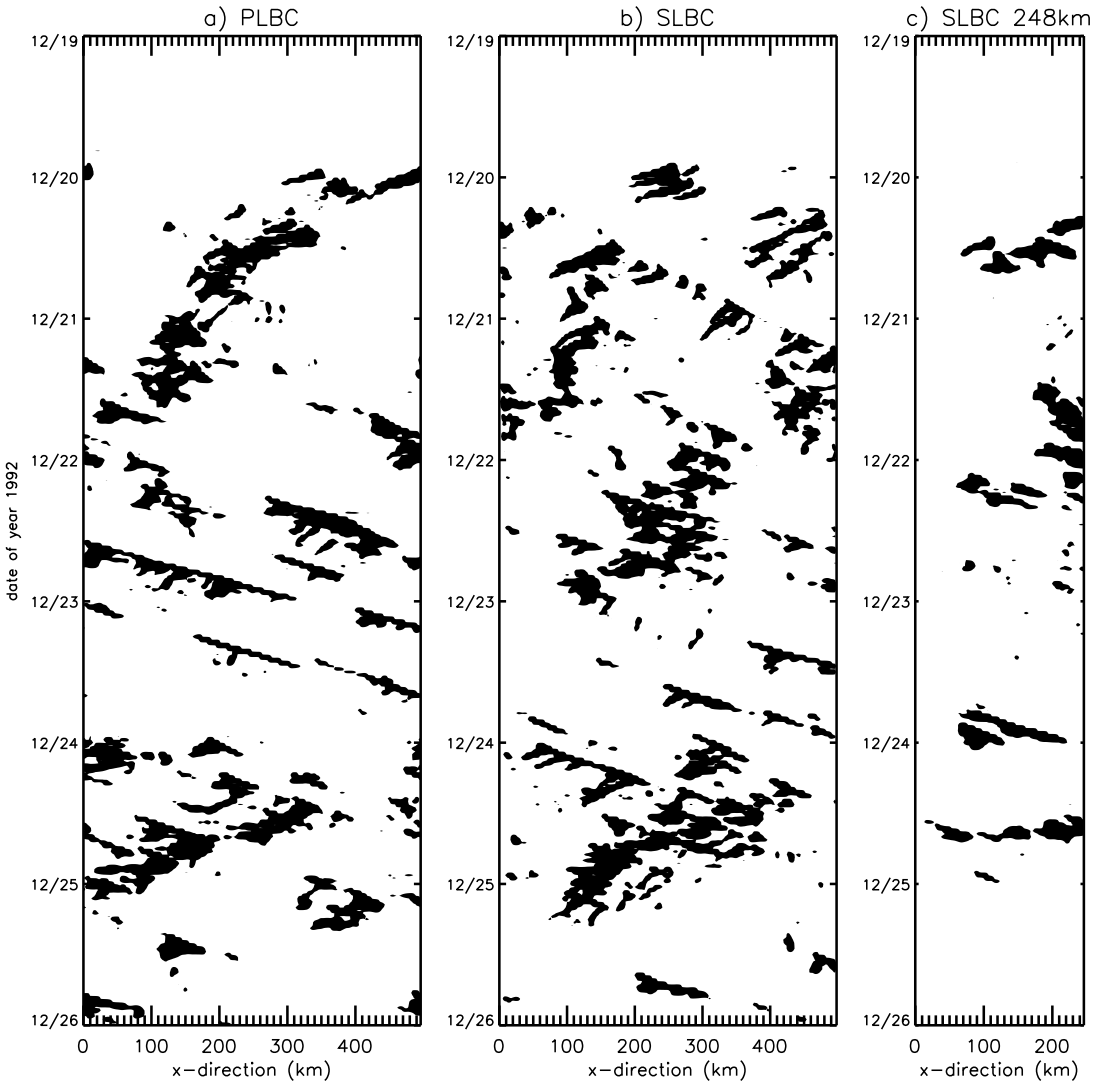

Figure 3.6: Hovmöller diagrams: 1 mm h^{-1} filled contour of model computed rainfall rates for **(a)** PLBCs, and **b)** specified water vapor and wind LBCs. **(c)**: Same as (b) but for 248 km long domain.

contrast, with SLBCs the domain averaged horizontal flux divergence for water vapor at a given height level is determined by the model and is allowed to deviate from the observation derived values of the horizontal LSA, thus more easily allowing either an over- or an underestimation of the surface precipitation. Two 2-D sensitivity runs using SLBCs doubling the domain size and decreasing it to 248 km yielded small changes in the computed total precipitation (the values were 162.4 mm and 161.9 mm vs. 162.6 mm for the 500 km domain, only the latter is displayed in the figure). Good agreement for the precipitation rates was also achieved in earlier model studies (e.g. Johnson *et al.*, 2002). However, with another input dataset very (on the order of 50%) different rates of precipitation can be modeled for the same episode (see Fig. 4 of Gregory and Guichard, 2002). To the author's knowledge,

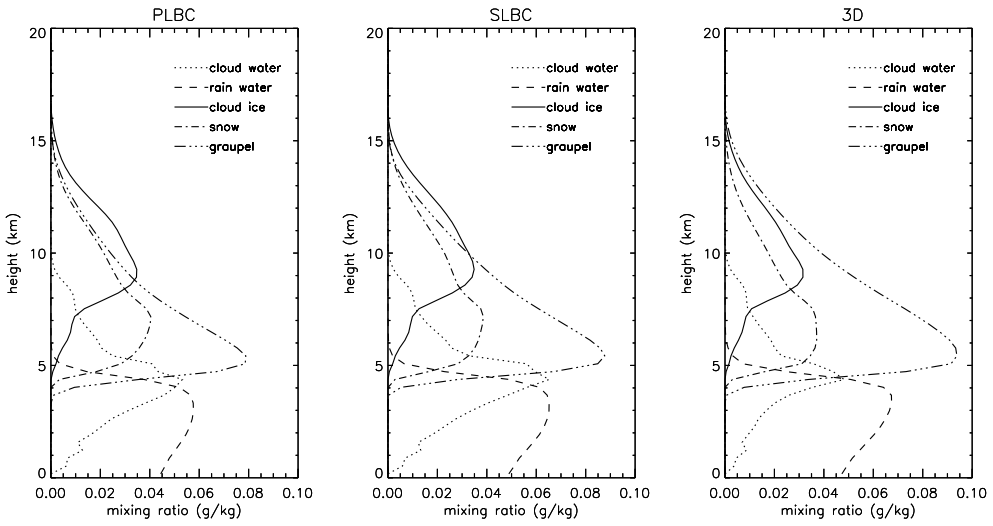

Figure 3.7: Horizontal domain averages of simulated cloudmeteor mass mixing ratios for different runs.

these large differences between different input datasets have not yet been addressed in the literature.

Figure 3.5 depicts the differences between model calculated and observed average temperatures and water vapor mixing ratios. The cold temperature bias in the model runs in the troposphere is comparable to the bias in the 2-D CRM study of Johnson *et al.* (2002) and for the 3-D run to the bias in the 3-D CRM model study of Su *et al.* (1999). The cold bias was discussed e.g. by Johnson *et al.* (2002). The different q biases in the SLBC runs compared to the PLBC runs are a consequence of the horizontal transport of water vapor into the domain, and of the differences in total precipitation discussed above.

For the 500 km domain 2-D runs the Hovmöller diagrams in Fig. 3.6a and b show deep convective systems propagating westwards at moderate speeds of mostly $\sim$3 m s^{-1} (low propagation speed implies a steep slope in the diagrams) and faster eastwards moving single clouds (thin "lines" in the diagrams) for both PLBCs and SLBCs. Perhaps the most striking differences between the two sensitivity runs occurred between December 20 and December 23. In the run with PLBCs a single large mesoscale convective system developed during the first two days of strong deep convective activity and during the next two days mostly single clouds and small squall lines dominated. In the SLBC run during the entire period, single clouds coexisted with large squall lines occurring during the latter half of the first four days of strong deep convective activity. In Fig. 3.6c a Hovmöller diagram for the 248 km domain 2-D run which will be utilized for the 2-D vs. 3-D tracer transport comparisons in the next chapter is shown. In this run the largest deep convective systems have smaller horizontal extents and shorter lifetimes compared to the larger domain run.

The simulated mass mixing ratios of the different cloudmeteor categories are shown in Fig. 3.7. In the next section, the modeled cloud fractions and the cloud top temperatures will be compared to data derived from satellite observations. The details of rather comprehensive microphysics parameterizations are often difficult to evaluate because such an evaluation requires a large observational database and the parameterizations contain a number of poorly constrained parameters. Since climate simulations are known to be quite sensitive to changes in microphysics parameterization schemes, the evaluation and improvement is an important subject of ongoing research, which is beyond the scope of this thesis.

3.6 Comparison with Satellite Data

In the previous section domain-averaged model results and observational data of precipitation rates, temperatures and specific humidities were compared. The model was run in a semi-prognostic manner (compare section 3.2) and the same observational data was used to derive the large scale advection terms for the model and for the comparisons. In order to better evaluate the simulations, a comparison of the modeled results to independent observational data is necessary. In this section model results will be compared to data derived from the ISCCP (International Satellite Cloud Climatology Project) DX dataset (Rossow and Schiffer, 1999). The DX dataset has a horizontal resolution of 30 km and a time resolution of 3 h. Data from an 8×8 grid points large region centered at 2°S, 156°W are compared to results from a 2-D WRF run for a 500 km long domain. The horizontal resolution was 2 km and SLBCs were used.

Cloud fractions derived from satellite observations and derived from model results are compared in Figure 3.8. In a first step, satellite data and model data were both averaged horizontally. The cloud fraction at each model grid point was assumed to be unity where the vertically integrated sum of all cloudmeteor masses exceeded $5{\cdot}10^{-3}\,\mathrm{kg\,m^{-2}}$ and zero otherwise. The horizontal domain averages (see thin solid line in Fig. 3.8) of the modeled cloud fractions are mostly lower than the satellite values. Since the model resolution is higher than the satellite resolution, in a second step the model derived cloud fractions were averaged horizontally to ∼30 km resolution and to 3 h time intervals. The cloud fraction on the new grid was assumed to be unity if the averaged cloud fraction exceeded f_{lim}=0.5 and zero otherwise. Subsequently, these values were averaged again horizontally (see dashed line in Fig. 3.8). These averaged values agree better with the satellite observed values. However, the values are sensitive to the somewhat arbitrary choice of f_{lim}. On 19 December, the modeled cloud fraction reaches a maximum and then drops off again. The reason is that initially a non-precipitating stratiform cloud forms for a while covering most of the domain. In this stratiform cloud, small cells eventually grow and form large cells which eventually organize into mesoscale convective systems. When the small cells from the cloud layer grow to become the first deep convective clouds, the stratiform cloud vanishes rapidly.

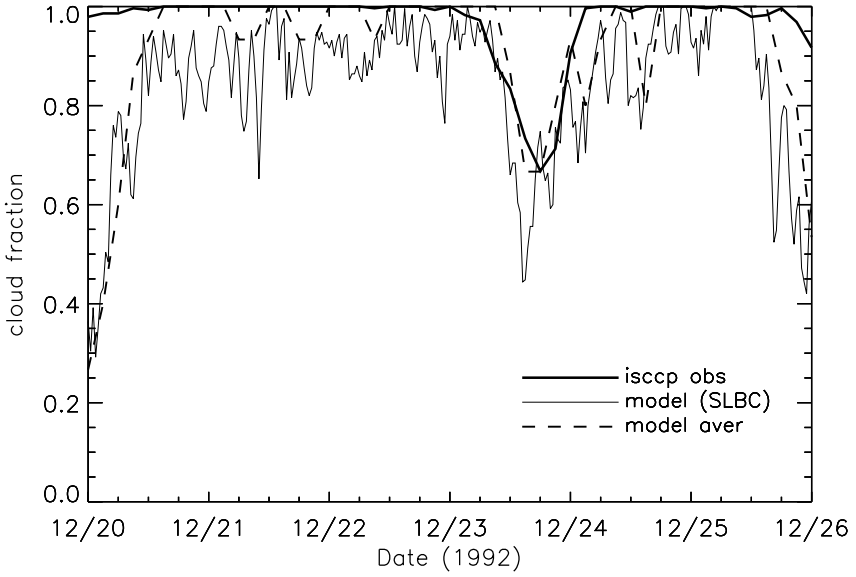

Figure 3.8: Cloud fractions derived from ISCCP satellite observations and from model output. Model output was either horizontally averaged (thin solid line), or first averaged to satellite resolution prior to domain averaging (dashed lines, see text).

In addition to the cloud fractions, cloud top temperatures and cloud top pressures derived from satellite observations and from model calculations were compared. The cloud top heights retrieved from the satellite data depend on how diffuse the cloud tops are. Tropical clouds often have diffuse cloud tops, and in this case the ISCCP "cloud top" has to be interpreted as the location where significant cloud mass is first encountered when moving downward through the atmosphere (Rossow and Schiffer, 1999). In the model, the cloud top is defined to be the height of the first model level, where the sum of all cloudmeteor masses integrated downwards starting from the model top exceeds $5{\cdot}10^{-3}\,\mathrm{kg\,m^{-2}}$. The resulting cloud top pressures and temperatures were binned into 2 K and 25 hPa intervals, respectively.

Histograms are shown in Figure 3.9. In order to reduce differences due to different model data and satellite spatial data resolutions, the model derived cloud top heights were again averaged horizontally to ∼30 km resolution. In order to eliminate the influence of the rather long-lived layer of clouds formed at an altitude of about 5 km during the first day, only data from the last 6 days of the simulated TOGA COARE episode was analyzed. The model overestimated the temperatures and the pressures of the highest cloud tops compared to the data derived from satellite observations. When the WRF microphysics scheme by Lin *et al.* (1983) was used instead of the scheme by Krueger *et al.* (1995), this model bias was smaller (not shown). This finding is sensitive to the somewhat arbitrary choice of the cloudmeteor threshold value of $5{\cdot}10^{-3}\,\mathrm{kg\,m^{-2}}$, but to a lesser extent still holds for lower threshold values. Other than that, the model data compares reasonably well with the satellite data within the uncertainties introduced by the different resolutions of the data and the sensitivity towards the choice of threshold values. In a previous study Su *et al.*

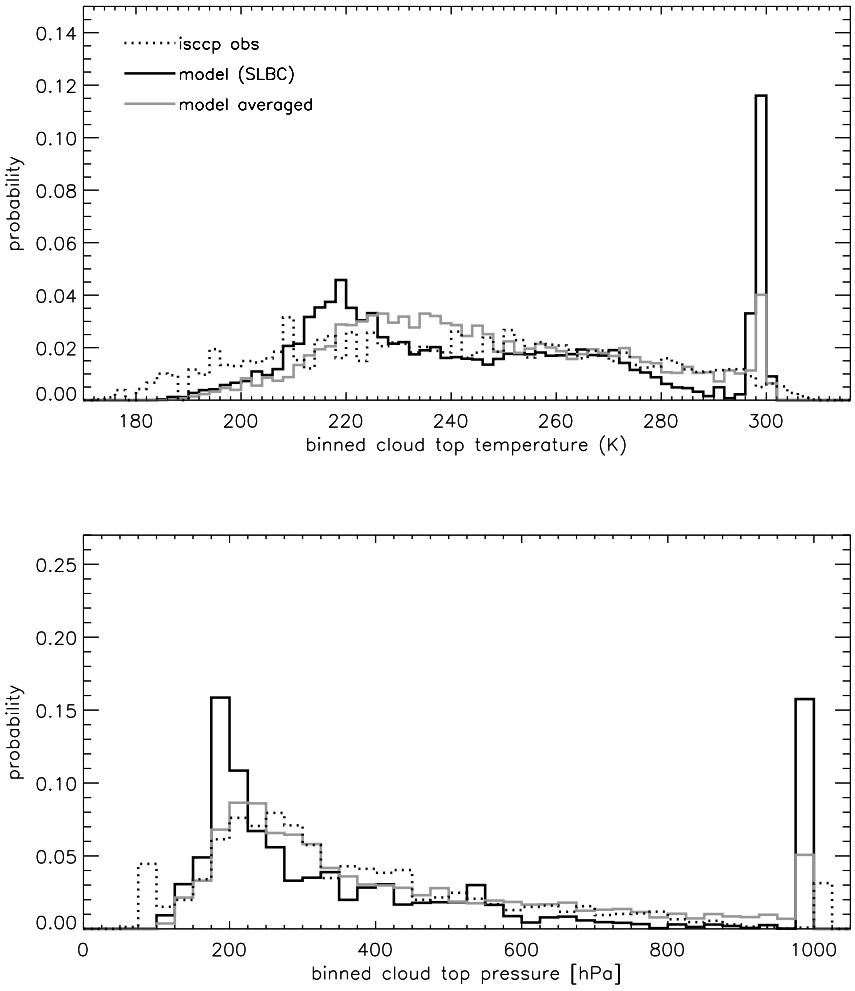

Figure 3.9: Histograms of satellite observation and model derived cloud top temperatures and cloud top pressures. The light gray line was obtained by averaging the model derived values horizontally to satellite resolution prior to binning. Only data from the last 6 days (20 December to 26 December) of the simulated TOGA COARE episode was used.

(1999) compared model results obtained with 15 and 60 km horizontal resolutions for the same TOGA COARE episode to ISCCP data from an averaged dataset with 2.5°×2.5°and 3 h resolution. Here, ISCCP data with a much higher resolution was compared to CRM results with 2 km horizontal resolution. It was shown that differences between model and satellite data resolution can have important implications for the comparison. Furthermore, the previous discussion suggests that small scale variations in cloud top height may play a role even for the retrievals of relatively high resolution satellite cloud top temperature data. However, with rapidly increasing horizontal resolution of satellite instruments, uncertainties related to resolution are bound to decrease. A comparison between cloud top heights simulated using different model setups is presented in Section 4.4, Fig. 4.9.

Chapter 4

Tracer Transport Sensitivity Studies

In this chapter, the results from tracer transport sensitivity studies using different lateral boundary conditions and either prescribing or neglecting the VLSAT term are discussed. The setup of the different sensitivity runs was described in Section 3.4. The setup of the run using PLBCs is the same as the one used by Lu *et al.* (2000), except that Lu *et al.* (2000) re-initialized their tracer fields every 60 h. In the runs using specified lateral boundary conditions the domain averaged mass flux divergence (advection) of the tracers is due to the difference in influx and outflux across the domain boundaries. While the tracer mass flux at the inflow boundary depends on the specified tracer concentration and the wind, the mass flux at the outflow boundary is influenced by the modeled tracer transport inside the domain. When preparing this chapter, the transport of the ten tracers included in the sensitivity runs was analyzed using different methods. For the purpose of describing the main characteristics, it was found to be useful to choose three tracers for a detailed discussion. Subsequently, these tracers will be referred to as tracer A, B, and C. Tracer A was initialized in a lower tropospheric layer, tracer B in the mid-troposphere, and tracer C in the upper troposphere (UT).

4.1 Lower Tropospheric Tracer "A" in 2-D Runs

4.1.1 Periodic lateral boundary conditions

Tracer A was initialized at a horizontally and vertically constant concentration in a lower tropospheric layer between 0 and 1750 m height. Fig. 4.1a shows a time height contour plot of horizontally averaged modeled tracer mixing ratios. For plotting, the concentrations (unit of a density) were converted to mixing ratios and normalized to the maximum initial mixing ratio. Rapid upward transport immediately after the onset of modeled deep convection at ∼23 GMT on 19 December results in a steep increase of the upper tropospheric tracer mixing ratios in Fig. 4.1a. Within the next day the amount of tracer in the boundary layer decreases rapidly, while in the UT a local maximum of the tracer mixing ratio forms (at the height of

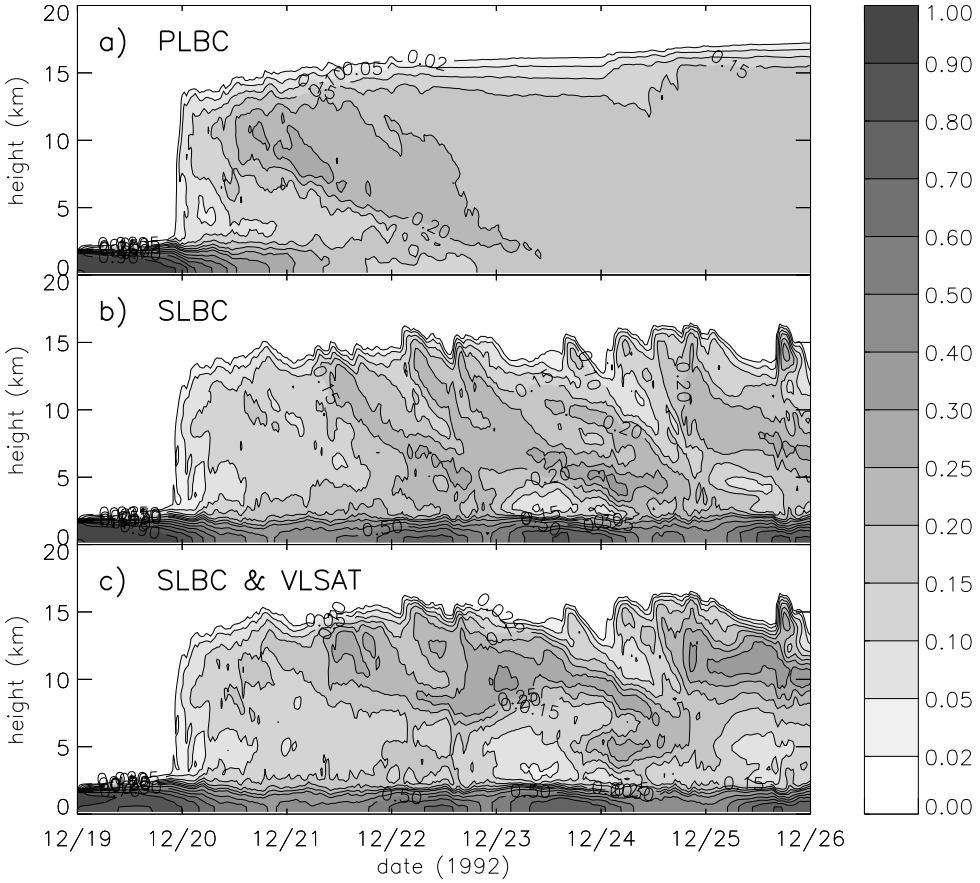

Figure 4.1: 2-D sensitivity runs: Time-height contour plots of domain averaged tracer mixing ratios for tracer A initialized at a horizontally and vertically constant concentration in a layer between 0 and 1750 m altitude. The mixing ratio values plotted in this figure are normalized to the maximum initial mixing ratio. **(a)** Periodic lateral boundary conditions, **(b)** specified water vapor, wind, and tracer lateral boundary conditions, **(c)** specified lateral boundary conditions and vertical large scale advection for tracers. Contour levels are: 0.0, 0.02, 0.05, 0.1, 0.15, 0.2, 0.25, 0.3, 0.4, 0.5, 0.6, 0.7, 0.8, 0.9. and 1.0.

the cloud anvils). The altitude of this maximum starts decreasing immediately because of tracer mass descending due to the mass balancing mesoscale subsidence induced by the deep convection. Furthermore the mixing ratio of the tracer close to the surface is sufficiently depleted so that air advected rapidly upwards does not contain high enough tracer mixing ratios to account for the formation of further upper tropospheric mixing ratio maxima. Later the vertical mixing is increased since some of the descending tracer is re-entrained into deep convective clouds and transported upwards. Four days after the onset of deep convection the tracer is well mixed throughout the model troposphere.

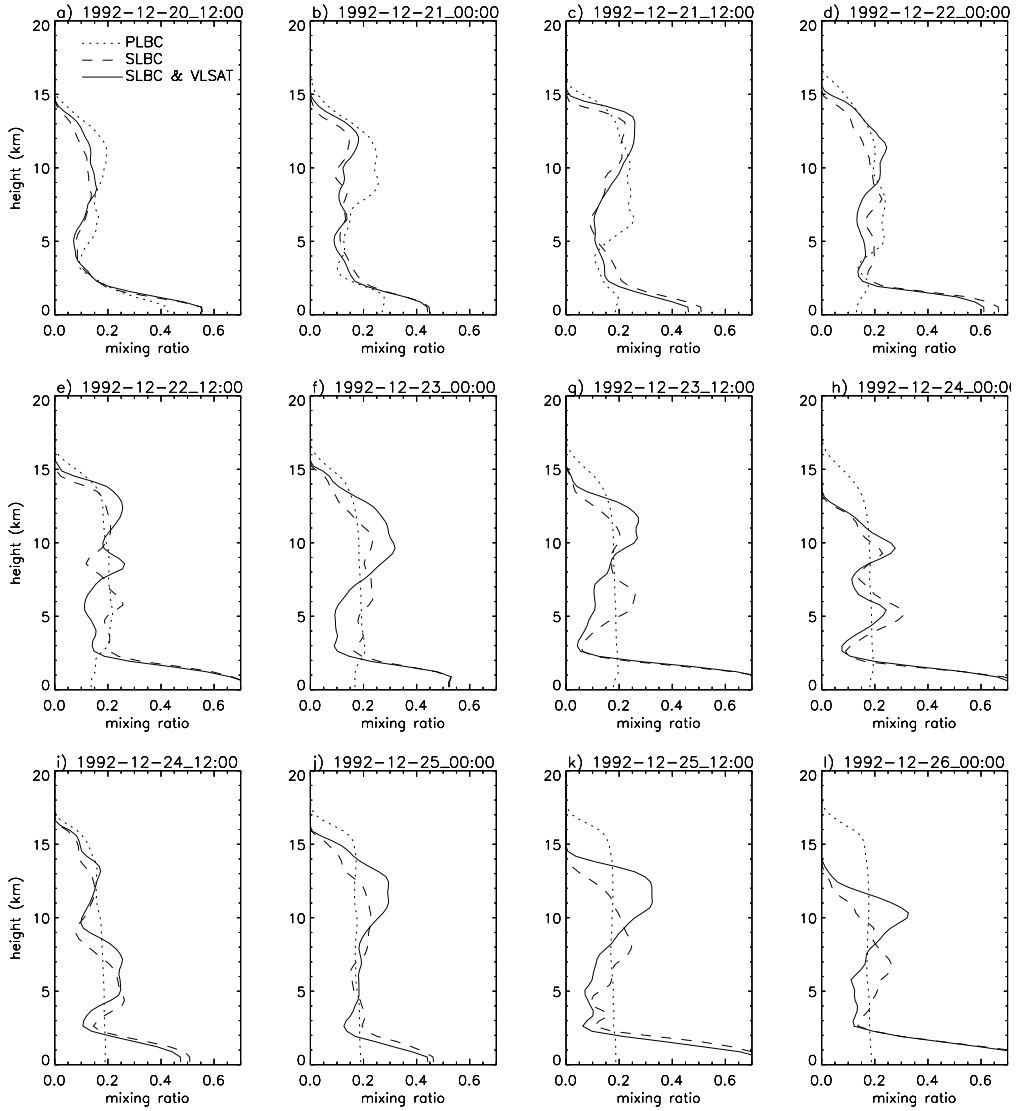

Figure 4.2: Domain averaged vertical tracer profiles for tracer A every 12 h after the modeled convection sets in for a run with PLBCs (dotted line), a run in which the tracer concentrations were specified at the lateral domain boundary (dashed line) and a run with specified LBCs and VLSAT (solid line). Mixing ratio values were normalized to the maximum initial mixing ratio.

4.1.2 Specified lateral boundary conditions

Specifying LBCs for tracers allows for tracer advection across the model's lateral boundaries and for the total amount of tracer mass inside the domain to be influenced by the mean horizontal wind. Like in the case of PLBCs tracer mass is rapidly transported from the lower troposphere (LT) to the UT when deep convection sets in (see Fig. 4.1b). Initially, the lower tropospheric mixing ratio decreases as in the case of PLBCs. But between 21 December and 22 December the westerly wind burst sets in and wind speeds in the LT increase (see Fig. 3.2a). Tracer mass transported

away from the LT inside the updrafts of the deep convective clouds is replenished by tracer mass horizontally advected into the model domain. Around the same time the wind increases in the UT and tracer mass is continously advected out of the domain across the lateral boundaries. The amount of tracer mass on the net advected into the domain in the LT and the amount of tracer mass on the net advected out of the domain at upper tropospheric levels could quantitatively be assessed calculating the time-integrated horizontal and vertical advection tendencies (compare e.g. Section 8.4). Integrated over longer episodes, the tendencies of horizontal and vertical advection at each vertical level approximately balance. As for the run with PLBCs (Fig. 4.1a), upper tropospheric mixing ratio maxima with contours sloping towards the Earth's surface indicate the strong effect of mesoscale subsidence. When the VLSAT term is taken into account (Fig. 4.1c) relatively rapid downwards transport occurs, especially at the time of the maximum in convective activity on 24 December, but once injected into the UT, the tracer mass often remains there for considerably longer times. Relatively rapid downwards transport takes place due to descending rear inflow which occurs in association with diabatic cooling due to the evaporation of rain. More recently, rear inflow has been interpreted in terms of a gravity wave response to heating by MCS (Houze, Jr., 2004, and references therein). For tracer A, domain averaged vertical profiles are plotted in Fig. 4.2 reflecting the differences between the results of the different sensitivity runs discussed here. Significant differences between the SLBC run and the run with PLBCs already become apparent in Fig. 4.2b (less than 24 h after the onset of deep convection in the model). The profiles in Fig. 4.2 will be discussed in more detail in Section 4.6.

4.2 Mid-Tropospheric Tracer "B" in 2-D Runs

4.2.1 Periodic lateral boundary conditions

Tracer B (see Fig. 4.3a) was initialized at a constant concentration in a layer between 7000 and 8750 m height and is chosen as a representative mid-tropospheric tracer. At the onset of deep convection this tracer is less effectively transported upwards since the levels of maximum entrainment of deep convective clouds are located in the LT. The amount of tracer B in the UT increases much less rapidly than that of tracer A (compare Fig. 4.3a to Fig. 4.1a), because tracer B is less efficiently entrained into deep convective cells than tracer A. The finding that tracer B is entrained less efficiently than tracer A and that tracer A is predominantly detrained in the UT provides a different perspective than the 'convective ladder' effect postulated by Mari *et al.* (2000). In the run with PLBCs, tracer B is also transported downwards due to the mesoscale subsidence and after two days of active deep convection a substantial fraction has reached the LT from where it is then rapidly transported upwards. At the end of the studied period this tracer is almost homogeneously distributed throughout the entire troposphere.

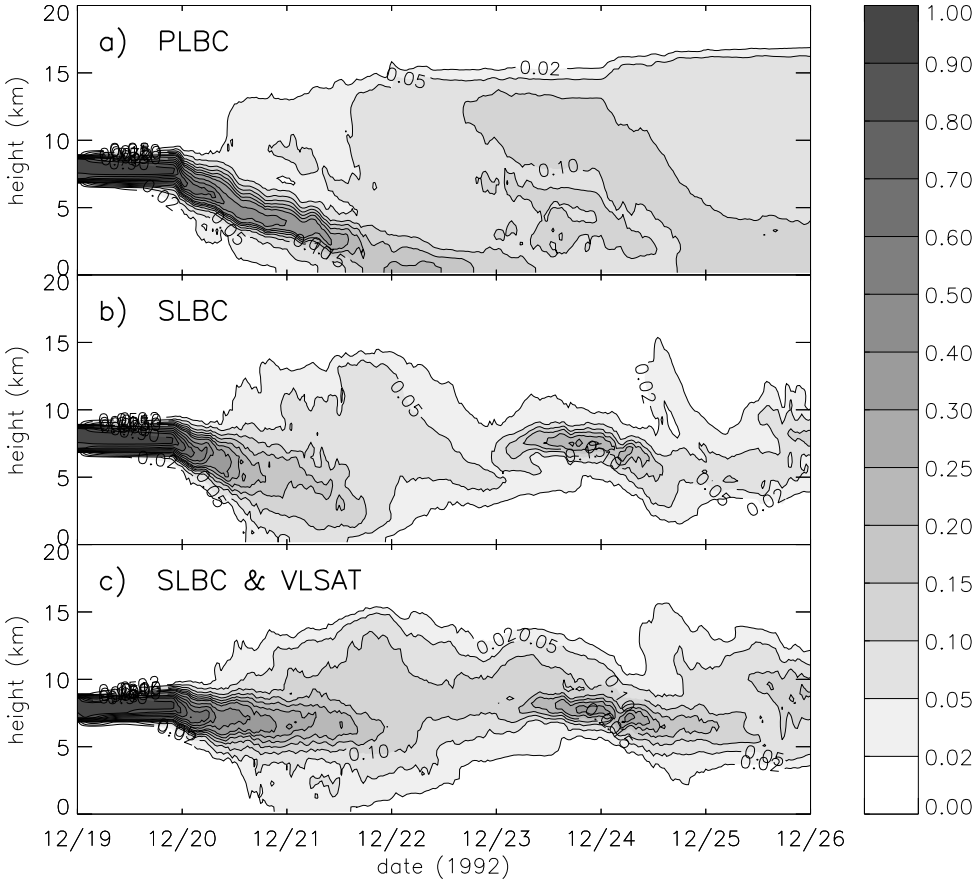

Figure 4.3: As Fig. 4.1 for tracer B initialized at a constant concentration between 7000 and 8750 m.

4.2.2 Specified lateral boundary conditions

During the first two days of the model run, the domain averaged mixing ratio for tracer B evolves similarly to its counterpart in the run with PLBCs when the VLSAT term is omitted (see Fig. 4.3b). When the VLSAT term is incorporated (see Fig. 4.3c) the mesoscale downward transport on 20 December is largely compensated. In Fig. 4.4 the mixing ratio contours of tracer B on 20 December 14:00 GMT are depicted for the three different sensitivity runs. In the run with PLBCs the mesoscale subsidence has caused the center of tracer mass to subside to nearly 3 km below its initial location. The strong effect of the mesoscale subsidence is also apparent for the SLBC run in Fig. 4.4b where the mixing ratio contours slope downwards from the inflow toward the outflow boundary. In the run in which the VLSAT term was included on the other hand, a large fraction of the tracer mass has remained at its initial height. Between 21 and 22 December (see Fig. 4.3b again) when the westerly wind burst sets in, the total amount of tracer B in the domain decreases as a consequence of mesoscale subsidence, wind shear and transport across the lateral domain boundary. First the tracer is transported downwards because of the mesoscale subsidence to altitudes below 5 km where the average westerly wind is

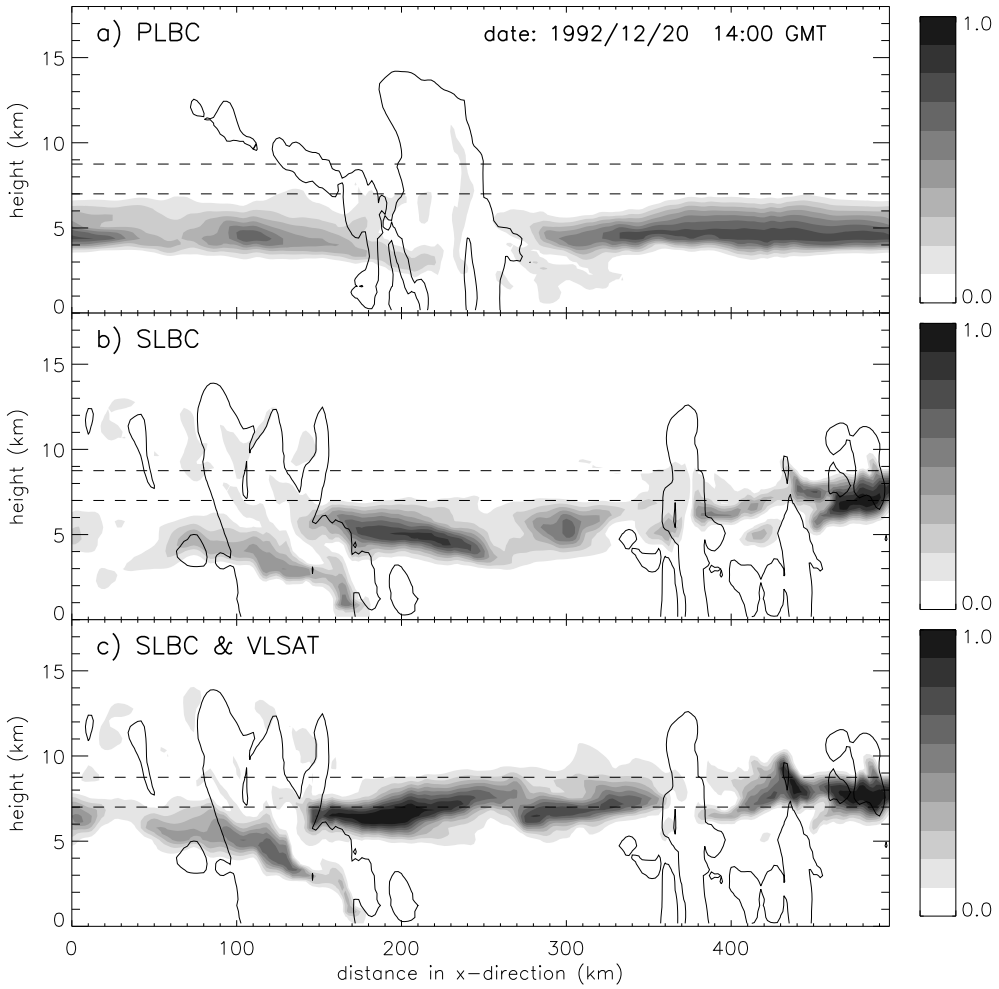

Figure 4.4: Tracer B: X-Z contour plot of the normalized mixing ratio ∼16 h after the onset of modeled deep convection. The contour interval is 0.1. Dashed lines indicate the initial tracer location, the solid line is the 0.1 g kg^{-1} mixing ratio contour of the sum of all masses of hydrometeors in the ice and the liquid phase.

strong. From there it is rapidly transported eastwards to where it leaves the domain across its lateral boundary. For the tracer in the VLSAT run, in total more tracer mass remains inside the domain because the transport due to the mesoscale subsidence is largely compensated by the VLSAT. Around 24 December the easterly wind at above 5 km height reaches a local maximum which transports 'fresh' tracer into the domain. For a smaller domain (e.g. 248 km, see Fig. 4.7a) the depletion of the tracer mass in the domain is weaker because during the time τ_{adv} it takes the tracer to be advected across the entire length of the domain a smaller fraction of the tracer mass is transported downwards due to the mesoscale subsidence. For a larger model domain (1000 km) the depletion is also weaker (figure not shown) because τ_{adv} is long enough so that not all of the tracer transported downward is transported out of the domain during the period before tracer mass is replenished

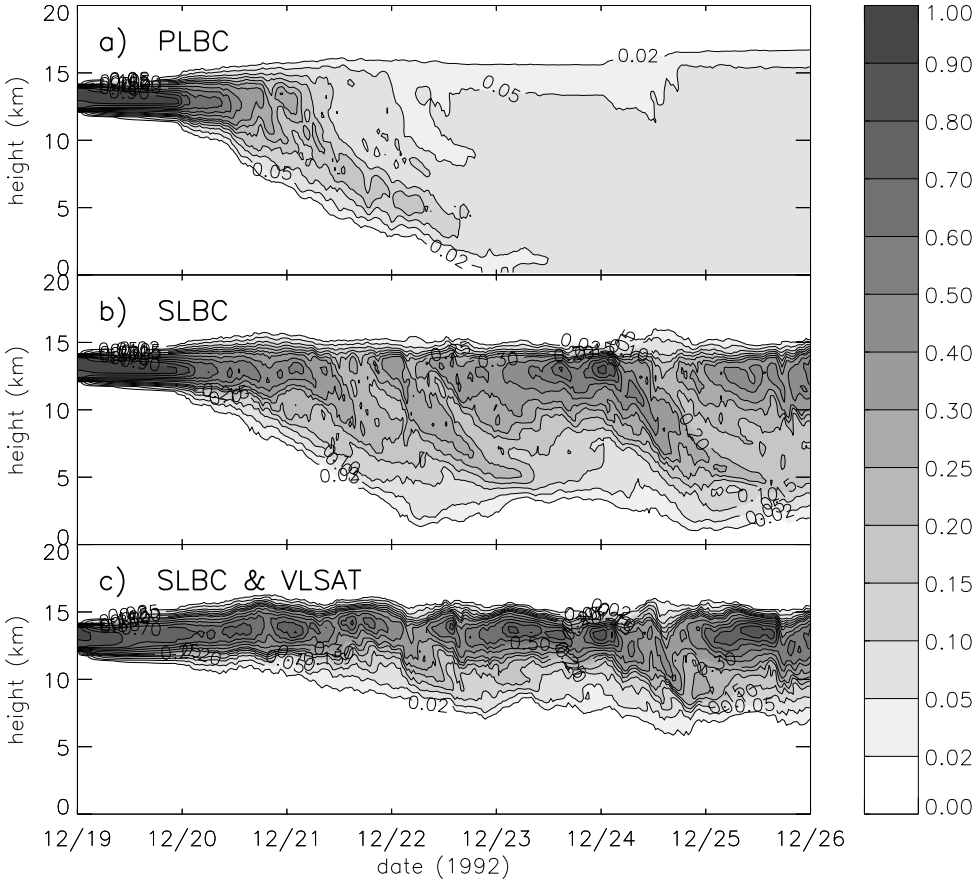

Figure 4.5: As Fig. 4.1 for tracer C initialized at a constant concentration between 12 250 and 14 000 m.

by the increasing easterly wind. The rapid downward transport on 20 December is due to rear inflow associated with the evaporation of rain and the related diabatic cooling (compare rear inflow in Fig. 4.4c between x=100 km and x=200 km).

4.3 Upper Tropospheric Tracer "C" in 2-D Runs

4.3.1 Periodic lateral boundary conditions

Tracer C (see Fig. 4.5a) was initialized in an upper tropospheric layer between 12 250 and 14 000 m. About 12 h after the onset of the deep convection the first cumulus towers penetrate this layer and initiate downwards transport. The air inside the anvils carries a low tracer mixing ratio and replaces the air with high mixing ratios in the UT (which is transported downwards along the lower edge of the anvils). Mesoscale subsidence acts to further transport tracer mass towards the Earth's surface. On 22 December a reduction in domain averaged mixing ratio located at ∼10 km altitude is calculated. The decrease of the mixing ratio leading to this

minimum is attributed to the transport of air with a low tracer mixing ratio from the LT to the UT. At the time of the subsequent increase of mixing ratio in the UT some air containing high tracer mixing ratios has reached the LT from where it is again transported upwards inside deep convective clouds. Four days after the onset of deep convection the tracer is fairly well mixed throughout most of the model troposphere.

4.3.2 Specified lateral boundary conditions

As for the run with PLBCs tracer C is influenced by the penetration of deep convective towers and by mesoscale subsidence (see Fig. 4.5b and c). Because of the upper tropospheric easterly winds some of the tracer mass advected downwards is replenished from outside the domain. If VLSAT is taken into account in the model (see Fig. 4.5c) considerably less tracer mass is transported to the LT than for the run with VLSAT switched off (Fig. 4.5b). Steep negative slopes in Fig. 4.5c indicating rapid downward transport from the upper troposphere appear mainly on 22 and 24 December. Details of the rapid downward transport of ozone will be investigated in Section 9.6. The amount of tracer that can reach the lower troposphere is limited by the domain size because of low level transport out of the domain and low level import of "fresh air".

4.4 Comparison 2-D vs. 3-D Model Runs

In this section tracer transport results from a 3-D run with a 248 km×248 km horizontal domain size are compared to results from a 2-D run with a 248 km long domain. Both runs were performed using SLBCs and taking into account the VLSAT term as described in Section 3.4. For tracer A, the results from both runs are depicted in Fig. 4.6. The time-height contours of the domain averaged tracer mixing ratio are smoother for the 3-D run than for the 2-D run, but the main features in Fig. 4.6a and b are similar, particularly during the first two days of active deep convection when the meridional wind component (see Fig. 3.2b) is small. On 22 December the southerly wind component in the UT starts increasing as well as the northerly wind component in the mid-troposphere. In the mid-troposphere tracer mass is advected out of the 3-D domain across the southern boundary on the 23rd (compare Fig. 4.6 b). On 25 December an increasing southerly wind component in the mid-troposphere leads to an increase of tracer advection out of the domain across the northern boundary, which is also reflected in Fig. 4.6b. For tracer B (see Fig. 4.7) the amount of tracer that remains in the lower troposphere differs between the 3-D run and the 2-D run, because in the 3-D run, meridional tracer transport in the layers below the initial tracer mass location acts to advect tracer mass out of the domain. Cross-boundary advection in the meridional direction is also found to play an important role for the differences of the domain averaged mixing ratios of tracer C (see Fig. 4.8). Again subsiding tracer mass is advected out of the do-

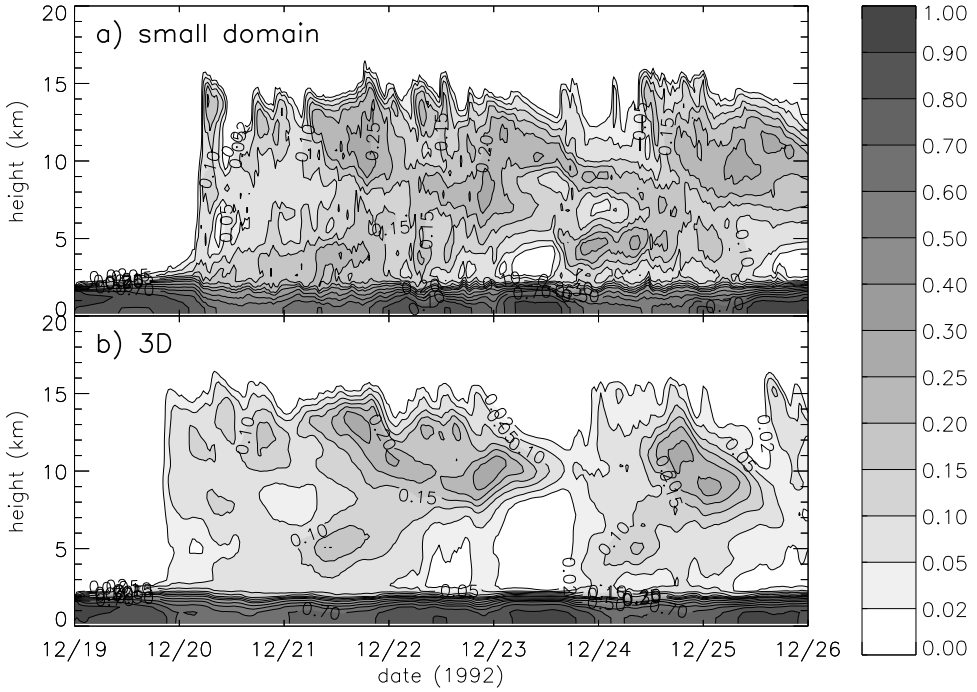

Figure 4.6: As Fig. 4.1 but **(a)** for the 248 km long 2-D domain and **(b)** for the 248 km×248 km horizontal area 3-D domain.

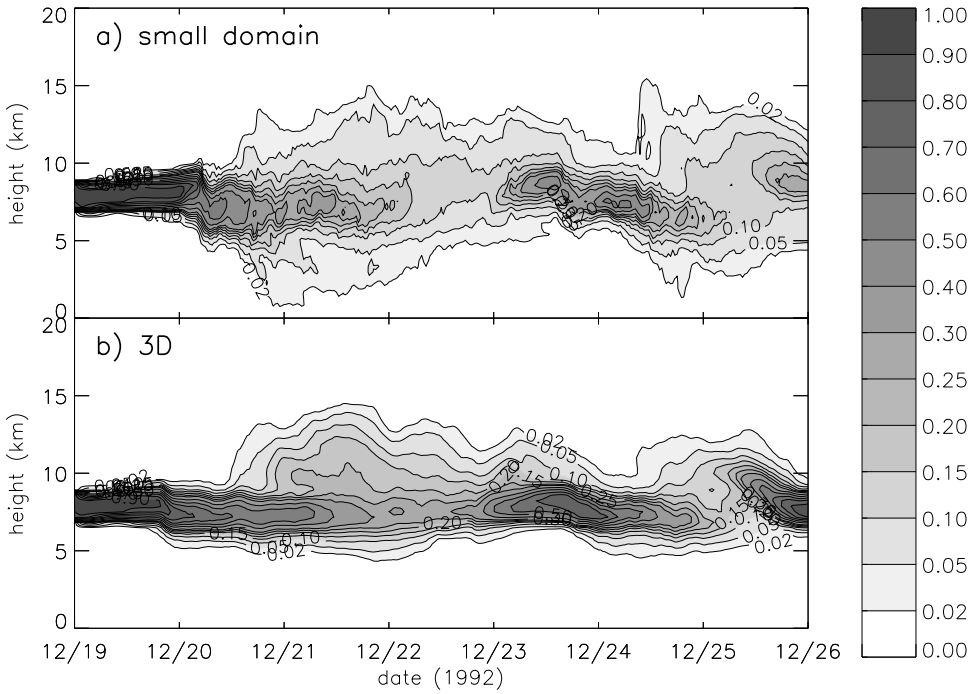

Figure 4.7: As Fig. 4.6 for a tracer initialized at a constant concentration between 7000 and 8750 m.

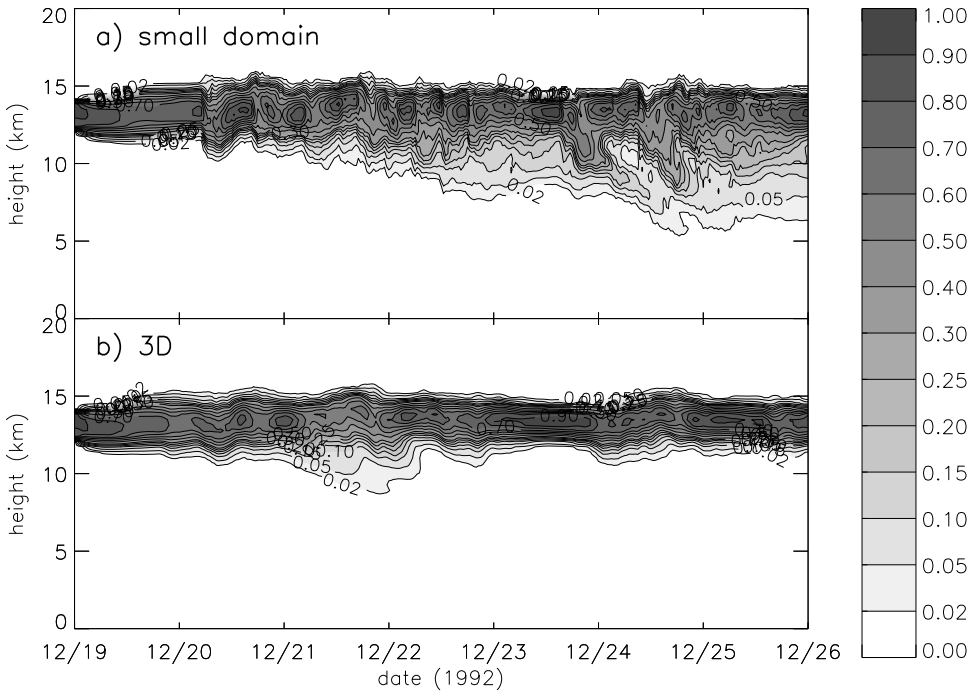

Figure 4.8: As Fig. 4.6 for a tracer initialized at a constant concentration between 12 250 and 14 000 m.

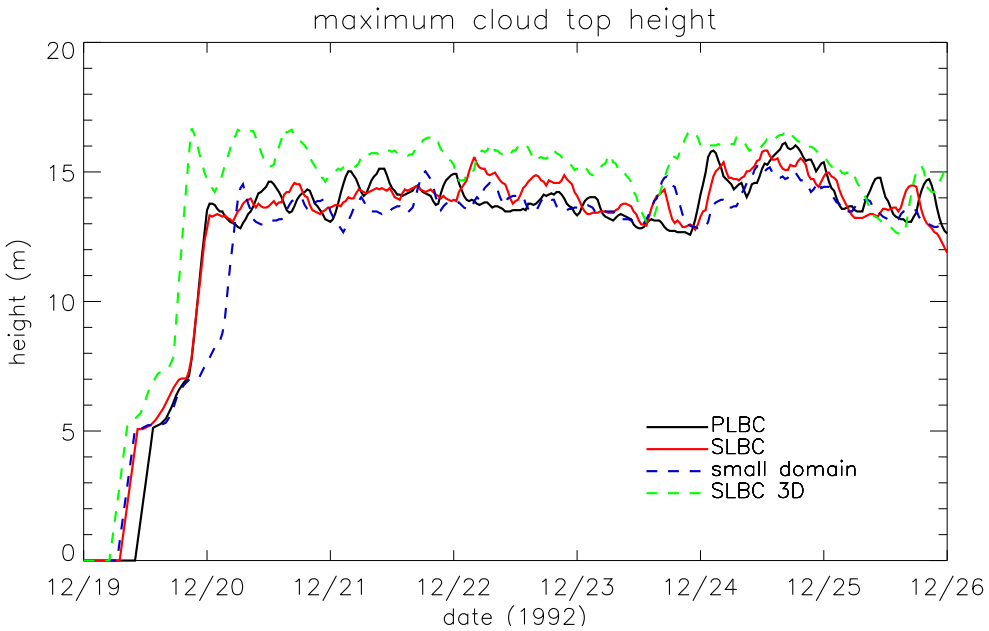

Figure 4.9: Domain maximum cloud top heights. The sampling time was 30min and a 3hr moving average is plotted. The cloud top height was defined as the first model level where the sum of all cloudmeteor masses integrated downwards starting from the model top exceeds $5{\cdot}10^{-3}$kg m^{-2}.

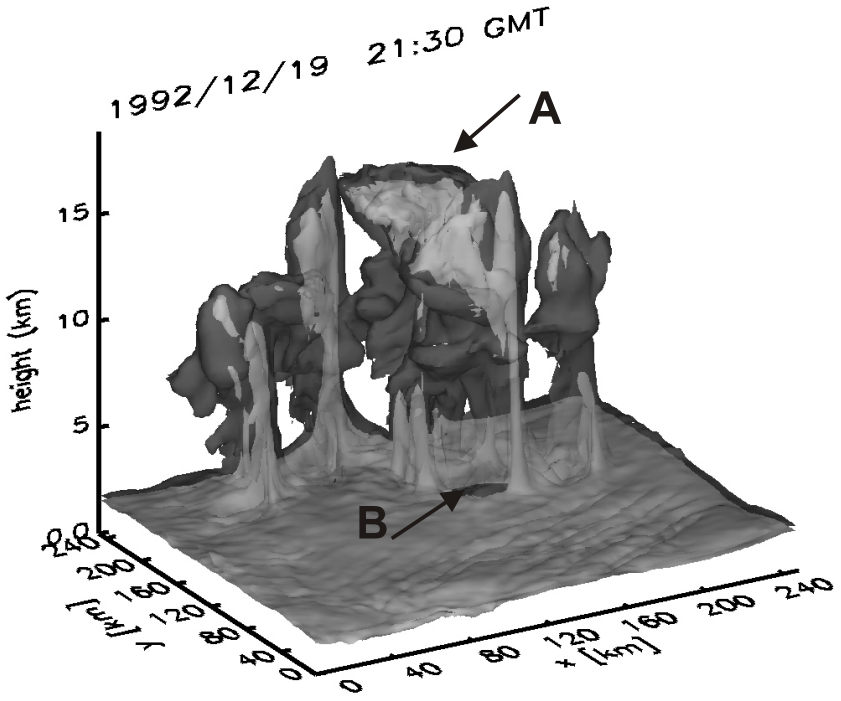

Figure 4.10: Mixing ratio iso-surfaces for tracer A in the 3-D run on 19 December 21:30 GMT, shortly after the onset of deep convection. The mixing ratios were normalized to the maximum initial mixing ratio as in Fig. 4.1. The 0.2 (dark shade) and the 0.5 (light shade) iso-surfaces are indicated.

main in the 3-D run due to the non-zero meridional wind component, while in the 2-D run advection in the meridional direction is not considered. Fig. 4.9 shows the maximum cloud top heights in the domain for different runs. The cloud top height was defined as the first model level where the sum of all cloudmeteor masses integrated downwards starting from the model top exceeds $5{\cdot}10^{-3}$kg m^{-2}. Most notably, the maximum cloud top heights for the 3-D run are generally above those for the corresponding 2-D run. For the 500 km domain 2-D runs, the maximum cloud top heights are largely independent of the boundary conditions applied. Differences of the downwards transport of tracer C are most likely caused by the application of VLSAT rather than by systematically different cloud top heights. Differences between 2-D and 3-D tracer transport model runs can also arise due to dynamical or microphysical reasons (e.g. Wang and Prinn, 2000). This study focuses mainly on the differences due to cross boundary transport. Cross boundary transport is believed to be the main reason for the differences between the results of the 2-D and the 3-D run presented here, but further research, including a 3-D simulation with PLBC, is needed in order to better differentiate between the different processes involved.

Fig. 4.10 shows iso-surfaces for tracer A after the onset of deep convection. A

number of updraft shafts stretch from the initial location of the tracer below 2 km to the tropopause. One of the shafts is already accompanied by a "trace gas anvil" (arrow marked "A" in Fig. 4.10). Below this anvil, a round region of minimum tracer concentration has formed (arrow "B"). This minimum is located where downward motion and divergence close to the Earth's surface occur. On the edges of the region, smaller shafts have formed indicating the triggering of new updrafts. The domain in this simulation is still too small to contain a large number of clouds at the same time.

4.5 Additional Sensitivity Studies, Dependence on Resolution

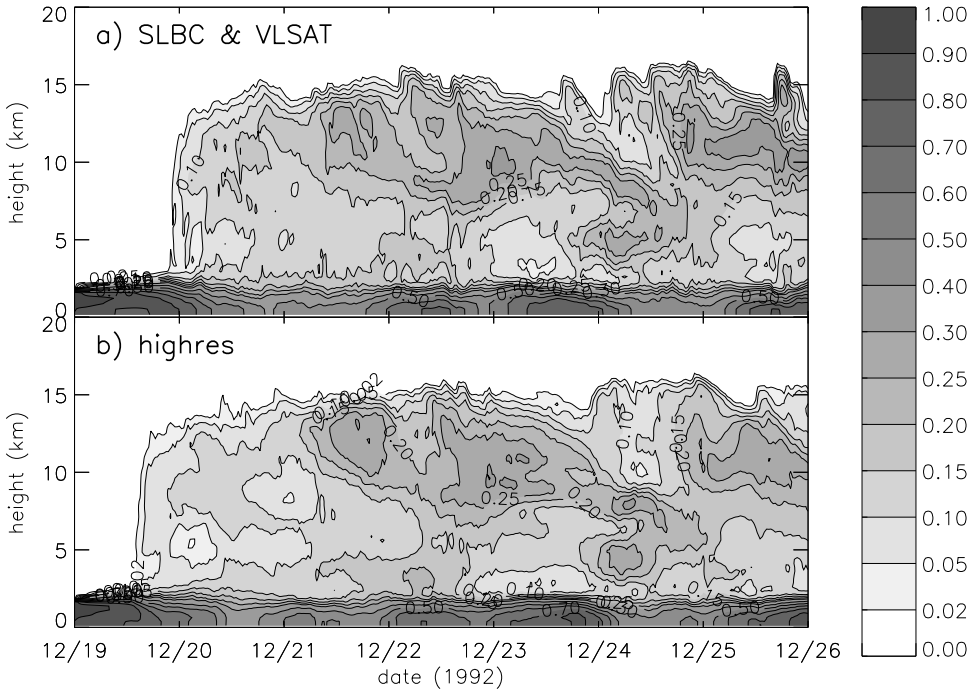

Figure 4.11: As Fig. 4.1 but **(a)** for the run using SLBC and VLSAT (identical to Fig. 4.1c) and **(b)** for a high resolution run (see text).

A number of additional sensitivity studies were conducted. These included sensitivity studies towards using two different microphysics schemes, towards using a PBL (planetary boundary layer) parameterization scheme, and towards using higher resolution. The sensitivities in these studies were smaller than the sensitivity towards using different boundary conditions. However, so far the total number of CRM sensitivity studies for tracer transport simulations is still small and additional studies under different conditions and for different model setups should be conducted in the future. In Fig. 4.11 results for tracer A from a higher resolution run are compared to results from the run using SLBC and VLSAT, which was previously discussed. In the high resolution run, the domain length was 500 km, the horizontal resolution was

400 m, the vertical resolution in the troposphere 250 m, and the timestep was 3 s. SLBCs and VLSAT were applied. The runs show qualitatively and quantitatively similar results, but convection sets in earlier in the high resolution run. This is most likely related to a larger buildup of CAPE prior to the onset of deep convection in the coarser resolution run. Very recent research (Skamarock *et al.*, 2005) has shown that grid spacings typically applied in CRMs may not be high enough to reproduce all aspects of deep convection. However, one could argue that current CRMs do reproduce major aspects of cloud system dynamics.

4.6 Discussion

Many trace gas compounds with tropospheric lifetimes between a few hours and a few weeks such NO_x (nitric oxide + nitrogen dioxide) or carbon monoxide have a source close to the Earth's surface. Measured vertical mixing ratio profiles of these compounds in the vicinity of deep convection are often 'C'- shaped, i.e. have a maximum in the LT and a second maximum in the UT (e.g. Dickerson *et al.*, 1987; Gidel, 1983). On the other hand, in post convective environments profiles of trace gases with a sink in the LT often have a minimum in the LT and a second minimum in the UT (e.g. Kley *et al.*, 1997). Sometimes such a profile is referred to as 'D'-shaped (or 'S'-shaped, when they have a stratospheric source like O_3).

Tracer A can be considered an idealization of a moderately long lived, insoluble trace gas with a surface source. Its initial profile represents its idealized profile in an environment which has not been influenced by (either local or remote) deep convection recently. Figure 4.2 shows vertical profiles of model calculated tracer profiles for this tracer. During the first 36 h the tracer profile in the run with PLBCs still displays the typical 'C'-shape caused by intermittent deep convective transport. After roughly three days the tracer is well mixed. If a constant wind speed of $5\,\mathrm{m\,s^{-1}}$ is assumed, three days would correspond to a horizontal transport distance of $\sim$1300 km which is still smaller than the entire Pacific Warm Pool, suggesting that moderately long lived tracers would be well mixed after having (hypothetically) been advected at this wind speed straight across the entire Pacific Warm Pool. This could possibly also be expected as a result in a tracer CRM study with SLBCs and a sufficiently large domain size.

If chemistry transport CRM results are to be compared to observations from field campaigns covering a limited area, a multi-day simulation with PLBCs would probably be of limited use since for moderately long lived tracers the effect of horizontal advection on these time scales is not negligible, as demonstrated by the differences in Fig. 4.2b to f and discussed previously. On the other hand, if LBCs would be specified from measurements, the method presented in this study could in principle be used for CRM simulations of trace gas dispersion due to deep convective clouds. However, in order to obtain the necessary input data for such a simulation, a comprehensive field campaign of the size of the TOGA COARE campaign encompassing both meteorological and trace gas measurements would be necessary. No

such campaign has been planned. Nevertheless, input data from different sources, including both field campaigns and results from global chemistry transport models (GCTMs) could be used to specify the necessary boundary conditions for CRMs with the setup proposed here. Since the onset time of deep convection was found to be resolution dependent (Section 4.5) and varied between 2-D and 3-D setups, the correct onset time of deep convection would be difficult to model, using the present setup. Furthermore, the setup presented here allows mainly comparisons in a statistical sense, while observed individual deep convective events are not likely to be reproduced exactly. In the future, nested model setups may help to avoid these problems (see Chapter 13). So far, nested models have been used successfully to model deep convection in situations with strong synoptic forcing or forcing by orography. To the authors knowledge, it has not been attempted to set up nested models for the TOGA COARE region. Note, that traditionally in CRM studies, deep convection is initiated by placing one or more artifical cold or warm bubbles inside the model domain. Skamarock *et al.* (2000), for example, prescribed three bubbles in order to re-produce the observed structure of a multi-cell storm. A promising method, which has been proposed recently is to destabilize the model troposphere using a gravity wave field derived from a preliminary model integration. Here, the transport of idealized tracers was studied and the boundary conditions were kept fixed. For more realistic studies, time-dependent boundary values for trace gases can be prescribed to the extent they are available. In Chapter 7, a model setup will be presented in which initial and boundary values were prescribed based on results from MATCH-MPIC.

Another potentially useful application for the setup described in this study could be the comparison between tracer transport results from CRMs and parameterizations used in global models. In global chemistry transport models convective transport constitutes a major source of uncertainty since it is highly sensitive to the convective parameterization applied (Mahowald *et al.*, 1995) and even to the treatment of transport based on the mass fluxes provided by individual schemes (Lawrence and Rasch, 2005). Cloud-resolving models (CRMs) in combination with single column models (SCMs) could perhaps help to better evaluate these parameterizations and thus reduce this uncertainty. For TOGA COARE a comparison between different single column models including deep convective tracer transport was presented by Rasch *et al.* (2003). More recently, a similar setup was used for CRMs and single column models by Bechtold *et al.* (2005). A similar framework as the one presented here could be used in multi-day single column model (SCM) studies. Comparisons between SCMs and CRMs would draw substantial benefits from the method presented here.

In global models, the tracer transport due to large-scale ascent is calculated separately using the so-called operator splitting technique. This method used in global models is similar to the method used here, in this CRM study. In the deep convection parameterizations in global models it is assumed that the upwards advection of air mass inside the convective clouds is balanced by the compensating subsidence in the same vertical model column (e.g. Staudt *et al.*, 2003). Implications of using

the operator splitting method for the tracer transport in global Eulerian and for Lagrangian models were recently discussed by Lawrence and Salzmann (2005). Note that although the mean vertical velocity is positive in the ITCZ, upwards transport of trace gases should not be expected to take place between clouds, since even lifting of air parcels with relatively low relative humidities over more than a km or so leads to condensation (Lawrence, 2005). Consequently, upwards transport in the ITCZ can be expected to predominantly take place inside deep convective clouds. Positive grid scale vertical velocities in the ITCZ calculated by global models have to be interpreted as mean velocities averaged over areas with strong cloud scale updrafts.

The CRM setup with specified LBCs for water vapor used here allows for larger differences between modeled and observed surface precipitation than the setup with PLBCs and thus could possibly be useful for evaluating different microphysics schemes. A drawback of specifying LBCs for tracers and retaining PLBCs for the air density is that the advection of tracer mass at a given height level due to the domain averaged horizontal air mass convergence or divergence into or out of the domain is neglected. In small domains containing a single convective system and under conditions of weak horizontal average winds, the domain averaged mass flux divergence due to large scale wind convergence and divergence into and out of the model domain is likely to become important.

The results of runs using SLBCs for tracers are domain size dependent, although in this study the differences between the runs with 500 km domain size (see Figs. 4.1c to 4.5c) and 248 km domain size (see Figs. 4.6c to 4.8c) are often small. For either much smaller or much larger domains, a stronger domain size dependence may be expected. This domain size dependence should not be considered a drawback of the method but is an advantage in cases in which model results from future multi-day chemistry transport CRM studies are to be compared to observations.

In the case study presented here, the VLSAT often has a strong effect on the domain averaged vertical profiles, particularly when τ_{adv} (which can be estimated from Fig. 3.2a) is long (e.g. Fig. 4.2e–g, and j–l) and should not be neglected. In CRM studies of reactive tracer transport the over-estimation of downwards trace gas transport, as seen in tracers B and C, could otherwise for example lead to unrealistically high chemical NO_x sources in the mid-troposphere due to the thermal decomposition of subsiding PAN (peroxy acetyl nitrate) or pernitric acid. The spurious downward transport of tracers when the VLSAT is neglected can easily be misinterpreted as the effect of mid-level detrainment.

The results for the PLBC runs in this study are similar to the results presented by Lu *et al.* (2000), i.e., in the model runs with PLBC, the tracers are transported from the mid- and upper troposphere to the LT with a timescale of approximately two days. Figures 15 and 16 of Lu *et al.* (2000) can be compared to Figs. 4.1a to 4.5a for the first days of modeled deep convection. Lu *et al.* (2000) chose to re-initialize their model every 60 h and used a domain length of 512 km. Using sensitivity runs for a 500 km domain, it was demonstrated in this study that the modeled tracer transport is highly sensitive to the choice of LBC, even on timescales of a few days. Furthermore it was shown that including VLSAT changes some

main characteristics of the modeled tracer transport. In multi-day CRM studies of tracer transport in regions with large scale vertical ascent, such as the Pacific Warm Pool, the VLSAT term has to be considered. Since current CRMs do not allow the exchange of airmass across the lateral domain boundaries, the VLSAT must be considered as well as the corresponding terms for q and θ. Particularly in situations with vertical wind shear, model calculated tracer fields obtained with PLBCs will not necessarily be meaningful if the model is run longer than the time $\tau_{adv} = L/\overline{v}_{max}$ it takes the tracer to be advected across the entire length of the domain and the tracer's chemical lifetime is longer than or comparable to τ, where $\overline{v}_{max} = max(\overline{v}(z))$ is the maximum domain averaged horizontal wind speed, and L is the horizontal domain length. On the other hand, if LBCs for trace gases and for the wind are specified, the horizontal wind is allowed to change the vertical tracer gradients and thus the vertical transport.

The result of this study concerning the role of VLSAT is in line with a conclusion of Mapes (1993), who pointed out that the often cited concept of mass balancing mesoscale (between clouds) subsidence induced by cumulus convection does not apply in parts of the tropics and is only valid for infinite uniform fields of cumulus clouds. Failing to represent the effect of a mean upward velocity on tracer transport in CRM studies could lead to errors even in relatively short transport simulations with limited area models. Based on quad-Doppler radar observations Jorgensen *et al.* (1997) presented mean vertical velocities derived from measurements in the vicinity of active deep convection reaching values above 500 m hour^{-1}. Consequently, large scale influences may have to be considered even in relatively short CRM simulations. Central results of this chapter were also included in Salzmann *et al.* (2004).

Chapter 5

Mass Flux Diagnostics

Before proceeding to the study of soluble and reactive trace gases, a brief discussion of vertical air mass flux diagnostics is presented. This subject is of particular interest because today's parameterizations of convective transport in global chemistry transport models are often based on convective air mass fluxes which themselves have to be parameterized in global models.

A comparison between various air mass flux profiles derived from CRM studies of deep convection in the TOGA COARE region reveals large qualitative and quantitative differences. For example, Johnson *et al.* (2002) presented mean cloud mass fluxes from their simulations which are roughly one order of magnitude larger than the updraft mass fluxes derived from CRM simulations by Petch and Gray (2001), the cloud mass fluxes by Costa *et al.* (2001) and the mass fluxes presented by Gregory and Guichard (2002) for the same TOGA COARE episode.

In the first part of this chapter, the influence of using a number of different definitions of updraft, downdraft, or cloud mass flux are investigated as well as the sensitivity of diagnosed mass fluxes to various model setups. While a rather large number of different definitions have commonly been used in previous CRM studies to calculate various kinds of mass fluxes, the documentation of the definitions was often found to be insufficient, thus almost entirely inhibiting meaningful intercomparisons.

In the second part of this chapter, it is argued that gravity wave-like oscillatory motions can account for a large part of the total air mass flux analyzed from CRM output. Oscillatory motions do not cause net vertical transport of trace gases in the absence of height-dependent chemical sources or sinks. In this case, only "irreversible" (non-oscillatory) flow accounts for the net transport, such as the mass balancing compensating subsidence. Xu *et al.* (2002) mentioned that diagnosed mass fluxes in CRM simulations contain contributions from gravity waves without qualitatively showing that they can play a large role. Based on conventional definitions of mass fluxes, it is difficult to determine how much of a diagnosed air mass flux is due to oscillatory motions or smaller closed eddies associated with deep convective clouds which can be resolved at sufficiently high resolution by the model. A

quantitative separation of the contributions of oscillatory, eddy, and non-oscillatory motions to the net vertical mass flux was not attempted here.

5.1 Sensitivities and Definitions

A rather large number of definitions have been used in the literature for calculating updraft, downdraft, cloud and convective mass fluxes. In order to be precise, a definition of a mass flux must contain two parts: Firstly, a definition for the updraft, downdraft, or cloudy area must be provided. In most of the TOGA COARE publications mentioned previously, various threshold criteria either based on microphysical properties such as cloud water and cloud ice contents (Johnson *et al.*, 2002; Costa *et al.*, 2001) or on updraft velocity (Petch and Gray, 2001) have been applied. Johnson *et al.* (2002) used a cloud definition by Xu and Krueger (1991): A grid box is defined cloudy if $q_c + q_i > 0.01 q^\star\,(\mathrm{T}, \mathrm{p})$, where q_c and q_i are cloud water and cloud ice mixing ratios, respectively and $q^\star$ is the saturated mixing ratio over water. Costa *et al.* (2001) defined a cloudy grid box as one containing at least $0.01\,\mathrm{g\,kg^{-1}}$ cloud water plus cloud ice. Petch and Gray (2001) defined convective updrafts as updrafts exceeding $1\,\mathrm{m\,s^{-1}}$, while Gregory and Guichard (2002) used various definitions based on threshold values for surface precipitation, or based on variations of vertical velocity in order to define convective mass fluxes.

With such criteria provided, it must be indicated whether cloud mass fluxes are computed with respect to the domain area or with respect to the area identified as an updraft, a downdraft, or a cloud. In the first case, using the domain area, the reference area is generally larger. Furthermore, the results depend on the fraction of cloudy air in the domain, and can therefore directly depend on the domain size in single cloud simulations. In the second case, the reference area per which the fluxes are computed is height-dependent unless a horizontal projection is calculated. There appears to be no generally accepted consensus regarding the reference area. Moreover, although both options seem to be in use, it has generally not been specified which option was used. In the study by Costa *et al.* (2001), updraft and downdraft mass fluxes are interpreted as contributions to a total cloud mass flux, implying the fluxes were probably computed using the total domain area. This total cloud mass flux differs from the total mass flux, which is expected to vanish for PLBCs. A similar argument can be applied to the fluxes calculated by Gregory and Guichard (2002), which will not be discussed here in detail.

Fig. 5.1 shows modeled vertical mass fluxes for different runs and different criteria which were computed using the cloud or the updraft and downdraft area. The percentage of columns where each of the criteria was met at least at one point is given in Table 5.1. In Fig. 5.2 the same mass fluxes as shown in Fig. 5.1 were computed using the entire domain area as reference area. The upwards cloud air mass flux profiles are readily interpreted in terms of net entrainment and net detrainment into or from clouds. Horizontal layers in which the cloud mass fluxes are increasing with height are regions of average entrainment while detrainment dominates in layers

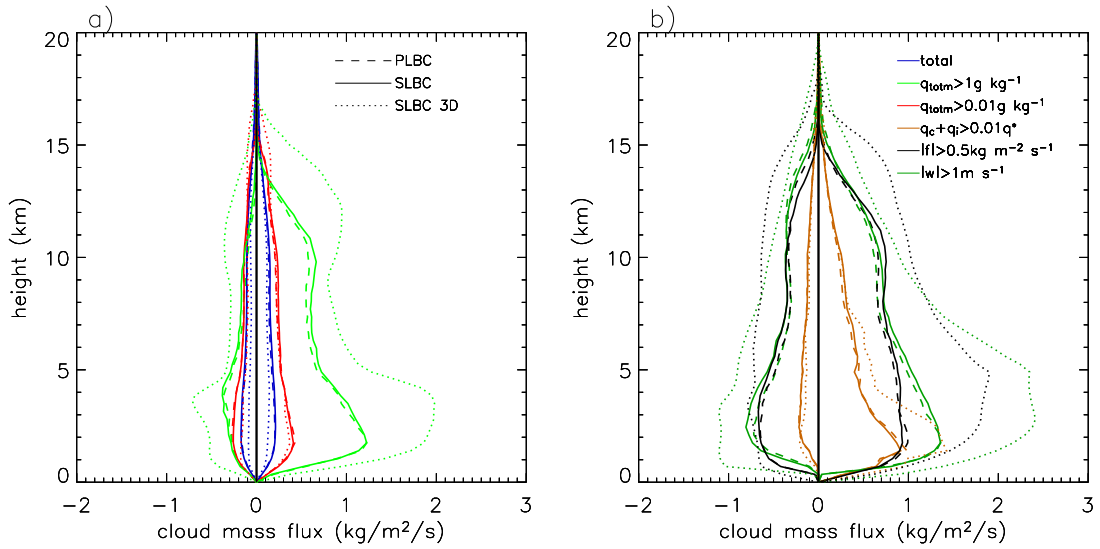

Figure 5.1: Domain and time averaged upward ($w > 0$) and downward ($w < 0$) cloud, updraft, downdraft, and total mass fluxes for different runs. **(a)** cloud defined by grid boxes where $q_{totm} > 1\,\mathrm{g\,kg^{-1}}$ (green lines) and where $q_{totm} > 0.01\,\mathrm{g\,kg^{-1}}$ (red lines). q_{totm} is the total cloudmeteor mixing ratio: $q_{totm} = q_c + q_i + q_r + q_g + q_s$, where q_c, q_i, q_r, q_g, and q_s are cloud water, cloud ice, rain, snow, and graupel mixing ratios, respectively. Blue lines: total mass flux. **(b)** Brown lines: cloud defined by grid boxes with $q_c + q_i > 0.01q^\star\,(\mathrm{T, p})$ where $q^\star$ is the saturated mixing ratio over water. Dark green lines: updraft and downdraft defined by grid boxes with $w > 1\,\mathrm{m\,s^{-1}}$ and $w < -1\,\mathrm{m\,s^{-1}}$, respectively. Black lines: updraft and downdraft defined by grid boxes with $f > 0.5\,\mathrm{kg\,m^{-2}\,s^{-1}}$ and $f < -0.5\,\mathrm{kg\,m^{-2}\,s^{-1}}$, respectively, where f is the air mass flux. The mass fluxes were diagnosed from model output. Cloud or draft mass fluxes were computed per cloudy or draft area as defined by the different criteria. This area varies with height. The legend on each panel applies to both panels.

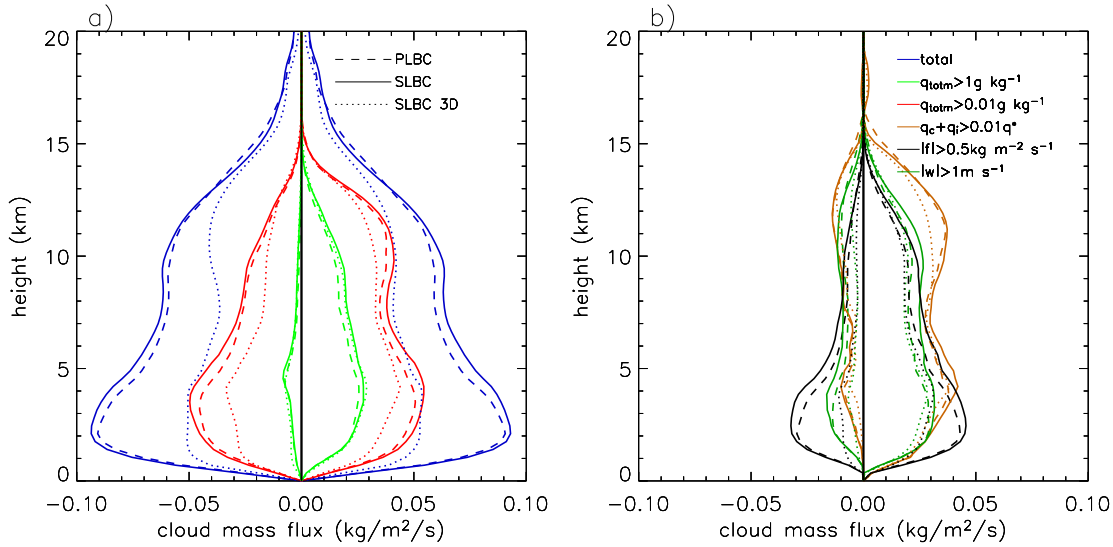

Figure 5.2: Same as Fig. 5.1, but per total area of the model domain.

Table 5.1: Percentage of columns where criterion (left column) is fulfilled at least at one point of the entire tropospheric column (TC, upper half of the table) or below 3 km (lower half) for different runs.

TC	PLBC		SLBC		SLBC 3-D	
	up	down	up	down	up	down
q_{totm} >1 g kg^{-1}	7.6	3.8	8.6	4.3	6.0	3.8
$q_{totm} > 0.01$ g kg^{-1}	60.9	59.7	65.1	64.5	66.4	69.5
$q_c + q_i > 0.01 q^\star$	62.5	53.6	65.2	56.1	67.3	60.9
$\lvert f \rvert > 0.5$ kg m^{-2} s^{-1}	9.2	7.5	10.3	8.3	7.1	4.7
$\lvert w \rvert > 1$ m s^{-1}	11.2	9.7	13.0	11.1	6.9	4.9
z < 3 km	PLBC		SLBC		SLBC 3-D	
	up	down	up	down	up	down
q_{totm} >1 g kg^{-1}	2.0	1.0	2.1	1.1	1.6	1.2
$q_{totm} > 0.01$ g kg^{-1}	21.5	23.9	24.3	27.2	24.7	30.9
$q_c + q_i > 0.01 q^\star$	7.2	3.1	7.3	3.4	4.4	2.0
$\lvert f \rvert > 0.5$ kg m^{-2} s^{-1}	2.1	1.4	2.3	1.6	1.3	0.6
$\lvert w \rvert > 1$ m s^{-1}	5.3	5.3	5.8	5.9	2.3	2.4

where the mass fluxes are decreasing. The opposite is true for downwards cloud mass fluxes. Note that only the mass fluxes computed by the model are shown. Mean mass fluxes due to the mean vertical velocity (compare Fig. 3.2c) are not reproduced by the model using PLBCs for air mass. Consequently, the domain total upward and downward mass fluxes in Fig. 5.1a and Fig. 5.2a are expected to balance.

The differences between the two different 2-D runs using PLBCs and SLBCs in Fig. 5.1 and Fig. 5.2 are generally small. The difference between the 2-D runs and the 3-D run is rather small for some mass flux definitions and rather large for others. This difference not only depends on the definition of the cloudy and the updraft or downdraft area, but also on how the reference area was chosen. The difference between the 2-D runs and the 3-D run is for example large when the cloud is defined by q_{totm}>1 g kg^{-1} and the fluxes are computed using the cloudy area (the light green lines in Fig. 5.1a). On the other hand, the difference appears very small if the flux is computed using the domain area (see Fig. 5.2a). The same applies for updraft mass fluxes which are defined by $w > 1$ m s^{-1} (black lines in Fig. 5.1a and Fig. 5.1b). The percentages of columns where the two criteria are fulfilled (see Table 5.1) also differs considerably between the 2-D runs and the 3-D run, especially if only the lowest 3 km of the column are taken into account. For comparison, Petch and Gray (2001) found much smaller differences between their 2-D runs and their 3-D run than those found in Fig. 5.1 for the w >1 m s^{-1} criterion. Furthermore, the values of their mass fluxes are in the range of the dark green lines in Fig. 5.2b. This strongly suggests that Petch and Gray (2001) computed their mass fluxes using the domain area and

not to the updraft area.

As mentioned, Johnson *et al.* (2002) presented mass fluxes which were one order of magnitude larger than those by Petch and Gray (2001) using the $q_c + q_i > 0.01q^\star\,(\mathrm{T, p})$ criterion described in the caption of Fig. 5.1 (brown lines). The profiles in Figure 9 by Johnson *et al.* (2002) are comparable to the profiles in Fig. 5.1b. The shape and the magnitude of the corresponding profiles in Fig. 5.2b are very different, strongly suggesting Johnson *et al.* (2002) computed their fluxes with respect to the cloudy area. Note that for the $q_c + q_i > 0.01q^\star\,(\mathrm{T, p})$ criterion, the shapes of the profiles are very different depending on the normalization. When using the cloudy area as the reference, the profiles have their maxima in the lower troposphere. Otherwise they possess two maxima: one in the lower troposphere and one in the upper troposphere. Neither Petch and Gray (2001) nor Johnson *et al.* (2002) stated which normalization was used. Costa *et al.* (2001) defined their cloud mass fluxes based on the contributions from cloud water and cloud ice only, while in the present study rain, graupel and snow were additionally considered. Their upwards cloud mass flux profiles (shown in their Fig. 10) are roughly comparable to the red lines in Fig. 5.2. The upwards cloud mass flux in the study by Costa *et al.* (2001) is somewhat lower than the one computed for the SLBC and PLBC 2-D runs. This could be due to the different definitions. The upwards cloud mass flux from the 2-D study by Costa *et al.* (2001) is similar to the upwards mass flux diagnosed from the SLBC 3-D run.

In order to develop some intuition concerning the differences between different mass flux definitions, it is helpful to investigate various relationships, for example between simulated mass fluxes and cloudmeteor mixing ratios. Fig. 5.3 shows mass flux contours (colored) as well as cloudmeteor mixing ratio contours on three different occasions. The strongest upwards mass fluxes are often contained in the regions with the highest cloudmeteor mixing ratios. Examples of high cloudmeteor mixing ratios which are not accompanied by high mass fluxes are found in Fig. 5.3a and c. High cloudmeteor mixing ratios are not always correlated to high mass fluxes, which is an indication of decaying storms. The $0.1\,\mathrm{g\,kg^{-1}}$ contour contains considerably larger regions of cloudy air without strong updrafts than the $1\,\mathrm{g\,kg^{-1}}$ contour. Furthermore, Fig. 5.3b shows positive and negative vertical air mass fluxes outside clouds. These mass fluxes will be discussed in the next section.

The extent to which mass fluxes agree between different model setups can depend on the choice of mass flux definition. This is once more illustrated in Fig. 5.4, where diagnosed mass flux profiles are plotted for two different runs using the two different single moment microphysics schemes described in Section 2.2.2. The mass fluxes in Fig. 5.4a were calculated per cloudy area and in Fig. 5.4b per updraft and downdraft area. If the cloud area is defined as containing all grid boxes where q_{totm}>$1\,\mathrm{g\,kg^{-1}}$ (green lines) the downward mass fluxes in Fig. 5.4a seem to agree fairly well between the runs. This is not the case, when the other definitions are used.

In general, it is important to note that depending on how the cloudy area is defined, the diagnosed magnitude of the downwards mass fluxes relative to the magnitude of the upwards mass fluxes can change considerably. In addition to the runs included in Fig. 5.4, a run with very low resolution in the upper troposphere

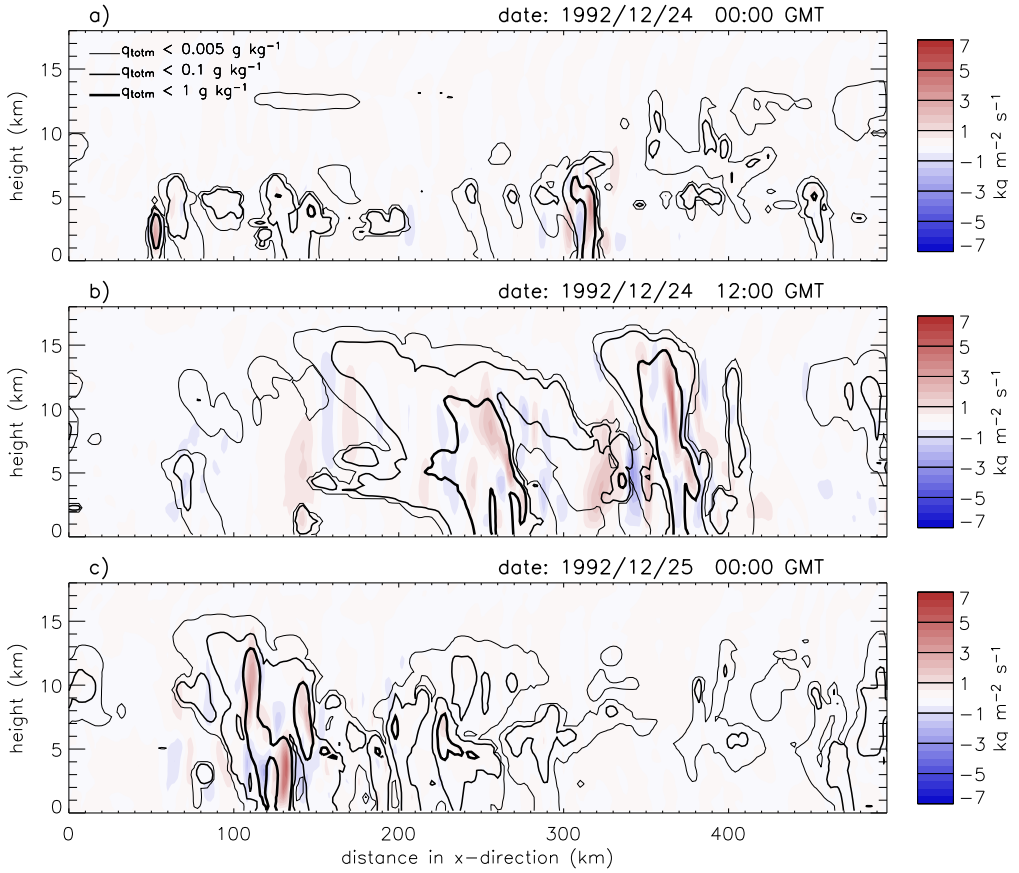

Figure 5.3: Mass fluxes (colored contours) and cloudmeteor mixing ratios (black contour lines, see legends). q_{totm} is the total cloudmeteor mixing ratio.

was conducted using the Krueger *et al.* (1995) microphysics scheme. The results indicated that the existence of an upper tropospheric cloud mass flux maximum is not very sensitive to the vertical resolution in the upper troposphere. It is, however, sensitive to the choice of the microphysics scheme, as illustrated in Fig. 5.4.

5.2 Oscillatory Motions

Deep convection is a source of gravity wave pulses which are thought to be responsible for the rapid temperature adjustment in environments with deep convection. The adjustment process can be viewed as a superposition of internal gravity waves propagating away from the clouds, whose net effect is to induce compensating subsidence that balances the upward mass flux within the cloud (Bretherton and Smolarkiewicz, 1989). In recent years, much has been learned regarding this process (Nicholls *et al.*, 1991; Mapes, 1993; Lane and Reeder, 2001). Mapes (1993) has used inviscid gravity wave dynamics to explain the existence of "superclusters" (see introduction). He

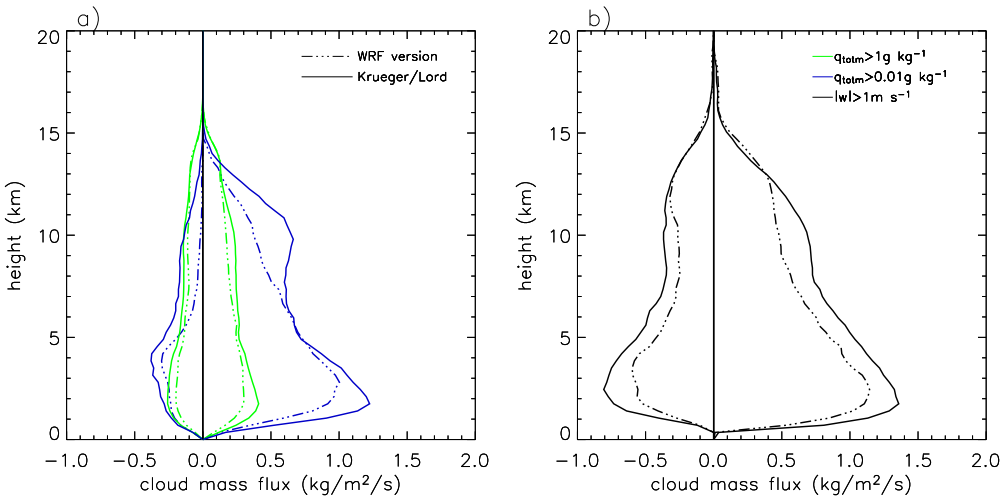

Figure 5.4: Domain and time averaged upward and downward cloud, updraft and downdraft mass fluxes for different runs using the original WRF version of the Lin *et al.* (1983) single moment microphysics scheme (solid lines) and using the scheme described by Krueger *et al.* (1995) (dotted lines). The cloud is defined by grid boxes with q_{totm} >1 g kg^{-1} (blue lines) and $q_{totm} > 0.01$ g kg^{-1} (green lines) , where q_{totm} is the total cloudmeteor mixing ratio. The mass fluxes were diagnosed from model output and computed per cloudy or draft area.

has shown that gravity wave pulses caused by heating due to mesoscale convective systems (MCSs) not only induce mass balancing subsidence, but can also cause upward displacement near existing MCSs. This displacement is induced beyond the area of MCS outflow and favors the formation of additional MCSs. Mapes (1993) noted that this result conflicts with a traditional assumption, valid only for infinite uniform fields of cumulus clouds, that the compensating subsidence associated with convective ascent occurs between the clouds. Lane and Reeder (2001) found in a 2-D cloud resolving model study that the first (and fastest) mode propagating away from a deep convective cloud acted to reduce environmental CAPE, while the second and the third mode acted to increase CAPE.

The focus of the present study is on the role of gravity waves for mass flux diagnostics. A comparison of the cloud mass fluxes and the total mass flux in Fig. 5.2 reveals that a large fraction of the total diagnosed mass flux is calculated to take place outside the cloudy air. High mass fluxes outside a cloud were already encountered in Fig. 5.3b. A more detailed picture regarding the evolution of mass fluxes outside the cloud during the evolution of a storm is provided in Fig. 5.5. In this figure small amplitude mass fluxes are highlighted, while larger amplitude mass fluxes are indicated by black filled contours. During the evolution of the storm, gravity waves with different vertical wavenumbers propagate away from the storm. The depth of the troposphere is often spanned by either half a wavelength or one wavelength. These waves could be interpreted as the $n = 1$ (gravest) mode and the $n = 2$ mode discussed by Nicholls *et al.* (1991) and by Mapes (1993). The $n = 1$ mode is predicted to propagate faster horizontally than the $n = 2$ mode.

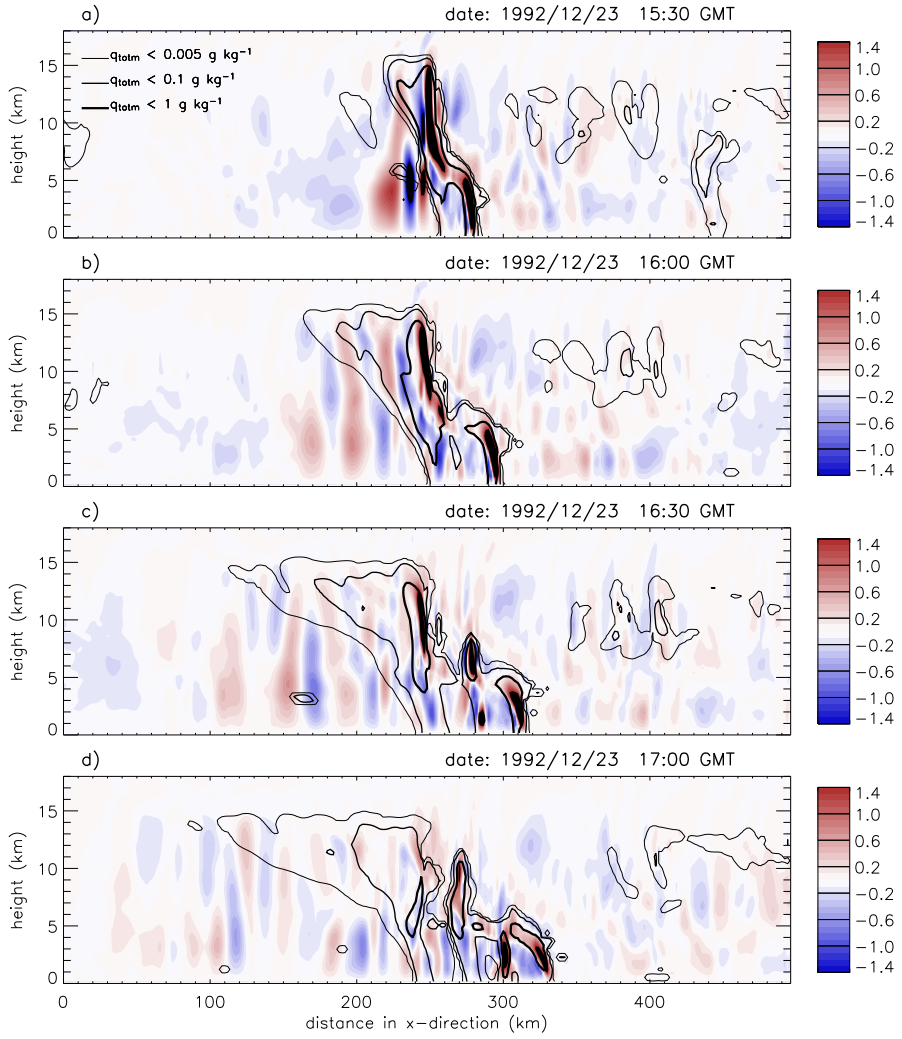

Figure 5.5: Small amplitude fluctuations of the vertical mass flux (filled contours) and cloudmeteor mixing ratio contours (black lines). Mass flux contour levels larger than 1.4 kg m^{-2} s^{-1} or below -1.4 kg m^{-2} s^{-1} are filled in black color.

Since the waves in Fig. 5.5 are excited by multiple updrafts instead of by a single symmetric heat source, the structure is rather complicated and the propagation is not symmetric in the two horizontal directions as is the case for a single heat source in an atmosphere at rest. It is most likely that this kind of motion commonly associated with deep convection causes the large differences between the total vertical and the cloud mass fluxes in Fig. 5.3b.

Fig. 5.6 shows normalized mixing ratios of the lower tropospheric tracer from Section 4.1 for the storm from Fig. 5.5. The storm acts to efficiently transport air containing high tracer mixing ratios from the boundary layer to the upper troposphere. Boundary layer air is carried up inside the strong updrafts and is detrained at the western edge of the anvil. Only weak signatures of the gravity waves propa-

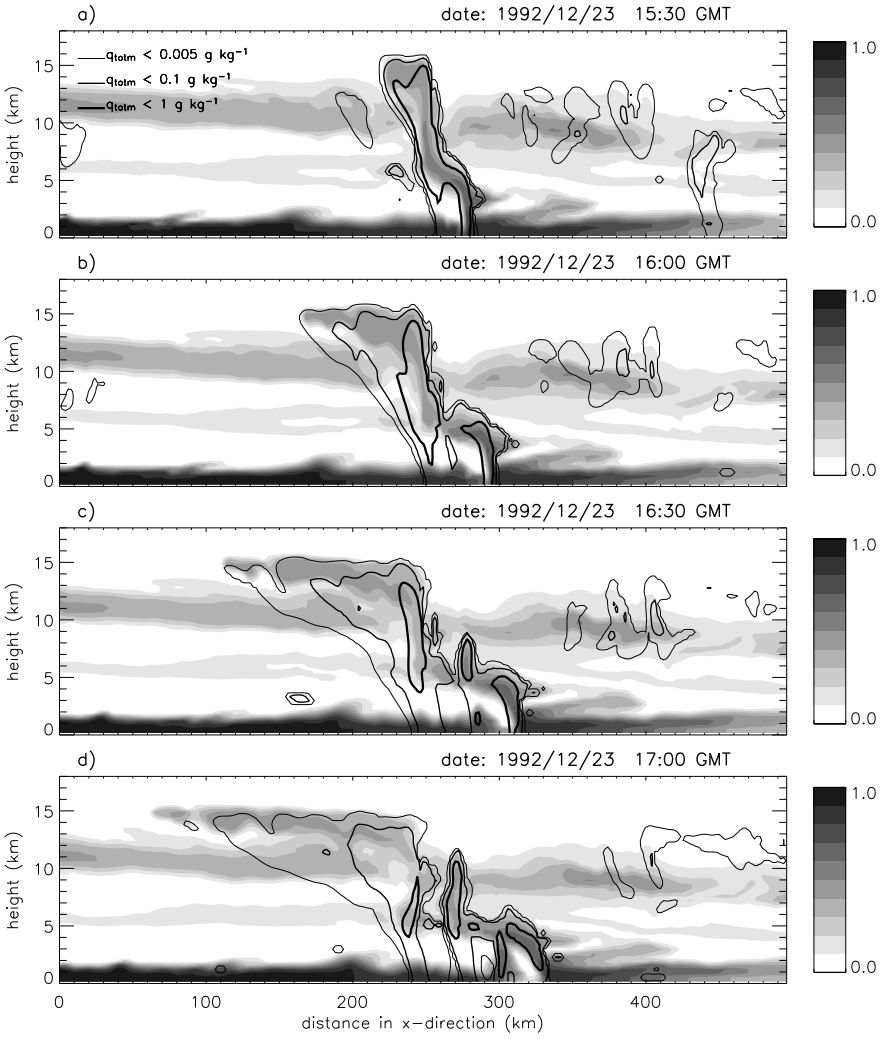

Figure 5.6: Filled contours: lower tropospheric tracer A from Section 4.1; cloudmeteor mixing ratio contours as in Fig. 5.5

gating away from the storm towards the west can be found in the tracer field.

5.3 Discussion

Parameterizations of deep convective trace gas transport often require vertical air mass fluxes as input variables. In GCTMs, the air mass fluxes are calculated by the deep convective parameterization. Evaluating such parameterizations is a challenging task. One approach is to combine in-situ observations with CRMs in order to derive appropriate data. For meteorological variables, this approach has been used in association with the TOGA COARE campaign (Bechtold *et al.*, 2000). Although CRMs are conceptually much better suited to model deep convection than simpler

models, this approach requires a very thorough evaluation of the CRM results. Air mass fluxes are not easily derived from observations and inter-comparisons between different studies are complicated by the use of a multitude of different definitions. The dependence of CRM diagnosed mass fluxes e.g. on threshold values is important to notice. It would be tempting to use convective mass fluxes derived from a CRM study as input for parameterizations of convective trace gas transport. This would allow the comparison of CRM results and results from the deep convective tracer transport parameterization without having to take into account differences due to different air mass fluxes. The question which arises from the results presented in the previous sections is: which would be the mass flux definition to choose in order for the diagnosed mass flux to determine transport, i.e. which would be the best definition to choose for deriving the input for a convective transport parameterization? This question cannot easily be answered here. Most likely a definition in which a lower threshold value for either vertical velocity or vertical mass flux is chosen would be most appropriate for use in such a comparison. Note that even for a given mass flux profile, different transport parameterizations yield different results (Lawrence and Rasch, 2005).

An aspect which has been omitted in this discussion is the influence of the mean vertical velocity on air mass fluxes. As in most studies only model simulated air mass fluxes were considered here. One could, however, calculate an additional air mass flux from the observed mean vertical velocity which is not reproduced by the model. Gregory and Guichard (2002) presented a study in which contributions from the mean vertical velocity were added to the calculated net air mass fluxes. Adding this air mass flux to the modeled air mass fluxes yields a net upwards air mass flux. This net mass flux is, however, small compared to the gross total air mass fluxes.

Chapter 6

The Influence of Solubility on Tracer Transport

It is well established that the fraction of a soluble trace gas that can be transported from the boundary layer to the upper troposphere in deep convection depends crucially on the solubility of the gas (e.g. Rodhe, 1983; Crutzen and Lawrence, 2000). Furthermore, the role of tracer retention in (or rejection from) freezing hydrometeors has been discussed in numerous studies (see e.g. Stuart and Jacobson, 2003, for references to a number of studies). Recently, Barth *et al.* (2001) suggested based on a pioneering set of sensitivity studies using a CRM that the simulated vertical distribution of water soluble trace gases which are not taken up by ice depends crucially on the (gas specific) retention coefficient k_{ret} (in Equation 2.15) determining to what extent a dissolved trace gas is retained by hydrometeors during freezing or rejected to the gas phase (e.g. upon freezing of cloud droplets in the upper troposphere). Barth *et al.* (2001) have suggested that trace gases retained in hydrometeors upon freezing are efficiently scavenged, while gases with low retention coefficients can escape scavenging in deep convective clouds and be transported to the upper troposphere.

In the next section, the focus is on resolving an apparent discrepancy between the studies of Crutzen and Lawrence (2000) and Barth *et al.* (2001) concerning the transport of idealized soluble and insoluble tracers. In Section 6.2 the influence of the ventilation coefficient on the model results is briefly discussed. A sensititivity study investigating the influence of the retention coefficient on vertical trace gas transport is presented in the final section of this chapter. The influences of scavenging on nitric acid, hydrogen peroxide, formaldehyde, and methyl hydroperoxide are discussed in association with the budgets of these compounds in Sections 8.5.2, 10.3, 10.4, and 10.2, respectively. Details regarding the scavenging of these gases are further discussed in Chapter 11.

6.1 CRCTM vs. Global CTM: A Qualitative Comparison

Barth *et al.* (2001) indicated the loss of highly soluble tracers in the upper troposphere may be overestimated in large scale models. They compared their CRM results to results from the study by Crutzen and Lawrence (2000), who examined the sensitivity of the vertical tracer transport towards solubility using a GCTM. Crutzen and Lawrence assumed tracers with fixed surface mixing ratios and calculated mixing ratios of highly soluble tracers in the mid- and the upper troposphere to reach 5% or less of that of an insoluble tracer. Barth *et al.* on the other hand calculated that upper tropospheric mixing ratios of highly soluble tracers were reduced by 40–60% compared to a non-soluble tracer after 2.5 hours in a simulation of a single multicell storm using a 120×120×20 km 3-D domain. Based on these findings they suggested that large-scale models may be overestimating the loss of highly soluble species in the upper troposphere. However, Barth *et al.* mention a number of points why the two results should not be compared directly. Here, the focus is directed towards one of the points mentioned, namely on the influence of the initial profile.

Fig. 6.1 shows the modeled profiles of two pairs of tracers. For the sake of performing sensitivity studies, the CRCTM was run with PLBCs, and the VLSAT term was not considered. The tracer fields were re-initialized every 24 h. The initial profile labeled 'Ba' is similar to the initial profile used in the study by Barth *et al.*, while the tracer labeled 'CrLa' is initially located in the boundary layer. Unlike in the study of Crutzen and Lawrence, the mixing ratio of the tracer labeled 'CrLa' is not assumed to be fixed at the surface. For each of the two initial profiles, it was assumed either that the tracer is highly soluble (Henry's Law constant K_H=10^6 mol l^{-1} atm^{-1}) and completely retained in the hydrometeors upon freezing, or that it is insoluble. Neither uptake on ice nor any other source or sink term was included in the model for this study. In Fig. 6.1, results from the 5^{th} time slice are displayed. The tracer which was initially assumed to be located in the lower troposphere ('CrLa') is only efficiently transported to the mid- and upper troposphere if it is assumed to be insoluble (blue dotted line). The soluble counterpart (blue dashed line) is efficiently scavenged. On the other hand, a substantial fraction of the highly soluble tracer with the initial profile labeled 'Ba' remains in the mid-troposphere and the upper troposphere (red dashed line). The ratio of the mixing ratio of this soluble tracer to the mixing ratio of the corresponding insoluble tracer (yellow dotted line) is at some levels in the upper troposphere reduced by more than 50% for the 5^{th} time slice. For some time slices reductions in excess of 80% (after 24 h) were calculated. For the 'Ba' tracer the reduction can be expected to depend on the domain size, in particular on the ratio of rainy to dry area in the domain and on the length of the simulated episode.

The strong sensitivity of the ratios of the mixing ratios of the soluble to the insoluble tracers to the initial profiles shown here suggests that the apparent disagreement between the studies by Barth *et al.* and by Crutzen and Lawrence can be attributed to the use of different assumptions about the initial or lower bound-

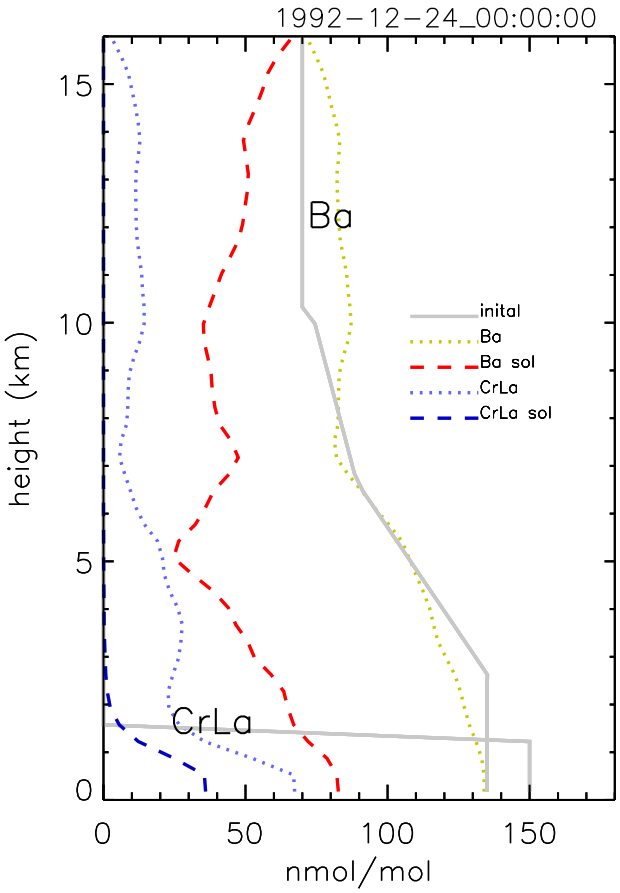

Figure 6.1: Model calculated horizontally averaged mixing ratios of highly soluble tracers in the gas phase (dashed lines) and insoluble tracers (dotted lines) for two different initial tracer profiles (solid lines) labeled 'CrLa' and 'Ba'. The tracer fields were re-initialized every 24 h. The model was run with PLBCs, and VLSAT was not considered. Here as an example, results from the 5^{th} 24-hour time slice are plotted.

ary values of the studied tracers. While Crutzen and Lawrence (2000) studied the transport of soluble tracers from the boundary layer to the upper troposphere, Barth *et al.* (2001) studied not only the transport from the boundary layer, but also the scavenging of tracers from the upper troposphere (examples of such tracers are tracers which have a photochemical source in the upper troposphere such as H_2O_2 in the tropical upper troposphere, compare Section 10.3).

6.2 Importance of the Ventilation Coefficient

In Section 2.3.1 it was argued that a ventilation coefficient f should be included in Equation 2.16. This coefficient was omitted by Barth *et al.* (2001), which is equivalent to assuming drops being at rest in the calculations of trace gas exchange. In

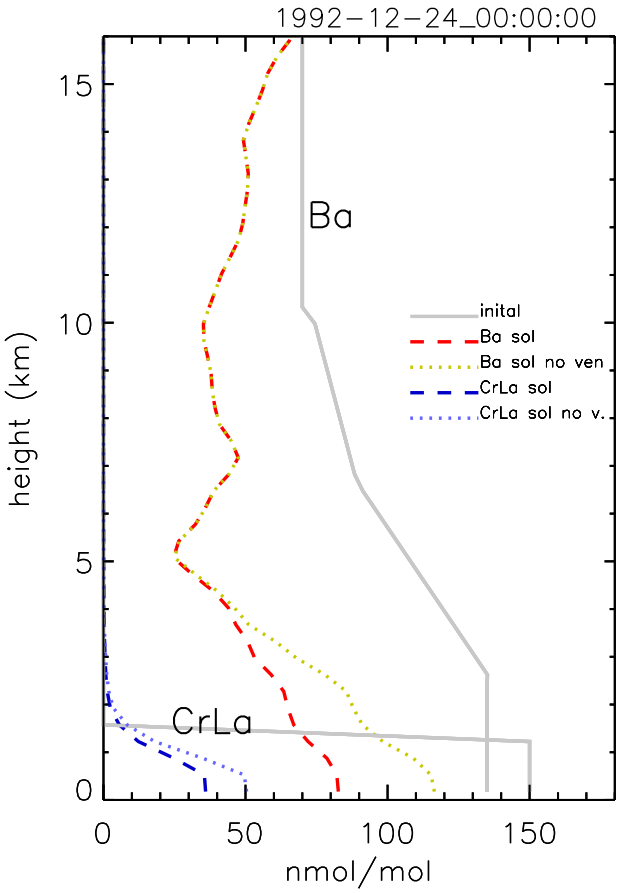

Figure 6.2: Model calculated horizontally averaged gas phase mixing ratios of highly soluble tracers. Dashed lines: if ventilation is considered (as in Fig. 6.1). Dotted lines: if the influence of ventilation is neglected (i.e. if the ventilation coefficient in Equation 2.16 is set to one).

order to study the sensitivity of the model results towards omitting f, a sensitivity run was conducted in which f=1 was assumed. The setup for the run was otherwise identical to the setup described in the previous paragraph. Fig. 6.2 shows resluts from the base run and the sensitivity run. The profiles of the 'Ba sol' and the 'CrLa sol' tracers in Fig. 6.2 are identical to the corresponding profiles in Fig. 6.1. The other two profiles are from the sensitivity run. When the ventilation coefficient is omitted, the domain averaged surface mixing ratios of the soluble tracers are overestimated by about 40%. Consequently, the ventilation coefficient plays an important role for the amount of tracer scavenged from the lower troposphere and should always be included in studies using the mass transfer equations by Schwartz (1986). Furthermore, when fast chemical reactions on rain drop surfaces are important, the ventilation coefficient should in the future be included in calculating the reaction rates.

6.3 Influence of the Retention Coefficient on Vertical Transport

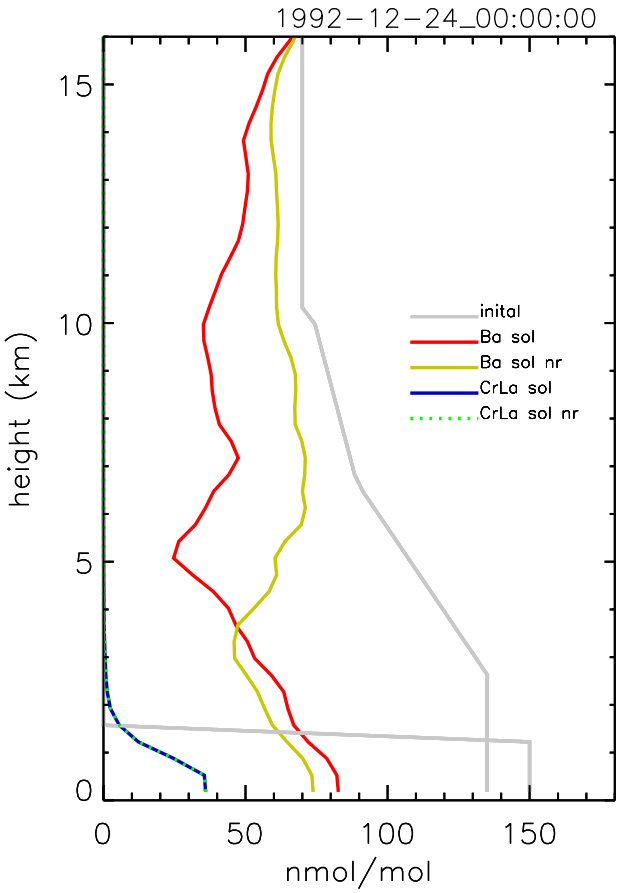

Figure 6.3: Model calculated horizontally averaged mixing ratios of highly soluble tracers (as in Fig. 6.1) for two different retention coefficients. For the tracers labeled "Ba sol" and "CrLa sol" k_{ret}=1 was assumed, while for "Ba sol nr" and "CrLa sol nr" k_{ret}=0.

In this section, the influence of the gas specific retention coefficient on the deep convective transport of a highly soluble gas which is not taken up by ice is investigated. Again, the results for a trace gas which is initially located in the boundary layer are compared to results for a trace gas with an initial profile as in Barth *et al.* (2001). Furthermore, it was assumed that either k_{ret}=1 or k_{ret}=0. The results are shown in Fig. 6.3. The first thing to note is that the amount of the "Ba sol" tracers in most of the mid- and upper troposphere strongly depends on whether complete retention or complete rejection upon freezing is assumed. For the "CrLa sol" tracers the absolute difference due to the assumptions about k_{ret} is much smaller, while the relative difference is, however, large. The average mixing ratio of the "CrLa sol" tracer at 10 km is about 140 pmol mol^{-1} if complete rejection is assumed and only about 0.04 pmol mol^{-1} if complete retention is assumed (not shown). The small absolute difference is not surprising since only a very small amount of the 'CrLa'

tracer is calculated to reach the freezing level. In contrast to this result, preliminary results from a short term 3-D simulation of a rapidly growing storm in an idealized mid-latitude environment yielded that a highly soluble tracer initially located in the boundary layer for which k_{ret}=0 was efficiently transported to the upper troposphere (where it was ejected from the freezing cloud droplets), while a comparable tracer was efficiently scavenged when k_{ret}=1 was assumed (not shown). However, in this idealized simulation, the cloud was initiated by placing an artificial warm bubble inside the model domain, and the cloud grew almost to the tropopause before precipitation set in. Storms simulated during TOGA-COARE, on the other hand, tend to produce rain earlier during their growth stage, largely preventing highly soluble tracers initially located in the boundary layer from reaching the upper troposphere in the present simulations. Since key results from this chapter depend on the modeled location of the precipitation region relative to the updrafts, additional 3-D studies are necessary to substantiate these findings (see also discussion of HNO_3 scavenging in Section 8.5.2, and outlook in Chapter 13). Furthermore, in the framework of a future project a study is planned focusing on the transport of idealized soluble gases by deep convective cloud systems in a case study of mid-latitude deep convection (GCSS WG4, Case 3; e.g. Xie *et al.*, 2002) based on data for the Southern Great Plains in June–July 1992 from the U.S. Department of Energy's Atmospheric radiation Measurement (ARM) program.

Chapter 7

Photochemistry and Meteorology in the TOGA COARE Region: Model Setup and Large Scale Perspective

7.1 Model Setup

In order to study the influence of the simulated cloud systems on the ozone related photochemistry in the troposphere, a number of sensitivity runs were performed. The CRCTM was run in 2-D mode with 500 km domain length using SLBC and VLSAT. Details of this setup were described in Section 3.4 (see also footnote in Table 3.1) except for the chemical initial and boundary values which are described in the next section. Subsequently, the results from a number of sensitivity runs aimed at determining the role of lightning produced NO_x are presented. The modeled meteorology in these runs differs slightly form that described in Chapter 3 (see Appendix B).

7.2 Initial and Boundary Conditions

Mathematically, the CRCTM is an initial boundary value problem. The chemical initial and lateral boundary values for the CRCTM chemistry runs were derived from MATCH-MPIC analysis runs based on NCEP/NCAR 40-year meteorological re-analysis (Kalnay *et al.*, 1996). Pre-processed data for these runs was provided by L. Horowitz of GFDL, Princeton. The horizontal resolution in the MATCH-MPIC runs was T42, which is about $2.8° \times 2.8°$ and 28 vertical levels up to 2 hPa were used. As in the study by von Kuhlmann *et al.* (2003a) the stratospheric flux of ozone was reduced artificially through reducing stratospheric ozone values by 50% before the advection routine and setting them back after that. Doing so results in a reduction of the calculated flux of ozone from the stratosphere and strongly reduces simulated ozone mixing ratios at the site of the TOGA COARE IFA. At a number of remote

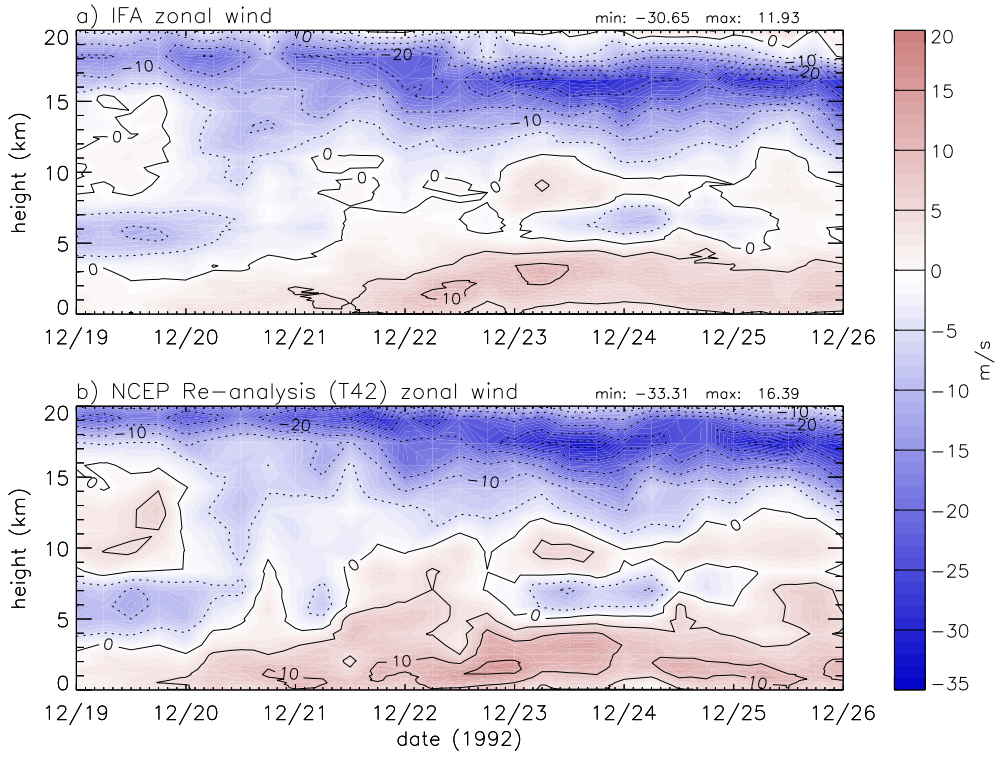

Figure 7.1: Time height contours of the zonal wind component **(a)** from observations during TOGA COARE and **(b)** from NCEP/NCAR meteorological re-analysis interpolated to T42 and plotted for the column located closest to the center of the TOGA COARE IFA.

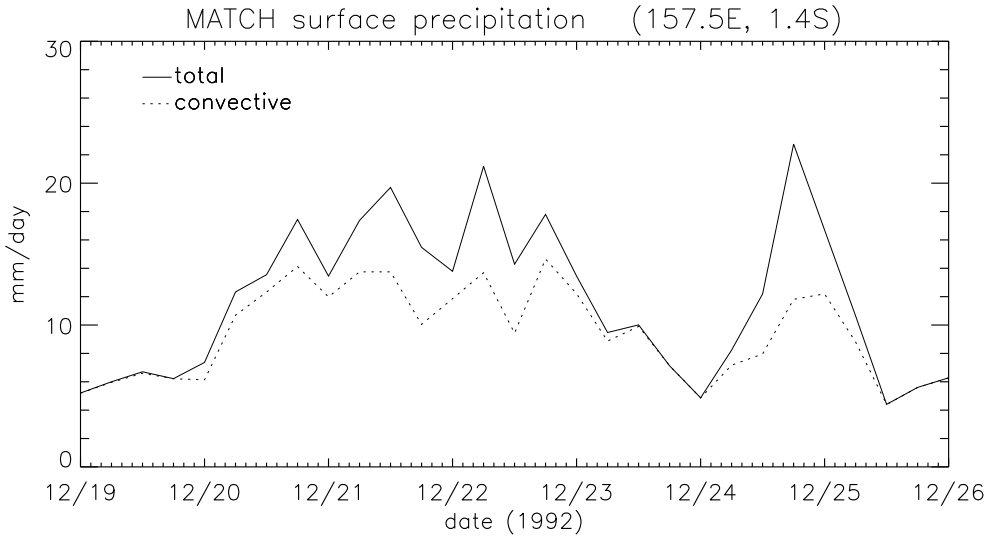

Figure 7.2: MATCH-MPIC calculated precipitation for the point located closest to the TOGA COARE IFA.

measurement sites, the annual cycle of surface ozone mixing ratios approximately follows the annual cycle of transport of stratospheric ozone to these locations, while in more polluted areas and at higher latitudes, the amount of surface ozone follows the annual solar cycle (see e.g. Fig. 1 von Kuhlmann *et al.*, 2003a). The spring ozone maximum observed at remote northern hemispheric mid-latitude stations is likely caused by the combination of transport from the stratosphere and photochemistry (e.g. Liu *et al.*, 1987; Monks, 2000).

Details on the model setup used to produce the initial and boundary values for the CRCTM can be found in Lawrence *et al.* (2003a). The output data from MATCH-MPIC was archived after every two hours of simulated time and the lateral trace gas boundary conditions for the CRCTM were derived by interpolating data from a MATCH-MPIC column centered close to (at 1.4°S, 157.5°E) the center of the TOGA COARE IFA. The trace gas concentrations were interpolated linearly in time and space to the CRCTM vertical grid and to the CRCTM timesteps. These initial and boundary values must be considered a first guess for conducting a number of sensitivity studies. For the sake of detailed comparisons between MATCH-MPIC and CRCTM results, it will be necessary to use a rather sophisticated approach, e.g. to employ a single column model based on MATCH-MPIC. Such a model has been developed, but has not yet been set up for usage with data from the TOGA COARE IFA. However, important features of the meteorological observations during TOGA COARE are well re-produced in the NCEP re-analysis data, in some cases facilitating qualitative comparisons between results from MATCH-MPIC and results from the CRCTM. Fig. 7.1 contrasts time height plots of the zonal wind speed based on observations during TOGA COARE and based on re-gridded NCEP re-analysis. The evolution and vertical structure of the horizontal wind compares well, but the westerly wind burst is somewhat stronger in the NCEP re-analysis dataset than in the observations.

Convection and rainfall are diagnosed in MATCH-MPIC while surface fluxes of heat and moisture are prescribed from the NCEP meteorological data. The temporal evolution of the surface precipitation calculated by MATCH-MPIC (in Fig. 7.2) is similar to the temporal evolution simulated by the CRCTM (Fig. 3.4), but the amount differs by roughly a factor of two. As discussed in Section 3.5, differences between two different large scale input data sets can account for roughly a factor two in the amount of surface precipitation in CRM simulations. The amount of rain calculated by MATCH-MPIC is lower than the amount calculated by the CRCTM with the input dataset used here, but is in better agreement with the amount that was calculated from the dataset used by the GCSS Science Team (1993). An example of the 850 hPa CO mixing ratio calculated by MATCH-MPIC during the westerly wind burst is shown in Fig. 7.3. The ITCZ is located close to the equator. North of the ITCZ north-easterly trade winds prevail and the CO mixing ratios are much higher than south of the ITCZ. The descending branch of the Hadley cell is located north of 20°N in the western Pacific. Large scale cross equatorial flow occurs over the Indonesian Archipelago in association with the low level westerly wind over the TOGA COARE region (compare e.g. Yanai *et al.*, 2000; McBride *et al.*,

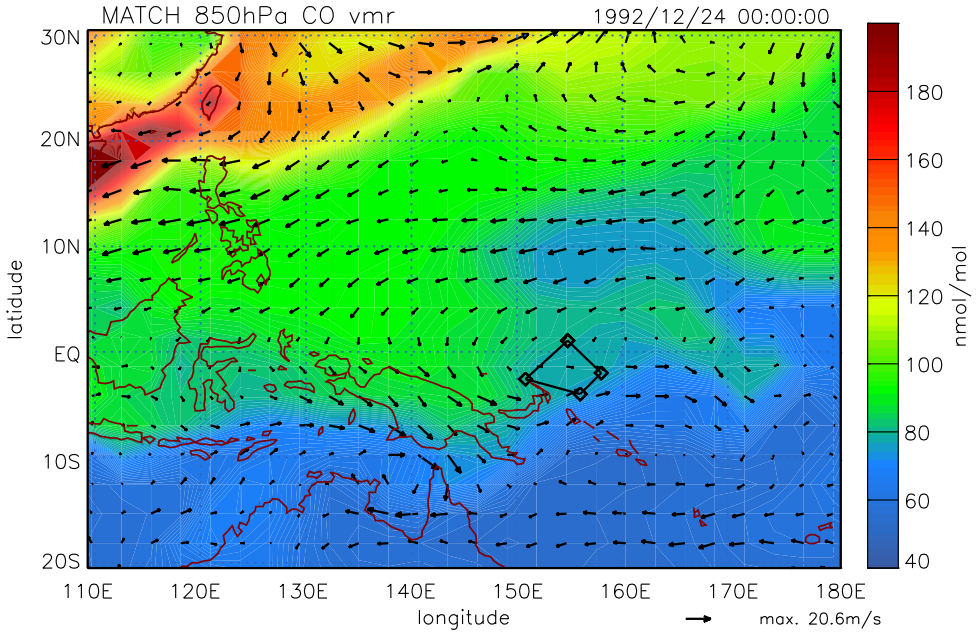

Figure 7.3: 850 hPa CO volume mixing ratio from MATCH-MPIC and interpolated wind vectors from the NCEP re-analysis dataset on 24 December 1992, 0:00 GMT. The location of the TOGA COARE IFA is indicated by a polygon.

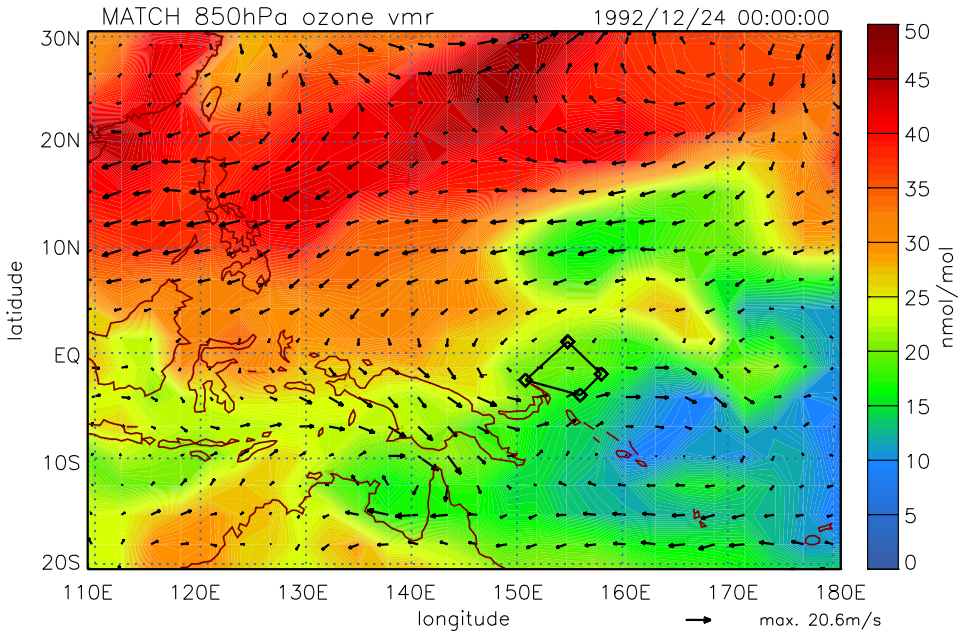

Figure 7.4: As Fig. 7.3, but for ozone.

1995). South of the equator at about 165°E a weak cyclonic anomaly is located. During westerly wind bursts, closed cyclonic anomalies can occur on either side of the equator (e.g. Rui and Wang, 1990; Kiladis *et al.*, 1994). South of the area of the westerly wind burst, in the Australian monsoon trough, the 850 hPa winds are easterly. The direction of the flow at 200 hPa above the TOGA COARE IFA (not shown) is roughly opposite to that at 850 hPa. West of the IFA, at 200 hPa air flows towards the north across the equator. A more detailed discussion regarding the evolution of westerly wind bursts can e.g. be found in Kiladis *et al.* (1994). Ozone mixing ratios from MATCH-MPIC (see Fig. 7.4) also show a large north-south gradient, as did a number of observations in the region for different seasons (see Section 7.3.2). Cross equatorial tracer advection is a consequence of large hemispheric tracer gradients and cross-equatorial flow. A prominent example in the Pacific is the so-called "river of pollution" where anthropogenically polluted northern hemispheric air was found to travel into the Southern Hemisphere near the surface in the vicinity of the dateline (Staudt *et al.*, 2001). Fig. 7.5 shows time series of horizontal winds at 10 m altitude from observations and from the NCEP-Reanalysis dataset at the location of the IFA as well as MATCH-MPIC calculated surface layer mixing ratios of ozone, CO and NO_x. The mixing ratios of ozone and CO drop to lower values in January after the end of the westerly wind burst. The sudden jump of NO_x concentrations in Fig. 7.5d is due to an increase of the monthly ship emissions in the MATCH-MPIC grid by a factor of 100. This increase in emissions over the TOGA COARE area occurs only in January and February and is limited to a single oceanic grid point. This points towards a possible error in the ship emission dataset from Corbett *et al.* (1999). Fig. 7.6 shows profiles based on the MATCH-MPIC data used to specify the lateral boundary conditions in the CRCTM runs. The initial profiles, the 7 day average profiles, and the standard deviations from the averages for ozone, NO_x and CO are plotted. The initial ozone volume mixing ratio shows a local maximum at about 400 hPa. The ozone and NO_x profiles will be further discussed in the next sections. CRCTM calculated profiles of CO and methane will not be analyzed in the next chapters. The lifetime of methane is long enough so that methane can be considered well mixed for the purpose of this study.

A general problem with specifying initial and boundary conditions from a large scale model is that the CRCTM results can be influenced by biases in the large scale model as well as by biases in the CRCTM. If for example the amount of a soluble, relatively long lived trace gas such as HNO_3 in the upper troposphere is underestimated by the large scale model, the amount of HNO_3 transported into the CRCTM domain and subsequently scavenged will also be underestimated. The advantage of large scale models is that they tend to re-produce the spatial and temporal variability of trace gases, (see Lawrence *et al.*, 2003a, for an example), despite possible biases. If instead a seasonal or monthly mean values of mixing ratios would be used to specify initial and boundary conditions for a CRCTM, the strong dependence of trace gas mixing ratios on the meteorological conditions could not be taken into account. This may easily give rise to misleading results.

This is the first CRCTM study using specified boundary conditions, and the

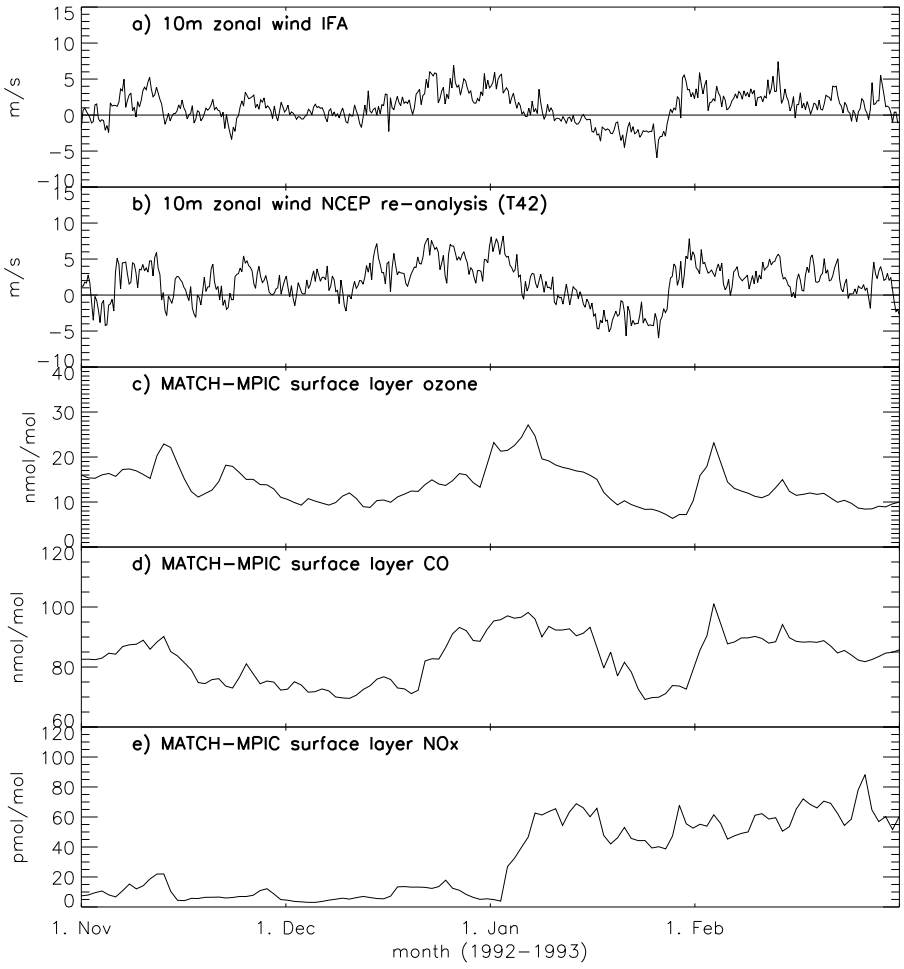

Figure 7.5: Time series at the site of the TOGA COARE IFA: **(a)** 10 m observed zonal wind, **(b)** 10 m zonal wind from the interpolated NCEP re-analysis data, **(c)** ozone volume mixing ratio in the lowest model layer (surface layer) calculated by MATCH-MPIC, **(d)** surface layer CO, **(e)** surface layer NO_x. The steep increase of surface layer NO_x after 1 January is caused by a jump in the ship emissions in the model (see text).

success of future studies using a similar setup will crucially depend on the availability of adequate initial and boundary conditions for trace gases. In order to obtain improved input data, in the future, data from global CTMs could be combined with data from measurement campaigns. Another option would be to run the CRCTM with meteorological data used to drive a global CTM. Then, CRCTM results from simulations could be compared to the simulations of the global CTM for the same region. Recently, Xie and Cederwall (2004) presented a method in which data from numerical weather prediction models is used to force CRMs or SCMs for long term simulations.

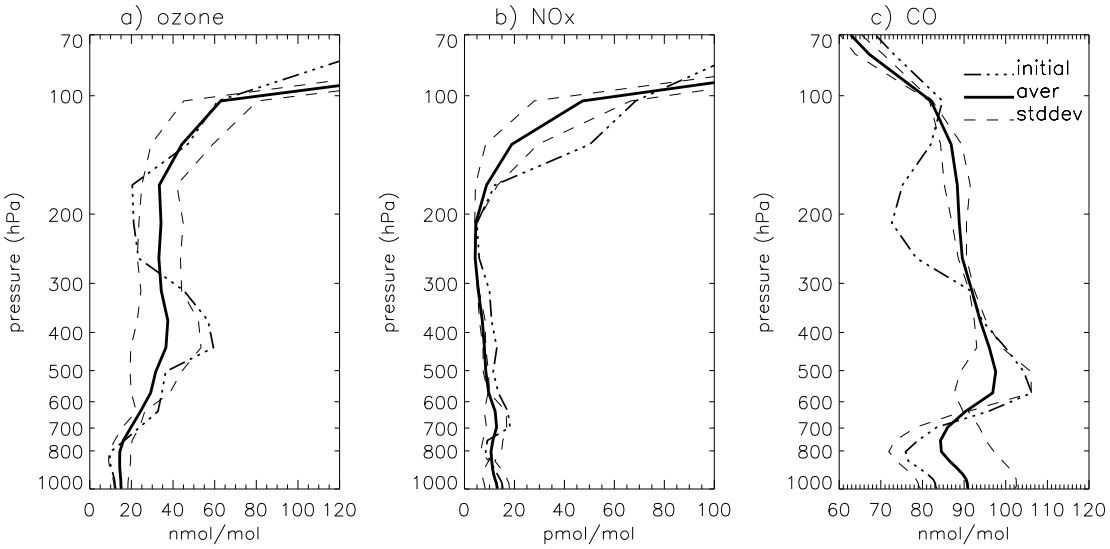

Figure 7.6: Initial values and averaged boundary values from MATCH-MPIC for **(a)** ozone, **(b)** NO_x and **(c)** CO.

A concept that has widely been used in single cloud studies of tracer transport is that of a pre-convective environment, i.e. an environment which has not been influenced by deep convection recently. However, because of the frequent wide spread deep convection in the equatorial western Pacific and the relatively short time scales for horizontal advection, it is difficult to define such an environment. Attempts to define a pre-convective environment by integrating a clear-sky single column model based on the CRCTM used in this study were not fruitful, because the troposphere is far from local chemical equilibrium and the adjustment times of individual reactive gases towards equilibrium vary over a large range of characteristic lifetimes on the order of seconds, hours, days, months, and even years for the oxidation of methane.

7.3 Photochemistry in the Region: Observations and Model Results

7.3.1 The CEPEX Campaign

Shortly after the TOGA COARE IOP, the Central Equatorial Pacific Experiment (CEPEX, Kley *et al.*, 1996, 1997) was launched. CEPEX took place from 8 March to 6 April 1993. The Research Vessel *Vickers* left the TOGA COARE region and cruised along 2°S latitude towards the date line and beyond. Balloon borne ozone observations during this cruise yielded near zero ozone mixing ratios at several locations over the Pacific (Kley *et al.*, 1996, 1997). These extremely low upper tropospheric ozone mixing ratios suggested that convection had lifted low level ozone-poor air

to the upper troposphere without significant entrainment (Kley *et al.*, 1996). Since in repeated cases upper tropospheric ozone mixing ratios were below the values in the marine boundary layer, Kley *et al.* (1996) and Lawrence (1996) also considered the possibility that ozone might be destroyed in clouds due to heterogenous reactions in cloud droplets or on ice surfaces (see Kley *et al.*, 1996; Lawrence, 1996, and references therein for details).

During the first week of the CEPEX cruise, relatively strong westerly winds were observed throughout the lower troposphere, while in the upper troposphere the winds were easterly and southeasterly (see Fig. 16 of Kley *et al.*, 1997). At that time, the *Vickers* was still cruising west of 170°E. The observed strong vertical shear of the zonal wind is characteristic of a westerly wind burst. Judging from Fig. 7.5, minimum values of surface ozone in the TOGA COARE region should not be expected to occur during westerly wind bursts. Indeed, during this part of the cruise, observed surface ozone values were around 10 nmol mol^{-1} (see Fig. 1 of Kley *et al.*, 1997), comparable to those simulated in the TOGA COARE region by MATCH-MPIC in the end of February (compare Fig. 7.5). The relatively high low level ozone values during westerly wind bursts are likely caused by cross equatorial transport associated with westerly wind bursts. The upper level winds during westerly wind bursts are, however, southerly, possibly importing southern hemisphere maritime ozone-poor air masses, which have previously been lifted by deep convection occurring in association with the westerly wind burst. This could possibly explain the near zero values of ozone encountered in the upper troposphere during the first week of the CEPEX cruise while at the same time elevated high ozone values were observed in the lower troposphere (compare Fig. 1 of Kley *et al.*, 1997). Lawrence (1996) and Lawrence *et al.* (1999b) used MATCH-MPIC to simulate the ozone chemistry during CEPEX and found that ozone minima were reproduced qualitatively but not quantitatively by MATCH-MPIC. The lowest upper tropospheric ozone values simulated by MATCH-MPIC were found to still be above the minimum values observed during CEPEX. During the latter part of the CEPEX experiment easterly and south easterly surface winds most often prevailed (see Figs. 16 and 17 of Kley *et al.*, 1997) and in many occasions low surface ozone mixing ratios were observed (compare Fig. 1 of Kley *et al.*, 1996). This low level air most likely had southerly origins.

Wang *et al.* (1995) studied a storm during CEPEX using a CRM and found a decrease of ozone volume mixing ratios due to the transport of ozone-poor air from the boundary layer in the cloud tower and in some areas in the middle of the anvil. Wang and Prinn (2000) considered photochemical reactions and lightning NO_x production in their CRM study of a different storm during CEPEX and they found that the upward transport of O_3-poor air from the boundary layer does not significantly decrease O_3 concentrations in the upper troposphere. Based on results from a run in which they assumed a very large production of NO molecules per flash, they suggested that lightning-related O_3 loss in cloud anvil regions can help explain the occasional formation of an O_3 poor layer in the troposphere.

7.3.2 Selected Results from Other Campaigns and Related Model Studies

Table 7.1: Selected tropospheric chemistry campaigns in the Pacific (ordered by season) and biomass burning regions.

Campaign	Date	Coverage	biomass burning regions [1]
PEM-West A	Sep–Oct 1992	West[2]	Africa (S) and S. America[3]
PEM-Tropics A	Sep–Oct 1996	central	"
PEACE-A	Jan 2002	NW rim	South East Asia, Africa (N)
PEM-West B	Feb–Mar 1994	West	"
TRACE-P	Feb–Apr 2001	NW rim	"
PEM-Tropics B	Mar–Apr 1999	central	"

[1] Andreae (1993) shows the number of fires detected from space as a function of season and latitude. The seasonal cycle of south east Asian biomass burning emissions is depicted by Kondo *et al.* (2004a) who studied the influence of south east Asian biomass burning during TRACE-P.

[2] The PEM-West campaigns included flights in the region of the northwestern Pacific rim and in the northern tropical West Pacific.

[3] Southern tropical biomass burning had large influences on the South Pacific during PEM-Tropics A (see text). It probably had little influence during PEM-West A, since PEM-West A missions were largely confined to the northern hemisphere.

Unfortunately, no observations of ozone or related trace gases were made during the TOGA COARE IOP. A number of campaigns aimed at understanding the photochemistry in the Pacific focused on different seasons and/or different regions. Some of these campaigns aimed at sampling Asian outflow. Table 7.1 provides a list of selected campaigns. Each of these campaigns comprised a number of aircraft missions. With one exception, all campaigns were conducted either in northern hemispheric fall or in northern hemispheric late winter/early spring. NASA's Pacific Exploratory Mission (PEM) campaigns in the western Pacific, phase A and B (PEM-West A and PEM-West B, Hoell *et al.*, 1996, 1997), were components of the East Asia/North Pacific Regional Study (APARE), a project within the International Global Atmospheric Chemistry (IGAC) Program. The PEM-Tropics campaigns (Hoell *et al.*, 1999; Raper *et al.*, 2001), and the Transport and Chemical Evolution over the Pacific (TRACE-P, Jacob *et al.*, 2003) campaign were conducted by the NASA Global Tropospheric Experiment (GTE). The Pacific Exploration of Asian Continental Emissions campaign, phase A (PEACE A, Kondo *et al.*, 2004b) was conducted by the Earth Observation Research Center (EORC) of the Japan Aerospace exploration Agency (JAXA). Aircraft missions not listed in the table include PACE (Tsutsumi *et al.*, 2003), and BIBLE (Ko *et al.*, 2003). During the PACE campaign ozone was monitored west of the TOGA COARE region during one flight in January. The BIBLE campaign mainly focused on Australian outflow.

The PEM-West campaigns included flights in the region of the north western Pacific rim and in the western tropical Pacific. The latter flights departed from

Guam and concentrated on the northern hemisphere. One of these flights extended to about 10° south of the equator. Of all missions flown during the campaigns listed in Table 7.1, these flights were the ones closest to the TOGA COARE region. However, observations of a number of compounds such as ozone and NO during these flight show very large temporal variability and spatial gradients, and averages for these flights are not necessarily representative for the TOGA COARE case. While the PEACE-A and TRACE-P campaigns concentrated on outflow along the Pacific rim off the coasts of China and Japan north of about 20°N, the PEM-Tropics campaigns focused on the remote tropical Pacific including flights over the south Pacific, away from Asian emissions.

PEM-West

The dates of PEM-West A and PEM-West B were selected in order to maximize the seasonal difference (Hoell *et al.*, 1997). The southern boundary of the region in which the most pronounced continental influences were observed was located at about 40°N in PEM-West A and at about 20°N during PEM-West B (Hoell *et al.*). During PEM-West A, the semipermanent subtropical anticyclone appeared over the western and central North Pacific, and the flow around it brought maritime air masses into the western Pacific ocean (e.g. Kondo *et al.*, 1997, and references therein). During PEM-West B, cross-equatorial flow occurred in the vicinity of the Indonesian Archipelago. This flow turned into a northwesterly flow south of the equator which fed into the southern hemisphere monsoon (Merrill *et al.*, 1997). These conditions are similar to the conditions during the TOGA COARE episode studied here (compare Fig. 1c by Merrill *et al.* to Fig. 7.3). While the NO_y measurements during PEM-West A were problematic (Crosley, 1996), they were better in PEM-West B (Kondo *et al.*, 1997).

PEM-West Tropical Component

Crawford *et al.* (1997b) and Kawakami *et al.* (1997) noted very variable NO_x levels in the data recorded to the northwest of the TOGA COARE region during PEM-West B in late winter/early spring 1994. According to Crawford *et al.*, NO mixing ratios exceeded 100 pmol mol^{-1} during portions of four flights, while the values almost never exceeded 20 pmol mol^{-1} during two other flights. Back trajectory calculations suggested that air parcels in both cases had been strongly influenced by deep convection. While the low NO_x cases appeared to have been predominantly impacted by marine convection, the high NO_x cases showed evidence of having been more influenced by deep convection over a continental land mass (Crawford *et al.*). Satellite observations strongly pointed to lighting as a major source of NO_x in the latter case. Crawford *et al.* and Kawakami *et al.* concluded that lightning was probably largely responsible for the elevated NO levels. Based on observed ratios of propane (C_3H_8) to NO_x, Crawford *et al.* argued that biomass burning had played a minor role, but they acknowledged the possibility that recycling of NO_x from reservoir species could have influenced these ratios. The back trajectory analyses performed

by Crawford *et al.* suggested a southeasterly origin of air for the low NO_x cases and a more northwesterly origin during high NO_x episodes. They did not analyze their results in light of the intra-seasonal oscillation, but the differences between the the low NO_x and the high NO_x "regimes" could probably be linked to the easterly and the westerly phase of the intra-seasonal oscillation (westerly wind bursts).

Crawford *et al.* estimated tendencies for in-situ ozone loss and formation using photochemical box model simulations. They found that the net effect of photochemistry on the tropospheric ozone column in the low NO_x regime was strong net loss while the high NO_x regime showed only weak net loss. When evaluated for a 0–17 km tropopause height with added acetone chemistry, small net formation occurred in the the high NO_x regime, while the low NO_x regime was still dominated by net loss, albeit at a somewhat lower rate. The column budget was dominated by photochemical activity in the lowest 2 km. In the lower troposphere ozone loss dominated in both regimes. Above 4 km net ozone formation occurred in the high NO_x regime, while ozone loss dominated in the low NO_x regime up to about 8 km. The column amounts of ozone and NO_x in the tropical sector during PEM-West A in fall 1992 were similar to those in the tropical sector during the low NO_x episodes in PEM-West B (Crawford *et al.*, 1997b). The columns sampled during the low NO_x episodes in PEM-West B were more uniformly mixed than those observed in PEM-West A, which can have a profound impact on the photochemical ozone budget. The result of the enhanced mixing is that a larger fraction of the ozone column is placed at lower altitudes, where in combination with high water vapor levels, ozone destruction is very rapid (e.g. Crawford *et al.*, 1997b).

Asian Outflow (PEM-West, TRACE-P, PEACE)

Fig. 7.7 shows gridded 500 m ozone volume mixing ratios during PEM-West B. PEM-West B was conducted during a flow regime which was similar to the one during the TOGA COARE episode. Large latitudinal gradient occur associated with the outflow of emissions from Asia. Large latitudinal gradients of near surface ozone mixing ratios in the western and central Pacific with low values around the equator were reported by Liu *et al.* (1983) and by Johnson *et al.* (1990). Johnson *et al.* (1990) reported shipborne observations of near zero ozone mixing ratios in the western Pacific close to the equator during the SAGA 87 cruise in May 1987. In the central Pacific they also found near zero ozone mixing ratios during the RITS 88 cruise in late April/early May 1988. Much higher values were observed at higher latitudes. That relatively high values can occur in the latitude range from 20°N to 30°N, even during northern hemispheric winter, was observed during PEACE-A in January 2002. For this latitude range Kondo *et al.* (2004b) reported median values above 40 nmol mol^{-1} close to the surface. These observations were concentrated close to the western Pacific rim. For the mostly extra-tropical latitude band from 20–50°N, Crawford *et al.* (1997a) found net ozone production at all altitudes including the marine boundary layer for PEM-West B using a photochemical box model. Recently, Kondo *et al.* (2004b) presented results from the PEACE-A and B campaigns, which

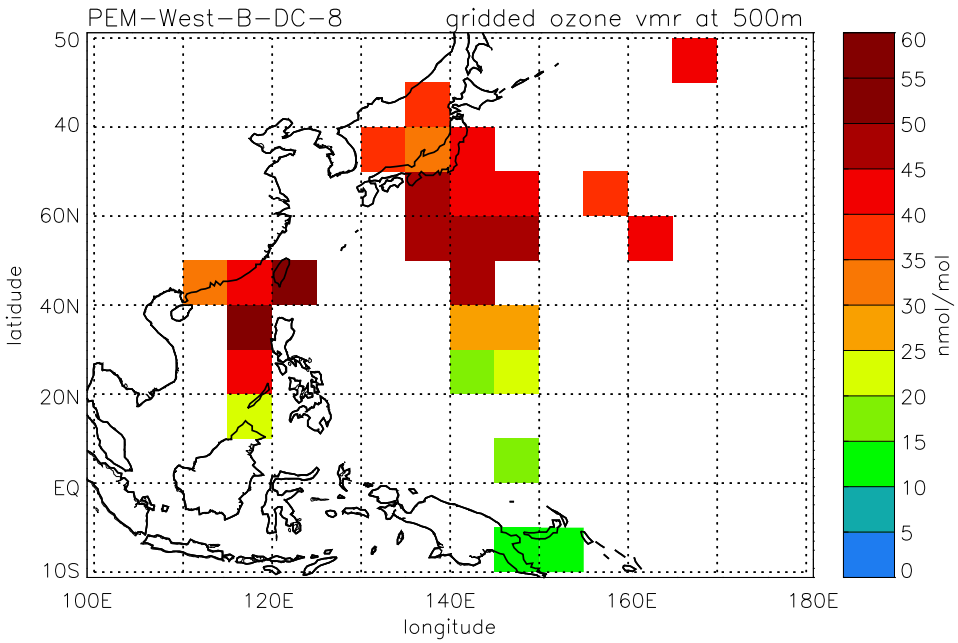

Figure 7.7: Gridded ozone volume mixing ratios at 500 m during PEM-West B. Sampled by the NASA DC 8 between 7 February and 14 March 1994. Data from Emmons *et al.* (2000) obtained at http://acd.ucar.edu/∼emmons/DATACOMP/camp_table.htm.

focused on sampling Asian outflow. Using photochemical box model simulations, they found the net formation rate of ozone was largely positive in the boundary layer at 30–40°N in January. Furthermore, they found that net O_3 formation continued from January to the end of March. Because of a lack of PAN data during the PEACE campaigns, the contribution of PAN decomposition to the observed NO_x abundance was not assessed by Kondo *et al.*. In fall, the outflow from Asia is on average less pronounced. Singh *et al.* (1996) found ozone values as low as 2–5 nmol mol^{-1} in the boundary layer during PEM-West A. Based on steady state model calculations, they suggested the these low ozone mixing ratios occurred as a result of net photochemical ozone destruction in a low NO_x environment, combined with sea surface deposition and low entrainment rates from the free troposphere. The importance of biomass burning for Asian outflow during PEM-West B was highlighted by Bey *et al.* (2001a). In a study using a GCTM, they estimated that fossil fuel combustion and biomass burning make comparable contributions to the budgets of CO, ozone, and NO_x in the Asian outflow. Kondo *et al.* (2004a) identified biomass burning in southeast Asia as a major source of reactive nitrogen and O_3 during TRACE-P. In the latitude range from 20°N to 35°N, Liu *et al.* (2003) found the upper tropospheric outflow during TRACE-P to largely reflect biomass burning emissions in southeast Asia lifted by convection. For winter they found that Asian pollution is capped in the boundary layer by the general subsidence over the Asian continent and is swept by northerly monsoons (i.e. anti-cyclonic flow across the Philippines) southward into the tropics. Biomass burning in southeast Asia takes mainly place from January to May (Kondo

et al., 2004a). The peak activity is around March.

South Central Pacific (PEM-Tropics)

A GCTM-guided analysis of the sources and sinks of ozone in the tropical South Pacific (0–28°S, 165°E–165°W) during PEM-Tropics A by Schultz *et al.* (1999) yielded the ozone mixing ratios below 4 km to be influenced by sources due to low level advection of ozone, vertical transport, and in-situ photochemical processes. The in-situ formation was more than balanced by chemical loss processes and dry deposition. The NO_x responsible for the in situ-formation was partially explained by the thermal decomposition of PAN transported into the region with biomass burning pollution from Africa and South America at higher altitudes. In the whole tropospheric column over the South Pacific, the chemical production of ozone was found to balance only half of the photochemical loss. PEM-Tropics A took place during September-October, 1996, at the end of the dry season in the southern hemispheric part of Africa and South America when biomass burning emissions are large. PEM-Tropics B, on the other hand, was conducted in the wet season of the southern tropics, when biomass burning in Africa and South America are minimum. The concentrations of NO_x, HNO_3, and PAN observed in the upper troposphere over the South Pacific during PEM-Tropics B were a factor of 2–3 less than those observed during PEM-Tropics A (Staudt *et al.*, 2003). Ozone concentrations over the South Pacific were nearly a factor of 2 lower during PEM-Tropics B than PEM-Tropics A, reflecting the lack of biomass burning as well as an approximately 30% shorter lifetime due to higher water vapor and a lower overhead ozone column (see Raper *et al.*, 2001, and references therein). Staudt *et al.* (2003) suggested oceanic lightning to be an important source of NO_x during PEM-Tropics B. They argued that since current models tend to underestimate the abundances of acetaldehyde and acetone, the decomposition of PAN could be overestimated in these models. According to Staudt *et al.*, such a model bias could challenge the conventional view of the importance of PAN as a source of NO_x in the remote troposphere.

7.3.3 Ozone Sondes

In Fig. 7.8a ozone profiles recorded in December from 1996 to 2003 at American Samoa (14.2°S,170.6°E) are plotted together with the average profile computed by MATCH-MPIC for December 1992. Fig. 7.8b shows the profiles for Hilo observed in December from 1990 to 2001 and the average profile computed by MATCH-MPIC for December 1992. Hilo is located on the island of Hawaii, the largest in the Hawaiian Archipelago (19.7°N,155.1°E). The sonde data was retrieved from the World Ozone and Ultraviolet Radiation Data Centre (WOUDC). Both sonde sites were operated by the Climate Monitoring and Diagnostics Laboratory (CMDL) of NOAA[1] (PI: S. Oltmans). The station at Samoa is part of the SHADOZ project (SHADOZ: Southern Hemisphere ADditional OZonesondes, Thompson *et al.*, 2003).

[1]National Oceanic and Atmospheric Administration, USA

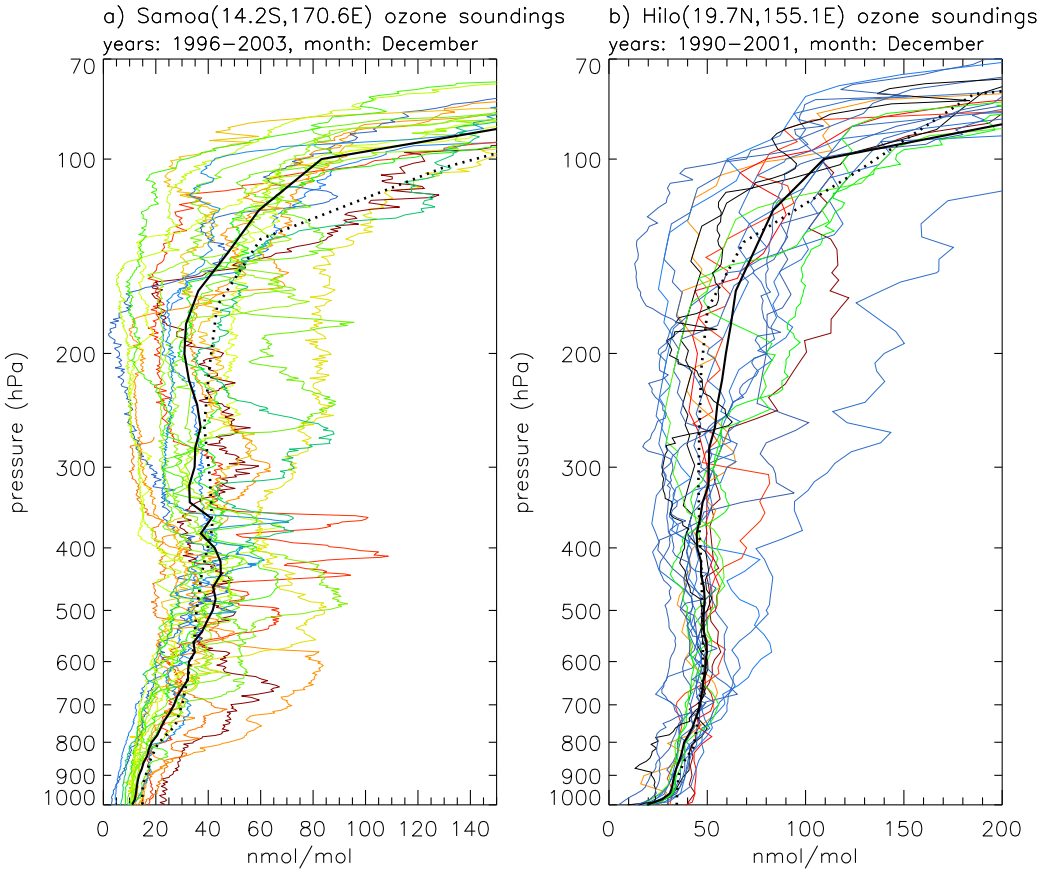

Figure 7.8: Ozone profiles at American Samoa and at Hilo. Thin lines: soundings launched in December, thick solid line: average of sondes launched in December, dotted line: average from MATCH-MPIC for December 1992. Three soundings at Hilo seemed suspicious and were excluded.

The average upper tropospheric ozone mixing ratio calculated for Samoa by MATCH-MPIC is a bit higher than the average observations and the chemical tropopause is a bit lower. In the lower troposphere, the difference between the averaged profiles is very small. For Hilo, the difference between the calculated average and the observed average is generally small. The individual soundings show considerable vertical structure. Newell *et al.* (1996, 1999) interpreted thin horizontal layers in the troposphere as frozen signatures of the transfer of boundary layer air into the free troposphere or of stratospheric air into the troposphere. A number of soundings launched from American Samoa yield very low ozone values in the upper troposphere, though never as low as the extremes observed during CEPEX.

Chapter 8

Lightning NO_x and Reactive Nitrogen Compounds

Satellite observations have shown that globally most lightning occurs over land areas with maximum flash densities in the tropics (e.g. Mackerras *et al.*, 1998; Christian *et al.*, 2003). Oceanic lightning is very infrequent compared to lightning over the continents. Orville *et al.* (1997) found the annual number of CG flashes per unit area in the TOGA COARE region for 1993 to be at least one order of magnitude lower than that observed close to the nearby Papua New Guinean islands. This large gradient between coastal and further offshore lightning rates is also apparent on global maps of lightning from the Optical Transient Detector (OTD) satellite instrument (see e.g. Christian *et al.*, 2003).

In spite of lightning over oceans being comparatively infrequent, the associated NO_x source can nevertheless be important. While globally most NO_x is emitted from continental sources (e.g. Brasseur *et al.*, 1999), in oceanic regions, the transport of NO_x precursors (especially upper tropospheric PAN transport), the transport of NO_x in the upper troposphere, and emissions from ships and airplanes contribute substantially to the NO_x budget. Levy II *et al.* (1996) found that during winter months lightning contributed 50 to 80% of all upper tropospheric NO_x in the tropical North Pacific. Staudt *et al.* (2003) suggested that lightning was the dominant source of NO_x above the equatorial and southern Pacific during PEM-Tropics B. However, uncertainties regarding the amount of NO_x produced by lightning are still large (see Table 8.1). Furthermore, the effect of ship emissions (e.g. Lawrence and Crutzen, 1999; Kasibhatla *et al.*, 2000; Chen *et al.*, 2005) (which can contribute to the upper tropospheric NO_x budget via deep convective transport) was most likely underestimated in the studies of Levy II *et al.* and Staudt *et al.*, who used an emission inventory by Benkovitz *et al.* (1996) in their global models. Lawrence and Crutzen (1999) noted that nearly all the ship emissions in this inventory were assigned to ports and inland coastal waterways, and only a small component in the northern Atlantic was included. In MATCH-MPIC the Corbett *et al.* (1999) ship emission dataset is used and industrial NO_x emissions over the ocean (including emissions from shipping and airplanes) are currently larger than emissions due to

oceanic lightning in this model (Fig. 2.8 of von Kuhlmann, 2001). Oceanic lightning is, however, mostly a bit underestimated in MATCH-MPIC (Labrador *et al.*, 2005). In the CRCTM, ship emissions inside the domain were not considered. The studies by Crawford *et al.* (1997b) and Kawakami *et al.* (1997) suggest that the NO_x budget in the TOGA COARE region could be influenced considerably by lightning over New Guinea and subsequent transport (see Section 7.3.2). The potential importance of the lightning NO_x source for the global tropospheric photochemistry was highlighted by Labrador *et al.* (2004), who found a strong sensitivity of the global tropospheric mean OH concentration and the lifetime of methane to the lightning NO_x production in a study using MATCH-MPIC.

8.1 Lightning during TOGA COARE

In severe continental thunderstorms rates of 20 and more flashes per minute can be sustained over an hour or more (see e.g. Skamarock *et al.*, 2003; Fehr *et al.*, 2004). In the TOGA COARE region, on the other hand, during more active storms flash rates of only 1–2 (and in one case 4) discharges (both IC and CG) per minute were observed by two NASA aircraft during storm overpasses (Orville *et al.*, 1997). Lightning was only observed during 19 out of 117 storm overpasses. In addition to these airborne observations, observations of CG lightning from an advanced lightning direction finder (ALDF) network are available for TOGA COARE (e.g. Lucas and Orville, 1996; Petersen and Rutledge, 1996). Nevertheless, the uncertainty regarding the total number of flashes during TOGA COARE is rather large. Unfortunately, the number of IC flashes was not observed and the ground truth from the airborne observations is not sufficient to determine the ratio of IC to CG flashes or the total number of flashes. Furthermore, the fraction of IC flashes erroneously recorded as CG flashes by the ALDF network is uncertain (see Lucas and Orville, 1996; Petersen and Rutledge, 1996). The antenna gains were increased by a factor of 1.5 in order to increase their range, at the same time increasing the probability of detecting nearby IC flashes (Petersen and Rutledge, 1996). An incident in which a large number of IC flashes was accepted by the direction finder was reported by Lucas and Orville (1996).

It is believed that tropical thunderstorms on average have higher ratios of z= (number of IC flashes)/(number of CG flashes) than mid-latitude thunderstorms. Pierce (1970) found that at the equator approximately 10% of the lightning flashes in a thunderstorm reach the earth (implying $z \approx 9$) compared to nearly 60% at 65° latitude (implying $z \approx 0.67$). Prentice and Mackerras (1977) found z to vary from approximately 6 at the equator to 2 at 60° latitude. Price and Rind (1993) found that the fraction of CG flashes varies only between 0.24 and 0.28 over the latitude range from 0° to 40° (implying z to vary from about 3.2 to about 2.6), but strongly depends on the cold cloud thickness, which is defined as the vertical extent of the cloudy region where $T < 0°\,C$. Price *et al.* (1997a) derived a global rate of 50–70 IC and 20–30 CG flashes per second, implying $z \approx 1.7$–3.5 globally. Mackerras *et al.*

Table 8.1: Estimates of lightning NO production, extended from Labrador *et al.* (2005), with values prior to 1995 adopted from Lawrence *et al.* (1995).

Reference (type of estimate)	Molec.(NO)/flash (10^{25} molec./flash)	Global rate[1] (flashes/s)	Global prod. (Tg(N)/yr)
Tuck (1976)[a]	1.1	500	4
Chameides *et al.* (1977)[a]	6–14	400	18–41
Noxon (1976)[c]	10	500	37
Chameides (1979)[a]	16–34	400	47–100
Dawson (1980)[a]	0.8	500	3
Hill *et al.* (1980)[a]	1.2	100	0.9
Levine *et al.* (1981)[b]	0.5	500	1.8±0.7
Kowalczyk and Bauer (1982)[a]			
CG	10	50	3.8
IC	1	2.5	1.9
Peyrous and Lapyere (1982)[b]	3.2	400	9.4
Drapcho *et al.* (1983)[c]	40	100	30
Chameides *et al.* (1987a)[d]	–	–	7
Franzblau and Popp (1989)[c]	300	100	220
Sisterson and Liaw (1990)[a]	8.2	200	12
Liaw *et al.* (1990)[e]	–	–	81
Lawrence *et al.* (1995)[e]	2.3(1-7)	100(70–150)	2(1–8)
Ridley *et al.* (1996)[c]	–	100	2-5
Levy II *et al.* (1996)[a]	–	–	2-6
Price *et al.* (1997a)[c]			12.2(5–20)
CG	67	20–30	
IC	6.7	50–70	
Price *et al.* (1997b)[a]	–	-	13.2(5–25)
Mackerras *et al.* (1998)			
CG	-	10–14	–
IC	-	51–55	–
Wang *et al.* (1998)[b]	3.1	30–100	2.5–8.3
DeCaria *et al.* (2000)[c]	12–30	–	–
Nesbitt *et al.* (2000)[c]	0.87–6.2	57	0.9
Huntrieser *et al.* (2002)[c]	$2.7{\cdot}10^{21}$molec/m flash	–	3 (1–20)
Christian *et al.* (2003)	–	44±5	–
Beirle *et al.* (2004)[c]	6(1.8–30)	63	2.8(0.8–14)
Fehr *et al.* (2004)[c]	21	–	–
Ridley *et al.* (2004)[c]	0.3–6.1	–	1.1–19.6
Boersma *et al.* (2005)[c]	–	–	1.1–6.4

[1] In most studies global flash rates have been assumed in order to calculate the global NO production which were not sustained by recent satellite observations. A recent estimate is 44±5 flashes s^{-1} for both IC and CG flashes (Christian *et al.*, 2003).

[a] Theoretical estimate.

[b] Laboratory-based estimate.

[c] Field observations-based estimate.

[d] Thunderstorm extrapolation-based estimate.

[e] Review-based estimate.

Table 8.2: Lightning NO sensitivity runs.

Label	molec CG[a]	molec IC[a]	Exp. in Eq. 2.29	N_{CG}[b]	N_{IC}[b]	z[c]	P_{tot}[d] CG	P_{tot}[d] IC	P_{tot}[d]
NOLTN	–	–	–	–	–	–	–	–	–
LTN1	10	5	4.8	125	1233	9.9[1]	1.3	6.2	7.4
LTN2	10	5	4.54	189	511	2.7	1.9	2.6	4.4
LTNWP	67[2]	6.7	4.54	189[4]	511	2.7	12.7	3.4	16.1
LTNHWP	300[3]	30	4.54	189	511	2.7	56.7	15.3	72.0

[a] 10^{25} molecules per flash.
[b] Number of flashes calculated for the 7-day TOGA COARE runs using Eq. 2.29.
[c] Ratio of number of IC flashes to number of CG flashes, see also Sect. 2.6.
[d] 10^{28} molecules.
[1] Diagnosed from calculated total flash numbers.
[2] Same as in LTN run of Wang and Prinn (2000), based on Price *et al.* (1997a) who suggested $6.7 \cdot 10^{26}$ NO molecules per CG flash.
[3] Same as LTNH case of Wang and Prinn (2000), based on Franzblau and Popp (1989).
[4] For comparison: Wang and Prinn (2000) calculated a total of about 750 flashes out of which ∼210 were CG flashes for the first hours of a 30 h 2-D run with 1000 km horizontal domain length.

(1998) found the mean global IC flash rate to be between $51\,s^{-1}$ and $55\,s^{-1}$ and the CG flash rate to be between $10\,s^{-1}$ and $14\,s^{-1}$, implying z in the range z =3.6–5.5. For the coastal site of Darwin, Rutledge *et al.* (1992) found z to vary considerably between storms, possibly due to different air mass origins at this site.

Orville *et al.* (1997) reported an incident in which a total of 17 flashes (IC and CG) were detected in one storm by the NASA aircraft, while during the same time interval 10 CG discharges were detected for this storm by two ALDF stations. Using this single observation to determine z would probably result in a large underestimation. It is possible that either not all flashes were detected aboard the airplane or that IC flashes were erroneously detected by the ALDF network or that a storm with an exceptionally low IC/CG ratio was encountered.

8.2 Lightning Sensitivity Runs

The flash parameterization used in the CRCTM was described in Section 2.6. Four lightning NO_x sensitivity runs with various assumptions regarding flash rate, NO production per flash, and the IC/CG ratio have been conducted. An overview is presented in Table 8.2. The number of molecules per CG flash prescribed in the LTN1 and the LTN2 run ($10 \cdot 10^{25}$ molecules per flash) was chosen from a range of values suggested by a number of recent studies (from 0.3 to $30 \cdot 10^{25}$ molecules per flash for studies since the year 2000, based on the overview of estimates from the literature presented in Table 8.1). In the LTN1 run the IC/CG ratio z was

calculated as a function of the vertical distance between the 0°C isotherm and the cloud top using the parameterization by Price and Rind (1993) as described in Section 2.6, while in the LTN2 run a relatively low ratio was prescribed based on global observations, which was also used by Wang and Prinn (2000). This ratio is lower than typically suggested for the tropics. The exponent in the the flash rate calculation (Eq. 2.29) was increased to 4.8 in the LTN1 run from the value of 4.54 suggested by Price and Rind (1992) in order to increase the calculated number of CG flashes towards observed values, but it is below the value of 5.3 used by Pickering *et al.* (1998) in their simulation of a TOGA-COARE storm. The simulation of Pickering *et al.*, however, yielded considerably smaller maximum vertical velocities compared to this study which were used to calculate the flash rates. The total NO production by all simulated flashes during the 7-day TOGA COARE episode P_{tot} in Table 8.2 is higher for the LTN1 run than for the LTN2 run due to the larger NO production by IC flashes in the LTN1 run. In the LTN1 run about 83% of the total NO is produced by IC flashes, which is below the recent estimate by Fehr *et al.* (2004), who found IC flashes to contribute up to 93% of the total NO_x production in a study combining observations and model simulations of a mid-latitude thunderstorm. The ratio of NO molecules per IC flash to NO molecules per CG flash in the LTN1 and the LTN2 run (P_{IC}/P_{CG}=0.5) was adopted based on recent observations (see Section 2.6).

In the LTNWP and the LTNHWP the same number of molecules per flash for IC and CG flashes and the same IC/CG ratio z have been adopted as in the LTN and the LTNH runs by Wang and Prinn (2000), respectively. The flash rates in the 7–day TOGA COARE runs are, however, generally much lower than those in the study by Wang and Prinn (2000) who calculated a total of about 750 flashes out of which ∼210 were CG flashes for a 30 h 2-D run using 1000 km domain length[1]. Lightning was mainly simulated to occur during the first few hours of their runs, in which deep convection was initiated by placing an artificial "warm bubble" in the model domain. Based on Table 8.1 and on a discussion by Ridley *et al.* (2004), the number of molecules produced per flash prescribed in the LTNWP run appears to be a good upper estimate given the current range of uncertainty. The number of NO molecules per flash adopted in the LTNHWP sensitivity run is based on a study by Franzblau and Popp (1989) and was also adopted by Wang and Prinn (2000) for the LTNH run in their CRM study. This number is well above the range suggested by other studies (compare Table 8.2), including a number of recent studies (e.g. DeCaria *et al.*, 2000; Fehr *et al.*, 2004; Ridley *et al.*, 2004; Beirle *et al.*, 2004).

8.2.1 Vertical Velocities and Flash Rates

Fig. 8.1a shows modeled 30 min flash rates derived from for the LTN1 run. The number of CG flashes per 30 min interval was multiplied by 10 for better readability. Long episodes of little or no lightning activity in the domain are interrupted by

[1]The numbers of flashes calculated by Wang and Prinn (2000) have been estimated from their Fig. 6.

shorter episodes of lightning. In a number of cases between 1 and 5 CG flashes were calculated to occur within 30 min, and the maximum was 11.6 CG flashes within 30 min. Except for the peak on 24 December, these CG flash counts are generally lower than observations by Petersen and Rutledge (1996), who studied four cells which all had similar characteristics on 15 February 1993, and calculated the average flash rates for the four cells peaking at slightly above 7 CG flashes within 20 min (see their Fig. 5). Petersen and Rutledge (1996) also noted that the majority of convection over the tropical oceans does not produce lightning. Petersen *et al.* (1999) also found somewhat higher maximum flash rates than those in Fig. 8.1a for storms with a relatively higher degree of electrification than other observed storms, albeit located around 159.5°E and 4.5°S where lightning tends to be more frequent than in the TOGA COARE region (see Fig. 4 Orville *et al.*, 1997). At the time of maximum flash rates simulated by the CRCTM, two cells in close proximity were identified by the storm location algorithm (described in Section 2.6). At times, several storms and either one or sometimes two larger mesoscale convective systems were contained in the 500 km 2-D model domain (see the Hovmöller diagram in Fig. B.1). Nevertheless, usually only one updraft at a time contributed most to the 30 min average flash rates (not shown in the figure). The CG flash rate in the LTN2 run (Fig. 8.2) reached about 5 CG flashes per 30 min for a number of 30 min intervals and peaked at 20 CG flashes within 30 min. Since in 2-D simulations all lightning NO_x is assumed to be produced within a thin slice of the troposphere, relatively low flash rates compared to observations can nevertheless lead to relatively high NO_x concentrations (see discussion of the lightning NO_x production at the end of this section).

Lucas and Orville (1996) analyzed CG lightning observations from the ALDF network operated in the TOGA COARE region. The analysis was based on data for January and February 1993, during which period about 40% of the annual CG lightning occurs (Orville *et al.*, 1997), and yielded very variable daily flash counts. They suggested, the lightning frequency in the TOGA COARE region may be modulated by the intra-seasonal oscillation. The second highest flash counts occurred at the start of the period, on 2 January, just before the end of the strong westerly wind burst (compare Fig. 7.5). The highest CG flash counts occurred from 11 to 17 February, again during a westerly phase of the intra-seasonal oscillation. During this period daily flash counts slightly exceeded 5000 for their oceanic sector spanning roughly 2.6 million square kilometers. Petersen and Rutledge (1996) reported flash counts for 31 January to 26 February 1993 performed from aboard the *Vickers* research vessel which was located within the region of the TOGA COARE IFA. For 10 and 11 February, more than 800 CG flashes daily were counted over a 600 km×600 km area (see their Fig. 10). From these numbers, the daily flash density can be estimated to equal roughly 0.002 CG flashes per km^2 during days with high lightning activity during seasons with high lightning activity. Unfortunately, evaluating the 2-D simulations using these observations is not straight forward. The daily average number of CG flashes during the last 6 days of the LTN1 run is about 21. For calculating the NO mixing ratio increase due to lightning, the "width" of the 2-D domain was assumed to equal the horizontal grid spacing of Δx=2 km. Viewing

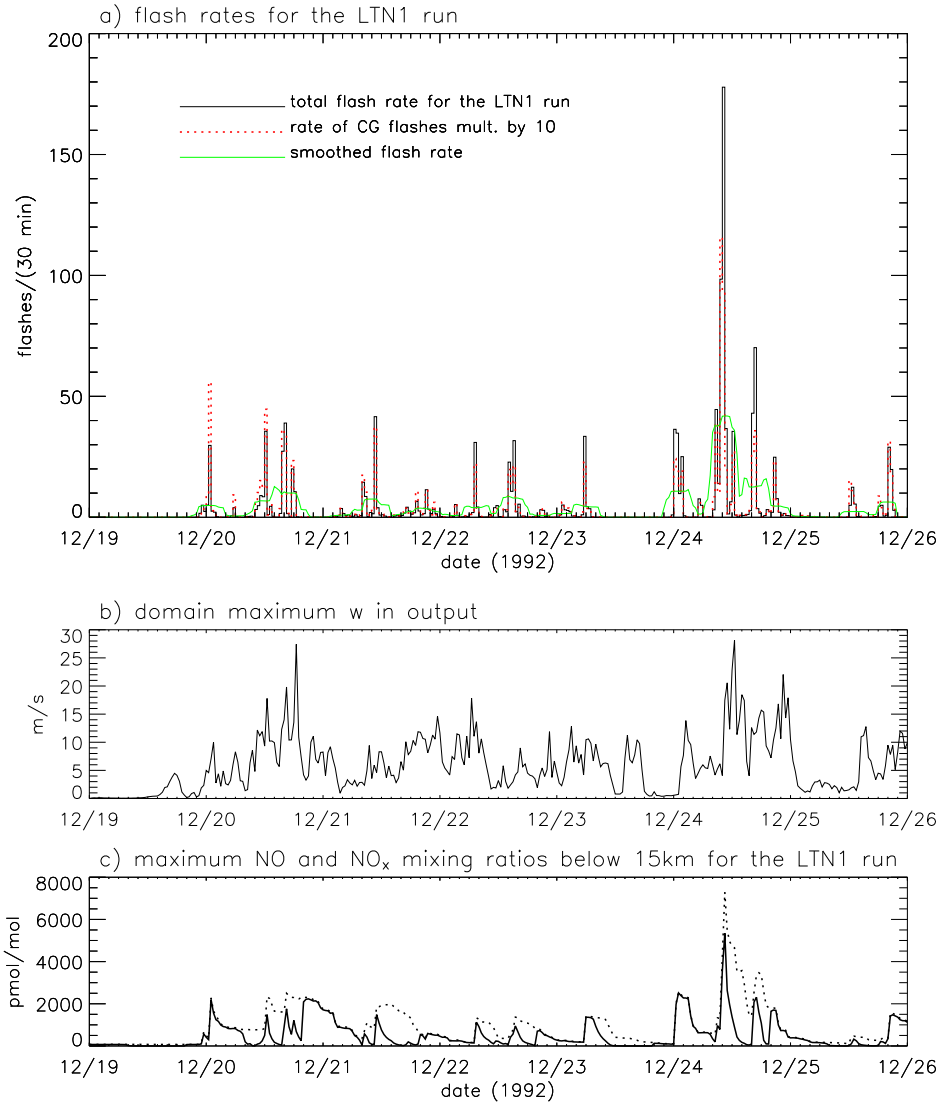

Figure 8.1: Results for the 500 km 2-D domain LTN1 run: **(a)** flashes per 30 min. The smoothing of the total flash rates (green line) was performed using a 5 point running mean. **(b)** Domain maximum vertical velocity w. **(c)** Maximum NO (solid line) and NO_x (dotted line) mixing ratios below 15400 m. The maximum values in (b) and (c) were calculated from model output. The output interval was 30 min and local 'solar' time is GMT plus 10.5 h.

a 2-D domain as a thin vertical slice is, however, problematic (see discussion below). Instead, for most purposes it is somewhat more correct to imagine the 2-D domain as the representation of a 3-D volume assuming homogeneity in the third dimension. In order to calculate reasonable flash densities in the light of the observations cited above, the imaginary width of this volume would have to be roughly 20 km, which is 10 times as much as is assumed for the "depth" of the domain in the calculation of the horizontal distribution of lightning NO (see discussion at the end of this section). In order to obtain better comparability and in order to better constrain the model

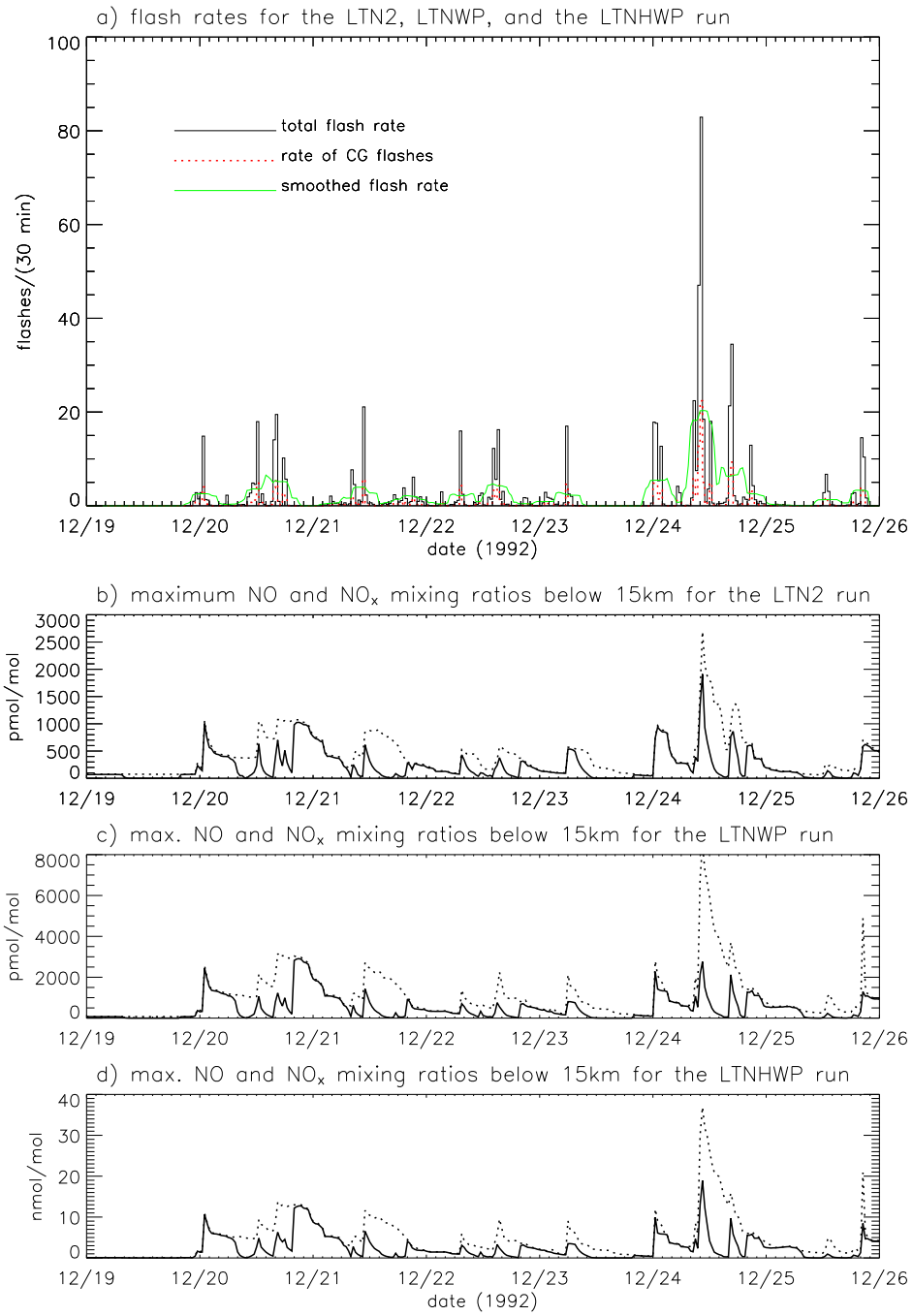

Figure 8.2: Results for 500 km 2-D domain: **(a)** Same as Fig. 8.1(a) for the LTN2, LTNWP, and the LTNHWP runs. **(b)**–**(d)** Same as Fig. 8.2c for the LTN2, the LTNWP, and the LTNHWP runs, respectively.

simulations, future 3-D simulations will be necessary. The additional 40 GB of disk space necessary to perform an additional 3-D study was not available at the time of the study.

The total calculated number of flashes for the LTN1 run was 1358 and 9.2% were

classified as CG flashes, implying z =9.9. This is a bit above the average values of Pierce (1970) and of Price and Rind (1993), and is 1.65 times above the average value of Prentice and Mackerras (1977). For the 22 February TOGA COARE squall line, Pickering *et al.* (1993) calculated that during most of the time more than 10% of all flashes were CG flashes (see their Fig. 5). They used the same parameterization for z in their CRM study, but defined the height of the cold cloud region based on horizontally averaged properties and simulated a 9 hour period. Here, the largest fraction of CG flashes occurred during the first storms in the simulation (see Fig. 8.1). This could possibly be due to a large buildup of CAPE before deep convection in the model sets in. As noted in Section 4.5, convection sets in earlier when a higher horizontal resolution is used.

A time series of the domain maximum vertical component of the wind velocity (sampled every 30 min) is shown in Fig. 8.1b. While it is often 10 m s^{-1} or below, on a few occasions values above 20 m s^{-1} are simulated. For tropical maritime convection, these peak values are high compared to a number of reported observations. However, Lee and Hildbrand (1995) reported peak updraft magnitudes of 22 m s^{-1} for a TOGA COARE storm on 9 February 1993 based on airborne dual-Doppler radar measurements. Trier *et al.* (1997) simulated 18 m s^{-1} in their 22 February TOGA COARE simulations. The values simulated by Pickering *et al.* (1993) for the same storm were lower. Solomon and Baker (1998) report a maximum modeled vertical velocity of 25 m s^{-1} for a 31 January TOGA COARE storm. Jorgensen *et al.* (1997) reported a case during TOGA COARE in which low-level Doppler-radar derived vertical motions were weaker than the vertical velocities observed by airplane during the direct penetration of a squall line due to contamination by sea clutter. Judging from the figures of Jorgensen *et al.* (1997), the airplane may not have penetrated the most active cells in this case. Note that maximum vertical velocities often occur in the upper troposphere as has been shown in the CRM study by Trier *et al.* (1997). Note also that the maximum peak vertical velocity simulated by CRMs could be influenced by the parameterization of the sub-grid scale turbulence. Zisper (1994) suggested a critical mean updraft velocity of at least 6–7 m s^{-1} needed to develop electrical fields strong enough to produce lightning. For a storm during CEPEX, Wang and Prinn (2000) simulated mean updraft velocities in the convective core below 5 m s^{-1} (their Figs. 2a and b). They simulated considerable lightning at rates occasionally exceeding 10 flashes per minute. A detailed discussion regarding the lightning parameterization used by Wang and Prinn (2000) was presented by Wang and Prinn (2004) and Helsdon, Jr. (2004). Helsdon, Jr. argues that the parameterization of the flash rates by Wang and Prinn (2000) could likely lead to an underestimate in lightning flash rate by an order of magnitude. Wang and Prinn (2000, 2004) argue that their flash rates are close to the observed ones with short periods of exceptionally high flash rates.

8.2.2 Lightning NO_x in the 2-D model Runs

A number of airborne NO and NO_2 measurements aimed at determining the amount of NO_x produced by lightning have been conducted. A survey including 17 studies at different latitudes is presented by Huntrieser *et al.* (1998). Three of these studies were conducted south of Hawaii and yielded maximum NO mixing ratios of 0.9 nmol mol^{-1}. The mean mixing ratios in the anvils were 0.4, 0.7 and 0.4 nmol mol^{-1}, respectively. Kawakami *et al.* (1997) reported a maximum NO mixing ratio of 0.9 nmol mol^{-1} in the West Pacific Ocean at 6°S which they attributed to lightning. This observation was made close to the eastern parts of Papua New Guinea, south of Kavieng, where the eastern station of the TOGA COARE IFA was located. In 12 out of the 17 studies cited by Huntrieser *et al.* (1998), maximum observed NO volume mixing ratios were reported. A few studies reported several maximum values, and the average of all maximum mixing ratios is 1.6 nmol mol^{-1}. The highest mixing ratios listed (two studies, both in the continental United States) were 4.0 nmol mol^{-1}. Huntrieser *et al.* (1998) report additional observations for storms in Germany with maximum NO observations between 1.1 and 3.8 nmol mol^{-1}. The simulated maximum NO and NO_x mixing ratios (not necessarily occurring at the same locations within the domain) for the lightning sensitivity runs are shown in Fig. 8.1c and Fig. 8.2b–d. For calculating the maxima, only NO mixing ratios below 15400 m were considered. The values of the maxima in the figure are, however, insensitive to choosing a slightly higher threshold height. Based on animations (not shown) it was judged that the maxima are due to lightning and not caused by transport of NO_x from the stratosphere (compare also the next Section, Fig. 8.4). The maximum NO volume mixing ratios during the LTN1 run are higher than the maximum 0.9 nmol mol^{-1} observed above the western Pacific on a number of occasions, but most of the time well below maximum values observed for mid-latitude thunderstorms. For the LTN2 run, the maximum NO mixing ratios are clearly above available observations from the western Pacific only on 24 December. The peak NO mixing ratio on 24 December in the LTNWP run is below that in the LTN1 run in spite of the total NO production in the LTNWP run being more than twice as high as in the LTN1 run. The maximum NO_x mixing ratio occurring during nighttime on 24 December is, however, more than twice as high in the LTNWP run compared to the LTN1 run. Incidents with low daytime NO to NO_x ratios due to lightning NO production occur mainly for the LTNWP and the LTNHWP runs, while in general the maximum NO_x mixing ratios below ∼15 km around local noon differ from the domain maximum NO mixing ratios by less than 10% of the domain maximum NO mixing ratio. The NO maxima calculated for the LTNHWP run appear unrealistically high in light of the observations cited above. The values of the maximum NO mixing ratios in the lightning sensitivity runs are generally the consequence of a number of flashes contributing to the same maximum. In the model, a "single" flash would result in lower mixing ratios even when the NO production is assumed to take place in a single model column.

For the purpose of calculating the horizontal lightning NO distribution, the "depth" of the 2-D domain in the CRCTM is assumed to equal the horizontal grid

spacing of Δx=2km. For a given number of NO molecules which are produced by lightning for a certain (storm-specific) number of flashes in the model, this assumption results in a high average concentration of NO molecules in the 2-D domain when compared to a 3-D domain because of the smaller volume assigned to the 2-D domain. If the air inside the domain would be well mixed throughout the domain, this higher average concentration would translate into higher mixing ratios for the 2-D domain compared to the 3-D domain. On the other hand, scaling down the NO production in 2-D domains in order to account for higher mixing ratios possibly caused by less dilution in 2-D domains (which is equivalent to assuming a deeper domain than 2 km or a lower flash rate within the volume "slice" assigned to the 2-D domain) can result in an underestimate of the maximum NO_x concentrations in the lightning NO_x plume and introduces additional uncertainties. Immediately after a certain number of lightning NO molecules are placed inside a model column the concentrations are identical for a column in a 2-D model and in a 3-D model. In the CRCTM the number of lightning produced NO molecules was not scaled down, because lightning NO_x does not tend to homogeneously be mixed across the domain on the time scale needed to be advected out of the domain (compare Fig. 8.4). Until the very recent 3-D study of a Colorado thunderstorm by DeCaria *et al.* (2005), only results from 2-D lightning sensitivity runs including chemistry have been presented. However, the discussion above illustrates the potentially large uncertainty related to using a 2-D domain in the studies of lightning NO_x on chemistry, which arises in addition to other uncertainties about the placing of lightning NO production in the model. On the one hand, the NO_x maximum mixing ratios in the lightning runs depend directly on the number of grid boxes over which the lightning NO is distributed horizontally (3 in the case of IC flashes). On the other hand, uncertainties also arise because of the assumptions concerning the location of flashes relative to the storm (see e.g. discussion in Section 9.1). An important uncertainty in comparing simulated NO mixing ratios to observed values arises from limited sampling, sampling away from the storms downwind of the lightning NO source (e.g. Kawakami *et al.*, 1997), and, in case average mixing ratios are compared, possibly from using different definitions of the anvil area. A method which has been used in a few previous CRM studies in is to compare data from airborne NO observations to model values sampled along virtual flight tracks through modeled cloud anvils. For TOGA COARE no such observations are available.

The maximum mixing ratio of NO calculated by MATCH-MPIC during the the 7 day TOGA COARE episode never exceeds 20 pmol mol^{-1} (compare Fig. 8.6b) in spite of continuous lightning NO emissions in the column located closest to the TOGA COARE region (not shown). This is in part due to the large horizontal grid spacing in MATCH-MPIC. Lightning produced NO_x is instantaneously distributed horizontally over an entire 2.8° by 2.8° grid box. Note that in global CTMs the amount of NO_x produced per grid cell does not explicitly depend on an assumption regarding the number of deep convective updrafts contained within that cell.

8.3 Modeled NO and NO_x

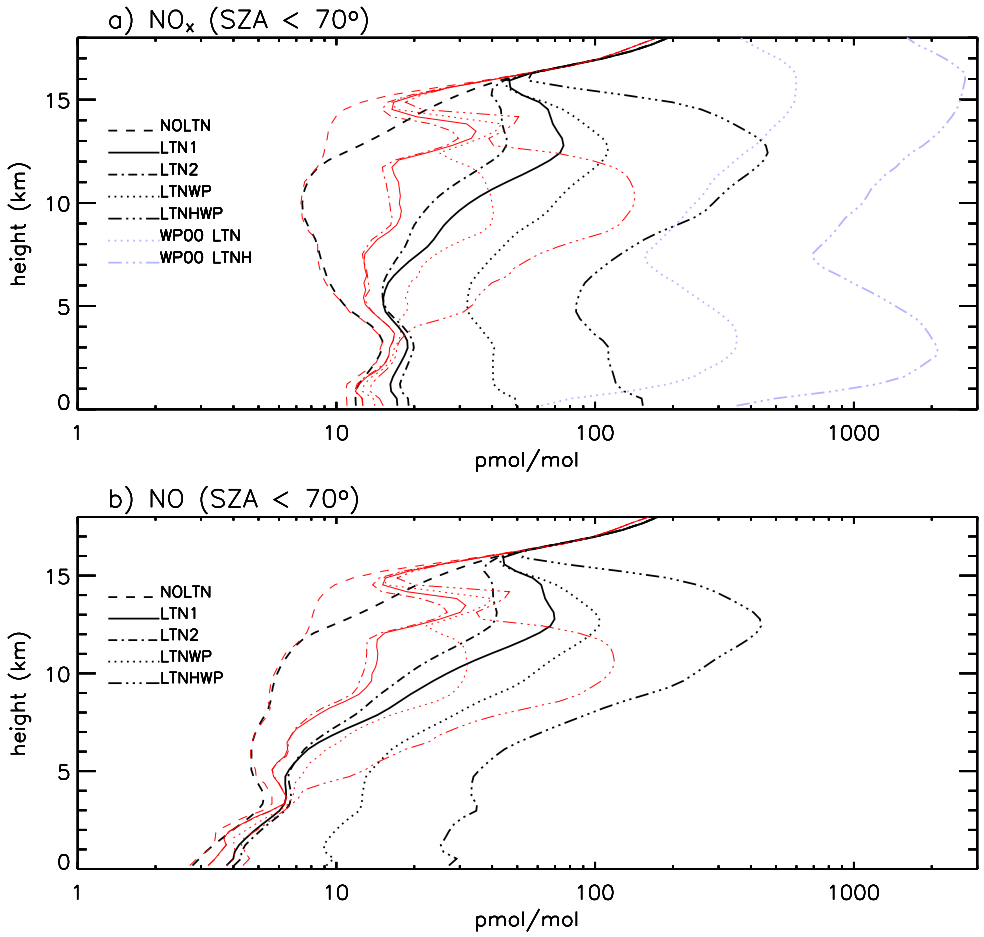

Figure 8.3: Modeled domain and time average (black lines) and median (red lines) volume mixing ratios of **(a)** NO_x and **(b)** NO for solar zenith angles (SZA) lower than 70° from the lightning sensitivity runs. Blue lines in (a): domain averaged NO_x volume mixing ratio from Fig. 11 of Wang and Prinn (2000) at the end of their LTN and LTNH runs.

Figure 8.3 shows domain and time averaged and median modeled NO_x and NO profiles for the lightning sensitivity runs and NO_x profiles from the study by Wang and Prinn (2000) which are discussed in the last paragraph of this section. A comparison to observations is not straight forward since NO and NO_x were not monitored during TOGA COARE. However, a rough impression can be gained by comparing Fig 8.3 and Table 8.3, which presents domain averaged NO and NO_x mixing ratios from the LTN1 run and from a number of observation based studies which focused on the western Pacific and did not explictly aim at the study of thunderstorms. The NO_x mixing ratios in the table except for those from the LTN1 run were calculated as the sum of observed NO and of NO_2 calculated using photochemical box models, since the inspection of NO_2 mixing ratios observed during PEM-West A had lead

Table 8.3: NO and NO_x volume mixing ratios from studies using observations and from the LTN1 run.

Reference	height (km)	NO (pmol mol^{-1})	NO_x (pmol mol^{-1})
Crawford *et al.* (1997b)[1]		*median*[2]	*median*[2]
low NO_x	0–1	5.0	19.2
	1–2	5.8	19.1
	2–4	4.2	11.8
	4–6	5.6	9.5
	6–8	5.3	8.0
	8–10	6.8	6.8
high NO_x	0–1	6.9	29.1
	1–2	6.1	24.1
	2–4	11.1	32.0
	4–6	18.9	41.6
	6–8	30.0	48.1
	8–10	60.7	69.0
Kondo *et al.* (1996)[3]		*median*[4]	*median*[4]
marine/tropical	0–1	2.3	6.6
	1–4	3.3	9.6
	4–7	7.3	12.5
	7–12	12.4	16.4
maritime western	0–1	3.7	12.5
Pacific	1–4	5.1	13.8
	4–7	11.5	19.4
	7–12	26.6	36.4
Kondo *et al.* (1997)[5]		*median*[4]	*median*[4]
marine/tropical	0–1	4.6	44.2
	1–4	3.3	14.4
	4–7	7.3	–
	7–12	59.9	84.2
this study		*median*[6]	*median*[6]
LTN1	0–2	3.6	12.9
	2–4	5.5	16.2
	4–6	5.9	13.8
	6–8	7.1	13.0
	8–10	12.1	16.7
	10–14	20.3	23.0

[1] Analysis for the "remote tropical component" of PEM-West B, i.e. most flights northwest of the TOGA COARE region (latitudes ranged from about 10°S to 30°N and flights along the Pacific rim were excluded). The values in the table were estimated based on Figs. 3 and 4 of Crawford *et al.* (1997b).

[2] For SZA$< 60°$.

[3] Air mass classification based on back trajectory calculations for PEM-West A .

[4] For SZA$< 70°$.

[5] Same classification as Kondo *et al.* (1996) for PEM-West B.

[6] Vertically averaged median mixing ratios for SZA$<70°$ from Fig. 8.3.

investigators to the judgment that the measured NO_2 mixing ratios were influenced by an interference with other reactive nitrogen containing compounds (Crawford *et al.*, 1996; Crosley, 1996). Crawford *et al.* binned observations vertically and considered only mixing ratios for SZA$< 60°$. However, changing the SZA range from SZA$< 70°$ to SZA$< 60°$ in Fig. 8.3b would only have a small effect on the median NO volume mixing ratios. Kondo *et al.* (1996, 1997) used back trajectory calculations in order to classify the NO and NO_x observations during PEM-West A and PEM-West B. While the median NO mixing ratios sampled in marine tropical air during PEM-West A were increasing with height, very low values of NO and O_3 were occasionally observed in maritime air masses in the upper troposphere, indicating that marine boundary layer air deficient in NO and O_3 had been transported to the upper troposphere (Kondo *et al.*, 1996).

Relatively low median NO and NO_x volume mixing ratios close to the surface in the NOLTN, the LTN1, and the LTN2 run are consistent with observations over the remote tropical Pacific (see Staudt *et al.*, 2003), and with observations during flights in very clean air masses off the coasts of Japan and China during PEM-West A (Kondo *et al.*, 1996), while Crawford *et al.* (1997b) reported slightly higher mixing ratios for the remote tropical component of PEM-West B. Considering the mainly westerly low level wind during the TOGA COARE case studied here, one could argue that the "high NO_x regime" during PEM-West B is best suited for comparisons. On the other hand, TOGA COARE was located slightly more remote than most flights during PEM-West B, which were mainly conducted northwest of the TOGA COARE region, and the chemical lifetime of NO_x near the surface is short. Furthermore, the seasonally averaged emissions by South East Asian biomass burning (Kondo *et al.*, 2004b) and the seasonally averaged NO_x production due to coastal lightning at the nearby Papua New Guinean coast (Orville *et al.*, 1997) are lower in December than in February and March, when PEM-West B was conducted.

Crawford *et al.* (1997b) attributed elevated NO and NO_x mixing ratios observed above 6 km during their "high NO_x regime" to lightning over land and subsequent transport, while for their "low NO_x regime" the NO mixing ratios were nearly independent of height and the NO_x mixing ratios decreased with height. A decrease of NO_x mixing ratios with height was also calculated in the NOLTN run (Fig. 8.3) and is consistent with the NO_x boundary values from MATCH-MPIC (Fig. 7.6b). In the runs including lightning NO_x production, the upper tropospheric median mixing ratios are considerably lower than the corresponding average values because lightning is highly intermittent (e.g. Figs. 8.1, 8.6), and because horizontal mixing is not efficient enough to completely mix the air during the time it takes to be advected across the domain, which is illustrated in Fig. 8.4. Close to the tropopause, a thin layer with low median values and high average values exists since flashes reach this altitude only on a few occasions while the flash rates during these occasions are, however, very high (compare next section, Fig. 8.6). The air masses sampled during the "high NO_x regime" discussed in Crawford *et al.* (1997b), on the other hand, had presumably been more chemically aged and had undergone some dilution during transport. Comparing the median NO_x mixing ratios calculated for the "high NO_x

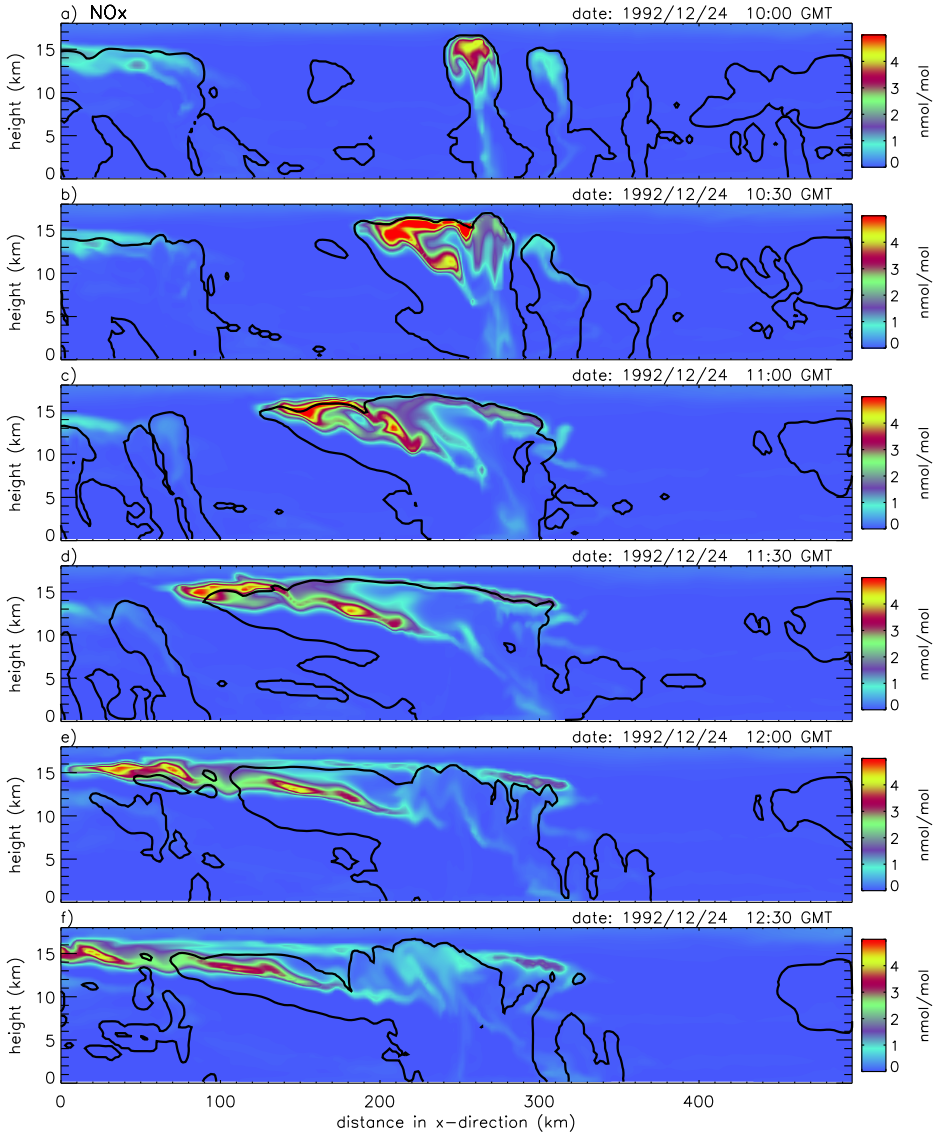

Figure 8.4: Volume mixing ratios of NO_x and $q_{totm} < 0.01 \text{g kg}^{-1}$ contour during the development of a multicell storm from 24 December 1992, 10:00 GMT to 24 December 1992, 12:30 GMT from the LTN1 run.

regime" to the median NO_x mixing ratios calculated for the lightning sensitivity runs in Fig. 8.3 supports the idea that in-situ lightning over the ocean did not account for the elevated NO_x mixing ratios reported by Crawford *et al.* (1997b), and that these may instead have been caused by more frequent lightning over land and by subsequent transport.

Wang and Prinn (2000), who performed 30 h, 2-D simulations of a storm during CEPEX using a domain length of 1000 km calculated about 3 times as many flashes per day per km domain length (producing about 3 times as much NO per km per day) in their LTN and LTNH runs compared to the LTNWP and the LTNHWP

runs. The column integrated amount of NO_x after 30 h in the study by Wang and Prinn (2000) is roughly estimated to be between about 4–6 times as high as the average column integrated amount of NO_x in the LTNWP and the LTNHWP runs (estimated using air densities from TOGA COARE and the NO_x the profiles presented in their Fig. 11 and reproduced in Fig. 8.3a). A part of this difference is due to Wang and Prinn (2000) using periodic boundary conditions, and in part due to different chemical loss rates (see the end of Section 8.4). Not considering non-linearities in the NO_x chemistry, one could argue that the differences in total NO_x mass due to the different flash rates are larger than those due to the different boundary conditions, in the sense that they are larger than the changes one would expect if the runs by Wang and Prinn (2000) were to be repeated using specified boundary conditions instead of periodic boundary conditions. Note that Wang and Prinn (2000) calculated large increases of NO_x due to lightning above the height of the "chemical tropopause" as indicated by the steep increase in ozone at about 15 km in their Fig. 11.

8.4 The NO_x Budget

In the following, budgets are analyzed which were calculated from the tendency terms on the right hand side of Equation(s) 2.1. Height dependent contributions to the budgets are defined for each tendency as the time integrated horizontal domain averages:

$$proc_i\left(z, t_0, \Delta t_{bud}\right) = \frac{1}{L}\int_0^L \int_{t_0-\Delta t_{bud}}^{t_0} \partial_t C_{i,g}\left(x, z, t\right)|_{proc}\, dt\, dx, \tag{8.1}$$

where L is the length of the domain and Δt_{bud} is a time interval starting from an initial time t_0. $C_{i,g}$ is the gas phase concentration (partial density) of the trace gas with the index i. The term on the left hand side of Eq. 8.1 has often been divided by a time averaged air density in order to express it in mixing ratio units. In addition to the "height resolved" term in Eq. 8.1, the corresponding height integrated budget term is analyzed for layers between z_1 and z_2:

$$proc_i\left(t_0, \Delta t_{bud}\right) = \frac{1}{L}\int_{z_1}^{z_2} \int_0^L \int_{t_0-\Delta t_{bud}}^{t_0} \partial_t C_{i,g}\left(x, z, t\right)|_{proc}\, dt\, dx\, dz. \tag{8.2}$$

Two terms for the horizontal advection $\partial_t C_{i,g}|_{hadv} = -\nabla \cdot (\mathbf{v}_h C_{i,g})$ and the vertical advection $\partial_t C_{i,g}|_{vadv} = -\partial_z\left(w C_{i,g}\right)$ (where $\mathbf{v}_h = (u, v)$ is the horizontal wind vector) are considered. All other terms are referred to by the subscripts in Eq. 2.1. The chemistry terms represent net contributions, i.e. the differences between formation and loss terms.

In Fig. 8.5a, the domain and time averaged NO_x mixing ratio profile, the profile $\pm$ the standard deviation, the domain averaged initial profile, and the domain averaged final profile at the end of the simulation after seven days are plotted for the LTN1

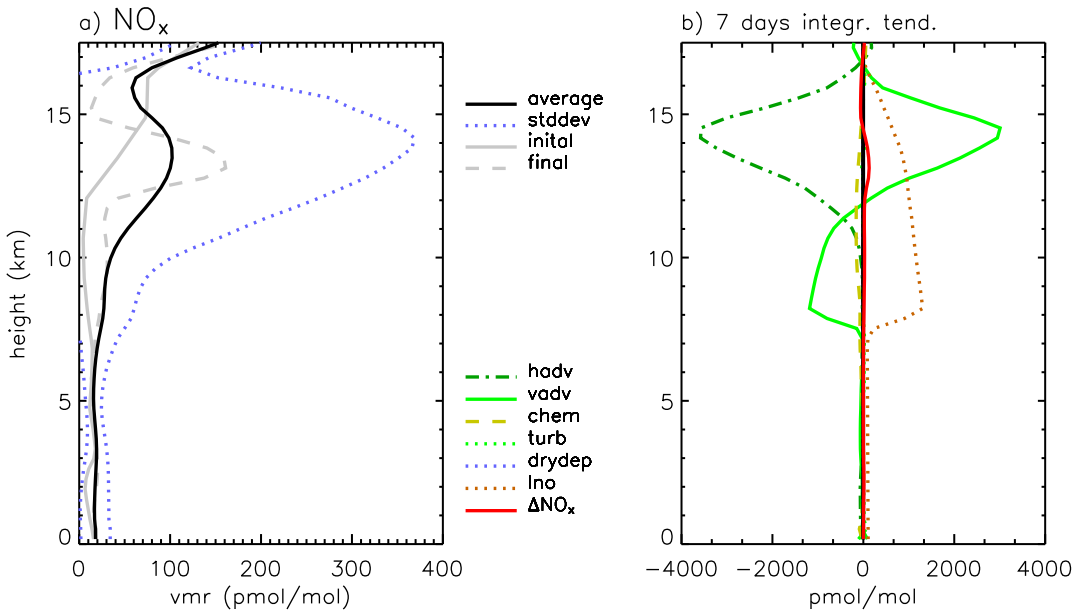

Figure 8.5: Results from the LTN1 run: **(a)** Time and domain averaged NO_x mixing ratio, averaged NO_x mixing ratio ± standard deviation, initial, and final NO_x mixing ratio profiles. **(b)** Budget terms (time integrated and domain averaged tendencies divided by the average air density, see Eq. 8.1) and the difference between the initial and the final profile (red line).

run. The time integrated domain averaged tendencies are plotted in Fig. 8.5b. The difference between the initial and the final profile (ΔNO_x) is also indicated. The first thing to note is that the sum of the tendency terms in each layer tend to balance each other, so that the ΔNO_x term is comparatively small. On the whole the largest terms contributing to the NO_x budget in this run are the production of NO due to lightning, the horizontal advection, and the vertical advection.

In the LTN1 run most lightning NO is produced in the upper half of the troposphere as a consequence of the high calculated IC/CG ratio ($z = 9.9$) and the assumption that IC flashes produce half as many molecules of NO per flash as CG flashes (Section 2.6). The vertical advection term is negative in the layer from about 7 km to about 12 km, where it changes sign. This is interpreted as the consequence of convective upwards transport of lightning NO_x from the 7–12 km layer (in which the lightning NO_x production is large) to the uppermost troposphere above ∼12 km where the negative contribution from horizontal transport across the domain boundaries is large (discussed below). On the other hand, very little NO_x reaches the lowest kilometer of the atmosphere, a region where detrainment from deep cloud downdrafts can be expected. This result is consistent with a result by Pickering *et al.* (1993) from a CRM study of a single storm during TOGA COARE. Pickering *et al.* found only about 7.5% of the lightning produced N mass in the lowest km be-

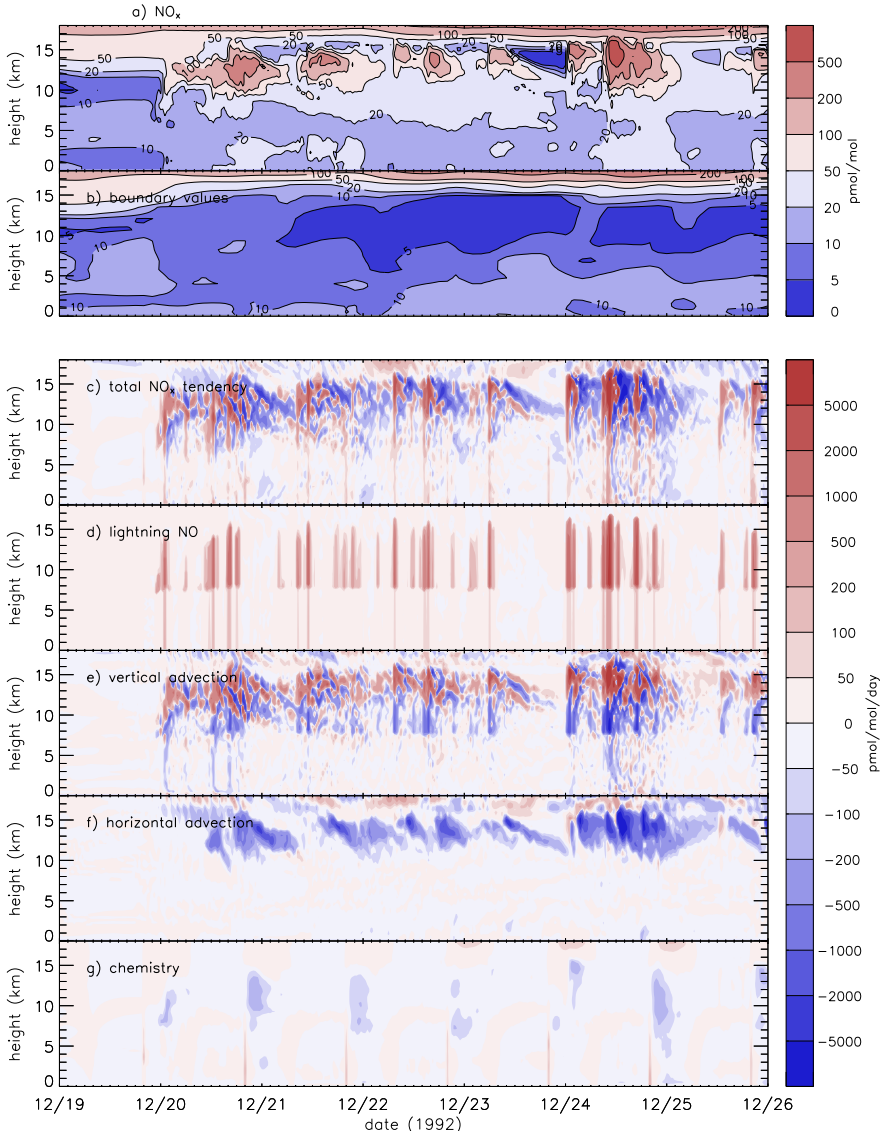

Figure 8.6: **(a)** Time series of domain averaged NO_x volume mixing ratios for the LTN1 run. **(b)** Boundary values. **(c)**–**(g)** NO_x budget terms as defined in the text.

cause of the very weak downdrafts in their simulated storm. In mid-latitude storms they found considerably higher fractions. In the CRCTM, the downwards transport could be underestimated because lightning produced NO is assumed to be emitted into and around the maximum updrafts.

The vertical advection and the lightning NO_x production in Fig. 8.5b are roughly balanced by the horizontal advection above 12 km. Negative contributions by the horizontal advection in the upper troposphere indicate that more NO_x is transported across the lateral domain boundaries out of the domain than flows into the domain reflecting the net source of NO_x inside the domain. For a reactive trace gas, the magnitude of the net import or export depends on the boundary values (amongst other factors). Higher boundary values could lead to increased net chemical loss. In the absence of a source this loss would lead to net import (i.e. a negative flux

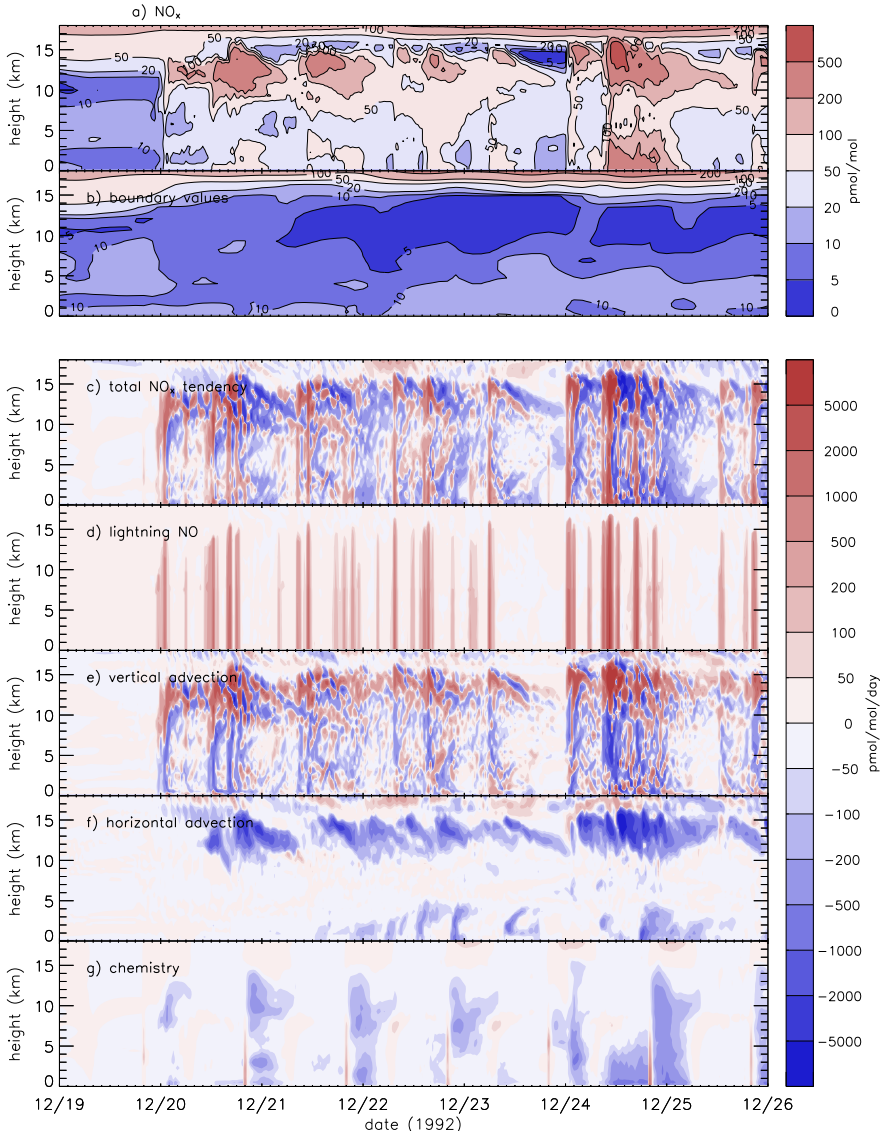

Figure 8.7: Same as Fig. 8.6 for the LTNWP run.

divergence), while a source could act to balance this import, in which case the net horizontal advection term would vanish (at a given horizontal layer if the influence of the vertical transport is neglected). On the other hand, smaller boundary values can lead to increased export of a gas with a source and a net chemical sink inside the domain. Because lightning causes lower NO_x mixing ratios in MATCH-MPIC than the peak mixing ratios in the CRCTM lightning runs and because the data from MATCH-MPIC was used to calculate the chemical boundary values for the CRCTM, the export of NO_x from the model domain could be slightly overestimated. However, the upper tropospheric chemical lifetime of NO_x is in general long enough for considerable export of lightning NO_x from the 500 km domain to occur. Lightning NO_x in the LTN1 run is on the whole transported upwards (from below about 12 km) and then transported out of the domain, or it is directly transported out of the domain at high altitudes (above ∼12 km) in agreement with what the NO_x contour

plot in Fig. 8.4 suggests. The net contribution of the gas phase chemistry to the NO_x budget is small compared to that of lightning NO_x production in the upper half of the troposphere. In the lower troposphere, on average net photochemical loss takes place in the LTN1 run (see Table 8.4). The hypothetical export of NO_x from the model domain in the troposphere would lead to increased upper level NO_x mixing ratios and increased ozone formation downstream of the domain. In the present model study, only the sensitivity to changes inside the domain can be investigated.

The temporal evolution of the domain averaged NO_x mixing ratios for the LTN1 run is shown in Fig. 8.6a. Fig. 8.6b shows the lateral boundary values from MATCH-MPIC. The budget terms depicted in Fig. 8.6d–g were defined in Equation 8.1 and are calculated for each output time t_0 for the output timestep (interval between two output times) $\Delta t_{bud} = \Delta t_{output}$=30 min. The unit was converted to pmol mol^{-1} day^{-1}. The total rate of change in Fig. 8.6c was calculated at each output time-step by dividing the difference between the averaged mixing ratios at this time-step and at the previous time-step by Δt_{output}=30 min. Fig. 8.6 can be compared to Fig. 8.7 showing results from the LTNWP run. The dates are as usual indicated in GMT and local "solar" time is GMT plus 10.5 h. In Fig. 8.7g large negative net chemical tendencies are found in the lower troposphere during nighttime on December 24 related to high lightning NO production. These large chemical nighttime losses of NO_x in the LTNWP run coincide with a temporary decrease of near surface domain minimum ozone mixing ratios in this run (see Section 9.8), indicating that ozone was titrated by NO. The decrease of NO_x during nighttime on 24 December is in line with Wang and Prinn (2000), who found that the reduced UV fluxes inside and below the convective tower and anvils and during the nighttime combine with large conversions of NO to NO_2 and then to N_2O_5 and HNO_3 to produce reductions of both NO_x and O_3, despite the massive production of NO by lightning[2]. The "NO_x tropopause" heights in Figs. 8.6a and 8.7a are determined by both inflow across the lateral boundaries and deep convection.

[2]The loss of lightning NO at night is initiated by the reaction of NO with ozone:

$$O_3 + NO \longrightarrow NO_2 + O_2. \tag{1.9}$$

While during daytime the photolysis of NO_2 together with Eq. 1.9 works towards the equilibrium between NO_2 on the one side and ozone and NO on the other side (compare Section 1.2), this is not the case at night. The most important daytime NO_x loss reaction

$$NO_2 + OH \xrightarrow{M} HNO_3 \tag{1.17}$$

does not play a role either at night, since OH radicals are very short lived (their lifetime is on the order of seconds) and since their production ceases during nighttime. Instead the reaction of NO_2 with O_3 in which nitrate radicals (NO_3) are formed becomes important. Reactions that determine the loss of NO_x during nighttime are:

$$NO_2 + O_3 \longrightarrow NO_3 \qquad \text{(R28 in Table 2.3)}$$

$$NO_3 + NO_2 \xrightarrow{M} N_2O_5 \qquad \text{(R36 in Table 2.3)}$$

followed by the reaction of N_2O_5 (dinitrogen pentoxide) and NO_3 radicals to form HNO_3 on aerosols

Table 8.4: NO_x column densities and height integrated NO_x budget terms as defined in Equation 8.2 for the last six days of the lightning sensitivity runs.

	LT[a]	MT[b]	UT[c]	TC[d]
NOLTN				
av. column density[1]	1.27	0.55	0.42	2.25
vertical advection[2]	-0.12	0.05	0.04	-0.03
horizontal advection[2]	-0.18	-0.04	-0.19	-0.42
chemistry[2]	0.37	-0.04	0.00	0.34
turbulence param.[2]	-0.02	0.02	0.01	0.01
total tendency[2,3]	0.05	-0.01	-0.15	-0.11
LTN1				
av. column density[1]	1.76	1.46	2.99	6.21
lightning NO[2]	1.53	5.25	5.29	12.07
vertical advection[2]	-0.45	-4.31	4.74	-0.02
horizontal advection[2]	-0.68	-0.21	-9.14	-10.03
chemistry[2]	-0.24	-0.71	-0.67	-1.62
turbulence param.[2]	-0.05	0.05	-0.04	-0.04
total tendency[2,3]	0.11	0.06	0.19	0.36
LTN2				
av. column density[1]	1.96	1.22	1.73	4.91
lightning NO[2]	2.32	2.80	2.16	7.28
vertical advection[2]	-0.67	-2.07	2.62	-0.12
horizontal advection[2]	-0.92	-0.18	-4.35	-5.46
chemistry[2]	-0.51	-0.55	-0.38	-1.44
turbulence param.[2]	-0.07	0.06	-0.01	-0.02
total tendency[2,3]	0.13	0.06	0.03	0.21
LTNWP				
av. column density[1]	5.19	3.17	4.29	12.65
lightning NO[2]	16.22	8.45	3.03	27.70
vertical advection[2]	-5.09	-5.26	9.89	-0.46
horizontal advection[2]	-4.24	-0.54	-11.50	-16.27
chemistry[2]	-5.97	-2.60	-1.02	-9.60
turbulence param.[2]	-0.36	0.28	-0.01	-0.10
total tendency[2,3]	0.47	0.28	0.38	1.12

[a] Lower troposphere (LT) defined from surface to about 5 km (4900 m) height.
[b] Mid troposphere (MT), from about 5 km to about 10 km (10150 m).
[c] Upper troposphere (UT), from about 10 km to about 16 km (16100 m).
[d] Tropospheric column (TC), from surface to about 16 km.
[1] Expressed in 10^{14} molecules cm^{-2}. (The tropospheric air column density is about $1.9 \cdot 10^{25}$ molecules cm^{-2}.)
[2] In 10^{14} molecules cm^{-2} day^{-1}.
[3] Diagnosed from the change of column density.

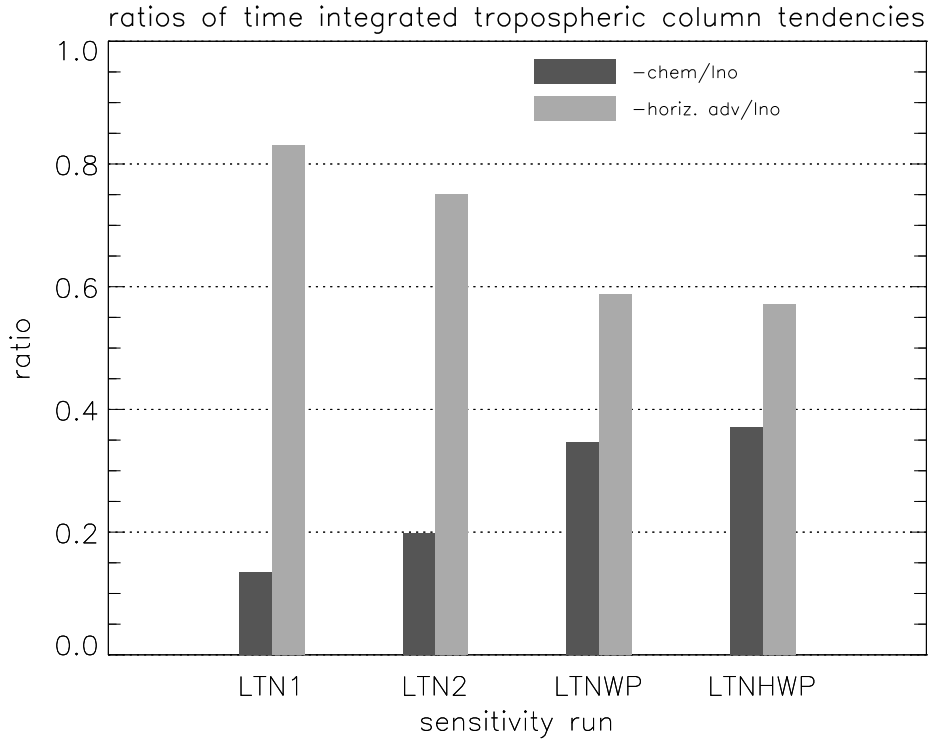

Figure 8.8: Ratios of time integrated tropospheric column NO_x tendencies for the lightning sensitivity runs (calculated from the column densities in Table 8.4).

Table 8.4 shows computed average NO_x column densities as well as time, height, and horizontally integrated NO_x tendency terms for the NOLTN, the LTN1, the LTN2, and the LTNWP run. Here, only the last six days of the model runs were taken into account. The first day was omitted because deep convection in the model did not set in until the end of this day. The troposphere was divided into lower troposphere (LT), mid-troposphere (MT), and upper troposphere (UT), reaching from the surface to ∼5 km, from ∼5 to ∼10 km and from ∼10 to ∼16 km altitude, respectively. The tropospheric column (TC) is defined from the surface to ∼16 km. For the tropospheric column, non-zero vertical advection terms could loosely be interpreted as caused by exchange between the troposphere (as defined by the tropospheric column from the surface to ∼16 km) and the stratosphere. The vertical advection terms integrated over the tropospheric column are negative and small compared to the other terms for all lightning sensitivity runs, which can be interpreted as a small net transport out of the troposphere. A discussion about the exchange between stratosphere and troposphere, taking into account the complexity of the model setup including VLSAT terms, is postponed to Section 9.5.1.

Fig. 8.8 shows the negative of the ratios of the net chemistry budget term and the horizontal advection budget term of NO_x to the lightning NO_x budget term for the lightning sensitivity runs. The fraction of NO_x that is lost via photochemistry[3]

and liquid hydrometeors (R40 in Table 2.3).

[3]Note that high NO_x mixing ratios inside lightning NO_x plumes during daytime result in an

inside the domain increases from the LTN1 run to the LTN2 run, although the total NO_x production in the LTN1 run is about 1.7 times the production in the LTN2 run, as a consequence of more NO_x being produced at lower altitudes in the LTN2 run, where loss processes are more efficient. As lightning NO_x production increases in the LTNWP run, the fraction of NO_x photochemically lost inside the domain increases. This increase is smaller from the LTNWP to the LTNHWP run, which is linked to more NO_x being advected out of the domain before being lost via chemistry. Wang and Prinn (2000) calculated the fraction of NO_x molecules produced by lightning which was chemically lost to decrease with increasing NO_x production from 28% in their LTN run to 12% in their LTNH run. They noticed that in their LTNVH run, the NO_x destruction was HO_x limited. While time and domain averaged upper tropospheric HO_x values decreased in the LTNHWP run compared to the other runs (see Section 10.1), this limitation appears to have played a less important role in the TOGA COARE simulations, presumably because average NO_x concentrations in the TOGA COARE lightning runs were lower. In continental deep convection, where lightning is more frequent, higher NO_x concentrations and different ratios of net chemical loss to lightning NO_x production can be expected. The loss of lightning produced NO_x in the vicinity of convective storms is difficult to represent in global models. It may, however, play a role for estimates of the global impacts of lightning produced NO_x, although other uncertainties in the estimates of the NO_x formation caused by lightning are also large. The possible influences of a shortened lifetime of NO_x on scales which are not resolved by global models has been discussed e.g. in association with ship plumes (Kasibhatla *et al.*, 2000; Davis *et al.*, 2001b; von Glasow *et al.*, 2003; Chen *et al.*, 2005). The lifetime of NO_x close to very localized sources such as lightning is not only expected to depend on the altitude of the source, but also on the abundance of hydrocarbons in the environment (e.g. Ryerson *et al.*, 2001), which are generally present at low concentrations over the Pacific Warm Pool outside the main outflow from Asia.

8.5 Other Reactive Nitrogen Compounds

This section focuses on peroxyacetyl nitrate (PAN, $CH_3C(O)O_2NO_2$), nitric acid (HNO_3), and pernitric acid (HNO_4). The budgets of these compounds and their role for NO_x in the TOGA COARE simulations are discussed. A part of the discussion again focuses on net chemistry terms in the budget. Modeled average and median volume mixing ratios of PAN, HNO_3, and HNO_4 are plotted in Fig. 8.9. Only the

increase of gross OH production and a shortened photochemical lifetime of NO_x, primarily due to the reaction of NO_2 with OH in which HNO_3 is formed. Higher NO levels increase the probability of HO_x cycling via the oxidation of NO by HO_2 radicals in Reaction 1.11 instead of via the reaction of ozone with HO_2 (Reaction 1.6). In both reactions OH radicals are formed, but the first pathway leads to an amplification of the OH production via the formation of ozone and the subsequent photolysis in the presence of water vapor, while the second pathway leads to a loss of ozone and a decrease in OH production (compare introduction in Section 1.2). Extremely high NO_x concentrations can lead to a depletion of HO_x and an anti-correlation between HO_x and NO_x concentrations (see Section 10.1).

non-dissolved gas phase HNO_3 is plotted.

8.5.1 Peroxyacetyl Nitrate (PAN)

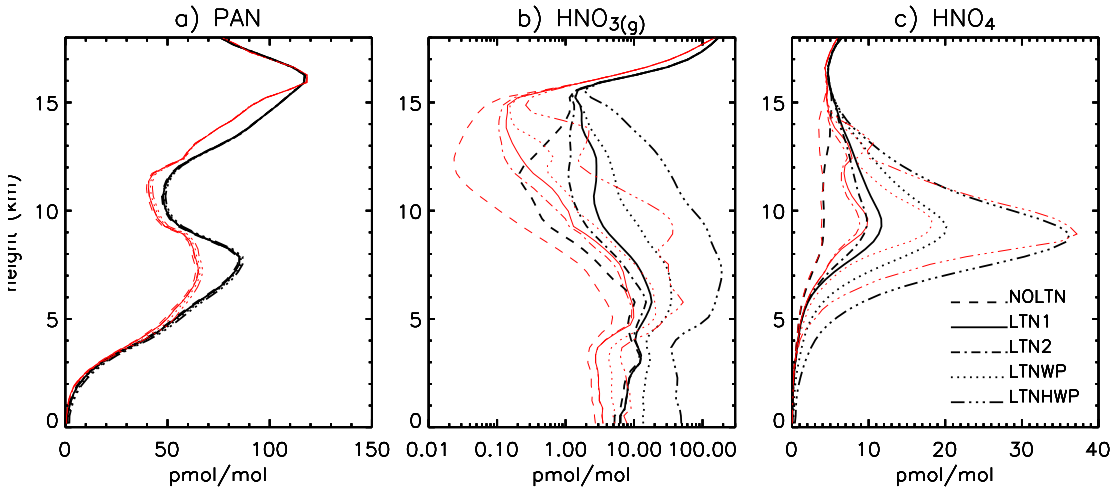

Figure 8.9: Domain and 7-day time averaged volume mixing ratios (black lines) and day-time median values (red lines) for the lightning sensitivity runs: **(a)** PAN, **(b)** non-dissolved gas phase HNO_3, and **(c)** HNO_4. Only mixing ratios for SZA<70° were used.

PAN is thermally unstable: at high temperatures it decomposes rapidly to form NO_2 and the peroxyacetyl radical ($CH_3C(O)O_2$) through R59 (see Table 2.3). The lifetime of PAN increases rapidly with height from a few hours at warm surface air temperatures to about a month in the upper troposphere. Kondo *et al.* (1997) found large differences in PAN levels observed during PEM-West B depending on air mass origin. The median volume mixing ratios in maritime tropical air (defined as originating south of 15 °N) were 0.5, 2.0, 40.1, and 38.8 pmol mol^{-1} for observations from the surface to 1 km, from 1 to 4 km, from 4 to 7 km, and from 7 to 12 km altitude, respectively. The median volume mixing ratios in maritime western Pacific air (originating between 15 °N and 40,°N) were 2.4, 3.8, 64.1, and 58.1 pmol mol^{-1} for observations from the surface to 1 km, from 1 to 4 km, from 4 to 7 km, and from 7 to 12 km altitude, respectively. The median values in continental air decreased with height from 280.9 pmol mol^{-1} between the surface and 1 km to 100.8 pmol mol^{-1} between 7 and 12 km altitude. The values in Fig. 8.9 are somewhat higher than the values for maritime tropical air reported by Kondo *et al.*. On the one hand this is in line with the TOGA COARE region having been influenced by cross-equatorial transport. On the other hand, PAN is generally over-predicted by MATCH-MPIC (von Kuhlmann *et al.*, 2003b), possibly resulting in elevated boundary values for the CRCTM.

PAN is formed from NO_2 and the peroxyacetyl radical in the reverse reaction of R59, which is reaction R50. The peroxyacetyl radical is also formed from ac-

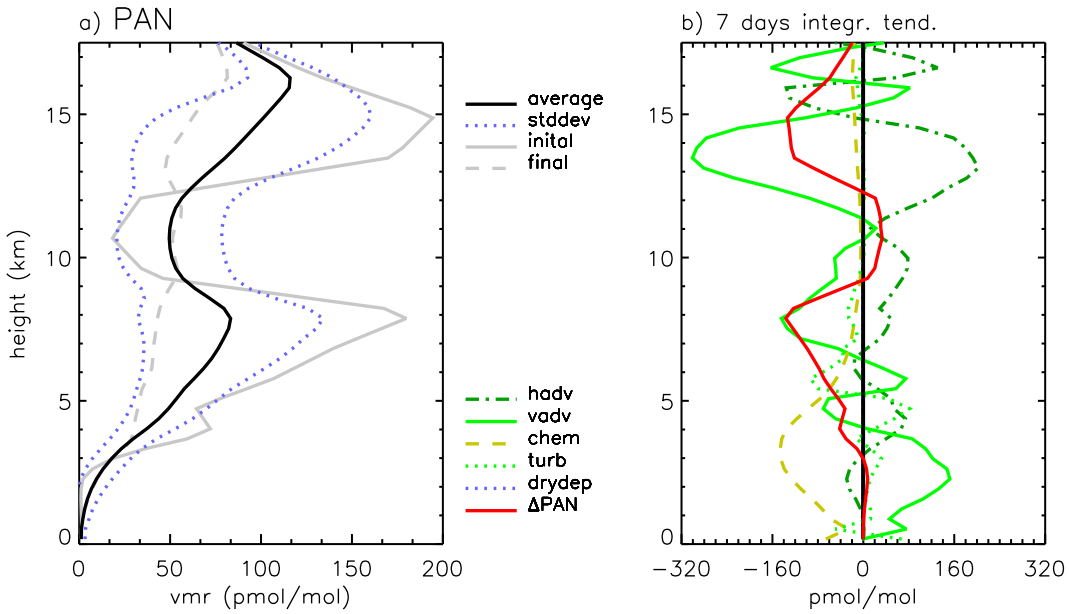

Figure 8.10: As Fig 8.5 for PAN.

etaldehyde (CH_3CHO), acetone (CH_3COCH_3) and biacetyl ($CH_3COCOCH_3$), all of which are produced by the oxidation of NMHCs (Singh and Hanst, 1981; Kasting and Singh, 1986). In the CRCTM, only acetone is considered as a direct precursor for the peroxyacetyl radical (R61). Consequently, the gross in-situ formation of PAN may be underestimated in the CRCTM and the net loss may be overestimated. Staudt *et al.* (2003) argued that the conventional view regarding the importance of PAN as a precursor for NO_x in the remote troposphere may be challenged in the light of large model underestimates of the abundances of acetaldehyde and of acetone. Acetaldehyde was measured in considerable amounts during the PEM-Tropics B campaign (Singh *et al.*, 1996), but the sources are not yet well quantified. Acetone will briefly be discussed in Section 10.5. Large net PAN formation generally takes place close to the continental sources of precursor gases. Here, the focus is on processes leading to a net loss of PAN. The domain integrated volume mixing ratios of PAN in Fig. 8.9 are largely insensitive to the changes in lightning NO_x production and the associated changes in OH concentrations, which are discussed in Section 10.1. Height dependent budget terms for PAN from the LTN1 run are plotted in Fig 8.10b. In the UT and the MT, horizontal advection is an important source of PAN, from where it is on average transported downwards towards the lower troposphere. The maximum net chemical loss occurs around 3 km. Close to the surface, the lifetime is too short for large horizontal transport to occur.

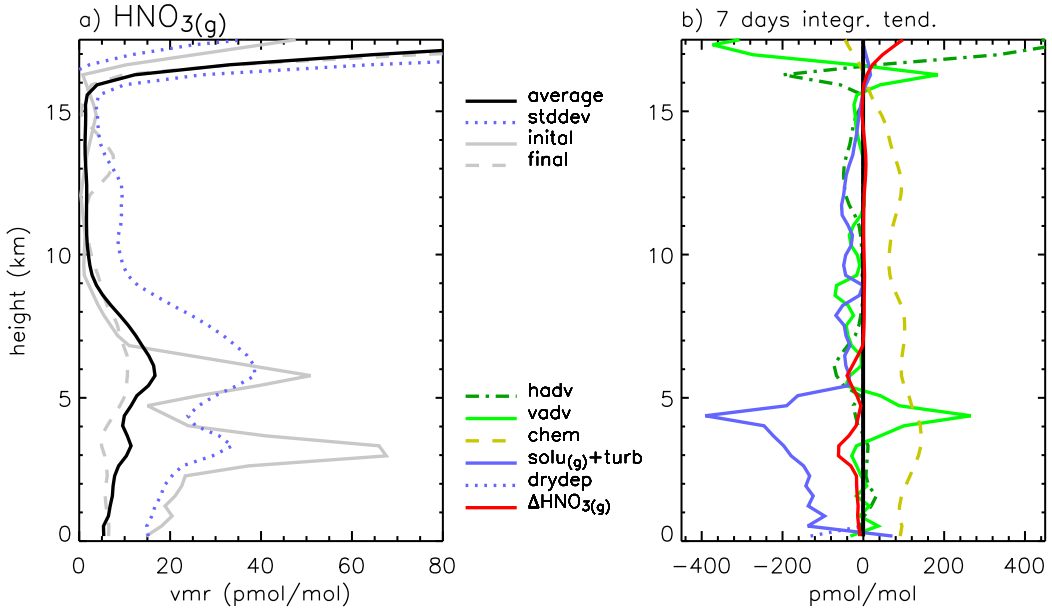

Figure 8.11: As Fig. 8.5 for HNO_3. The subscript g indicates that only results for HNO_3 in the gas phase are plotted.

8.5.2 Nitric Acid (HNO_3)

While PAN is generally over-predicted in MATCH-MPIC, HNO_3 is often underestimated (von Kuhlmann *et al.*, 2003b). The HNO_3 values in Fig. 8.9b are also very low compared to values by Kondo *et al.* (1997), independent of assumptions regarding lightning (except for the LTNHWP run). In tropical air masses Kondo *et al.* derived volume mixing ratios of 81.5, 107.0, 85.0 and 54.0 pmol mol^{-1} from the surface to 1 km, from 1 to 4 km, from 4 to 7 km, and from 7 to 12 km altitude, respectively. Because of the time it takes to form HNO_3 from NO_2 and OH, Chameides *et al.* (1987a) argued that one would not expect NO production by lightning to result in immediate nitrate (NO_3^-) enhancements in the rainwater collected during the same storm. This is in line with the finding that most NO_x in the lightning runs was transported out of the domain. However, some HNO_3 was formed inside the 500 km 2-D domain (see also Section 11.1). The very low values of HNO_3 in the CRCTM runs compared to observations were largely 'inherited' from the initial and boundary conditions. In the NOLTN run, the in-situ production of HNO_3 was limited by relatively low NO_x values.

The reaction of NO_2 with OH to form HNO_3 (R29) and subsequent scavenging of HNO_3 is a major sink of NO_x in the troposphere. Fig. 8.11b shows budget terms for HNO_3 in the gas phase ($HNO_{3(g)}$) from the LTN run. Subsequently, the subscript "g" for gas phase will usually be omitted. Unless otherwise noted, "HNO_3" always refers to gas phase HNO_3, not including HNO_3 which is dissolved or taken up by ice.

The same convention will be used for other soluble trace gases. The budget term for the exchange between gas phase and hydrometeors in the liquid or ice phase ("$solu_g$") and the budget term for the parameterized turbulence ("turb") were combined into one term in order to mask out local compensations of these terms, which for example occurred due to a relatively long lived layer of thin clouds which formed during the first day of the TOGA COARE model runs and from which later deep convection developed. This aspect will be discussed in some detail later in this section.

Net chemical production of HNO_3 was calculated to occur throughout the troposphere. HNO_3 production in the upper troposphere was favored by most lightning NO_x in the LTN1 run being produced in the upper half of the troposphere, while in the lower troposphere, HNO_3 formation is efficient due to high OH concentrations. On average, however, very little HNO_3 was calculated to exist in the upper troposphere, both in the CRCTM and in MATCH-MPIC (compare initial profile in Fig. 8.11). Above about 5.5 km, the net chemical production in Fig. 8.11b was largely balanced by combined scavenging/turbulence including uptake on ice, by vertical advection, and by net horizontal advection out of the domain. Below about 5.5 km, HNO_3 was efficiently scavenged by rain (compare detailed discussion in Section 10.2 regarding the scavenging of CH_3OOH). Some HNO_3 in the gas phase was vertically advected to a layer below 5.5 km, where the HNO_3 sink due to scavenging was large (compare also Fig. 11.1). The efficiency of scavenging could possibly be over-estimated in 2-D simulations, since in a 2-D model setup, very localized areas of strong precipitation associated with very active cells can travel across much of the domain. These areas of strong precipitation can be associated with systems moving relative to the wind direction at low levels in the opposite direction (compare Hovmöller diagrams in Fig. 3.6). In 3-D domains, on the other hand, the small areas of strong precipitation would only traverse a much smaller area fraction of the entire domain and encounter a smaller fraction of the air advected through the domain while moving relative to the average wind. In the future, 3-D runs will be needed to explore this possibility (compare Chapter 13).

The calculated domain averaged mixing ratio of HNO_3 in the lower troposphere varied enormously between different days of the simulation (both in MATCH-MPIC and in the CRCTM, not shown), in association with a large temporal variability of the horizontal advection term. However, the time averaged horizontal advection term is generally small compared to the other terms of the budget. Furthermore, the amount of HNO_3 dissolved in water or taken up by ice which was advected across the lateral boundary conditions was found to be negligibly small compared to the gas phase budget terms (not shown). Some details regarding the scavenging of HNO_3 will be examined in Section 11.1. Results from a sensitivity study examining the uptake of HNO_3 on ice will be presented in Section 11.2 .

The stratiform cloud layer which formed during the first day of the simulation caused large vertical gradients of the HNO_3 volume mixing ratios and of the volume mixing ratios of dissolved HNO_3. The large local compensations between the "$solu_g$" and the "turb" term can be explained as follows: Parameterized turbulence acts to smooth out the vertical gradient of dissolved HNO_3 and the vertical gradient of the

cloud water (or ice) mixing ratio. When the cloud water evaporates in the undersaturated air above the cloud top, the dissolved HNO_3 is assumed to be released to the gas phase. Again, parameterized turbulence acts to smooth out the resulting gas phase HNO_3 gradient, mixing it back to where it can be taken up by cloudmeteors. The result of this interaction is large local compensations between parameterized turbulence tendencies and uptake/release tendencies. A similar effect also occurs at the upper boundary of the region where rain forms (compare Fig. 11.1). Combining the tendencies for these two processes has the advantage of masking out these compensating effects. A disadvantage of combining these tendencies is that effects of the release of dissolved trace gases from evaporating hydrometeors and effects of the release of dissolved trace gases which could occur in cloud updrafts already at the freezing level at about 5 km altitude could be masked out. However, since homogeneous nucleation was assumed below -40°C, liquid water still existed between ∼5 km and ∼10 km (Fig. 3.7), causing rejection to play an important role at around 10 km altitude for gases (other than HNO_3) for which rejection (e.g. $k_{ret} = 0.2$) was assumed (compare Sections 10.4, 10.3). The uptake of HNO_3 on cloud ice particles and snow was treated as a reversible process, thus in principle allowing the (unrealistic) rejection of HNO_3 from the ice phase after freezing in spite of the retention coefficient being set to one. Inspecting contour plots from individual storms (compare Section 11.1), it appears that rejection at the freezing level at about 5 km altitude did not play an important role in the case of HNO_3. For some of the other trace gases with lower Henry's law constants, the tendencies were not combined (compare e.g. Section 10.2). While it is believed that the large compensating tendencies do not have large net effects, this compensation complicates the analysis of the role of other processes, especially those occurring at about 5 km height, such as the effect of the possible rejection of gases (especially those with lower Henry's law constants) from the ice phase already at that altitude. This subject will be further discussed in Section 10.2.

A sensitivity run was conducted in which the hydrolysis reaction of N_2O_5 was omitted. The horizontally domain and time averaged mixing ratios of HNO_3 (not shown) did not change considerably compared to the profile in Fig. 8.11a. The contributions from photochemistry and from scavenging to the HNO_3 budget in the lower troposphere were, however, considerably smaller in magnitude in the sensitivity run. The effect of decreased net photochemical HNO_3 formation in the sensitivity run was balanced by decreased scavenging in that run.

8.5.3 Pernitric Acid (HNO_4)

HNO_4 is thermally quite unstable in the lower troposphere, and therefore appreciable amounts are only calculated in the upper troposphere (von Kuhlmann, 2001). Fig. 8.12 shows considerable net formation of HNO_4 in the UT. A simple formulation of the photodissociation of HNO_4 in the near infrared, R63, was included in the chemistry runs. In a sensitivity run not including R63, the net formation of HNO_4 was somewhat larger. Net HNO_4 formation in the tropical UT is in line with results

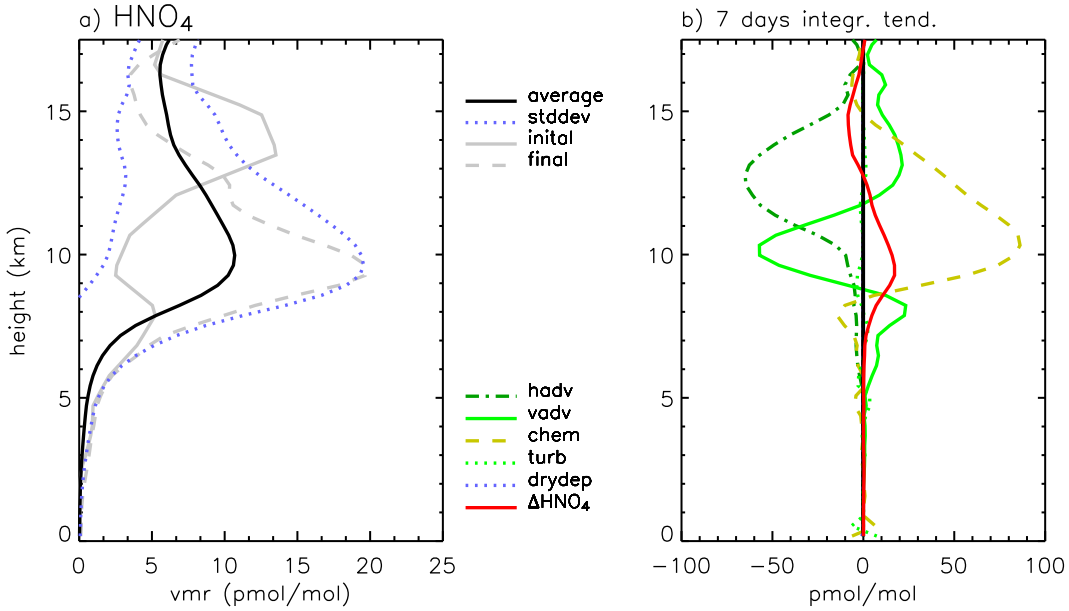

Figure 8.12: As Fig. 8.5 for HNO_4.

by von Kuhlmann (2001). It could, however, be overestimated in the CRCTM due to the lack of PAN precursors discussed above.

8.5.4 Photochemical Budget of Nitrogen Compounds

The net chemistry budget terms for PAN, HNO_3, HNO_4, and NO_x for the last six days of the lightning sensitivity runs are shown in Table 8.5. In the lower troposphere, for the NOLTN run the loss of PAN largely balanced the source terms of NO_x and HNO_3, which is in line with Wang *et al.* (2001), who used their model to study the effects of deep convection during PEM-Tropics B. They found that in the lower troposphere, the thermal decomposition of PAN transported by subsidence provided the necessary NO_x source to account for scavenging and deposition of HNO_3. Wang and Prinn (2000) did not include PAN in their cloud resolving model study , and found that in a run in which they did not assume lightning NO production, gas phase chemistry acted to remove more than 30% of the total NO_x mass within 30 h. During the 7–day TOGA COARE simulation, on the other hand, the total tropospheric NO_x column density changed by only ∼5% (Table 8.4), mainly due to the decomposition of PAN which was horizontally advected into the model domain (compare Section 8.5.1).

The magnitude of the lower tropospheric net formation of HNO_3 was similar in all four runs, except for the LTNWP run, where it was much larger reflecting the influence of more lightning produced NO_x. In the upper troposphere, the net chemistry term for PAN was small and negative for all four runs in Table 8.5. At high

Table 8.5: Height integrated net chemical budget terms as defined in Eq. 8.2 for the last six days of different lightning sensitivity runs.

	LT[a]	MT[a]	UT[a]	ET[a]
NOLTN				
NO_x	0.37	-0.04	0.00	0.34
PAN	-1.52	-0.27	-0.06	-1.85
HNO_3	1.12	0.33	0.02	1.46
HNO_4	-0.01	-0.02	0.04	0.01
LTN1				
NO_x	-0.24	-0.71	-0.67	-1.62
PAN	-1.45	-0.22	-0.04	-1.71
HNO_3	1.61	0.85	0.41	2.86
HNO_4	0.00	0.09	0.28	0.36
LTN2				
NO_x	-0.51	-0.55	-0.38	-1.44
PAN	-1.43	-0.23	-0.05	-1.70
HNO_3	1.84	0.70	0.19	2.73
HNO_4	0.00	0.07	0.23	0.30
LTNWP				
NO_x	-5.97	-2.61	-1.02	-9.60
PAN	-1.29	-0.17	-0.04	-1.49
HNO_3	6.9	2.39	0.73	10.04
HNO_4	0.03	0.35	0.28	0.65

[a] same as in Table 8.4.
[1] 10^{14} molecule cm^{-2} day^{-1}.

tropospheric altitudes, both HNO_3 and HNO_4 were calculated to be formed in appreciable net amounts. The lower tropospheric net chemistry term for NO_x changed sign from positive to negative when lightning NO_x production was considered, and the term for the tropospheric column became more negative with increasing lightning NO_x production (note that the lightning NO_x source was larger in the LTN1 run than in the LTN2 run). While a number of uncertainties regarding PAN, HNO_4, and HNO_3 have been discussed, as far as ozone results from the CRCTM TOGA COARE runs are concerned, uncertainties regarding lightning related NO_x are likely more important. It is nevertheless likely that in the future CRCTM studies will help to e.g. better quantify the scavenging of HNO_3 by deep convective clouds.

8.6 The HNO_3/NO_x and the PAN/NO_x Ratio

The ratios of HNO_3 to NO_x and PAN to NO_x are often diagnosed in order to gain some insight about the chemical age and processing of air masses. In global chemistry transport models, the ratio of HNO_3 to NO_x is rather sensitive towards

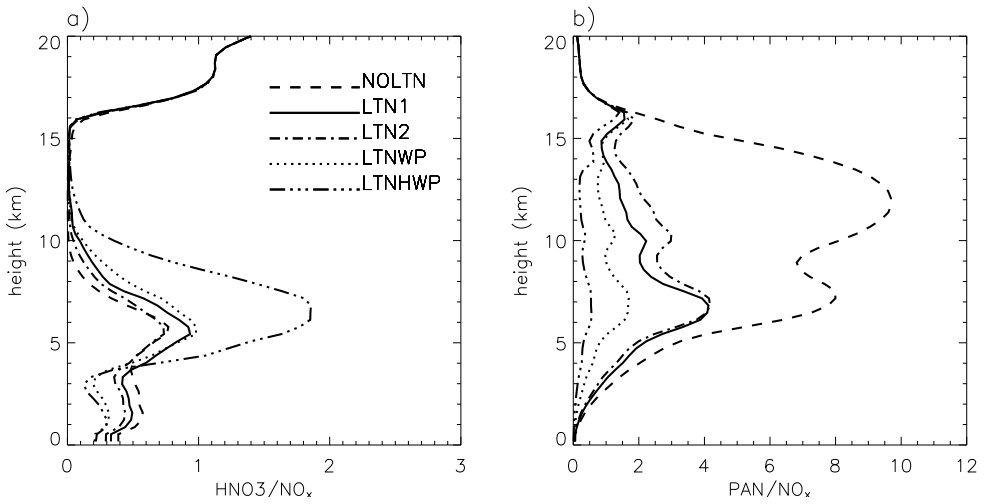

Figure 8.13: Ratios of a) HNO_3 to NO_x and b) PAN to NO_x volume mixing ratios.

the model representation of scavenging (e.g. Staudt *et al.*, 2003). Staudt *et al.* (2003) attributes low observed HNO_3 to NO_x ratios during PEM-Tropics B (in the range from 0.5 to 1.3 between 6 and 12 km altitude and in the range from 4.6 to 8.3 between the surface and 6 km) to NO_x formation by lightning and to frequent convective overturning which depletes HNO_3.

Here the influences of relatively recent lightning NO_x production (within the time span it takes for the trace gases to be advected out of the domain) on the vertical profiles of domain averaged HNO_3 to domain averaged NO_x ratios and on the profiles of domain averaged PAN to domain averaged NO_x ratios are investigated. Fig. 8.13a indicates that the HNO_3 to NO_x ratios are not very sensitive to assumptions about the lightning NO_x source for the NOLTN, the LTN1, and the LTN2 run. A larger sensitivity only occurs in the LTNWP (in the lower troposphere) and in the LTNHWP run in which high or extremely high lightning NO_x production was assumed. The modeled HNO_3 to NO_x ratios in Fig. 8.13a are very low compared to many observations, which is most likely a consequence of the underestimate of HNO_3 in the model. For example, Singh *et al.* (1998) presented averaged values of the HNO_3 to NO_x ratio in the upper troposphere as a function of latitiude based on observations during PEM-West B, which are considerably higher. However, Hauglustaine *et al.* (1996) reports HNO_3 to NO_x ratios below one to have been occasionally observed at the Manua Loa Observatory. Since HNO_3 is considerably depleted by scavenging, deep convective clouds can cause large gradients of HNO_3 in space and time (compare Fig. 11.1).

The ratios of domain averaged PAN to domain averaged NO_x, on the other hand, depend strongly on the assumptions about lightning NO_x production in the 500 km 2-D domain run. This is caused by the long time it takes to form PAN. The result is expected to depend on the availability of PAN precursor gases in the CRCTM. In the upper troposphere, where the lifetime of PAN is long, the simulated ratio of PAN to NO_x in the NOLTN run also strongly depends on the boundary

values. The PAN to NO_x ratios in the NOLTN run are considerably above the the average upper tropospheric ratios inferred from observations at southern latitudes during PEM-West B (Singh *et al.*, 1998). A number of points which could help explain these higher values have previously been discussed. Temporal variability, the slightly more remote location of the TOGA COARE IFA, the over-estimate of PAN in MATCH-MPIC, the underestimate of oceanic lightning rates in MATCH-MPIC (compare Labrador *et al.*, 2005), or an occasional strong influence of NO_x produced by lightning over nearby land-masses during PEM-West B could have contributed.

Chapter 9

Ozone

The tropospheric photochemical lifetime of ozone in the tropics varies between a few days close to the surface and a few weeks at higher altitudes. In some studies of maritime tropical convection, ozone has been suggested as a tracer for deep convection (Kley *et al.*, 1997; Folkins *et al.*, 2002). The relatively short lifetime of ozone in the remote marine tropical boundary layer is due to high water vapor abundances, low NO_x levels, and high photolysis rates (in part caused by the small thickness of the ozone layer above the tropics, e.g. Crutzen *et al.*, 1999). In the next section, the results from the lightning sensitivity studies are discussed. Then the focus will be on the influence of using specified boundary conditions and of horizontal advection across the lateral boundaries of the domain. As expected, the ozone mixing ratios inside the CRCTM domain depend strongly on the initial and boundary values.

9.1 Sensitivity to Lightning NO_x

Fig. 9.1a shows domain and time averaged and median volume mixing ratios for the lightning sensitivity runs. Only values for SZA$<70°$ were used. However, since the modeled ozone mixing ratios do not show a pronounced daily cycle, the values in Fig. 9.1a are largely independent of this choice. The sensitivity of the domain averaged ozone levels to in-situ lightning NO_x production is small and merely the modeled ozone mixing ratios in the mid-troposphere increase moderately with increasing lightning NO_x production, which is also reflected in the net chemistry budget terms in Fig. 9.1b. Wang and Prinn (2000), on the other hand, found slightly decreased domain averaged ozone mixing ratios due to increased lightning at the end of their 30 h lightning NO_x sensitivity runs for a storm during CEPEX (their Fig. 11b). In particular, Wang and Prinn suggested that near zero mixing ratios of O_3 observed during CEPEX had possibly been caused by lightning NO_x production (as discussed in Section 9.8).

The small sensitivity in Fig. 9.1a is caused by a strong influence of horizontal advection on ozone and small to moderate changes in the photochemical budget terms in Fig. 9.1b. In the lower troposphere, the ozone mixing ratios in Fig. 9.1a

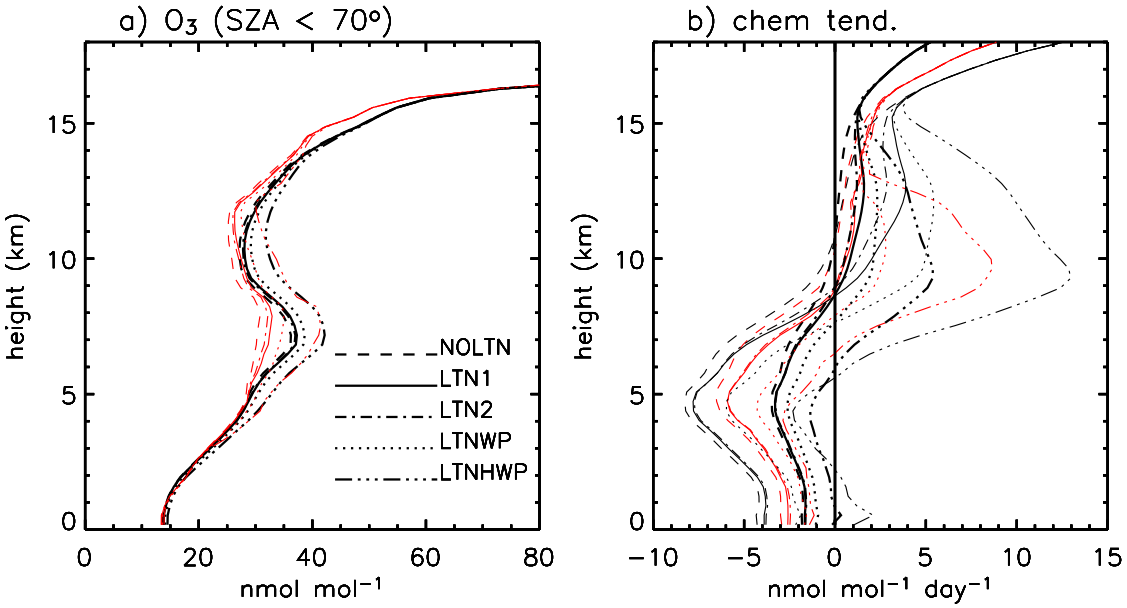

Figure 9.1: Ozone: **(a)** domain and time averaged volume mixing ratio (black lines) and median values (red lines). Only values for SZA<70° were used. **(b)** Domain and time averaged net chemistry tendency for all output times (diurnal averages, thick black lines), for times when SZA<70° (thin black lines), and median values for SZA<70° (thin red lines).

are almost independent of the assumptions about lightning NO_x production, even in the sensitivity runs with large NO_x production by CG flashes. While the average lower tropospheric NO_x volume mixing ratios in the LTNWP and the LTNHWP sensitivity runs were several times as high as in the other runs, the median values varied less strongly, indicating large, but relatively localized (in time and/or space) enhancements. The intermittency of lightning and the lack of complete horizontal mixing of NO_x, which is also apparent in Fig. 8.4, can have important implications for ozone production. The number of ozone molecules produced for each NO_x molecule lost strongly decreases with increasing NO_x mixing ratio (Liu *et al.*, 1987). Consequently, for a constant emission of NO_x, a spatially diffuse source will lead to a significantly greater ozone production than a point source (e.g. Brasseur *et al.*, 1999). The dilution of NO_x due to atmospheric turbulence and (differential) advection on the other hand will enhance the efficiency of O_3 production (Liu *et al.*, 1987; Ryerson *et al.*, 2001). Thus, (oceanic) lightning can act to increase ozone levels over relatively large distances. Pickering *et al.* (1990) found (in agreement with e.g. Crawford *et al.* (1997b) and Kawakami *et al.* (1997)) that outflow from deep convection can cause enhanced ozone production in the upper troposphere hundreds of kilometers downstream from the clouds. In fact, maximum ozone levels are often encountered downwind from strong NO_x sources (compare Section 1.2), while at very high NO_x concentrations close to the sources, ozone mixing ratios are reduced.

In the CRCTM, CG flashes are placed in the columns where the maximum up-

drafts occur, leading to very efficient upwards transport of NO_x. A similar assumption was also made in the CRM study by Wang and Prinn. However, CG flashes can also occur between cloud anvils and the surface and the branches of inter-cloud flashes[1] can stretch over large horizontal distances; i.e. the lightning NO_x source could be more diffuse than currently assumed in the model[2]. Implementing a more realistic flash distribution is unfortunately outside the scope of this thesis, but will be an important step in the future development of the CRCTM. Although the upwards transport of lightning NO_x may be overestimated, some NO_x was horizontally transported out of the domain at low levels in all the runs including lightning NO_x production. One could again argue that this theoretical export would eventually lead to increasing gross ozone formation and decreasing lower tropospheric net ozone loss outside the model domain.

While here the sensitivity of local ozone levels to in-situ lightning NO_x production was found to be small, Crawford *et al.* (1997b) found considerably higher ozone mixing ratios for their high NO_x regime compared to their low NO_x regime in air masses with relatively high NO_x mixing ratios which had been more chemically aged and better mixed. The median ozone mixing ratios for the two different regimes by Crawford *et al.* as well as ozone mixing ratios and photochemical tendencies from a number of other studies including this study are presented in Table 9.1. The ozone mixing ratios from the LTN1 run are between the mixing ratios reported for the high NO_x and the low NO_x regime by Crawford *et al.*, except for in the lowest two kilometers, where they are lower. Kondo *et al.* (1997) also found higher near surface median mixing ratios for tropical marine air masses during PEM-West B. While the NO_x values in the NOLTN run were found to be characteristic of a weak influence of in-situ or upwind NO_x sources, the ozone values in the mid-troposphere are found to be somewhat elevated, which is consistent with medium or long range cross-equatorial transport and a sufficiently long photochemical lifetime of ozone in the mid-troposphere in the upwind regions (compare Section 7.2). Various influences of the initial and boundary values (in Fig 7.6a) are further discussed in Section 9.3.

9.2 Photochemical Tendencies

Fig. 9.1b shows horizontally averaged net chemistry budget terms for ozone from the lightning sensitivity runs. Twenty-four hour averages are plotted as well as average and median values for SZA$<70°$. The net chemistry budget terms exhibit a pronounced daily cycle (Section 9.3) and the values for SZA$<70°$ in Fig. 9.1b are highly sensitive to the choice of this threshold value (not shown). Differences between the median and the average net loss rates also arise because of the daily cycle. The

[1] Inter-cloud flashes (between two clouds) are not considered in the model

[2] This uncertainty is unique to cloud resolving models. In global models, lightning produced NO_x is usually assumed to be instantaneously mixed across an entire grid box at present typically spanning an area of more than 100×100 km. However, due to the small scale nature of flashes resolution remains an issue even in cloud resolving models, albeit to a lesser extent than in global models.

Table 9.1: Tropical Pacific ozone mixing ratios and photochemical net tendencies from selected studies.

Reference	height (km)	ozone $\left(\frac{\text{nmol}}{\text{mol}}\right)$	net tend. $\left(\frac{\text{nmol}}{\text{mol day}}\right)$	% per day[1]
Thompson *et al.* (1993)		*mean*	*diurn. aver.*	–
5°S	near surface	6	-0.5	-8.3
0°	near surface	10	-1.3	-13.0
10°N	near surface	20	-2.3	-11.5
Crawford *et al.* (1997b)		*median*[2]	*diurn. aver.*	
low NO_x	0–1	18.9	-2.00	-11.1
	1–2	19.7	-1.92	-9.7
	2–4	21.5	-2.19	-10.2
	4–6	16.9	-0.90	-5.3
	6–8	17.5	-0.69	-3.9
	8–10	18.9	-0.07	0.04
high NO_x	0–1	25.8	-1.77	-7.0
	1–2	29.4	-2.23	-7.6
	2–4	54.0	-0.11	-0.02
	4–6	50.4	0.35	0.7
	6–8	45.3	0.99	2.2
	8–10	40.1	1.62	4.0
Kondo *et al.* (1997)		*median*[3]		
marine/tropical	0–1	19.0	–	–
	1–4	20.7	–	–
	4–7	15.7	–	–
	7–12	38.6	–	–
Wang and Prinn (2000)		*range*[4]	*range*[5]	
REF	0–5	6–11	0.0 to 0.2	–
LTN	0–5	6–11	-0.2 to -0.5	–
LTNH	0–5	5–9	-1.0 to -2.5	–
		range[6]	*range*[6]	
Mari *et al.* (2003)	0–5	8–24	-0.5 to -3.0	–
this study		*median*[7]	*diurn. aver.*	
LTN1	0–2	15.0	-1.7	-11.2
	2–4	21.6	-2.5	-11.4
	4–6	28.5	-3.1	-10.9
	6–8	32.1	-1.7	-5.6
	8–10	29.5	0.3	0.9
	10–14	29.6	1.4	4.7

[1] Estimates are based on daytime median or mean ozone mixing ratio and diurnal averaged tendency, and are merely indicated to facilitate comparisons.
[2] For SZA<70°.
[3] For SZA<60°.
[4] Estimated from Fig. 9 of Wang and Prinn (2000) for a 30 h simulation.
[5] Mixing ratio at the end of a 30 h simulation. Estimated from Fig. 11 of Wang and Prinn (2000).
[6] Estimated from Fig. 13 of Mari *et al.* (2003) for 9:30 to 17:15 local solar time.
[7] Vertically averaged median mixing ratios for SZA<70° from Fig. 9.1.

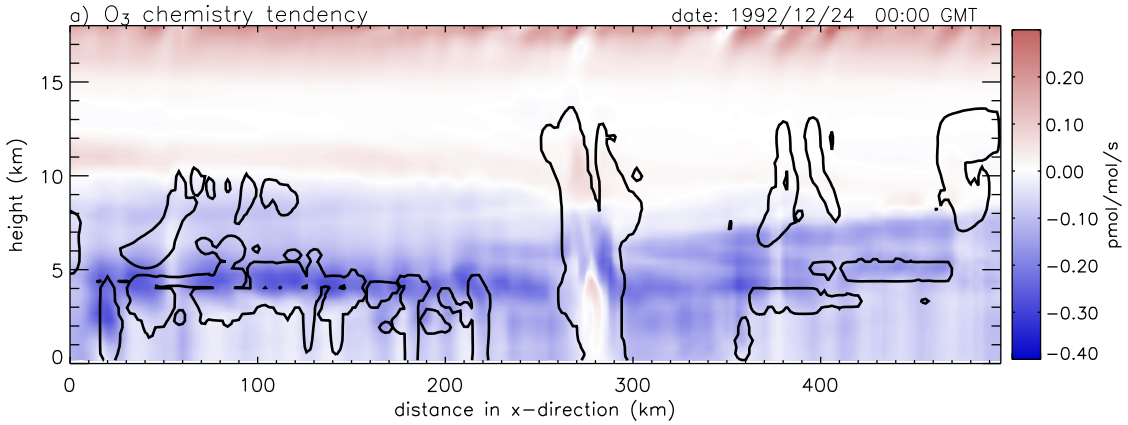

Figure 9.2: Gridded net chemistry tendencies for ozone from the LTN1 run: time average calculated for 30 min time integral from 23 December 1992, 23:30 GMT to 24 December 1992, 24:00 GMT and instantaneous cloudmeteor mixing ratio contour ($q_{totm} < 0.01\,\mathrm{g\,kg^{-1}}$) for 24 December 1992, 24:00 GMT.

signs of the net chemistry term for the NOLTN run changes from net loss below about 10 km altitude to net formation above, where small net formation takes place (diurnal averages below 1 nmol $\mathrm{mol^{-1}\ day^{-1}}$). In the LTN1 and the LTN2 run the sign changes at about 8 km height. Lower tropospheric photochemical net ozone loss was found to occur in a number of studies for the tropical Pacific (see Table 9.1). Thompson *et al.* (1993) reported diurnal net ozone loss rates near the surface based on results from a 1-D numerical model and on trace gas observations during the SAGA 3 cruise in February and March 1990. Crawford *et al.* (1997b) used medians of observations during PEM-West B for a number of compounds as input to photochemical box model runs in order to calculate diurnal loss rates. The ratio of the diurnal loss rate of ozone to the ozone mixing ratio calculated in the LTN1 run appears reasonable in the light of these studies. Over the entire tropospheric column it is somewhat higher than the one calculated by Crawford *et al.* (1997b) (see discussion in Section 9.5). For the studies by Wang and Prinn (2000) and by Mari *et al.* (2003) these percentages are not indicated, since the ranges cited in Table 9.1 were inferred from vertical profiles which varied with height. Mari *et al.* (2003) used a mesoscale chemistry transport model in a study of deep convection during PEM-Tropics B for an episode between 9:30 local solar time and 17:15 local solar time on the same day and found net photochemical loss of ozone to occur below 7 km and small net photochemical formation (about 1 nmol $\mathrm{mol^{-1}\ day^{-1}}$) above. Wang and Prinn (2000) on the other hand found net chemical formation of ozone at all altitudes up to about 15 km in their reference (REF) simulation (without lightning NO_x production) of a storm during CEPEX (their Fig. 9). Height integrated photochemical budget terms are further discussed in Section 9.5.

Fig. 9.2 shows 30 min time average photochemical tendencies for the time interval from 23 December 1992, 23:30 GMT to 24 December 1992, 24:00 GMT for the LTN1 run and instantaneous cloudmeteor mixing ratio contours for 24 December

1992, 24:00 GMT. The largest local net ozone loss is calculated above relatively low cloud tops. The second largest net ozone loss is calculated in the cloud free lower troposphere. Decreased photolysis rates below optically thick clouds cause the photochemical destruction of ozone to be slower relative to cloud free air. However, increased photolysis rates above low clouds can act to accelerate ozone destruction. In the updraft of the storm between x=250 km and x=300 km, lightning produced NO_x is responsible for net production of ozone which occurs in the lower troposphere (in a region of reduced photolysis rates). Currently, 3-D effects are not considered in calculating photolysis rates in the CRCTM. Barth *et al.* (2002) studied the effect of marine boundary layer clouds on tropospheric chemistry in a 20° by 20° region centered over Hawaii. They highlighted the importance of considering the radiative effect of clouds on photochemistry when estimating ozone depletion in and near clouds. Since the chemical lifetime of ozone is long compared to the time needed for transport in a deep convective cloud, the local vertical advection tendencies at a given time are much larger than the photochemical tendencies for the same time interval (not shown). Detecting ozone changes due to enhanced photolysis rates above low cumulus clouds is expected to be difficult, even in cases of persistent low cloud covers, e.g. for trade wind cumuli. Enhanced photolysis rates due to deep convective clouds can lead to enhanced ozone formation in the upper troposphere, where less water vapor is available.

9.3 Dependence on Lateral Boundary Conditions and Importance of Horizontal Advection

Fig. 9.3 shows results from the LTN1 run: time height contour plots of domain averaged volume mixing ratios, boundary values, and budget terms for ozone. Some features of the domain averaged ozone mixing ratios in Fig. 9.3a are similar to the boundary values in Fig. 9.3b. The total rate in Fig. 9.3c clearly reflects the influences of the horizontal advection term in Fig. 9.3d. The ozone boundary conditions vary considerably in time and the abundance of ozone in the CRCTM run is strongly influenced by these variations. The strong temporal variation of ozone can be explained by the fact that the domain is located in an area where large horizontal gradients are likely to occur (compare Fig. 7.6a from MATCH-MPIC). While ozone depends directly on the boundary conditions, shorter lived gases can indirectly depend on the boundary conditions for their longer lived precursors. The vertical advection term in Fig. 9.3e is mostly positive below 5 km and the net chemistry term in Fig. 9.3f is mostly negative below 5 km. The largest net chemical loss in the LT occurs during daytime, while the averaged chemistry tendencies are smaller during nighttime. The diurnal maximum loss rates in Fig. 9.3f are in the range ∼16–19 nmol $mol^{-1}day^{-1}$ except on the first day when the maximum reaches 20.5 nmol $mol^{-1}day^{-1}$, and on 23 and 25 December, when the maxima are ∼11 and ∼13 nmol $mol^{-1}day^{-1}$. In the UT, the diurnal cycle is opposite to that in the LT, exhibiting average net formation during daytime and net loss during nighttime. The

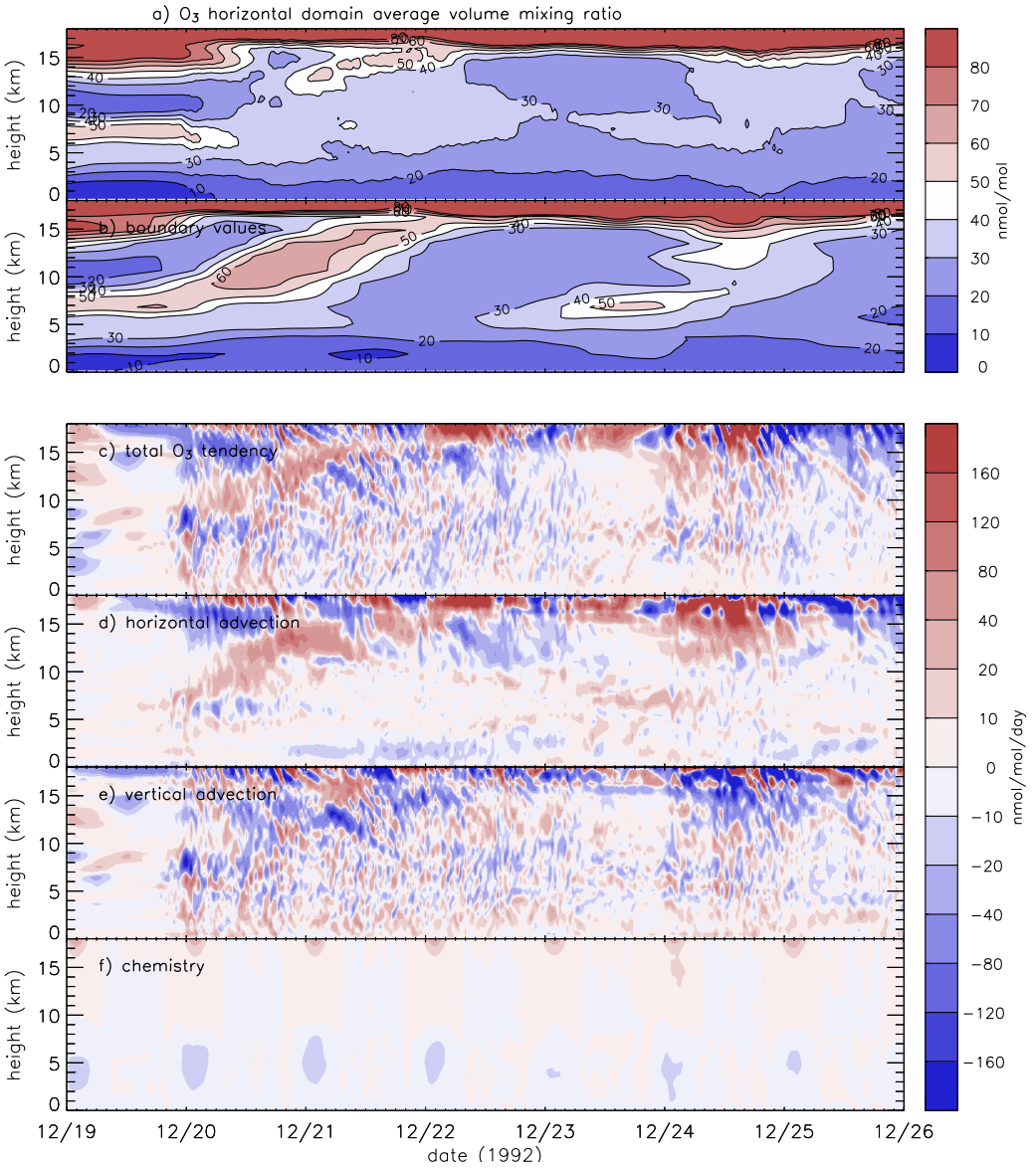

Figure 9.3: As Fig. 8.6 for ozone.

diurnal cycle in the LT is also opposite to the diurnal cycle in a more polluted (NO_x rich) LT, where daytime net formation and nighttime net loss lead to daytime ozone maxima and nighttime ozone minima. The horizontal advection term in Fig. 9.3d is often negative in the lower troposphere, and positive in the upper troposphere, where the vertical advection term is negative, i.e. ozone is horizontally advected into the domain above the boundary layer and is then advected downwards. This point is further discussed in the next sections.

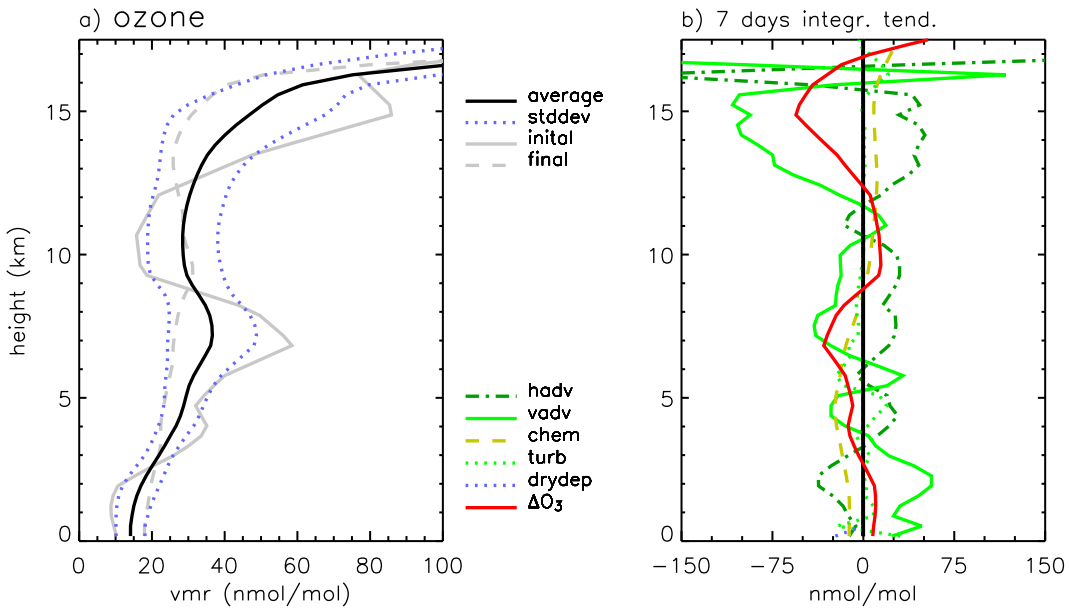

Figure 9.4: As Fig 8.5 for ozone.

9.4 Dependence on Initial Values

Fig. 9.4a shows the domain and time averaged ozone mixing ratio profile, the profile ± the standard deviation, the domain averaged initial profile, and the domain averaged final profile at the end of the simulation after seven days for the LTN1 run. Fig. 9.4b shows height dependent 7-day integrated budget terms for ozone for the LTN1 run. The averaged vertical advection term is mostly negative above 5 km and mostly positive below, reflecting the net downwards transport of ozone. The horizontal advection term partially balances the vertical advection term, indicating that horizontal advection acts to partially compensate the influence of modeled vertical advection. Another important term in the budget is the difference between the initial and the final ozone profiles shown in Fig. 9.4a . For a number of trace gases, this difference was small compared to the other terms, as can be expected for relatively short lived trace gases. In the limit of very long model runs, the difference at the location of the TOGA COARE region is expected to be negligibly small compared to the other terms of the budget. Even for somewhat longer simulations, this difference can be expected to be much smaller than the other budget terms. For the 7-day TOGA COARE case study it is, however, of the same order of magnitude as the other budget terms. This indicates that the initial values have an important influence on the other terms of the budget. The rather complicated vertical profiles of the advection terms are most likely a consequence of the influences of the initial and the boundary values.

9.5 Height Integrated Budget Terms

Table 9.2 shows calculated ozone column densities as well as time, height, and horizontally integrated tendency terms for ozone for the last six days of the NOLTN, the LTN1, the LTN2, and the LTNWP run. The model domain was divided into three different altitude ranges as in Table 8.4. The average column density of ozone in the tropospheric column (TC) varies by at most 5% between these runs. The net chemistry term in the tropospheric column is dominated by net losses in the lower troposphere, where these losses are more than compensated by vertical advection. The excess ozone coming from the upper and mid-troposphere is in part advected horizontally out of the domain at low altitudes in all runs (compare discussion of the mid-tropospheric tracer B in Section 4.2). This suggests that some of the ozone which has originated in the mid- and upper troposphere in regions with deep convective clouds can be exported from the domain in the lower troposphere, in spite of the lifetime being relatively short there. In the TOGA COARE simulation low level westerlies favor the low level export of ozone. However, the calculated export must be expected to depend to some extent on the boundary conditions: If the lower tropospheric ozone values at the lateral boundaries were much higher, net low altitude import instead of export could probably occur in combination with the lower tropospheric photochemical sink. The ozone which is advected towards the Earth's surface is for the largest part not formed within the model domain, but is imported at high altitudes.

For a tropospheric column up to 10 km, Crawford *et al.* (1997b) calculated net ozone loss to occur at a rate of -2.4·10^{11} molec cm^{-2} s^{-1} or -7.2% per day for their low NO_x regime. The average net chemical loss rate in the NOLTN run was somewhat higher (-3.9 · 10^{11} molec cm^{-2} s^{-1} or -9.2% per day for the column up to 10 km). In the LTN1 run, the net chemical loss rate up to 10 km is -3.2 · 10^{11} molec cm^{-2} s^{-1} or -7.4% per day, and in the LTN2 run it is -3.4 · 10^{11} molec cm^{-2} s^{-1} or -7.7% per day. Including acetone chemistry in their model, Crawford *et al.* (1997b) still found their low NO_x regime to be dominated by ozone loss, but the rate dropped to -1.7 · 10^{11} molec cm^{-2} s^{-1}. Olson *et al.* (2001) compiled an overview of net photochemical column O_3 tendencies derived from five different studies for a number of different locations and seasons over the Pacific. The low NO_x regime of Crawford *et al.* (1997b) was calculated to have the largest absolute net column (up to 12 km) loss tendency of the studies included in the compilation[3]. As noted in Section 8.3, Crawford *et al.* studied averages over an area in which slightly higher NO_x values could be expected than in the TOGA COARE region.

The lower NO_x values than in the study by Crawford *et al.* (1997b) in combination with elevated ozone values in the MT due to long or medium range transport during the TOGA COARE episode are favorable conditions for larger net ozone

[3]In a study which was not included in the compilation by Olson *et al.*, Wang *et al.* (2000) found higher net column loss rates over the tropical Pacific during PEM-Tropics A than Crawford *et al.* (1997b) in the low NO_x regime, albeit at higher ozone concentrations, which were in part related to the strong influence from biomass burning emissions during PEM-Tropics A.

Table 9.2: Ozone column densities and height integrated budget terms for ozone as defined in Equation 8.2 for the last six days of the lightning NO_x sensitivity runs.

	LT[a]	MT[a]	UT[a]	TC[a]
NOLTN				
av. column density[1]	1.85	1.83	1.25	4.93
vertical advection[2]	0.36	-0.12	-0.30	-0.06
horizontal advection[2]	-0.14	0.16	0.20	0.23
chemistry[2]	-0.22	-0.12	0.01	-0.33
turbulence param.[2]	0.06	-0.06	0.00	0.01
dry deposition[2]	-0.03	-	-	-0.03
total tendency[2,3]	0.04	-0.14	-0.08	-0.18
LTN1				
av. column density[1]	1.87	1.89	1.27	5.03
vertical advection[2]	0.37	-0.13	-0.30	-0.06
horizontal advection[2]	-0.16	0.15	0.17	0.15
chemistry[2]	-0.20	-0.08	0.05	-0.23
turbulence param.[2]	0.06	-0.06	0.00	0.01
dry deposition[2]	-0.03	-	-	-0.03
total tendency[2,3]	0.04	-0.12	-0.08	-0.15
LTN2				
av. column density[1]	1.87	1.88	1.26	5.01
vertical advection[2]	0.37	-0.12	-0.30	-0.06
horizontal advection[2]	-0.16	0.15	0.17	0.16
chemistry[2]	-0.20	-0.09	0.04	-0.25
turbulence param.[2]	0.06	-0.06	0.00	0.01
dry deposition[2]	-0.03	-	-	-0.03
total tendency[2,3]	0.04	-0.12	-0.08	-0.16
LTNWP				
av. column density[1]	1.91	1.98	1.29	5.18
vertical advection[2]	0.38	-0.14	-0.29	-0.05
horizontal advection[2]	-0.22	0.13	0.13	0.03
chemistry[2]	-0.13	-0.01	0.08	-0.06
turbulence param.[2]	0.06	-0.06	0.00	0.01
dry deposition[2]	-0.03	-	-	-0.03
total tendency[2,3]	0.06	-0.09	-0.07	-0.11

[a] Same as in Table 8.4.

[1] In 10^{17} molecule cm^{-2}. One Dobson unit (DU) is $2.69 \cdot 10^{16}$ molecule cm^{-2}. The average tropospheric ozone column in the LTN1 run is $4.95 \cdot 10^{17}$ molecule cm^{-2} or 18.4 DU.

[2] In 10^{17} molecule cm^{-2} day^{-1}.

[3] Diagnosed from the change of column densities, the values are, however, identical to the rounded sum of unrounded values for the individual processes.

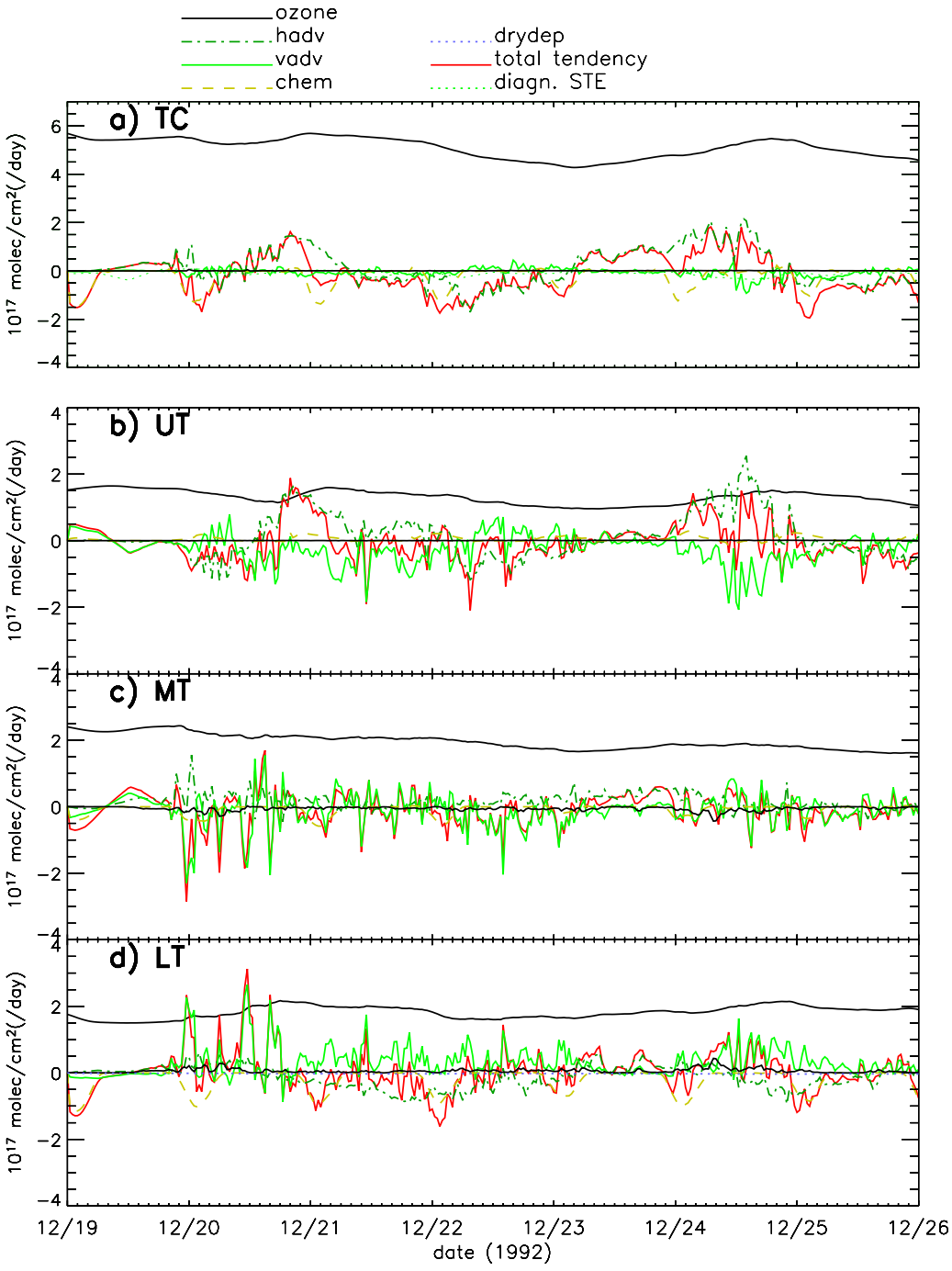

Figure 9.5: Result from the LTN1 run: Time series of average column density and domain averaged, height integrated and 30 min time averaged tendency terms for ozone. The model domain was divided into MT, UT and LT as in Table 8.4. The ozone column densities (black lines) are expressed in 10^{17} molecules cm^{-2} and all other terms are expressed in 10^{17} molecules cm^{-2} day^{-1}. The "exchange between stratosphere and troposphere (STE)" was diagnosed using $\overline{w}_{obs}$ at ∼16 km altitude as described in the text.

loss to occur. Furthermore, it was shown that deep convection during the TOGA COARE episode induces net downward ozone transport in the troposphere, which could lead to increased net ozone loss in the lower troposphere. However, a sensitivity run ("NOCONV", results not shown in Table 9.2) using specified lateral boundary conditions and suppressing cloud formation by turning off the microphysics scheme and the not using the large scale advection terms (in Eqs. 3.1 and 3.2), yielded a column integrated chemical net loss rate of ozone which did not differ considerably from the net loss rate calculated for the NOLTN run. The loss was only slightly (∼1.6%) smaller suggesting that the influence of deep convection on the calculated net column integrated photochemical ozone loss in the CRCTM is not sufficient to explain the differences between this study and the study by Crawford *et al.* (1997b). Note, however, that the boundary values used in the CRCTM had been influenced by previous deep convection calculated in MATCH-MPIC. Problems about defining a so-called pre-convective environment have been discussed in Section 7.2. The diagnosed differences of the chemistry term between the NOLTN and the NOCONV run were also small for all three individual height ranges (i.e. in the LT, MT, and UT) in the limited domain model runs. While in the NOLTN run a considerable amount of ozone was horizontally advected into the domain in the MT and in the UT, the corresponding term was small and negative for the NOCONV run. Consequently, the column integrated amount of ozone in the NOLTN run was somewhat higher than in the NOCONV run. The difference arose mainly in the LT due to average downwards transport in the NOLTN run. Furthermore, in the LT more ozone was horizontally advected out of the domain than advected into the domain in the NOLTN run, but not in the NOCONV run. This suggests that increases of the net lower tropospheric ozone loss due to deep convection would likely occur outside the domain. The sensitivity of the net chemical loss towards neglecting effects of deep convection in the NOCONV run compared to the NOLTN run could be expected to increase if a much larger domain were used. Using global chemistry transport models, Lelieveld and Crutzen (1994), Lawrence *et al.* (2003a), and Doherty *et al.* (2005) found deep convective transport to influence global budgets of tropospheric ozone considerably.

Figure 9.5 shows time series of the average column density and height integrated ozone budget terms for different altitude ranges from the LTN1 run. The total tendency for the tropospheric column in Fig. 9.5a clearly reflects influences from the horizontal advection, as was discussed in Section 9.3. The height integrated horizontal advection term changes sign several times at all altitudes during the duration of the 7 day TOGA COARE episode. The largest downward transport from the UT occurs on 24 December, when the value for the horizontal advection into the upper tropospheric model domain also reaches its maximum. Furthermore, maximum rain rates were simulated on this day, which is a good proxy for strong deep convection. In the MT and the LT, relatively large contributions from horizontal advection were calculated during the first day of active deep convection. These changes also coincide with changes of the boundary values during this day (compare Fig. 9.3). Note that a number of processes including horizontal advection have to be considered in order to understand the effect of individual cloud systems on ozone fields in a given environ-

ment. In the 500 km 2-D domain simulation, horizontal advection is rapid enough to influence domain averaged ozone column densities on relatively short timescales.

9.5.1 Stratosphere Troposphere Exchange

The column integrated vertical advection tendencies in Table 9.2 are small and negative for the tropospheric column from the surface to ∼16 km. This is the consequence of a calculated net upwards transport of ozone from below ∼16 km. Here, this time integrated flux divergence will be referred to as "Stratosphere Troposphere Exchange" (STE), although the definition of the tropopause at ∼16 km is arbitrary and not based on physical principles. Furthermore, the diagnosed STE is influenced by the method of prescribing the VLSAT (compare Section 3.2). The net vertical flux across z_m= 17.375 km was scaled to a value which was calculated using $\overline{w}_{obs}$ (see Appendix C) in the chemistry runs. This technique ensures a net vertical flux at 17.375 km which is consistent with a positive $\overline{w}_{obs}$ (compare Fig. 3.3) at this altitude reflecting average ascent. The positive sign of $\overline{w}_{obs}$ at this altitude is consistent with the tropics being a region of average lower stratospheric ascent and troposphere to stratosphere transport (Holton *et al.*, 1995; Corti *et al.*, 2005). The STE in Fig. 9.5a was diagnosed from the ozone concentration in the CRCTM and from $\overline{w}_{obs}$ at ∼16 km. The diagnosed values in Fig. 9.5a are, however, largely consistent with the residual calculated by vertically integrating the vertical advection tendency. This consistency is largely assured by the technique of scaling the fluxes, although the corresponding inconsistency in sensitivity runs without applying a scaling was very moderate.

It is shown in the next section that deep convective clouds can cause transport of ozone from the tropopause region into the troposphere. At the same time ozone rich air in the tropospheric region is replaced by tropospheric air containing less ozone. Downwards transport from the stratosphere was also reported in a number of other CRM studies (Scala *et al.*, 1990; Wang *et al.*, 1995; Wang and Prinn, 2000). The small net upwards transport calculated in this study suggests the cloud scale downwards transport of ozone from the stratosphere does not offset the effect of large scale vertical ascent in the tropospheric ozone budget. In previous CRM studies of deep convection, the VLSAT term was not considered. Kley *et al.* (1996) argued that the extreme steepness of the ozone gradient at the tropopause was a powerful indicator that cumulonimbus convection had reached the top of the troposphere and, conversely, that no ozone from the stratosphere was able to diffuse into even the uppermost layers of the troposphere. In the next section, it will be demonstrated that ozone can be transported downwards in well defined stream-like layers or filaments (compare Fig. 9.8), i.e. that cloud scale downwards transport can take place while maintaining a sharp gradient over large fractions of the tropopause. The net transport of ozone in the TOGA COARE case was calculated to be upwards as a consequence of mean ascent across the tropopause. However, uncertainties exist in the magnitude of upwards transport which could for example arise due to uncertainties of the observed large scale vertical velocities, which are difficult to

quantify.

Wang and Prinn (2000) found in their study that the upward transport of O_3-poor air from the boundary layer did not significantly decrease O_3 concentrations in the upper troposphere (using an initial ozone mixing ratio profile which varied by only ∼3–4 nmol mol^{-1} between the surface and the upper troposphere in their simulations). Comparing runs with and without convection, they found that deep convection induced downward transport and actually led to increases in O_3 volume mixing ratios in the upper troposphere, despite the local ozone reduction in convective areas caused by high NO_x in their lightning runs. On the other hand, Fig. 9.4b and Table 9.2 showed negative contributions of the vertical advection term to the ozone budget in the upper troposphere, indicating that the vertical transport acts towards reducing the average upper tropospheric ozone mixing ratios in the TOGA COARE runs.

9.6 Rapid Transport

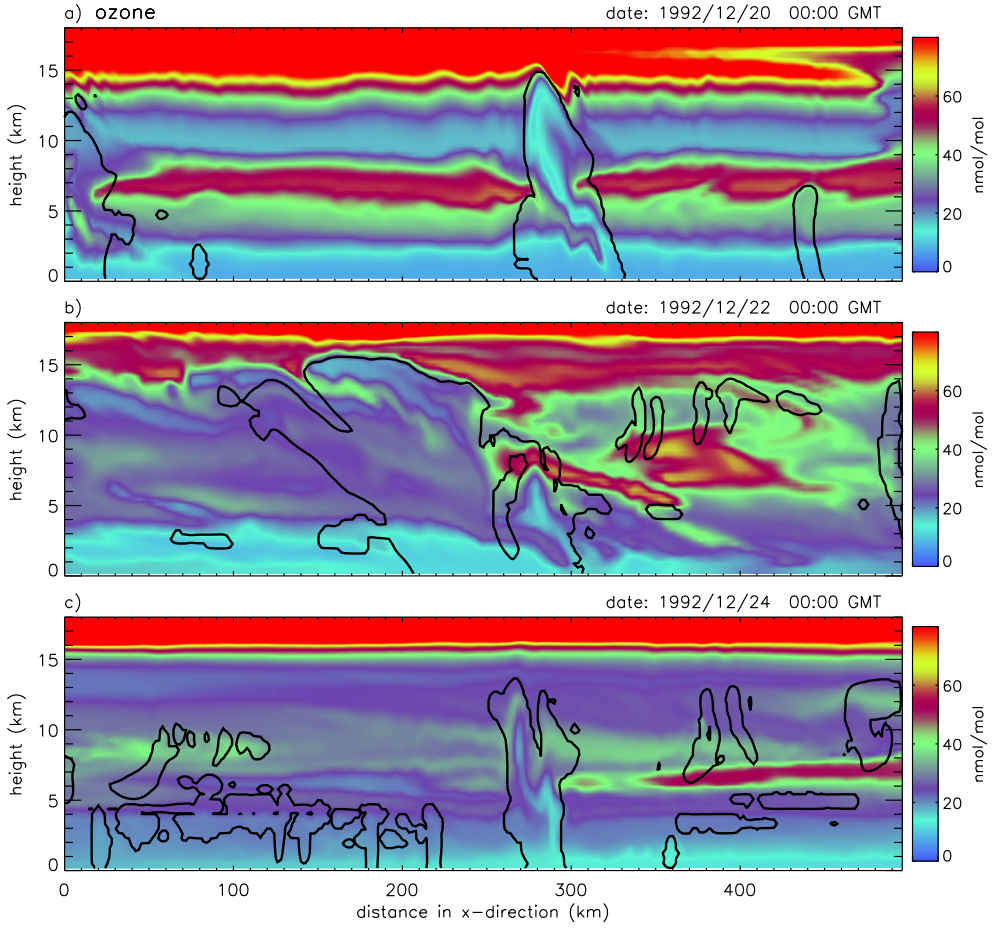

Figure 9.6: Examples of modeled ozone volume mixing ratio contours (filled) from the LTN1 run after 1,3, and 5 days. Furthermore, the $q_{totm} < 0.01$g kg^{-1} contour is plotted.

So far, the discussions for ozone were largely limited to domain averaged or median properties. The subsequent sections aim at investigating some details. Examples of the modeled ozone fields on three different occasions are plotted in Fig. 9.6a–c. The figure is intended to give an impression of a few typical situations occurring throughout the entire 7 day TOGA COARE episode. The ozone fields during the development of selected individual storms are investigated in more detail later, in some cases sustaining points made here. In Fig. 9.6a, modeled deep convection has set in rather recently. A mid-tropospheric layer of elevated ozone values also present in the initial field is still largely intact. The deep convective system located approximately in the middle of the domain advects air containing low volume mixing ratios of ozone upwards. In the same system mid-tropospheric air is transported downwards in what may be considered rear inflow. The larger clouds associated with large mesoscale convective systems are moving westward, presumably driven by the upper tropospheric easterlies (compare Hovmöller diagram, Fig. B.1). Consequently, the rear inflow is effectively located at the leading edge of these clouds. In the upper troposphere, near the eastern boundary of the domain in Fig. 9.6a, the ozone mixing ratios exhibit a local minimum. A detailed analysis yields that this minimum was caused by horizontal advection of low ozone air from the eastern domain boundary. Forty-eight hours later, a different, more mature storm is located approximately in the middle of the domain (Fig. 9.6b). In the upper troposphere regions of elevated ozone mixing ratios exist. From animations, it appears that air containing the elevated ozone mixing ratios was advected into the domain horizontally from the lateral boundaries. Air containing low ozone mixing ratios has been advected to the UT, and in the western half of the domain, the deep convective outflow has formed a "low ozone anvil" which is located east of the updraft region. Filaments of elevated ozone mixing ratios in the UT indicate that upper tropospheric air containing elevated ozone mixing ratios has been advected downwards along the lower edge of the anvil. Fig. 9.6c shows some decaying clouds and a growing storm located approximately in the middle of the domain. The thin layer of elevated ozone above 5 km altitude was horizontally advected from the lateral boundaries. The development of the growing storm in Fig. 9.6c during four hours is shown in Fig. 9.7. Fig. 9.7a is identical to Fig. 9.6c. The active storm consists initially of a single cell. During its further growth, fresh cells form at the eastern edge of the simulated storm. The whole multi-cell storm, however, moves westward. Some shallower clouds develop east and west of the largest storm. East of the large storm, the layer of elevated ozone above 5 km has remained largely intact. The eastward propagation of a gravity wave along the tropopause can be traced from Fig. 9.6b to Fig. 9.6i.

A second example of a westward moving multi-cell storm that appeared a few hours later in the model is shown in Fig. 9.8. A very interesting feature of this simulated storm which was also noted in other simulated storms during the TOGA COARE episode are filaments of high ozone mixing ratios which originate in the tropopause region and extend along the lower edges of the "low ozone anvils" (which do not have to coincide with the anvils formed from cloud ice). From Figs. 9.7 and 9.8, it appears that large scale mixing across the tropopause did not play a large role in the runs using specified lateral boundary conditions for ozone and

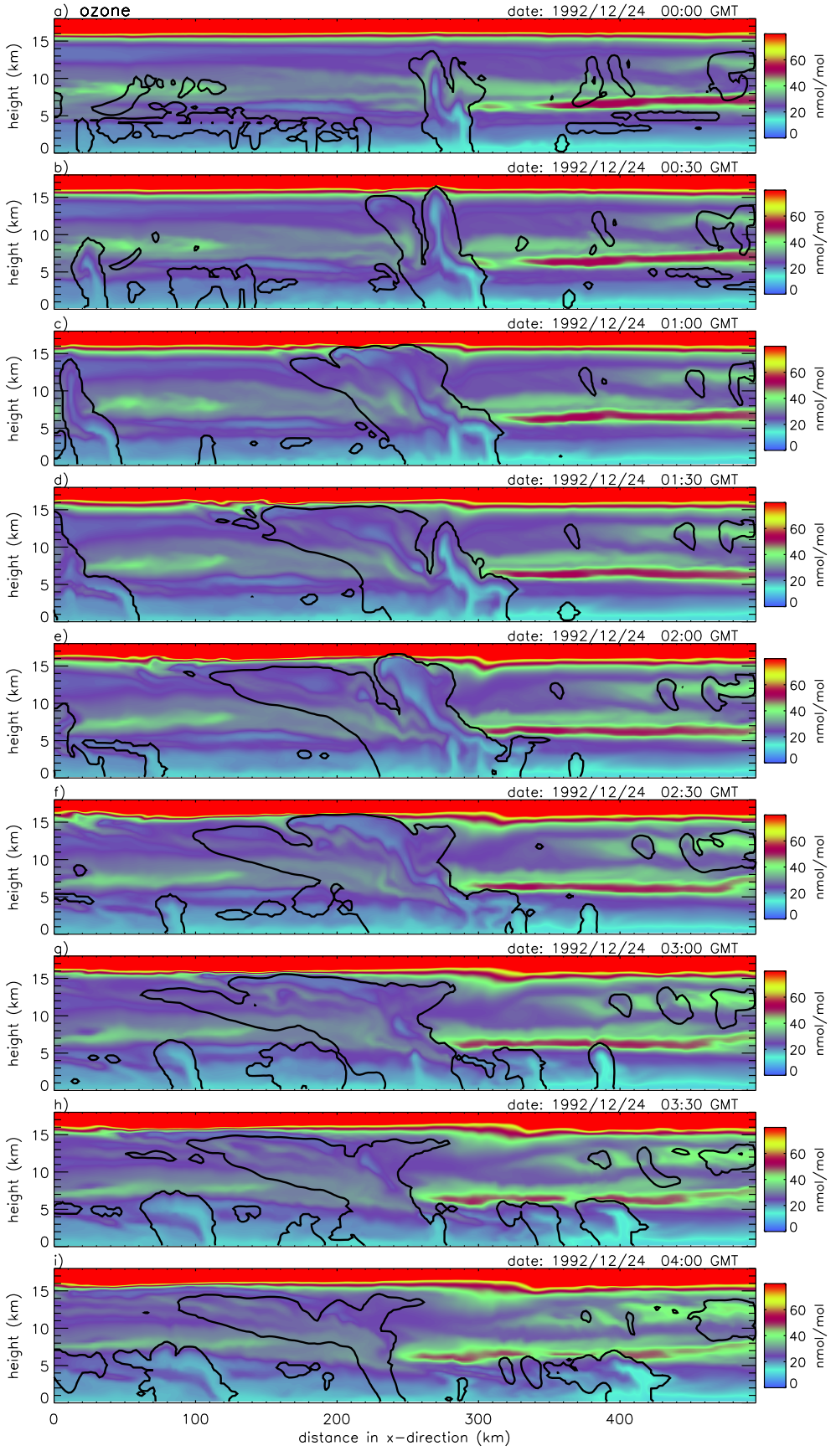

Figure 9.7: Volume mixing ratio contours (filled) of ozone and $q_{totm} < 0.01$g kg^{-1} mass mixing ratio contour during the development of a multi-cell storm from 24 December 1992, 0:00 GMT to 24 December 1992, 4:00 GMT from the LTN1 run.

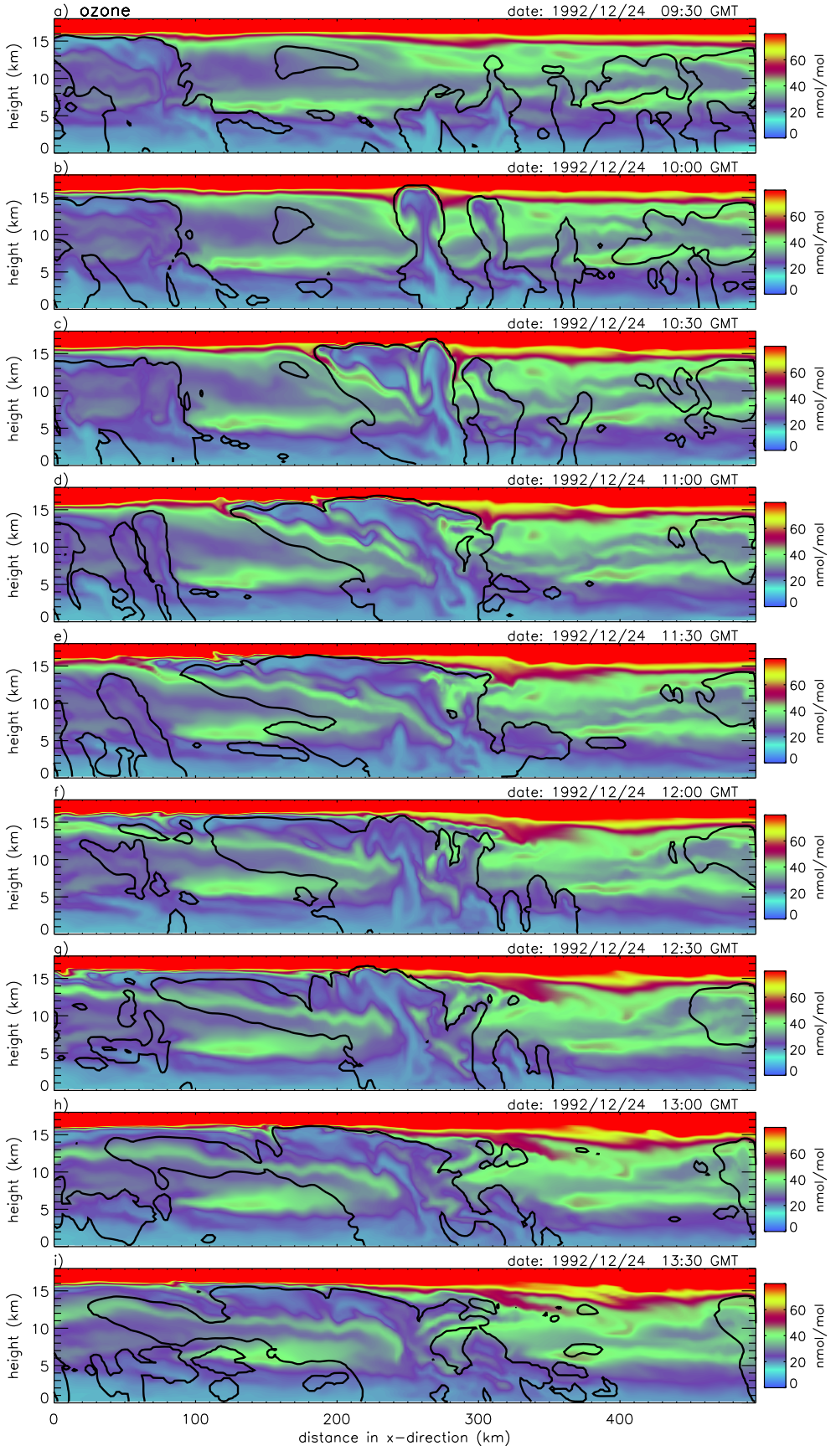

Figure 9.8: As Fig. 9.7 from 24 December 1992, 9:30 GMT to 13:30 GMT.

VLSAT. On the other hand, from Plate 5 by Wang and Prinn (2000), it appears that vertical mixing at the tropopause probably in association with gravity wave breaking (and possibly with model calculated mass balancing subsidence) acted to smoothen the ozone gradient at the tropopause across the entire domain in their 30 hr 2-D simulations with periodic boundary conditions. The thin horizontal layer of elevated mid-tropospheric ozone mixing ratios extending over large parts of the domain in Fig. 9.8a was caused by horizontal advection from the eastern boundary, as well as the thicker layer of elevated ozone mixing ratios in most of the upper troposphere. The interplay of deep convection and horizontal advection causes the modeled ozone fields to appear fairly complex, exhibiting large horizontal and vertical gradients.

9.7 Vertical Profiles

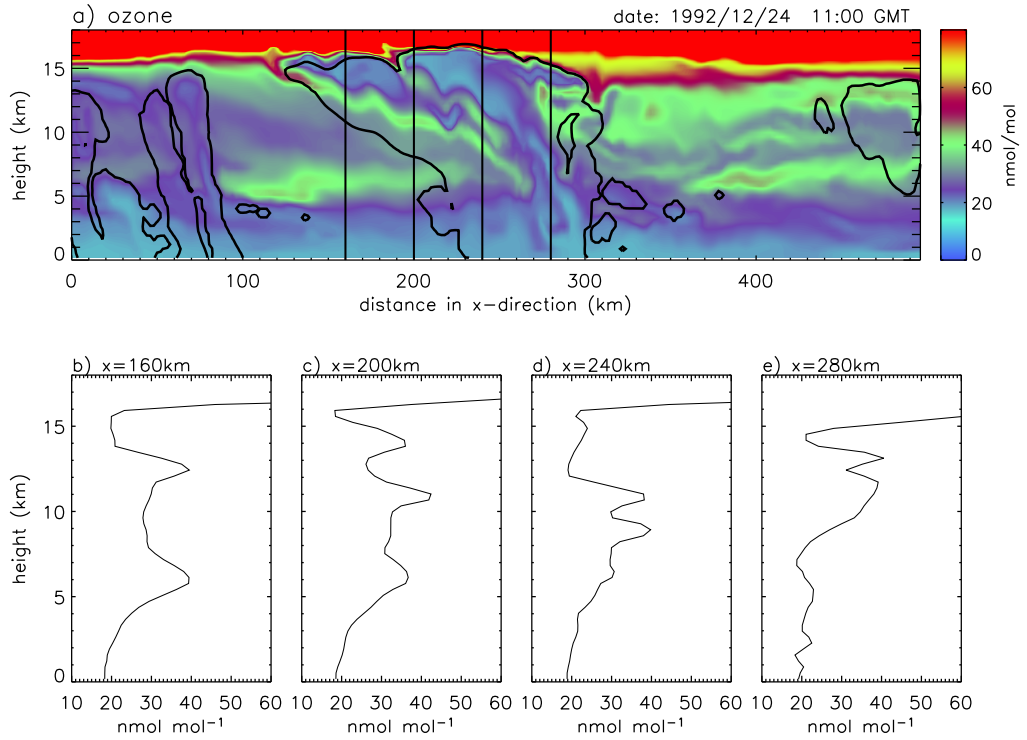

Figure 9.9: (a) As Fig. 9.8d. (b)–(e) Vertical profiles at the locations indicated by the vertical lines in (a).

This section focuses on analyzing a few individual profiles. As an example, profiles from a storm on 24 December 1992 at 11:00 GMT are chosen. The evolution of this storm was discussed in the previous section. Fig. 9.9 shows a contour plot of ozone volume mixing ratios and some corresponding vertical profiles for ozone. The locations of the profiles in Fig. 9.9b–e are indicated by the black vertical lines in Fig. 9.9a. All vertical profiles in the figure show local minima in the upper troposphere. These minima coincide with the anvil of the storm in Fig. 9.9a. Below

the upper tropospheric local minima, local maxima occur which have been caused by the downwards transport of ozone from the tropopause region. The time it takes for the local maxima and the local minima to decay can vary from the time it takes for the storm to decay. Newell *et al.* (1996, 1999) interpreted thin horizontal layers in the troposphere as frozen signatures of the transfer of boundary layer air into the free troposphere or of stratospheric air into the troposphere. Fig. 9.9 suggests that the existence of horizontal layers could be directly linked to the dynamics of a single storm. On the other hand, horizontal layers could also be caused by strong vertical mixing in one location and subsequent differential horizontal advection under conditions of strong vertical wind-shear. However, Newell *et al.* (1996) did not find a clear relationship between the layers and wind velocity profiles measured simultaneously. Newell *et al.* (1996) identified over 500 layers with a mean thickness of about 400 m from 105 vertical profiles sampled during PEM-West A. They found these layers to extend over distances of 100–200 km or more. Using a different method to identify horizontal layers, Newell *et al.* (1999) found the average thickness of horizontal layers during PEM-West A to be about 800 m. The vertical grid spacing used in the TOGA COARE study was 350 m, which is not sufficient to numerically resolve layers much thinner than about 1 km. Observed profiles, on the other hand (e.g. Fig 7.8a), indicate the existence of very thin layers.

9.8 Upper Tropospheric Minima

Wang and Prinn (2000) suggested that lightning-related ozone loss in cloud anvil regions could help explain the occasionally observed low O_3 layers in the tropical upper troposphere. They studied a storm observed during CEPEX (see section 7.3.1) on 8 March 1993, when the research vessel *Vickers* was located southeast of the TOGA COARE IFA. Low level westerlies in association with upper level easterlies suggest the influence of a westerly wind burst on that day. Wang and Prinn derived initial trace gas profiles for their CRM study from a 6-hour clear-sky model integration. Their initial ozone profile had a minimum of about 6 nmol mol^{-1} close to the surface and increased by about 3–4 nmol mol^{-1} between the surface and the upper troposphere. They indicated in the text that they calculated minimum mixing ratios in the upper troposphere which were slightly less than 2 nmol mol^{-1}. Their Plate 6 shows individual, instantaneous ozone profiles, in which the minimum upper tropospheric ozone mixing ratio is about 2.5 nmol mol^{-1} in the profile from their LTNH run, and about 13 nmol mol^{-1} in the profile from their LTN run, indicating that in their LTNH run, considerable amounts of ozone had been titrated by lightning produced NO (Reaction 1.9).

Fig. 9.10a shows the time series of the minimum ozone mixing ratios in the lowest model layer (surface layer) $\mu_{min,surf}$ and of the minimum ozone mixing ratio in the upper troposphere $\mu_{min,UT}$ for the TOGA COARE lightning sensitivity runs. Steep decreases of the ozone mixing ratios in the LTNHWP and to a lesser extent also in the LTNWP run indicate that considerable ozone titration had occurred in these

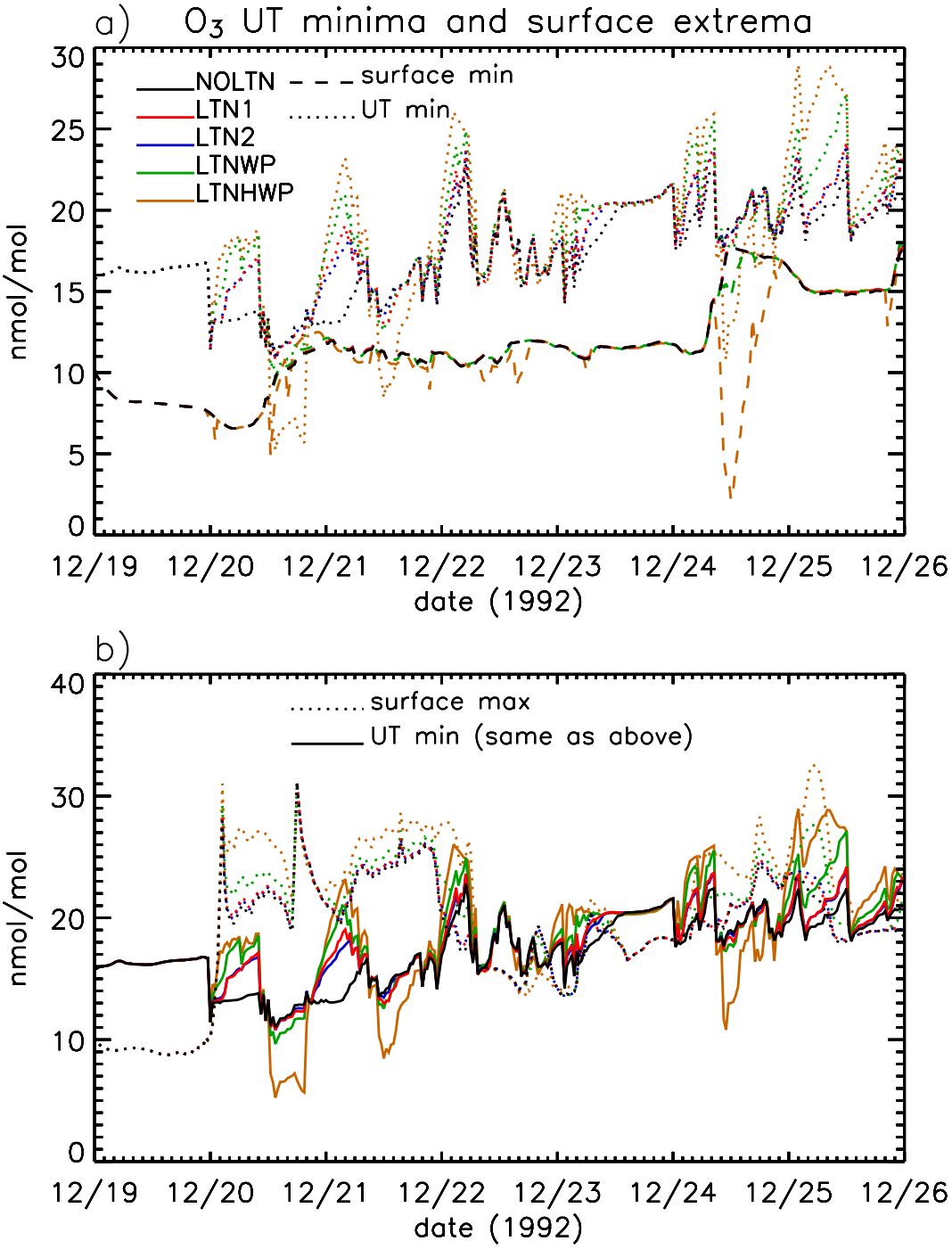

Figure 9.10: Time series **(a)** of the minimum ozone mixing ratios in the lowest model layer (surface layer) and of the minimum ozone mixing ratio in the upper troposphere (UT), and **(b)** of the maximum ozone mixing ratio in the lowest model layer and of the minimum ozone mixing ratio in the UT. The UT was defined from about 10 km to about 16 km altitude as in Table 8.4.

Table 9.3: Statistics for vertical profiles where the minimum upper tropospheric ozone mixing ratio was lower than the surface mixing ratio in the same column.

	NOLTN	LTN1	LTN2	LTNWP	LTNHWP
$n^{(a)}$	59	55	54	62	90
$p^{(b)}$ (%)	6.4	6.3	6.2	7.1	11.7

(a) The model output was scanned for columns in which the minimum upper tropospheric mixing ratio of ozone $\mu_{pmin,UT}$ was below the surface mixing ratio $\mu_{pmin,surf}$. The number of output times in which such columns were found is n. The output interval was 30 min and the total number of output times was 337 (including output prior to the onset of convection in the model). The UT is defined as in Table 8.4 between roughly 10 and 16 km.

(b) $p = 100 \cdot m/m_{tot}/n$ where m is the total number of columns with $\mu_{pmin,UT} < \mu_{pmin,surf}$ and m_{tot} is the number of columns in the model run (grid points in x-direction in the 2-D chemistry runs).

runs. The most prominent steep decreases occur during nighttime on 20 December and on 24 December. A detailed analysis of the results of the LTNHWP sensitivity run yields that on 24 December ozone titration was calculated in the lower and the upper troposphere, and that it was confined to regions of pronounced lightning NO_x outflow. The minimum upper tropospheric ozone mixing ratios $\mu_{min,UT}$ did not fall below the corresponding values $\mu_{min,surf}$ at the same output times for the the NOLTN, the LTN1, and the LTN2 run, nor did they fall below 5 nmol mol^{-1} as observed during CEPEX. However, in all runs a number of individual profiles were detected in the model output for which the minimum upper tropospheric ozone mixing ratio $\mu_{pmin,UT}$ was lower than the surface mixing ratio $\mu_{pmin,surf}$. Table 9.3 shows the number of output times n for which such profiles were detected. Furthermore, the average percentage (fractional surface area coverage) p of such profiles during the output times when they occurred is shown. Note that n can be expected to depend on the domain size used and that p depends on the domain size relative to the area covered by deep convection. The values of n and p were larger for the NOLTN run than for the LTN1 and the LTN2 run, reflecting the effect of increasing ozone formation with increasing lightning NO_x production. Further increases of lightning associated NO_x production in the LTNWP and the LTNHWP run caused n and p to increase, reflecting the occurrence of instances in which ozone titration was calculated to occur. The time series in Fig. 9.10a suggests that instances in which $\mu_{min,UT}$ and $\mu_{min,surf}$ are almost equal in the NOLTN, the LTN1, and the LTN2 run occurred shortly after $\mu_{min,surf}$ had increased substantially on 20 December and on 24 December. The time-height contour plot of the horizontal advection budget term in Fig. 9.4d indicates that these increases can be attributed to the influence of low level horizontal advection. During the rest of the time, the values of $\mu_{min,UT}$ remained above the values of $\mu_{min,surf}$ for the NOLTN, the LTN, and the LTNH run,

indicating that air originating at the lowest model layer has undergone some dilution before reaching the UT. Wang and Prinn (2000) also found that very little undiluted O_3-poor air from the boundary layer can reach the upper troposphere. During the first days of deep convection, the values $\mu_{min,UT}$ appear to be anti-correlated to convective activity as indicated by the simulated surface precipitation (in Fig. 3.4).

Although in general no completely undiluted air from ozone poor regions in the lowest model layer appears to have reached the upper troposphere in the model, the results from Section 9.5 indicate that the upwards transport of relatively undiluted O_3 poor air plays an important role for the upper tropospheric ozone budget in the model. Furthermore, based on the results from this section it appears that deep convection in combination with horizontal advection under conditions of vertical wind shear could easily account for observed upper tropospheric minima with comparable or smaller mixing ratios than those observed in the lower troposphere at the same location. The minimum upper tropospheric ozone mixing ratio in the LTNHWP run was above the minimum of 2 nmol mol^{-1} calculated by Wang and Prinn (2000) in their LTNH run, presumably because of lower flash rates and consequently lower lightning NO_x production (Section 8) in the LTNHWP than in the LTNH run of Wang and Prinn (2000). Furthermore, unless an extremely high lightning NO_x production was assumed, which appears to be unrealistic in the light of more recent studies, the minimum tropospheric minimum mixing ratios (not shown) did not fall below 5 nmol mol^{-1} as observed during CEPEX. However, such extremely low upper tropospheric ozone mixing ratios were not anticipated to appear in the runs without or with small to moderate lightning NO_x production, since it was argued that minimum values of surface ozone in the TOGA COARE region should not be expected to occur during westerly wind bursts (Section 7.3.1). Furthermore, the boundary values from MATCH-MPIC (in Fig. 9.4) did not exhibit extremely low upper tropospheric ozone mixing ratios.

Fig. 9.10b shows time-series of the maximum ozone mixing ratio in the lowest model layer (surface layer) $\mu_{dmax,surf}$ and of the minimum ozone mixing ratio in the upper troposphere $\mu_{min,UT}$. The latter time-series was already included in Fig. 9.10a and is shown again for better comparability. The values of $\mu_{dmax,surf}$ and $\mu_{min,UT}$ appear to be anti-correlated, reflecting the fact that deep convection not only rapidly transports low ozone air from the lowest model layer to the upper troposphere, but also rapidly transports air containing relatively high ozone mole fractions from higher altitudes to the lowest model layer as was already discussed in the previous section. Observations of increased near surface ozone values in the outflow from deep convection have been reported by Betts *et al.* (2002), and the global effects of downward transport associated with deep convection were considered in Lelieveld and Crutzen (1994), Lawrence *et al.* (2003a), and Doherty *et al.* (2005).

One question which arises is whether the chemical reactions included in the CRCTM could be sufficient to explain the very low ozone concentrations observed during CEPEX under (hypothetical) conditions of isolated air masses and little vertical exchange. Two idealized clear-sky integrations were performed to help answer this question. The CRCTM was run in two setups in which lightning NO_x produc-

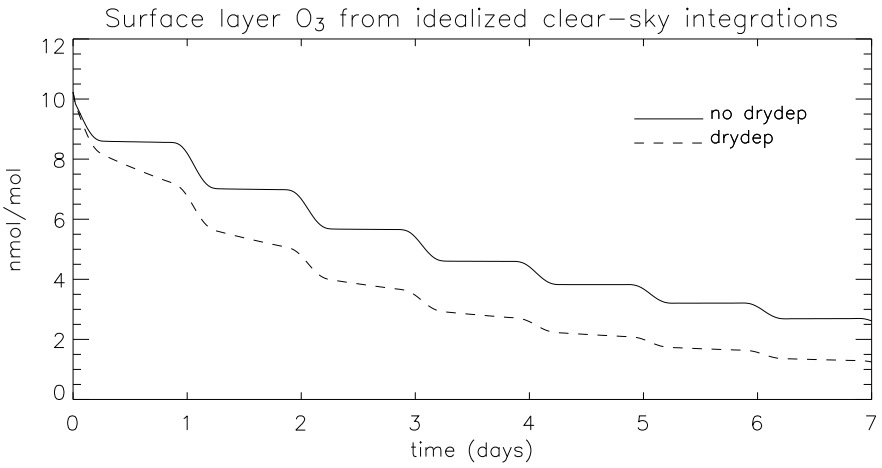

Figure 9.11: Surface layer ozone for two highly idealized clear-sky runs using the CRCTM in a "chemistry only", and a "chemistry and dry deposition only" setup, i.e. setups in which lightning NO_x production, microphysics, and advection are turned off, T and q are kept constant, the horizontal wind is set to zero, and dry deposition was either turned on or off.

tion, microphysics, and advection were turned off. The horizontal wind was set to zero and dry deposition was either turned on or off. The initial conditions were the same as for the other runs but the results were not influenced by the boundary values because the horizontal advection was turned off. In contrast to the "NO-CONV" sensitivity run introduced in Section 9.5, here air masses were assumed to be "isolated" from influences of horizontal advection. This setup is for all practical purposes identical to a box model (and results from this setup have been compared to box model results in order to test the correctness of the implementation of the photochemistry in the CRCTM).

Fig. 9.11 shows a time series of ozone mixing ratios from these runs for the lowest model layer. After seven days, the simulated ozone mixing ratio still exceeds 2.5 nmol mol^{-1} for the "chemistry only" run and has dropped below 1.5 nmol mol^{-1} for the "chemistry and dry deposition only" run. Based on the model runs, the time can be estimated it would take for ozone mixing ratios to drop below the detection limit in a highly idealized, isolated, non-advected air mass near the surface . During CEPEX, the ozone detection limit was 3 to 5 nmol mol^{-1} (Kley *et al.*, 1996). For the highly idealized parcel, it would take several days for the ozone volume mixing ratio to drop below this detection limit. Singh *et al.* (1996) explained ozone values as low as 2–5 nmol mol^{-1} observed in the boundary layer during PEM-West A by net photochemical ozone destruction in a low NO environment, sea surface deposition, and low entrainment rates from the free troposphere. Additional sensitivity studies (not shown) indicated that including artifical NO_x or HNO_3 sinks would not have a large influence on the rate at which net ozone loss in the lowest model layer occurs for the seven-day model run under the prescribed low NO_x conditions. The gross loss rate of ozone under low NO_x conditions was shown to be largely independent of

the NO_x mixing ratio while the gross formation rate under these conditions increases about linearly with the NO_x mixing ratio (see Liu *et al.*, 1992).

The reason for the near-zero ozone mixing ratio observed during CEPEX was studied in a more comprehensive study by Lawrence *et al.* (1999a) using global chemistry transport model (MATCH-MPIC). Since their simulated surface mixing ratios in the marine boundary layer did not fall below some 3 nmol mol, they suggested that critical loss processes of ozone were not represented in the model. A candidate for an additional chemical loss of ozone in the marine boundary layer is reaction cycles involving bromine, whose precursors can be released from sea-salt aerosols (see Sander *et al.*, 2003, for a review). Observations of ozone values aboard commercial aircraft indicate that incidents in which very low ozone values can be observed in the upper troposphere over the tropical Atlantic are rare (Asman *et al.*, 2003). The ozone profiles for American Samoa (Fig. 7.8) on the other hand show a few observations of very low values in the upper troposphere. Rare or not rare, explaining observed near-zero ozone values over the tropical Pacific is a useful benchmark for the theoretical understanding of the processes contributing to these observations.

Chapter 10

Hydrogen Compounds: HO_x and some Reservoir Compounds

In this chapter, model results for the hydroxyl and the hydroperoxy radicals will be discussed as well as the vertical transport and scavenging of some reservoir compounds. Constructing a budget for the family of $HO_x(=OH + HO_2)$ and related gases was not attempted here. Furthermore, the contribution of the vertical transport of water vapor to the HO_x budget was not investigated. In the upper troposphere, high supersaturations above ice are often observed (e.g. Gao *et al.*, 2004, and references therein), which are generally not represented in current CRMs. Consequently, the amount of water vapor advected to the upper troposphere may be slightly underestimated. This effect may have to be included in future studies of the upper tropospheric HO_x budget. In the final section of this chapter, a sensitivity study regarding the vertical transport of methyl hydroperoxide is presented.

10.1 Hydroxyl and Hydroperoxy Radicals

As was mentioned in the introduction, the hydroxyl and hydroperoxy radicals play key roles in tropospheric chemistry (e.g. Levy II, 1971; Crutzen, 1973; Logan *et al.*, 1981). Tan *et al.* (2001) found median daytime lifetimes of OH and HO_2 throughout the tropospheric column during PEM-Tropics B of 4 s and 4 min, respectively. Because of this difference in lifetimes, HO_2 radicals are much more abundant than OH radicals unless NO levels are very high. Consequently, the median amount of HO_x is almost equal to the median amount of HO_2 for the TOGA COARE region. The sensitivity of OH and HO_x to nitrogen monoxide mixing ratios for a tropospheric $CH_4-CO-HO_x-NO_x$ "background" chemistry was e.g. investigated by Logan *et al.* (1981) and references therein (see also Brasseur *et al.*, 1998). For moderate NO levels below about 200 pmol mol^{-1}, the surface concentration of HO_2 (and HO_x) was found to be largely independent of NO, while the concentration of OH increased considerably as a function of NO above NO mixing ratios of about 10 pmol mol^{-1}. At moderate NO concentrations, the reaction of NO with HO_2 (R26 in Table 2.3) to

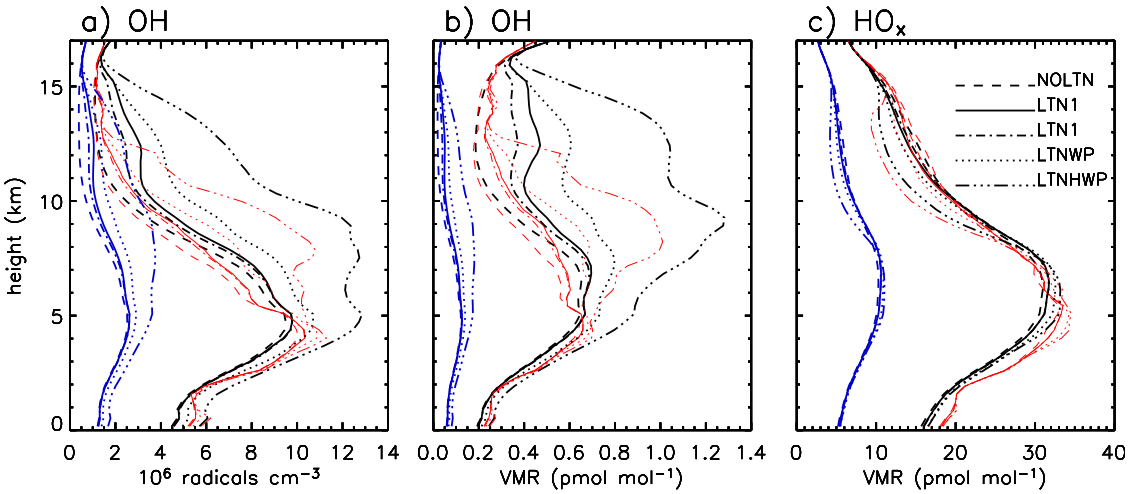

Figure 10.1: (a) OH concentration, **(b)** OH volume mixing ratio, and **(c)** HO_x volume mixing ratio: Median values (red lines) and domain and time averaged values (black lines) from two output times around local noon. Blue lines: diurnal averages.

form NO_2 and OH becomes more important for the cycling of HO_x than the reaction of OH with ozone (R6). R26 shifts the partitioning between OH and HO_2 towards higher values of the OH/HO_2 ratio while leaving the HO_x concentrations constant and decreasing the HO_2 concentrations relatively little. Above about 500 pmol mol^{-1} of NO, the HO_x concentration calculated by Logan *et al.* (1981) started decreasing considerably. This suppression of OH and HO_2 values under conditions of very high NO levels occurs mainly due to the termination reaction of OH with NO_2 (R29) in which HNO_3 is formed. In the upper troposphere, the termination reaction in which pernitric acid (HNO_4) is formed (R30) is also important (Brasseur *et al.*, 1998). An anti-correlation between NO_x and HO_x values at high NO_x mixing ratios was observed in highly polluted metropolitan environments (e.g. Martinez *et al.*, 2003).

OH and HO_2 values exhibit a pronounced diurnal cycle with a maximum at local (solar) noon and close to zero values at night. Fig. 10.1 shows horizontally domain and time averaged values and median values of OH concentrations, of OH mixing ratios, and of HO_x mixing ratios from the different lightning sensitivity runs. Values calculated for the two output times closest to local noon are presented as well as 24 h time and domain averages. The OH concentrations in Fig. 10.1 show a maximum at about 5 km altitude, where the ozone loss rates in pmol mol^{-1} were maximum. Elevated OH concentrations above the boundary layer have previously been observed above the eastern tropical Pacific under conditions of high NO_x and CO values at these altitudes (Davis *et al.*, 2001a). The average OH in the CRCTM increased with increasing lightning NO emissions. Wang and Prinn (2000), on the other hand, found extreme reductions in the domain average OH concentrations for their LTN and LTNH runs, in which the lightning NO_x production was higher (compare, e.g., discussion in Section 8.4).

The ability to measure the abundance of OH radicals in the troposphere has improved in the early 1990's and data from a limited number of field observations has become available since then. The uncertainties in the data are still large: Tan *et al.* (2001) estimates the uncertainty in the calibration of their instrument to be ±40% (at the 95% confidence level) for both OH and HO_2. According to Davis *et al.* (2001a) the typical 2σ uncertainty for OH values expressed in the observations is ±45% and that for box models is ±60%. Potential systematic errors in box models due to uncertainties in reaction and photolysis rates have been investigated e.g. by Crawford *et al.* (1997a). They derived height dependent model uncertainties based on Monte Carlo calculations. Their calculations showed that the 1σ potential systematic error for HO_2 should be within ±18% and ±35% for 0–1 km and 10–12 km, respectively. Note that such Monte-Carlo calculations are computationally expensive, currently prohibiting their use in CRMs. Tan *et al.* (2001) presented data based on observations during the PEM-Tropics B campaign. For the southwestern Pacific (south of the equator and west of 170°W, including flights from Fiji), they reported mean OH values of 0.106 pmol mol^{-1}, 0.244 pmol mol^{-1}, and 0.301 pmol mol^{-1}, for sampling heights <2 km, 2–8 km, and >8 km, respectively. The mean HO_2 values in this region were 9.59 pmol mol^{-1}, 14.60 pmol mol^{-1}, and 9.05 pmol mol^{-1} for sampling heights <2 km, 2–8 km, and >8 km, respectively. The values in Fig. 10.1 appear reasonable in the light of these observations, although a direct comparison is complicated by the strong dependence on the sampling times, the different sampling regions, and the uncertainties discussed above. Here again only the sensitivity of the local OH concentrations to the in-situ lightning NO_x source was investigated.

10.2 Methyl Hydroperoxide (CH_3OOH)

The advection of methyl hydroperoxide (CH_3OOH) from the lower to the upper troposphere in deep convective clouds and subsequent photochemical destruction has been suggested to be an important source of upper tropospheric HO_x under tropical conditions (Prather and Jacob, 1997; Jaeglé *et al.*, 1997, 2001; Wang *et al.*, 2001). Methyl hydroperoxide is formed at the expense of two radicals, CH_3O_2 and HO_2 (R14 in Table 2.3). It is destroyed by photodissociation or by reaction with OH. When CH_3OOH is photolyzed, HO_2 and OH are formed (R19), offsetting the radical loss which occurred during CH_3OOH formation. In addition, formaldehyde (HCOH) is formed which can photodissociate to yield additional HO_2. When CH_3OOH reacts with OH, either a CH_3O_2 radical (and H_2O) is formed or an OH radical (and HCOH and H_2O) is formed (by abstraction of a hydrogen atom from the CH_3 group followed by breaking of the weak O-O bond). In Table 2.3 the reactions of CH_3OOH with OH were combined in R20. In these reactions the number of radicals remains constant, while two radicals are needed to form the CH_3OOH molecule. The CH_3O_2 radical, which can be formed during the reaction of CH_3OOH with OH, can react with HO_2 to form CH_3OOH, leading to a net loss of radicals.

Fig. 10.2a shows the time and domain averaged $CH_3OOH_{(g)}$ mixing ratio, the

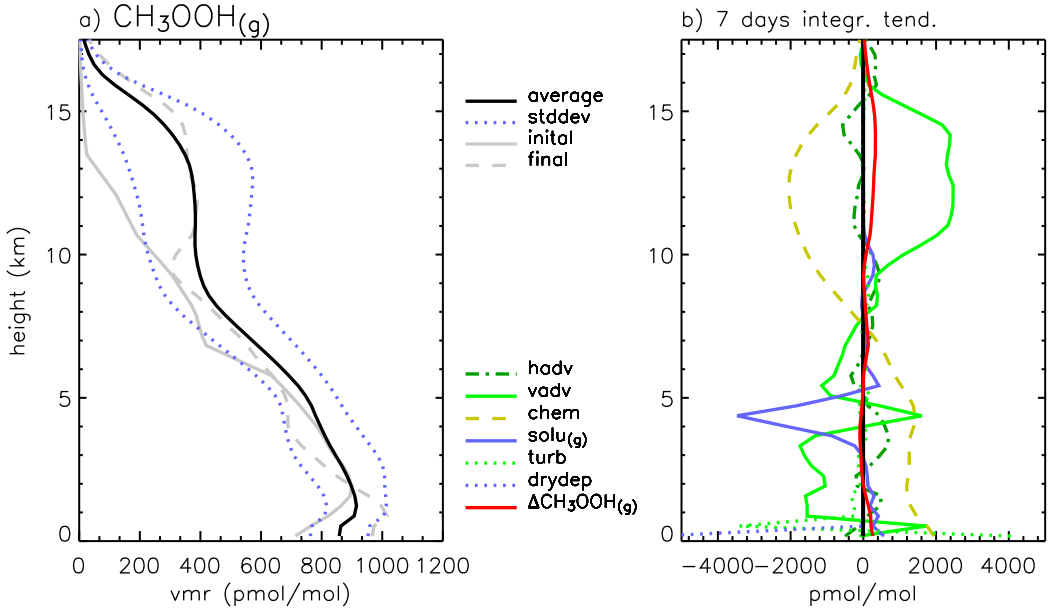

Figure 10.2: As Fig. 8.5 for methyl hydroperoxide in the gas phase.

averaged $CH_3OOH_{(g)}$ mixing ratio ± the standard deviation, and the initial and the final $CH_3OOH_{(g)}$ mixing ratio profiles for the LTN1 run. The corresponding budget terms are shown in Fig. 10.2b. Methyl hydroperoxide was formed in the lower half of the troposphere and transported upwards. In the upper troposphere, some of the CH_3OOH was advected out of the domain across the lateral boundaries. This indicates that the convective injection of CH_3OOH is likely to influence the upper tropospheric HO_x budget downwind of the convective source (see also Jaeglé *et al.*, 1997). Using a single column model, Jaeglé *et al.* (1997) found that it takes more than 10 days after the injection of peroxides for the model to return to its diel steady state level, corresponding to the lifetime of the HO_y family (6 days) which is much longer than the individual lifetimes of the peroxides (1–3 days). Jaeglé *et al.* defined the HO_y family as the sum of HO_x, HNO_4, HNO_2, and peroxides.

Fig. 10.2b shows considerable net uptake of CH_3OOH by cloudmeteors to have occurred at about 5 km and below, where the amount of liquid water (rain drops and cloud droplets) was maximum (compare Fig. 3.7). The steep increase of the scavenging tendency below about 6 km is certainly a consequence of rain drops being more efficient at removing CH_3OOH than cloud droplets, which sediment more slowly and for which sedimentation was not considered in the CRCTM simulations. The amount of CH_3OOH which was taken up in water or taken up by ice during hydrometeor freezing and was advected across the domain boundaries was negligibly small compared to the gas phase budget terms (not shown).

The amount of CH_3OOH that can be taken up by cloud droplets is limited by its relatively low Henry's law constant. Once rain is formed, the rain drops sediment

more rapidly than cloud droplets, providing an efficient means of transport. Since Henry's Law equilibrium constant K_H decreases at higher temperatures, rain water entering a grid box from above can contain more dissolved trace gas than if it were in Henry's law equilibrium. In a bulk microphysics model, this tends to inhibit further uptake, and can lead to the release of dissolved trace gas to the gas phase, unless sufficient amounts of rain water are newly formed at lower altitudes. As a consequence, efficient uptake can occur at the highest model levels with considerable amounts of rain water. Below 3 km, Fig. 10.2b yields net release of CH_3OOH from the liquid phase, indicating that scavenging in the lower model layers was more than balanced by the release of CH_3OOH from (evaporating) cloudmeteors. Ice scavenging was not considered for CH_3OOH, and the release of CH_3OOH from freezing hydrometeors did not play an important role for the CH_3OOH budget in the upper troposphere compared to upwards transport of gas phase CH_3OOH.

Dry deposition of CH_3OOH had a considerable influence on the tropospheric budget of CH_3OOH. The magnitude of the dry deposition loss term was 35% of the column integrated net chemical formation of CH_3OOH in the lowest 5 km of the tropospheric column. Compared to the average tropospheric column (up to 16 km), the value of the dry deposition term was about 5% per day. For HNO_3 and H_2O_2 on the other hand, the dry deposition term was calculated to be small compared to the other terms of the budget, presumably because in the lower troposphere HNO_3 and H_2O_2 were much more efficiently removed by wet deposition (see e.g. Fig. 11.1).

The average mixing ratios in Fig. 10.2a appear to be reasonable in the light of average vertical profiles of CH_3OOH which Singh *et al.* (1998) presented based on observations over the tropical Pacific during PEM-West A and PEM-Tropics A. At about 10 km, the average mixing ratio calculated by the CRCTM is, however, somewhat higher than the averages of the observations over the tropical oceans during PEM-West A and PEM-Tropics A. The local maximum of the average CH_3OOH profile in Fig. 10.2a between ∼10 and ∼15 km height is attributed to deep convective transport from the lower troposphere. A local CH_3OOH maximum at this altitude was also simulated in the study of deep convective transport by Mari *et al.* (2003) using a mesoscale model, albeit at lower CH_3OOH mixing ratios throughout the troposphere. Mari *et al.* studied a case during PEM-Tropics B, where the median CH_3OOH levels from observations were lower than for PEM-Tropics A (Olson *et al.*, 2001). In addition to their model results, Mari *et al.* presented CH_3OOH profiles derived from observations during an individual flight during PEM-Tropics B, exhibiting an upper tropospheric local maximum. The ceiling (maximum altitude reached by the research aircraft) was only about 12 km for the NASA DC-8. Elevated standard deviations for CH_3OOH observations between 10 and 12 km altitude during PEM-Tropics B are another possible indicator of occasional enhancements of CH_3OOH levels due to deep convection (Olson *et al.*, 2001).

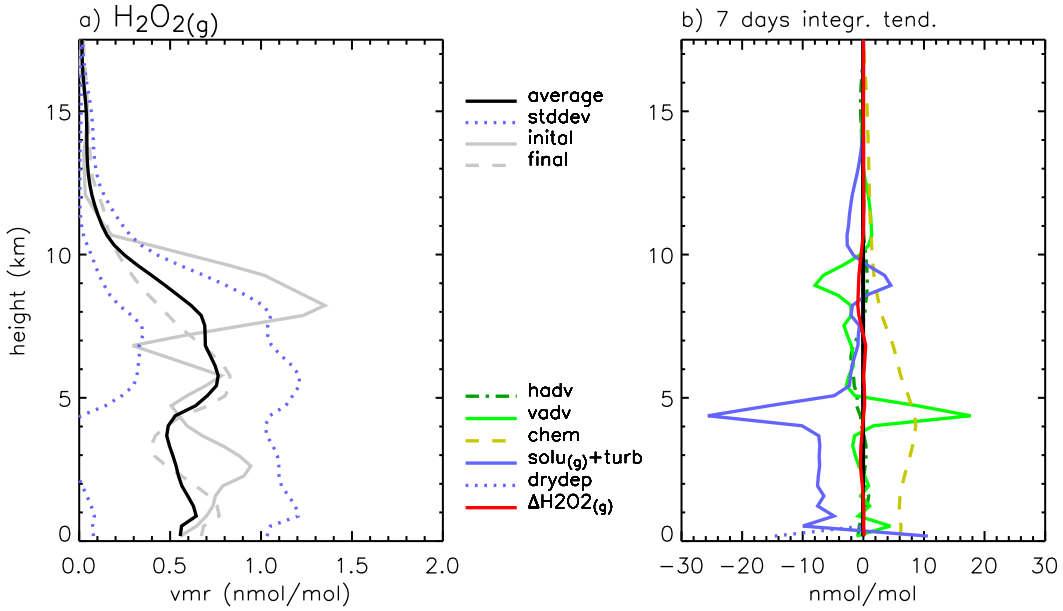

Figure 10.3: As Fig. 8.5 for hydrogen peroxide in the gas phase.

10.3 Hydrogen Peroxide (H_2O_2)

Hydrogen peroxide is far more water soluble than methyl hydroperoxide. It has been argued that the transport of H_2O_2 in deep convective clouds is very inefficient, and that consequently large contributions of deep convective H_2O_2 transport to the abundance of HO_x in the upper troposphere are unlikely to occur (e.g. Prather and Jacob, 1997; Crawford *et al.*, 1999). The simulated vertical distribution of H_2O_2 is, however, rather sensitive to assumptions about ice uptake and rejection from freezing hydrometeors. In Section 11.3 it is shown that assuming H_2O_2 to be rejected from freezing hydrometeors and at the same time not to be taken up by icemeteors leads to increased upper tropospheric H_2O_2 mixing ratios. Here, rather efficient monolayer uptake of H_2O_2 on ice crystals was assumed in the CRCTM (compare discussion in Section 2.3.2). H_2O_2 is formed from the self-reaction of HO_2 radicals (R9), which is a complicated reaction with not only a bimolecular component, but also a termolecular component and an enhancement due to water vapor (e.g. Sander *et al.*, 2000). The photolysis of one H_2O_2 molecule yields two OH radicals (R10), and the reaction with an OH radical yields an OH radical and a water molecule (R9). In the troposphere, hydrogen peroxide is an important aqueous-phase oxidant for sulfur dioxide (SO_2) and other compounds.

Fig. 10.3 shows modeled profiles and budget terms for H_2O_2. As for HNO_3, the budget terms for parameterized turbulence and for the exchange between the gas phase and hydrometeors in the liquid or ice phase were combined into one term. Net photochemical H_2O_2 formation was calculated to occur throughout the tropo-

sphere with a maximum below about 5 km, where the uptake by liquid cloudmeteors was very efficient. The sudden decrease of uptake between ∼5 km and about 6 km height can again be interpreted as a consequence of rain being more efficient at removing H_2O_2 from the troposphere than cloud droplets. Monolayer uptake on ice and subsequent scavenging (horizontal advection of H_2O_2 taken up by ice across the lateral boundaries was negligibly small compared to the other terms) caused large losses above 10 km. Below 10 km H_2O_2 was on average released in a relatively thin layer. This peak below 10 km is presumably caused by the release of H_2O_2 from cloud droplets in updrafts upon freezing (Figs. 11.1b and 11.2b give an impression). Such a peak does not occur for HNO_3 (Fig. 8.11), which was assumed to be completely retained in cloudmeteors during freezing, while it is more pronounced in the H_2O_2 sensitivity run (Fig.11.5). Below about 6 km, a positive peak of the "$solu_g$" term occurred, which was largely compensated by parameterized turbulence (not shown). The net photochemical budget term is small and positive in the upper troposphere, i.e. small net H_2O_2 formation is calculated to take place there. This is in line with the results of Crawford *et al.* (1999), who suggested local photochemistry to be responsible for observed enhancements of H_2O_2 at 11–12 km altitude. However, in Fig. 10.3, vertical transport to the upper troposphere also plays a role. For their data from the tropical Pacific, Crawford *et al.* (1999) also found that when observations of CH_3OOH were above their calculated steady-state values, H_2O_2 observations tended to be below their steady-state values, which supports the argument that while CH_3OOH is transported upwards in deep convective clouds, H_2O_2 is largely scavenged. Crawford *et al.* argued that elevated H_2O_2 levels at 11–12 km could be caused by elevated HO_x levels. Observations of enhanced upper tropospheric H_2O_2 values after deep convection were reported by Mari *et al.* (2000), and references therein. Mari *et al.* suggested that this enhancement could be caused by the rejection of H_2O_2 from freezing hydrometeors. This is in line with the results from the sensitivity study in which no ice-uptake was assumed (see Section 11.3).

10.4 Formaldehyde (HCHO)

Formaldehyde (HCHO) is a major intermediate in the oxidation chain of methane. Two photolysis channels (R21) and (R22) exist for formaldehyde, with the former yielding two HO_2 radicals per HCHO molecule. The loss reactions of formaldehyde included in the CRCTM are the reaction with OH (R23), which does not change the amount of HO_x radicals, and the abstraction of one hydrogen atom by NO_3 (R24), which may be important at night. The effective Henry's law coefficient used for formaldehyde in the CRCTM is $3.2 \cdot 10^3$ mol l^{-1} atm^{-1}, adopted from Staudinger and Roberts (1996). Formaldehyde is not taken up on ice directly from the gas phase in the CRCTM. With these assumptions, the photochemical source of formaldehyde was smaller than the sink of formaldehyde due to scavenging in the lower troposphere (Fig. 10.4b). The advection of formaldehyde across the lateral boundaries of the model domain at low altitudes also contributed positively to the formalde-

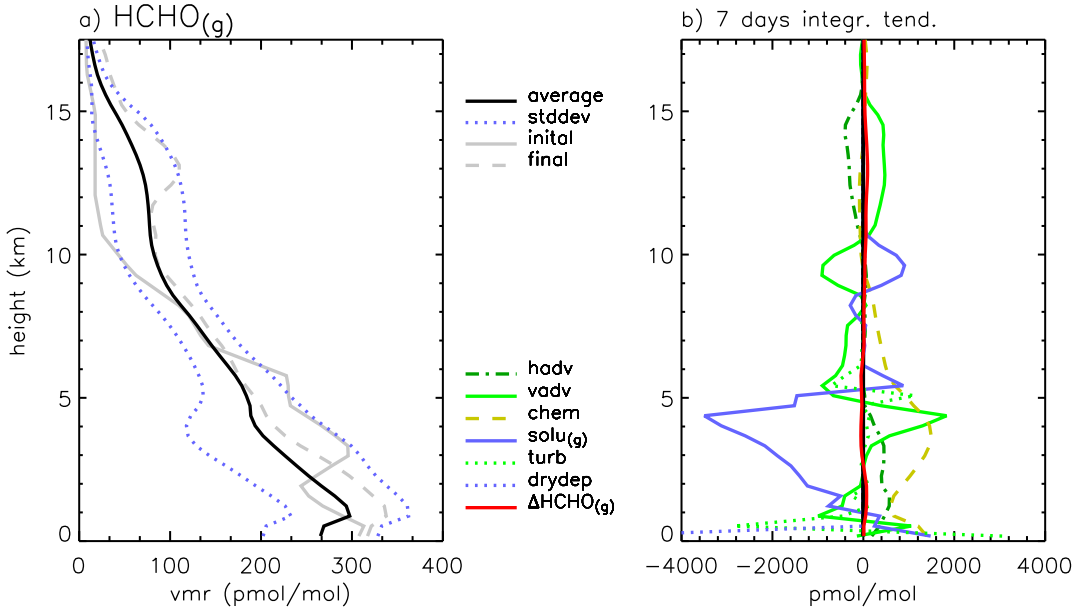

Figure 10.4: As Fig. 8.5 for formaldehyde.

hyde budget. Some formaldehyde escaped scavenging in deep convective clouds and was transported to the upper troposphere, where net photochemical destruction and transport out of the domain occurred. The profile for the average uptake of formaldehyde by or release of formaldehyde from cloudmeteors in Fig. 10.4 is similar to the one discussed in the previous section for hydrogen peroxide, except that uptake of formaldehyde on ice was not assumed to take place whereas for hydrogen peroxide the corresponding term dominated above 10 km.

Wang and Prinn (2000) found gas phase reactions to be by far the most important processes determining the budgets of HCHO and H_2O_2 in the free troposphere (which they defined from 1.5 to 17 km). Mari *et al.* (2003), on the other hand, found that scavenging played an important role for the budgets of H_2O_2 and HCHO in their study using a mesoscale model including photochemistry. In the present study, scavenging was also found to be a large contributor to the budgets of these compounds. A number of differences between this study and the study by Wang and Prinn (2000) were discussed in previous chapters, but an apparent reason for the discrepancy about the importance of scavenging for the budgets of H_2O_2 and HCHO between the two studies was not found. For H_2O_2 aqueous phase reactions which were included in the study by Wang and Prinn (2000) could have played a role. These reactions were not included in the present model study. One could argue that since the number of CRM studies including photochemistry is still small, further research on this subject is warranted.

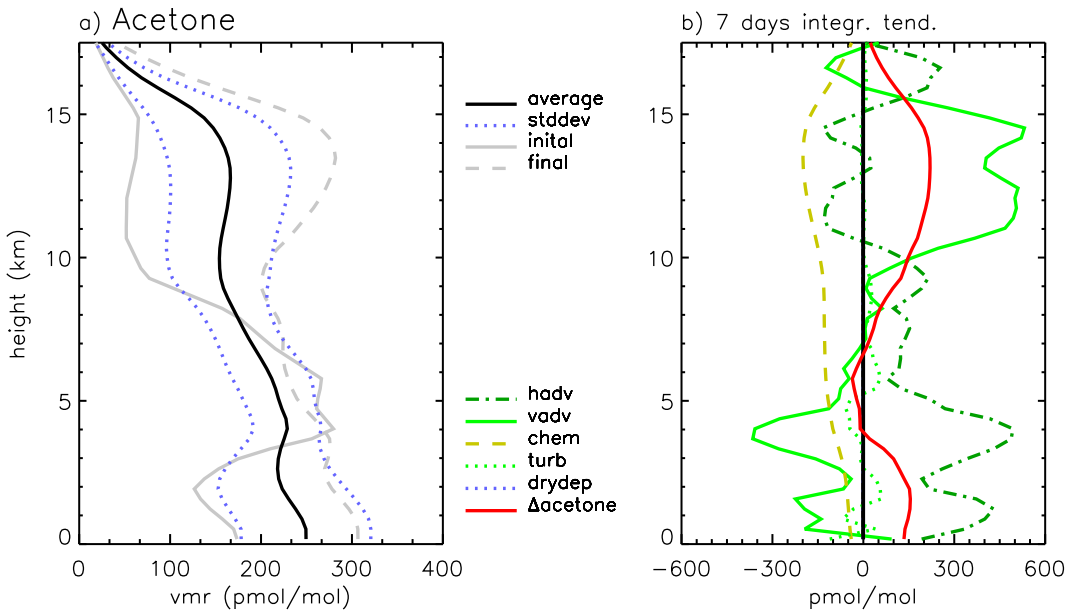

Figure 10.5: As Fig 8.5 for acetone.

10.5 Acetone (CH_3COCH_3)

The photolysis of acetone (CH_3COCH_3) is believed to be another important contributor to the HO_x budget in the upper troposphere (e.g. Singh *et al.*, 1995; Folkins *et al.*, 1998; Jaeglé *et al.*, 2001). Furthermore, acetone was found to play an important role for the conversion of NO_x to PAN (Singh *et al.*, 1995). In remote regions, the abundance of acetone was shown to be under-predicted by MATCH-MPIC, possibly due to an oceanic source (Singh *et al.*, 2001; Jacob *et al.*, 2002) which is not represented in the model (von Kuhlmann *et al.*, 2003b). Recently, Blitz *et al.* (2004) presented measurements which showed quantum yields for acetone to be temperature dependent. Based on these measurements, Arnold *et al.* (2004) calculated the estimated lifetime of acetone in the upper troposphere to increase from ∼75 to ∼250 days at mid latitudes and from ∼10 to ∼20 days in the tropics. In the study by von Kuhlmann *et al.* (2003b) and in the CRCTM calculations discussed here, the temperature dependence of the quantum yields for acetone was not taken into account. In the CRCTM, the effect of assuming too high quantum yields in the upper troposphere is to over-estimate the importance of acetone for the upper tropospheric HO_x budget. On the other hand, the effect of the lateral boundary values from MATCH-MPIC being most likely too low is probably to under-estimate the effect of the deep convective transport of acetone on the upper troposphere. Acetone is emitted (mainly from biogenic sources) and formed photochemically from the oxidation of numerous non-methane hydrocarbons (e.g. from propane, which in oceanic regions is also underpredicted by MATCH-MPIC, see von Kuhlmann,

2001). In the CRCTM, higher alkenes were not included. Although known sources of higher alkenes are concentrated in continental regions, not including these compounds into the CRCTM could lead to under-estimating the gross formation and consequently to over-estimating the net loss of acetone in the CRCTM. All in all, the uncertainties associated with acetone in the CRCTM must be considered large. In the earlier cloud resolving model study of tropospheric chemistry by Wang and Prinn (2000) acetone was not considered.

Fig. 10.5 shows the acetone volume mixing ratio profiles, and time integrated domain averaged tendencies from the LTN1 run. On average, net photochemical loss of acetone is calculated to occur inside the domain throughout the depth of the troposphere. This photochemical loss is in part balanced by the horizontal advection of acetone into the domain below 10 km and by vertical advection above 10 km. The difference between the initial and the final abundance of acetone also plays an important role in the model budget. Based on the arguments above, the photochemical loss rate of acetone was most likely over-estimated by the CRCTM, while the absolute amount was too low.

10.6 CH_3OOH Sensitivity Study

One way to develop an appreciation for the factors controlling ozone formation and loss are sensitivity studies. In some cases, even unrealistic assumptions (e.g. assuming no lightning NO_x formation) in such studies can help to address interesting questions. Based on results from sensitivity studies with column and box models, it was suggested that in tropical regions the upwards transport of CH_3OOH to the upper troposphere is rather important for the budget of ozone in the upper troposphere. Here, a sensitivity study (MHPS) was conducted based on the LTN1 run in which the transport of CH_3OOH to the upper troposphere was artificially suppressed by assuming a very high Henry's law coefficient for CH_3OOH. The ozone photochemical tendencies calculated in this sensitivity study are compared to results from other sensitivity studies, i.e. to the sensitivity towards including lightning NO_x production and to sensitivities towards assumptions regarding the uptake of H_2O_2 and HNO_3 by the ice phase. The latter studies (labeled H_2O_2_IS and HNO_3_IS in Fig. 10.6) were also conducted using the same lightning NO_x production as the LTN1 run and will be described and discussed in detail in Section 11.3 and in Section 11.2. Although the choice of which sensitivity studies to perform is mainly guided by a researcher's intuition and thus is not necessarily objective, such comparisons can help to identify key processes for ozone chemistry.

Since the sensitivity of average modeled ozone values and of the chemistry tendencies towards assumptions regarding lightning NO formation was low to moderate, in this section the differences between time and domain integrated photochemical ozone tendencies from different runs are compared (Fig. 10.6). The absolute values of the photochemical budget terms for the lightning sensitivity studies were previously presented in Fig. 9.1. The largest difference (LTN1-NOLTN) in Fig. 10.6

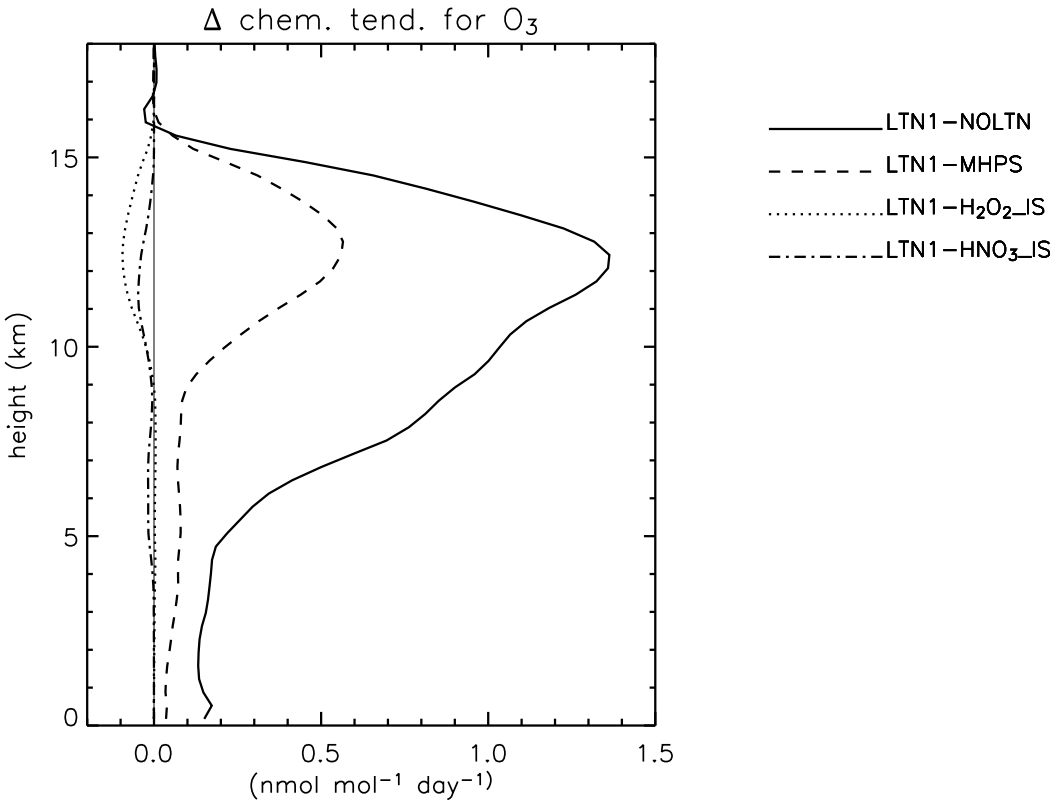

Figure 10.6: Differences between domain and 7 day time averaged net chemistry tendencies for ozone from different sensitivity runs (see text).

is caused by including lightning NO_x production. If the transport of CH_3OOH to the upper troposphere is artificially suppressed in the LTN1 run, smaller differences though of similar magnitude arise (LTN1-MHPS). Not assuming the uptake of H_2O_2 on ice results in considerable differences in simulated H_2O_2 (see Section 11.3), but only results in a relatively small increase in ozone production in the upper troposphere. The differences between the net chemistry budget terms for ozone are also small if the uptake of HNO_3 on graupel is limited (compare Section 11.2). Although these results were again derived for a specific model setup and should not be overinterpreted, this simple sensitivity study lends support to the conclusion that the transport of CH_3OOH to the upper troposphere can have comparably important influences on the chemistry of ozone in the upper troposphere, even on the relatively short time scale determined by horizontal advection and the limited size of the domain. The main difference between this study and other previous studies is that here the vertical transport of CH_3OOH was calculated using a rather sophisticated model, which does not rely on a number of assumptions made in the previous studies.

The influence of the deep convective injection of CH_3OOH is expected to increase

at higher ambient NO concentrations. Folkins *et al.* (1998) studied the dependence of the ozone production efficiencies of acetone and peroxides on NO concentrations in the upper troposphere. They found acetone to have a much greater potential for increasing ozone production rates than either CH_3OOH or H_2O_2. Note, however, that recently the photolysis rates of acetone in the upper troposphere were found to be lower than previously thought (see Section 10.5). Altogether, strong evidence exists from a number of studies that the deep convective injection of peroxides and acetone into the upper troposphere plays an important role for the photochemistry of the upper troposphere. Cloud resolving models provide a unique tool for studying the deep convective transport of peroxides and acetone under different conditions, and can help to better quantify the effects on the local photochemistry.

Chapter 11

Scavenging: Some Details and Sensitivity Studies

A number of specific results as well as some general aspects regarding the scavenging of trace gases were discussed earlier in this thesis (Section 8.5.2 for nitric acid; Sections 10.2–10.4 for methyl hydroperoxide, hydrogen peroxide, and formaldehyde; and in Chapter 6 regarding the scavenging of idealized tracers). In this chapter some details regarding the scavenging of gases by individual storms are discussed, and results from two sensitivity studies examining the uptake of HNO_3 by graupel and the uptake of H_2O_2 on ice are presented.

11.1 Examples from Individual Storms

Figs. 11.1 and 11.2 show volume mixing ratio contours of nitric acid, hydrogen peroxide, formaldehyde, and methyl hydroperoxide calculated for 24 December 1992, 2:30 GMT and for 21 December 1992, 7:30 GMT for the LTN1 run. While HNO_3 and H_2O_2 were not efficiently transported to the upper troposphere due to their high solubility, HCHO and CH_3OOH clearly show enhanced values in the upper tropospheric deep convective outflow. The enhancements of HNO_3 in the upper troposphere are caused by in-situ formation and not by transport, as a comparison of Fig. 11.1a to Fig. 11.3 for the NOLTN run shows. This is consistent with the discussion in Section 8.5.2. Local maxima of the HNO_3 and H_2O_2 mixing ratios close to x=250 km in Figs. 11.1a and b are generated by a combination of upper tropospheric production, uptake, transport in sedimenting cloudmeteors, the evaporation of these meteors, and the associated release of the compounds to the gas phase. In Fig. 11.2b a region of low H_2O_2 values was calculated to occur in the anvil outflow. The existence of this "low H_2O_2 anvil" is linked to scavenging which occurred during the upwards transport of air. Such a "low H_2O_2 anvil" was also calculated to occur in a sensitivity run in which H_2O_2 was assumed not to be taken up by ice (not shown). Low values of HCHO and of CH_3OOH in the mid-troposphere in Fig. 11.1 are related to the rear inflow into the large deep convective system, where

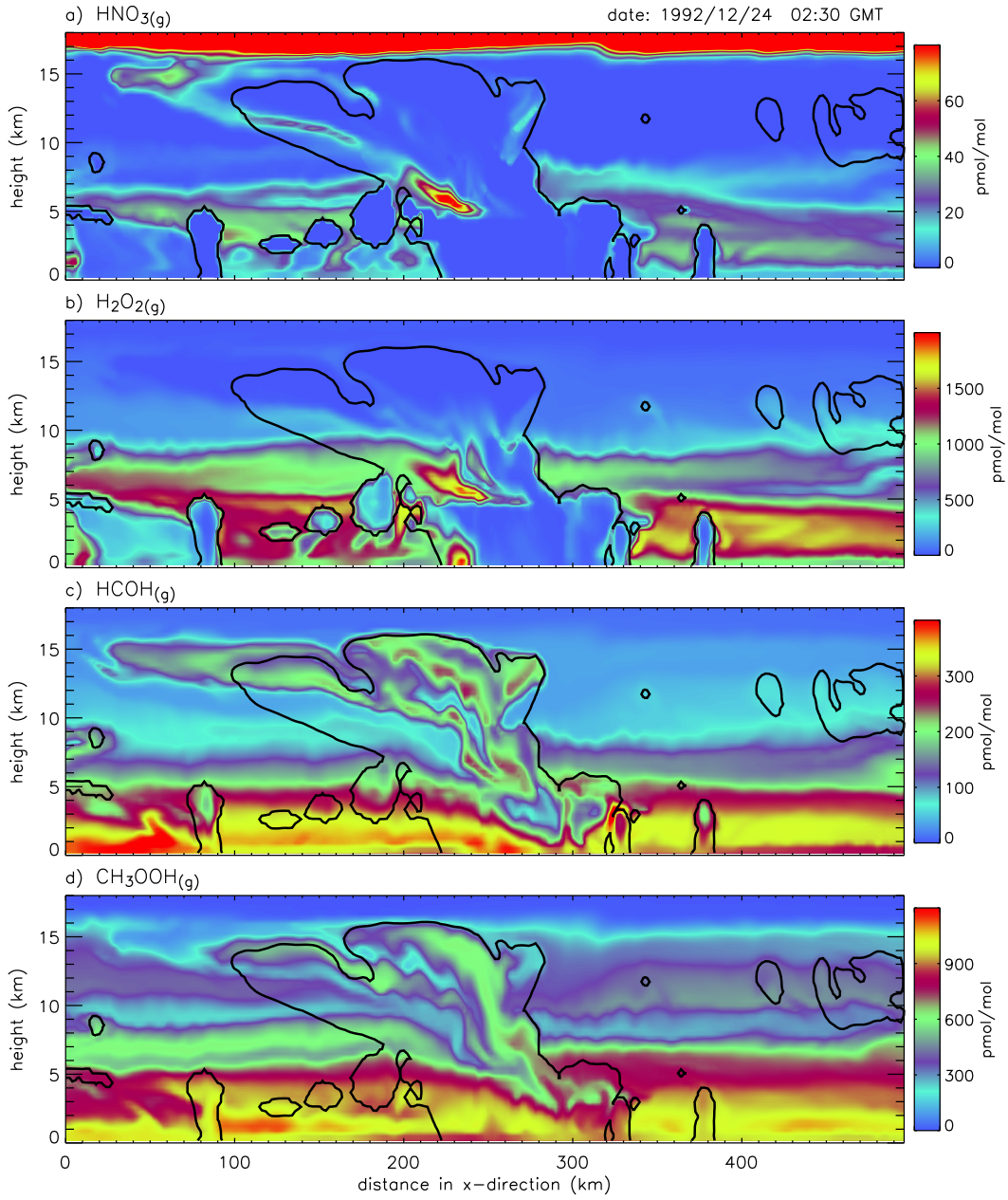

Figure 11.1: Results from the LTN1 run: volume mixing ratio contours for nitric acid, hydrogen peroxide, formaldehyde and methyl hydroperoxide on 24 December 1992, 2:30 GMT. The $q_{totm} < 0.01$g kg^{-1} mass mixing ratio contour is also plotted.

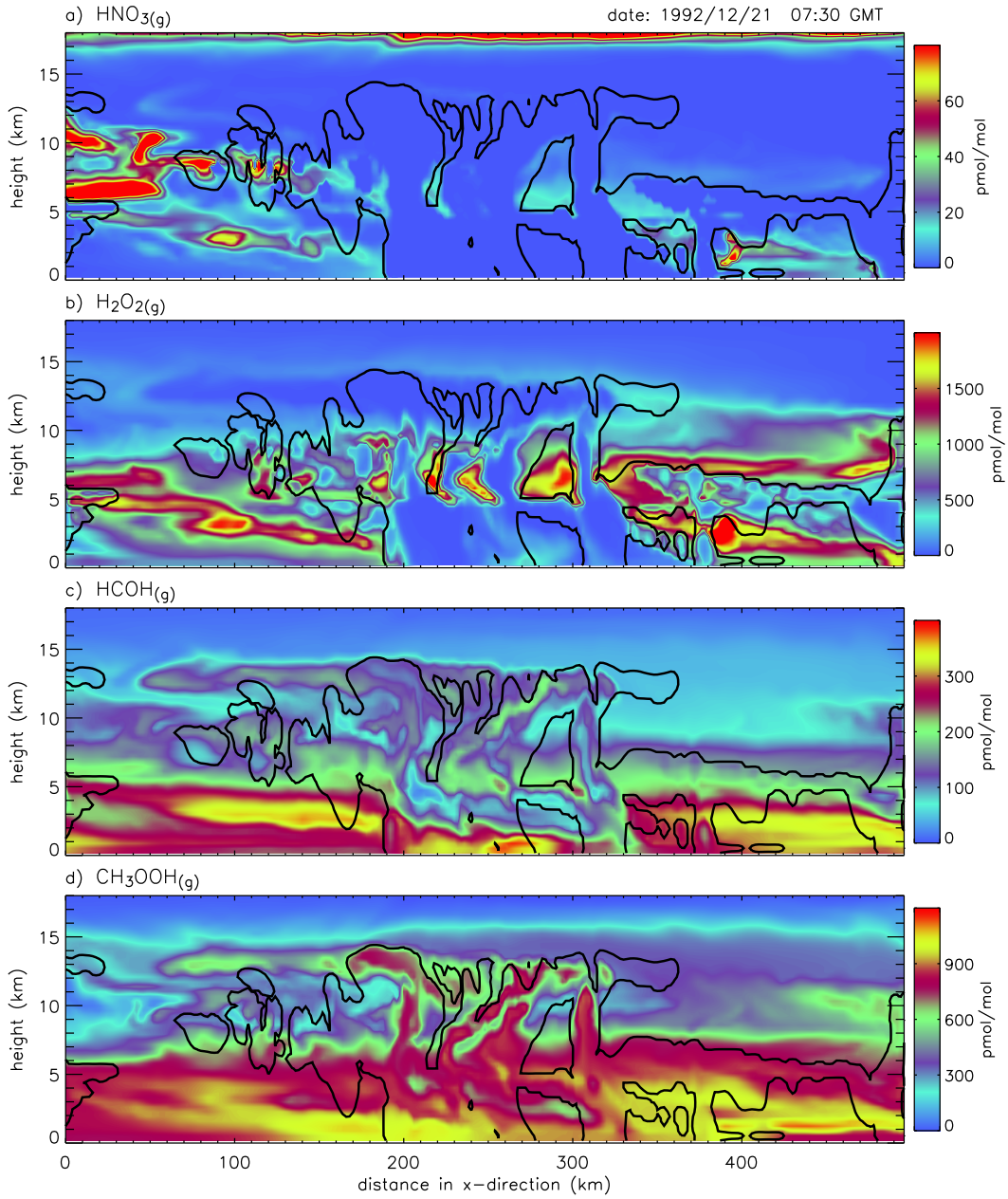

Figure 11.2: Same as Fig. 11.1 for 21 December 1992, 7:30 GMT.

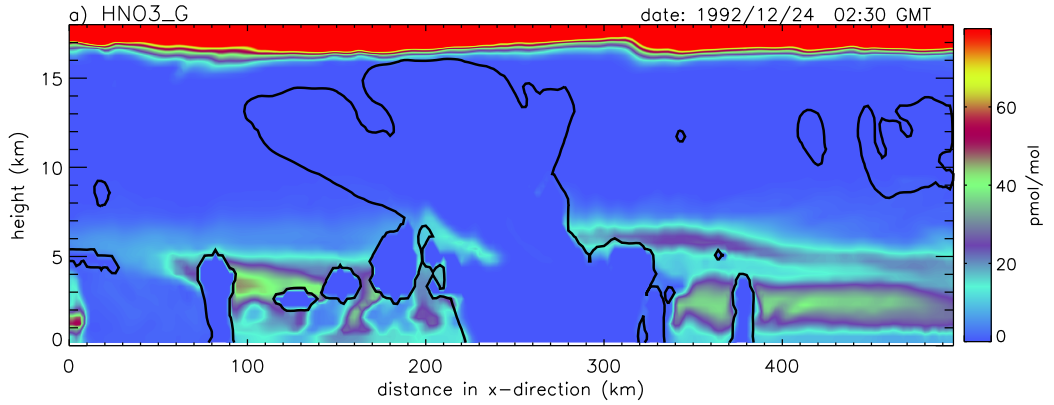

Figure 11.3: Same as Fig. 11.1a for the NOLTN run.

rapid descent is associated with diabatic cooling due to evaporating hydrometeors. The anvil outflow of HCHO and CH_3OOH extends beyond the $q_{totm} < 0.01$g kg^{-1} contour. Outflow extending beyond the ice anvil is also characteristic of insoluble gases.

11.2 Sensitivity Study: HNO_3 Uptake by Graupel

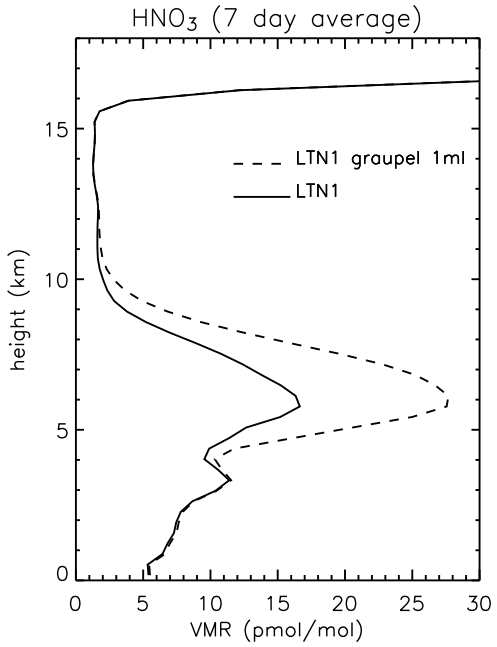

Figure 11.4: Sensitivity of time and domain averaged HNO_3 volume mixing ratios to two different assumptions regarding the uptake by graupel: In the "LTN1 graup 1ml" sensitivity run only one monolayer of HNO_3 was assumed to be taken up reversibly on graupel, and in the LTN1 run (base run) burial was parameterized by allowing 100 monolayers of HNO_3 to be taken up reversibly on graupel particles.

In all the runs previously discussed, nitric acid was assumed to be efficiently taken up by graupel. As was discussed in Section 2.3.2 describing the treatment of ice uptake in the CRCTM, the burial of HNO_3 inside graupel meteors was parameterized by allowing 100 monolayers of HNO_3 to be taken up reversibly on the surface of the graupel particles. In order to study the sensitivity of results from the LTN1 run to this assumption, a sensitivity run was performed in which the reversible maximum uptake of a single monolayer of HNO_3 on graupel was assumed. (Note, however, that in principle HNO_3 associated with graupel in excess of a single monolayer can be calculated since the release to the gas phase is assumed to be limited kinetically.) All other parameters, e.g. the assumptions regarding the uptake of H_2O_2 on ice, were kept fixed for the sake of this sensitivity run, and the lightning NO_x production was assumed to be the same as in the LTN1 run.

Fig. 11.4 shows domain averaged vertical profiles of HNO_3 for the LTN1 run and for the sensitivity run. At about 6 km height the difference of the average HNO_3 volume mixing ratio reaches about 9 pmol mol^{-1}. The relative effect on horizontally domain and time averaged ozone mixing ratios was less than 1‰ (part per thousand) at all altitudes. It should, however, be noted that in the setup used here, the effect of assuming different lightning NO_x production rates on domain averaged ozone was also very small for most runs. The sensitivity of ozone results to assumptions regarding the uptake of HNO_3 would certainly increase a bit if longer timescales (or larger domains) were considered. Once formed, the photochemical lifetime of HNO_3 can be days to weeks. In environments with active deep convection its photochemical lifetime is long compared to the lifetime with respect to scavenging. Consequently, a large fraction of HNO_3 is scavenged and does not contribute to the chemical source of NO_x via photolysis.

11.3 Sensitivity Study: H_2O_2 Uptake by Frozen Hydrometeors

Hydrogen peroxide was assumed to be taken up reversibly on hydrometeors in the ice phase (ice crystals, snow, and here also graupel) assuming the same adsorption enthalpy as derived from measurements for nitric acid (see discussion in Section 2.3.2). In order to test the sensitivity of the results from the LTN1 run to this assumption, a sensitivity run was performed in which no uptake of H_2O_2 from the gas phase by hydrometeors in the ice-phase was assumed. In addition, the retention coefficient for H_2O_2 was decreased from 0.2 in the LTN1 run to zero in this run, causing dissolved H_2O_2 to be completely released to the gas phase upon hydrometeor freezing. Again, all other parameters were kept fixed.

Fig. 11.5 shows domain averaged vertical profiles of H_2O_2 for the LTN1 run and for the sensitivity run. Not allowing H_2O_2 to be taken up by ice results in elevated H_2O_2 values almost throughout the entire depth of the tropospheric column and strongly affects the calculated budget of H_2O_2 (Fig. 11.6). The difference in horizontally domain and time averaged mixing ratios of ozone is less than 1‰ at all altitudes for these sensitivity runs. Large changes of H_2O_2 and small changes of

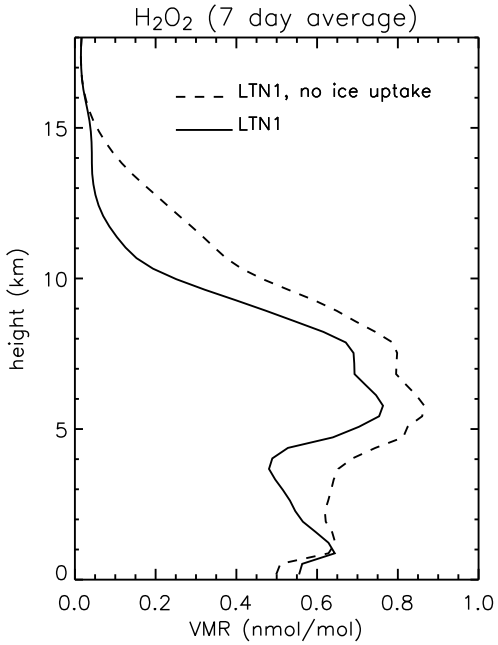

Figure 11.5: Sensitivity of time and domain averaged H_2O_2 volume mixing ratios to two different assumptions about the uptake of H_2O_2 on ice: in the LTN1 run reversible, kinetically limited Langmuir uptake by ice, snow and graupel was assumed. In the "no ice" sensitivity run no uptake on ice was assumed and the retention coefficient was set to zero.

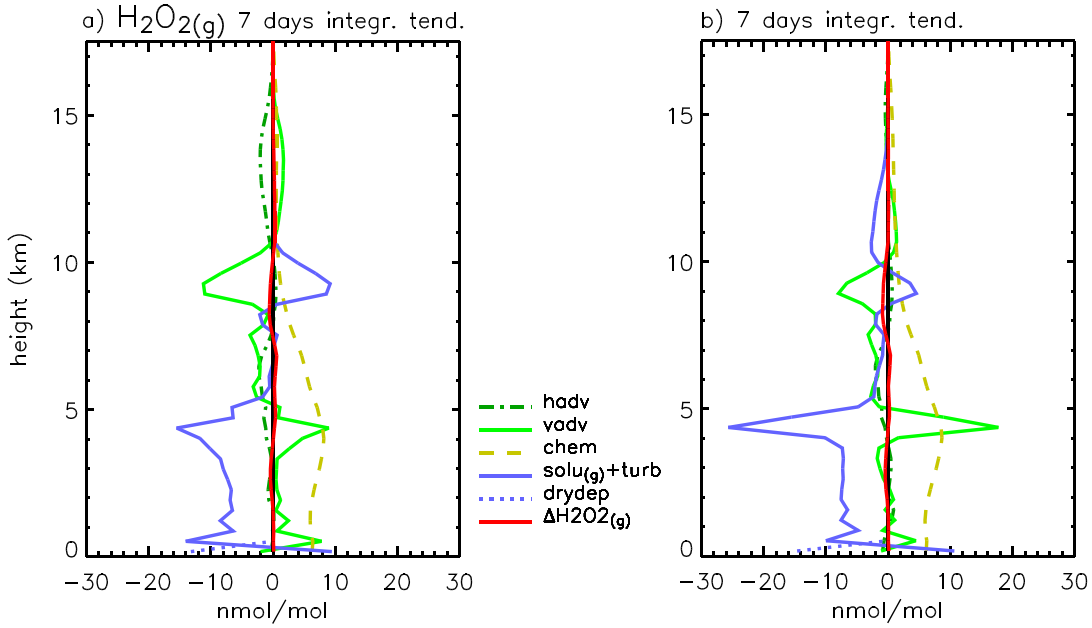

Figure 11.6: **(a)** Same as Fig. 10.3b for the sensitivity run assuming no uptake on ice and complete rejection during freezing **(b)** same as Fig. 10.3b (for easier comparison).

ozone were also found using a regional model for sensitivity studies about the role of aqueous chemistry (Barth *et al.*, 2002). While in the sensitivity run presented in this section, no ice uptake of H_2O_2 was assumed, very efficient ice uptake was assumed in the other runs. The assumption about the uptake of gas phase H_2O_2 on ice certainly represents an upper limit, due to large uncertainties about the adsorption enthalpy of H_2O_2 (compare discussion in Section 2.3.2).

Chapter 12

Conclusions

A cloud resolving chemistry transport model (CRCTM) based on the Weather Research and Forecast (WRF) model and on photochemistry from the Model of Atmospheric Transport and Chemistry – Max Planck Institute for Chemistry Version (MATCH-MPIC) was developed and used to examine influences of tropical deep convective cloud systems on different trace gases including ozone in a case study for the TOGA COARE region. In most of the model runs considered in this thesis, effects of larger scale flows were included in the computation of trace gas transport, which have not been taken into account in previous multi-day cloud resolving and single column model studies of deep convective tracer transport (Lu *et al.*, 2000; Rasch *et al.*, 2003; Bechtold *et al.*, 2005). Since today's limited area cloud resolving models cannot simulate large scale circulations, in the present study a tendency term representing the effect of the mean vertical velocity on the advection of trace gases (VLSAT) was defined based on the mean vertical velocity derived from observations in the study region. Furthermore, lateral boundary conditions for trace gases were specified.

Including the effect of the mean vertical velocity on trace gas transport largely reduced the downwards transport due to the mass balancing subsidence calculated to occur between clouds, and considerably changed modeled trace gas profiles. On the other hand, rapid downwards transport related to rear inflow (e.g. Section 4.2.2) into mesoscale convective systems occurred in runs with and without VLSAT. Although net ozone transport was computed to take place from the troposphere to the stratosphere in the runs using VLSAT, it was shown that downwards transport related to deep convective clouds was important for the budgets of ozone and other compounds such as PAN, which in oceanic regions outside the main continental outflow have photochemical sinks in the lower troposphere. This was expected based on the results from previous global model studies (e.g. Lelieveld and Crutzen, 1994). Since the downwards transport of ozone from the tropopause region was simulated to take place in thin filaments (Section 9.6), sharp vertical gradients were largely maintained at the tropopause. In some cases these filaments of air with origin close to the tropopause reached far into the troposphere. This finding complements a result by Kley *et al.* (1997), who argued that observed sharp ozone gradients indicated

a lack of vertical mixing across the tropopause. However, the simulated transport of ozone rich air from the tropopause region did not offset the effect of the upwards transport of ozone poor air from the lower troposphere into the upper troposphere. Wang and Prinn (2000), who did not include a VLSAT term into their cloud resolving model, on the other hand, found downward transport of O_3-rich air from the lower stratosphere to be very important for the O_3 mass budget in the upper troposphere. Furthermore, their simulations showed that the upward transport of O_3-poor air from below did not significantly decrease O_3 concentrations in the upper troposphere. Since the initial ozone mixing ratio profile used by Wang and Prinn varied only by $\sim$3–4 nmol mol^{-1} between the surface and the upper troposphere, this is not surprising given that current estimates regarding the chemical lifetime of ozone in the lower tropical marine boundary layer are of the order of several days. In the present study, the upward transport of ozone-poor air was found to more than compensate the downward transport of ozone rich air into the upper troposphere and to play an important role for the upper tropospheric ozone budget.

In most model runs lateral boundary conditions for trace gases were specified. It was argued that especially in situations with vertical wind shear, the horizontal advection due to larger scale flows should be considered, if limited area models with periodic boundary conditions or single column models are run longer than the time $\tau_{adv} = L/\overline{v}_{max}$ it takes to advect tracers horizontally across the entire domain, where $\overline{v}_{max} = max(\overline{v}(z))$ is the maximum domain averaged horizontal wind speed, and L is the horizontal domain length. The model calculated budgets of a number of trace gases such as ozone and NO_x were found to directly be influenced by horizontal advection across the lateral domain boundaries, while short lived trace gases were affected indirectly by the advection of longer lived precursors. Lightning produced NO_x was mainly transported out of the domain in the upper troposphere. Net advection of ozone into the domain took place at mid- and upper tropospheric levels, from where net downwards transport was computed. In the lower troposphere net advection of ozone out of the domain was simulated to take place in association with low level westerly winds related to the westerly phase of the intra-seasonal oscillation. The maximum net photochemical loss of ozone expressed in nmol mol^{-1} was computed to occur at about 4–5 km altitude, where ozone mixing ratios were higher than in the marine boundary layer, and where relatively low cloud tops occasionally lead to enhanced photolysis rates and more rapid photochemical loss. The computed ozone budget was found to be strongly influenced by both the initial and the lateral boundary conditions in 7–day 2-D TOGA COARE simulations using a 500 km domain length. The importance of large horizontal trace gas gradients related to the ITCZ (and of the intra-seasonal oscillation ISO) for the transport of ozone and CO in the TOGA COARE region was also illustrated based on results from MATCH-MPIC in Section 7.2.

To the author's knowledge, this was the first study in which results from a multi-day 3-D cloud resolving model run including idealized tracers were presented. These results were compared to results from a 2-D run. Differences between the 2-D and the 3-D run were mainly attributed to an increase in horizontal advection across the

lateral domain boundaries due to the meridional wind component in the 3-D model runs, which was not considered in the 2-D simulations. Furthermore, to the author's knowledge, this was the first cloud resolving model study including photochemistry aimed at studying the effect of cloud systems rather than of isolated storms, and was one of the very few studies so far to study the influence of lightning produced NO_x on local photochemistry using a cloud resolving model.

A number of sensitivity studies examining the role of lightning produced NO_x were conducted. It was shown that in order to obtain reductions of ozone associated with lightning NO_x production, which could explain near-zero ozone values observed during CEPEX, an extremely high number of NO molecules produced per flash had to be assumed. Considerable local reductions of upper tropospheric ozone volume mixing ratios were obtained in runs in which the number of NO molecules formed per flash was set to $3{\cdot}10^{27}$, based on the study by Franzblau and Popp (1989). The suggestion by Wang and Prinn (2000) that near-zero ozone values observed during CEPEX could be linked to lightning NO_x production (and not to vertical transport from the boundary layer, which had a relatively weak influence in their study due to the small vertical gradient of tropospheric ozone in their initial profiles) was also largely based on a cloud resolving model run in which they adopted the same estimate from Franzblau and Popp. However, since the study by Franzblau and Popp the observational evidence has been growing that the amount of NO_x formed per flash is generally much lower. Assuming a global flash rate of 44 flashes per second (Christian *et al.*, 2003, for both IC and CG flashes), a value of $3{\cdot}10^{27}$ molecules per flash yields an estimate of about 97 $\mathrm{Tg(N)\,year^{-1}}$ for the amount of NO_x produced globally through lightning. This value is clearly beyond current estimates of the range of uncertainty, which is widely accepted to be 2–20 $\mathrm{Tg(N)\,year^{-1}}$ (WMO, 1995; Huntrieser *et al.*, 2002). Values in excess of 20 $\mathrm{Tg(N)\,year^{-1}}$ are very unlikely (Ridley *et al.*, 1996; Price *et al.*, 1997a; Ridley *et al.*, 2004; Labrador *et al.*, 2005). More relevant, however, is the fact that the high number of NO molecules per flash estimated by Franzblau and Popp (1989) has not been supported by a number of more recent single storm observations (see Section 2.6).

Wang and Prinn (2000) cited the study of lightning NO_x production in a thunderstorm over New Mexico by Ridley *et al.* (1996), where flash rates are in general much higher than those observed in marine tropical deep convection, as a case in which ozone loss associated with lightning NO_x production was seen. According to Ridley *et al.* the majority of flights showed that ozone was reduced relative to the extra-cloud air owing to transport of ozone-poor air from lower altitudes. Ridley *et al.* found ozone to be a good tracer over the lifetime ($\sim$1 hour) of the storms they observed. Based on results from the observations of Ridley *et al.*, who sampled only the upper core and anvil of two storms, the amount of NO per flash can be estimated. This estimate yields 1.3 to $1.6{\cdot}10^{26}$ molecules per flash for their August 12 storm and less for the August 19 storm, which is in much better agreement with more recent studies than the estimate of Franzblau and Popp (1989). On the whole, Wang and Prinn (2000) computed about 3 times as many flashes per day per km domain length as in the LTNWP and the LTNHWP run in the present study. It could, however,

be argued that the total numbers of flashes in both studies are within the range of uncertainties associated with lightning observations during TOGA COARE.

While in the simulations by Wang and Prinn (2000) the upward transport of ozone-poor air from the boundary layer did not significantly decrease ozone concentrations in the upper troposphere, here ozone minima in the upper troposphere were found to be directly linked to the transport in deep convective clouds, in agreement with results from two previous modeling studies for CEPEX (Wang *et al.*, 1995; Lawrence *et al.*, 1999a). However, the reproduction of the extremely low ozone concentrations observed during CEPEX (which started in the TOGA COARE region) might not be anticipated in the present study, since near-zero ozone values in the lower troposphere were not expected to occur during the westerly phase of the intra-seasonal oscillation and since the boundary values in the upper troposphere did not yield extremely low ozone concentrations. The strong dependence of the modeled ozone values on the initial and boundary conditions found in this study suggests that low ozone values are not not necessarily caused by in-situ chemistry over a relatively small (here: 500 km domain length) region. Instead, extremely low ozone values in the marine boundary layer are probably the result of processes acting over longer time scales. In the meantime, the air masses can be advected over relatively large horizontal distances. In Section 7.3.1, it was discussed that the variable flow associated with the intra-seasonal oscillation could help to explain the lack of coincidence between upper and lower tropospheric ozone minima observed during CEPEX. As was argued in Section 9.8, additional studies are necessary in order to explain the extremely low ozone concentrations observed during CEPEX.

In the present study, net photochemical ozone loss was on average calculated to occur in the lower troposphere in all lightning sensitivity runs, while in the upper troposphere net ozone production was found to take place. This result is in line with results from previous box model studies for nearby regions, which used observed trace gas abundances as input (e.g. Crawford *et al.*, 1997b). Wang and Prinn (2000) on the other hand calculated net photochemical production to occur almost throughout the height of the troposphere up to about 15 km in their 30 hour long 2-D reference run not including lightning NO_x production. In their LTNH run, they computed net chemical ozone loss to occur throughout the troposphere. The latter is presumably mainly the consequence of the higher flash rates and the higher NO_x concentrations in their LTNH run compared to the LTNHWP run in this study. The choice of boundary conditions (e.g. specified vs. periodic) has most likely played a less important role since Wang and Prinn used a 1000 km domain length and limited their simulations to a 30 h episode, but it has a large effect on simulated NO_x concentrations in longer multi-day limited area simulations. During the last 6 days of the 7–day TOGA COARE episode, up to 83% (in the LTN1 run) of all the lightning produced NO_x was advected out of the domain across the lateral boundaries (Section 8.4).

The fraction of lightning produced NO_x which was chemically converted in the vicinity of the lightning source depended on assumptions regarding the strength and the altitude (i.e. on the IC/CG ratio) of the NO_x source. It was 13% for the LTN1

and 20% for the LTN2 run. In the LTNWP and the LTNHWP run it was 34% and 37%, respectively. Wang and Prinn (2000), who computed higher flash rates, calculated this fraction to be 28% in their LTN run and 12% in their LTNH run, in which they found the NO_x production to be HO_x limited. HO_x limitation appears to have played a smaller role in the present study, but could perhaps be more important in mid-latitude thunderstorms, where flash rates are generally higher. The relatively fast NO_x losses associated with lightning NO_x plumes are not straightforward to reproduce in global models. For the time being, uncertainties related to chemical loss processes in the vicinity of lightning are only one contributor among many to uncertainties regarding lightning NO_x in global models. One could certainly argue that the large but decreasing uncertainty regarding total NO_x production by lightning still largely outweighs this uncertainty. However, in-situ losses can be considerable as was suggested by Wang and Prinn (2000), and should not be ignored. While in the lightning sensitivity runs, lightning NO_x production was by far the largest source of domain integrated tropospheric NO_x, in the NOLTN run, the net photochemistry term was the most important source term of NO_x in the model domain. The largest contributor to the chemical source was the decomposition of PAN below 5 km, which was in part balanced by the formation of HNO_3. PAN was not included in the cloud resolving model study by Wang and Prinn (2000). In a run in which they did not assume lightning NO_x production, gas phase chemistry acted to remove more than 30% within 30 h of the total NO_x mass, while the total tropospheric NO_x column density changed by only ∼5% during the 7–day NOLTN run in this study (Table 8.4), mainly due to the decomposition of PAN which was horizontally advected into the model domain (see also Section 8.5.1).

Below 5 km altitude, scavenging was found to be very important for HNO_3, H_2O_2, and HCHO. The loss of these compounds due to scavenging was in large parts balanced by in-situ (i.e. inside the domain) chemical production below 5 km. CH_3OOH was chemically formed in the lower troposphere and transported to the upper troposphere, where photochemical loss and horizontal advection were the largest terms in the budget. Scavenging of CH_3OOH played a role for the budget between about 3 km and 5 km altitude, but did not have an obvious influence on the domain averaged vertical profiles. While HNO_3 was not transported to the upper troposphere in considerable amounts, a small fraction of HCHO escaped scavenging and was transported to the upper troposphere (above 10 km). The simulated H_2O_2 mixing ratios depended strongly on assumptions regarding the ice phase. Barth *et al.* (2001) has shown that the vertical transport of idealized soluble tracers strongly depends on the retention coefficient, i.e. on the fraction of a dissolved trace gas which is retained by (or alternatively rejected from) hydrometeors upon freezing. In the present study, the transport of idealized highly soluble tracers which were initially located in the boundary layer was found to be very inefficient independent of whether retention by ice was assumed, while the retention coefficient played an important role for tracers which had non-zero initial concentrations in the mid- and upper troposphere (such as the tracers studied by Barth *et al.*, 2001), i.e. for highly soluble trace gases with a chemical source above the boundary layer. Differences regarding the scavenging of idealized highly soluble tracers which were found between

the CRM study by Barth *et al.* (2001) and the global model study by Crutzen and Lawrence (2000) were attributed to the use of different initial/boundary values in the two studies.

An approach to modeling the uptake of trace gases on ice was discussed in Section 2.3.2. However, a satisfactory theoretical framework for the treatment of compounds which can be taken up by ice from the gas phase and which are in addition either partially or completely trapped in hydrometeors upon freezing is still lacking for CRMs. Sensitivity studies showed potentially large influences of different assumptions on the modeled volume mixing ratios of H_2O_2 and HNO_3. The sensitivity of the time and domain integrated photochemical tendencies of ozone was, however, small in these studies compared to the sensitivities towards uncertainties in lightning NO_x production. Large changes of H_2O_2 and of HNO_3 together with small changes of ozone were also found in sensitivity studies regarding the role of aqueous chemistry in boundary layer clouds by Barth *et al.* (2002), who used a regional model to study a 20° by 20° region centered over Hawaii.

A number of very large uncertainties still exist concerning the lightning NO_x production. First of all, the number of NO molecules produced per flash is still very uncertain. An additional uncertainty is related to the parameterization of flash rates and to the ratio of IC/CG flashes. From the work of Pickering *et al.* (1998) it became apparent that the exponent in the flash rate parameterization by Price and Rind (1992) may have to be adjusted for different storms. Pickering *et al.* (1998) used different exponents for CRM simulations of different storms. Furthermore, a 2-D model setup was used in this study and in the study by Wang and Prinn (2000) introducing additional uncertainties regarding the influence of lightning NO_x on chemistry (Section 8.2.2). The location of flashes relative to the storm/updraft is another poorly quantified parameter and a potentially important source of uncertainty. More research on these issues leading to new parameterizations is definitely needed. Furthermore, so far, the existing flash rate parameterizations (Price and Rind, 1992; Wang and Prinn, 2000; Petersen *et al.*, 2005, and others) have not yet been inter-compared in CRMs. Other uncertainties, in particular those related to using 2-D instead of 3-D simulations for soluble trace gases and to the model input for HNO_3, acetone, and PAN were also discussed. However, in the present study, these uncertainties weigh almost certainly less than uncertainties in total lightning NO_x production as far as the modeled ozone budget is concerned.

At present, cloud resolving models have only been used in a small number of studies regarding tropospheric photochemistry, but their use is becoming increasingly attractive as the computational resources to perform the simulations are gradually becoming available. These models allow a better representation than global models for a number of processes which are relevant for the influence of deep convection on photochemistry. However, a number of processes still have to be parameterized. Consequently, the need arises to evaluate the results of cloud resolving models using observations. Furthermore, sensitivity studies can help to identify key parameters and related uncertainties. A study, in which for the first time a number of contemporary cloud resolving transport models (a few of which include a lightning

parameterization and/or photochemical reactions) are intercompared and evaluated using observations is currently being conducted (Barth *et al.*, 2005). The major advantage of cloud resolving models is that they can help to study important details of deep convective transport and of the influences on chemistry, which would otherwise be difficult to assess.

Chapter 13

Outlook

The model developed within the framework of this study will continue to be used in order to study effects of deep convective cloud systems on local photochemistry. As increasing hard disk space is becoming available, detailed 3-D model studies including photochemistry will soon be feasible. Future studies have been planned on the roles of lightning NO_x production and on the roles of the ice phase in deep convective clouds for atmospheric photochemistry under different meteorological conditions at different latitudes. These studies will aim at improving the understanding of the roles of different processes, and at reducing existing uncertainties in the cloud resolving model. In particular, sensitivity studies will be co-ordinated with laboratory studies investigating the uptake of trace gases by the ice phase. Another main focus of future efforts is likely to be on model studies in association with field observations and global model studies of deep convection and photochemistry in order to better quantify the influences of deep convection on the budgets of NO_x, HO_x, and ozone. A mid-latitude case study using a similar setup as the one presented here will likely be based on the U.S. Department of Energy's ARM (Atmospheric Radiation Measurement program) in the Southern Great Plains for an episode in June–July 1992 (GCSS WG4 Case 3).

The setup presented in Chapter 3 was in part developed with the aim of eventually performing multi-day comparison studies using single column and cloud resolving model results (compare discussion in Section 4.6). In the near future, interactive global chemistry-climate models will increasingly be used to study chemistry-climate feedback mechanisms. As computer power increases, global weather forecast models, atmosphere-ocean climate models, and eventually also global chemistry-climate models will successively become cloud resolving. While global weather forecast models will certainly be resolving cloud systems in less than a decade from now, coupled chemistry-climate models will still rely on parameterizations of deep convective transport for some time. Comparisons between CRMs and single column models have previously been applied in the study of deep convection and its parameterization (e.g. Xu and Krueger, 1991; Xie *et al.*, 2002), and very recently Bechtold *et al.* (2005) presented the first (to author's knowledge) study of this kind considering tracer transport. Bechtold *et al.* did not, however, include large scale

influences. Studies as the one by Bechtold *et al.* could help to reduce the large differences between various tracer transport parameterizations known to be existing today (Mahowald *et al.*, 1995; Rasch *et al.*, 2003), in the future could also be extended to the scavenging of soluble tracers. However, continuing efforts to evaluate current cloud resolving models and to identify key uncertainties in these models are a valuable prerequisite for such studies.

Aqueous chemistry is currently not included in the CRCTM. While the effect on ozone may not be crucial for limited area simulations of the TOGA COARE region, other trace gases would most likely be strongly affected (compare discussion in Sections 2.4, 11.3, and in Chapter 12). Furthermore, a simple sulfur chemistry could be implemented in order to determine the pH value of cloud droplets. The pH value plays an important role in determining the uptake of soluble gases into the liquid phase and is currently kept fixed. Frozen hydrometeors are currently treated as liquid hydrometeors in the calculation of the photolysis rates. This should be improved in studies focusing on the influence of the ice phase on photochemistry. Sources of uncertainty regarding lightning produced NO_x, which will have to be addressed, have been discussed in the previous section. New observations of the location of lightning strokes relative to the structure of mesoscale convective systems which could help to assess uncertainties related to the horizontal and vertical positioning of the lightning NO source have recently been presented by Carey *et al.* (2005). A primary aim in developing new lightning parameterizations should be to better couple the flash parameterization to the simulated cloud microphysics. In simple parameterizations use could be made of empirical relationships between ice water content and lightning, which were found to exist on the global scale (Petersen *et al.*, 2005).

An advantage of the WRF-based CRCTM is that WRF in principle allows for multiple nesting and for nudging. In multiply nested model setups, finer grids are recursively placed inside a coarse resolution grid which can cover a much larger area than the fine resolution grids. Cloud resolving nested model setups have a large potential for the study of deep convective cloud systems and chemistry in association with observational campaigns, while the advantage of the meteorological setup used here is that it is well established for simulating cloud systems. Disadvantages of the setup used here are that this setup does not allow the convergence of air across the model boundaries, and that meteorological input data which is typically derived from comprehensive observation campaigns is needed to specify the terms in Equations 3.1 and 3.2. While multiply nested models have been proven useful for a number of purposes, they have not yet been used for TOGA COARE. Large scale models face great difficulty with accurately simulating the intra-seasonal oscillation (Zhang, 2005), and in mesoscale models most likely a nudging approach would have to be applied (i.e. an approach in which the model meteorology is nudged towards observations, as has e.g. been done here for the horizontal wind using the term in Equation 3.4). Furthermore, a considerable part of the large scale circulation would have to be simulated in these runs. High sea surface temperatures alone (along with some perturbations) are not sufficient to reproduce deep convection during TOGA

COARE, and the "large scale forcing" terms (Eqs. 3.1 and 3.2) applied in the present setup are designed for periodic air mass boundary conditions. Since some insights into the interaction between large scale environments and deep convection are likely to be gained from such an exercise, one could attempt to design a nested setup for TOGA COARE. An alternative is for example to study orographically initiated deep convection or deep convection initiated by the sea and land breeze at mid-latitudes, where nested models have often successfully been used to simulate phenomena that to a certain extent depend on the large scale conditions. Unfortunately, the results from such case studies are not always very general and cannot easily be extrapolated to larger scales. One strategy in order to derive a more general understanding from case studies is to combine results from case studies performed for a number of different conditions, e.g. for different geographical locations. The choice of the cases would ideally be based on statistical information, such as global distributions of deep convection. Classifications according to physical mechanisms, such as ITCZ and SPCZ, embedded into fronts, orographically triggered, and caused by surface inhomogeneities, would also be helpful. A problem with such classifications could be, however, that combinations of different influences may often play important roles. Moreover, the different roles for chemistry strongly depend on a number of additional circumstances, e.g. on whether the environment is clean or polluted.

In the near future, it will increasingly be possible to run nested chemistry transport models with very high resolutions, i.e. to use these models as cloud resolving models. As computing power increases, it will also increasingly be possible to study the roles of deep convection embedded into synoptic fronts for atmospheric chemistry. The amount of NO_x exported from large urban areas may in part depend on small scale meteorological processes, such as local wind systems and deep convection, and the chemistry on these scales. Using a single column model for modeling biomass burning emissions, Chatfield and Delany (1990) showed how sensitive model simulations of tropical ozone can in principle be to assumptions regarding dilution, vertical mixing, and artifical smoothing due to large grid spacings in global models. They found that if emitted gases were rapidly transported to the upper troposphere ("mix then cook" scenario), the efficiency in producing ozone was much higher than if the air was confined to the boundary layer for several days before dilution ("cook then mix" scenario). Sillman *et al.* (1990) showed that including a simple representation of chemistry and transport in power plant plumes into a coarse grid model resulted in a considerable decrease of net ozone production, even when the results were compared to a regional model with 80 km horizontal grid spacing. Recently, Esler *et al.* (2004) investigated the role of limited resolution in chemistry transport models on calculations of the oxidizing capacity and ozone production and found grid averaging to lead to significantly increased ozone production efficiency. A state of the art air pollution community model (WRF-Chem, e.g. Grell *et al.*, 2005, see also *http://www.wrf-model.org/WG11*) has recently been developed based on WRF, which will increasingly be used to study the dispersion of pollutants in and around urban areas in which non-methane hydrocarbons of both anthropogenic and biogenic origin play important roles (e.g. Ryerson *et al.*, 2001). The interface between WRF and KPP described in Section 2.4 could in the future be coupled with WRF-Chem,

considerably reducing the effort necessary to include different chemical mechanisms. How much anthropogenically emitted NO_x is exported and at which heights it is injected into the troposphere in view of the consequences for global ozone chemistry is a question which goes beyond traditional air quality research and is difficult to answer using global models alone.

Appendix A

Mass Transfer Equation

In this appendix, the equation for the trace gas mass transfer between icemeteors and the gas phase (Eq. 2.22) is derived. The equations for the rate of trace gas mass transfer between the gas phase and hydrometeors in the liquid or the ice phase (Eq. 2.22 for liquid and Eq. 2.16 for ice) in the CRCTM can be derived from the following mass transfer equation (Schwartz, 1986; Pruppacher and Klett, 1997; Seinfeld and Pandis, 1998):

$$\partial_t C|_{mt} = fkL\left(C_g^{\infty} - C_g^{surf}\right), \tag{A.1}$$

where f is the ventilation coefficient, k is the gas specific mass transfer coefficient (see Eq. 2.17) and L is the liquid water or ice volume fraction. C_g^{∞} is the grid box average gas phase concentration of a trace gas and C_g^{surf} is the gas phase concentration of tracer i near the surface of the hydrometeors in the liquid or ice phase. Eq. A.1 was derived solving the diffusion equation assuming spherical symmetry. For snow and cloud ice in the CRCTM, spherical symmetry is only assumed for the gas phase diffusion towards the meteor, while the surface area is parameterized using Eq. 2.25. In deriving Eq. 2.16, which describes the mass transfer between liquid hydrometeors and the gas phase, Henry's Law is used in Eq. A.1 to calculate C_g^{surf}.

Instead of using a so-called "quasi Henry's Law" for icemeteors (e.g. Conklin *et al.*, 1993), C_g^{surf} is calculated assuming dissociative Langmuir adsorption (e.g. Laidler *et al.*, 1940; Adamson and Gast, 1997):

$$P_{surf} = \frac{1}{K_L}\frac{\theta^2}{(1-\theta)^2} \tag{A.2}$$

Using the ideal gas law $P_{surf} = RTC_g^{surf}$, where R is the universal gas constant:

$$C_g^{surf} = \frac{1}{K_L RT}\frac{\theta^2}{(1-\theta)^2}. \tag{A.3}$$

Equation 2.22 follows from inserting Eq. A.3 into Eq. A.1:

$$\partial_t C|_{mt} = fkL\left(C_g^{\infty} - \frac{1}{K_L RT}\frac{\theta^2}{(1-\theta)^2}\right).$$

In Equation 2.22, the reversible uptake of a trace gas by frozen hydrometeors is described. The equation is discussed in Section 2.3.2.

Appendix B

Hovmöller Diagram for the Chemistry Runs

Although exactly the same random numbers for the water vapor perturbations were applied for the runs in Chapters 7–11 as for the corresponding runs in the previous chapters, the evolution of the modeled convection differed due to a technical finesse (compare Hovmöller diagram in Fig. B.1 to Fig. 3.6b), while the bulk properties such as the surface precipitation were very similar.

The difference is attributed to the fact that the simulations presented in Chapter 3 were performed on a single processor of a Linux PC cluster[1], while the those in Chapters 7–11 were performed on multiple processors of the same computing platform. For the parallelization of the WRF model based CRCTM, a domain decomposition strategy is applied in which the domain is horizontally partitioned into rectangular patches, and each processor is allocated its own patch which is stored in a local memory. During a model run, only values from within a few grid points wide boundary region of each patch are passed between the processors. This exchange is necessary for the computations of horizontal advection and turbulence. For calculating the right hand sides of Eq. 3.1 and Eq. 3.2, horizontal domain averaging becomes necessary during each integration timestep. In order to keep the cost arising from excessive communication between processors for this operation low, each processor calculates the sum over all grid points at each vertical model level (horizontal slice) of the patch stored in the local memory. The sums are then sent to one processor, where they are added up. This single processor calculates the horizontal averages and distributes them to all other processors. Unfortunately, the associative law is numerically only fulfilled to very good approximation during this operation, resulting in tiny departures from the sum calculated in a single processor run (double precession was used in both cases). After having searched for other possibilities to explain the departures, most probably, it is these small deviations that prohibit an exact reproduction of the results of a single processor run. While the statistics of key variables, such as the amount of surface precipitation, are very similar between the runs, the evolution of the individual clouds differ. A similar phenomenon is known to occur at the larger scale for climate simulations on different computer platforms.

[1] At present Linux clusters are cost-efficient alternatives to traditional distributed memory parallel computers.

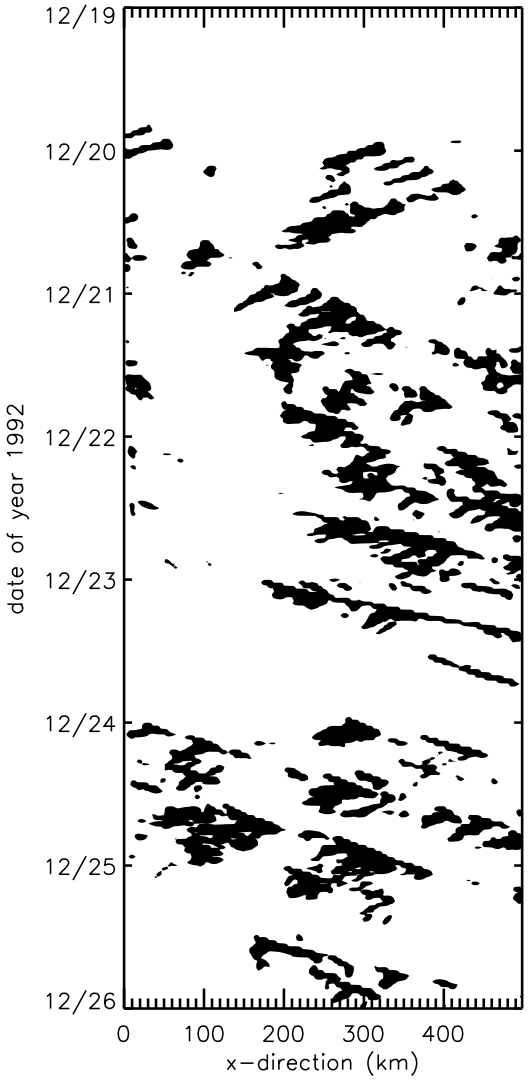

Figure B.1: Hovmöller diagram for the chemistry runs. The filled 1 mm h^{-1} contour of model computed rainfall rates is shown (compare to Fig. 3.6b).

Here, the chaotic behavior was possibly enhanced by the fact that the large scale tendencies in Eq. 3.1 and in Eq. 3.2 were applied horizontally homogeneously over the entire domain. In reality, deep convection often occurs in combination with larger scale (synoptic or mesoscale) flows or in association with orographical forcing or is triggered by surface inhomogeneities, and could thus possibly be a bit less chaotic on sufficiently short timescales.

Appendix C

Numerical Aspects of Calculating VLSAT

As discussed in Section 4.6 air mass is not allowed to enter the model domain through the domain's boundary and the observed mean vertical velocity $\overline{w}_{obs}$ is not used to advect the air mass inside the model domain. Equation 3.3, on the other hand, is formulated for a tracer which is advected with the flow. Unfortunately, the formulation of Equation 3.3 does not easily allow a simultaneously mass conserving and monotonic solution. Sensitivity runs solving Equation 3.3 for inert tracers and periodic boundary conditions (e.g. using the scheme by Walcek, 2000) in fact yield small mass changes which tend to be maximum in the UT. The usual method to avoid mass errors would be to numerically solve Equation 3.3 starting from its flux form[1]. For the transformation between Equation 3.3 and the corresponding flux form the mass continuity equation for $\overline{\mathrm{w}}_{\mathrm{obs}}$ has to be applied. In the model, however, the (3-D) mass continuity equation for $\overline{\mathrm{w}}_{\mathrm{obs}}$ is not solved. As a consequence, using a flux form of Equation 3.3 (or neglecting changes of the dimensional densities in the Walcek (2000) scheme) can lead to a non-monotonic solution for the tracer's mixing ratio. Since Equation 3.3 is a 1D advection problem with a divergent wind field, using the flux form implies that tracer mass can locally be either accumulated (in the case of convergence) or depleted (in the case of divergence), resulting in non-monotonic, and in the case of VLSAT non-physical solutions for the mixing ratios. For tracers with a 'smooth' vertical profile such as CO this can have important effects, while the idealized tracers used in Chapter 4 are not as strongly affected. In the chemistry runs this problem was solved by solving Equation 3.3, which is in advective form (preserving monotonicity), and then scaling the solution such that the column mass change during the calculation must be balanced by the vertically integrated flux divergence due to $\overline{w}_{obs}$ up to the height z_m= 17.375 km. The scale

[1] A conservation law in flux form in one dimension has the form:

$$\partial_t C = -\partial_x (uC) \tag{C.1}$$

Where $C = \rho\mu$ is the concentration of the tracer and ∂_x the spatial partial derivative in the direction of the wind u.

factor f is defined by the condition that the finite-difference equivalent of

$$f\left(\int_0^{z_m}\rho\mu\,\mathrm{dz}+\Delta t\int_0^{z_m}\rho\overline{w}_{obs}\partial_z\mu\,\mathrm{dz}\right)=\int_0^{z_m}\rho\mu\,\mathrm{dz}+\Delta t\int_0^{z_m}\partial_z\left(\rho\overline{w}_{obs}\mu\right)\mathrm{dz} \quad \text{(C.2)}$$

must hold. The integral which is part of the second term on the right hand side of Equation C.2 equals the column tracer mass change per unit area due to $\overline{w}_{obs}$ calculated from the flux form tracer continuity equation. The value of this integral depends on z_m and decreases rapidly to comparatively low, but generally non-zero values above the tropopause as a consequence of small, but positive $\overline{w}_{obs}$ values in the lower stratosphere. The scaled solution is very similar to the non-scaled solution of Equation 3.3. However, scaling can in principle introduce undesired features (see e.g. Jöckel *et al.*, 2001) and should be avoided. A very simple solution to this problem would be to neglect the influence of the mean vertical velocity on the vertical advection of trace gases, as was done previously by Lu *et al.* (2000). This leads, however, to a considerable over-estimation of the role of the mesoscale subsidence, as was shown in Chapter 4. The best way to avoid scaling here would be to try to design a nested model setup. However, for reasons discussed in Chapter 13, modeling the meteorology in the TOGA COARE region using a nested model may not be straightforward.

Appendix D

List of Acronyms

ALDF	advanced lightning direction finder
CAPE	convective available potential energy
CEPEX	Central Equatorial Pacific Experiment
CRM	cloud resolving model
CRCTM	cloud resolving chemistry transport model
CTM	chemistry transport model
CG	cloud to ground
ENSO	El Niño/Southern Oscillation
GCTM	global chemistry transport model
GFDL	Geophysical Fluid Dynamics Laboratory, Princeton, New Jersey
IFA	Intensive Flux Array (during the TOGA COARE campaign)
IC	intra-cloud
IOP	Intensive Observing Period
ISCCP	International Satellite Cloud Climatology Project
ISO	intra-seasonal oscillation in the tropics (Madden and Julian, 1972)
LBC	lateral boundary conditions
LSA	large scale advection
LT	lower troposphere
MATCH-MPIC	Model of Atmospheric Transport and Chemistry - Max Planck Institute for Chemistry Version
MT	mid-troposphere
NASA	National Aeronautics and Space Administration in the USA

NCAR	National Center for Atmospheric Research in the USA
NCEP	National Centers for Environmental Prediction in the USA
PEM	Pacific Exploratory Mission (see Section 7.3.2)
PEACE A	Pacific Exploration of Asian Continental Emissions, phase A
PLBC	periodic lateral boundary conditions
SCM	single column model
SHADOZ	Southern Hemisphere Additional Ozonesondes
SLBC	specified lateral boundary conditions
SST	sea surface temperature
SZA	solar zenith angle
TOGA COARE	Tropical Ocean Global Atmospheres/Coupled Ocean Atmosphere Response Experiment
UT	upper troposphere
VLSAT	vertical large scale advection of tracers
WRF model	Weather Research and Forecast model
WOUDC	World Ozone and Ultraviolet Radiation Data Centre, part of the Global Atmosphere Watch programme of the World Meteorological Organization

Bibliography

Abbatt, J. P. D., 1997: Interaction of HNO_3 with water-ice surfaces at temperatures of the free troposphere. *Geophys. Res. Lett.*, 24, 1479–1482.

Adamson, A. W., and Gast, A. P., 1997: *Physical Chemistry of Surfaces,* 6^{th} Ed. New York: John Wiley, 654pp.

Andreae, M. O., 1993: Global distributions of fires as seen from space. *EOS Trans.*, 74, 129–135.

Andronache, C., Donner, L. J., Seman, C. J., Ramaswamy, V., and Hemler, R. S., 1999: Atmospheric sulfur and deep convective clouds in tropical Pacific: A model study. *J. Geophys. Res.*, 104, 4005–4024.

Arakawa, A., 1993: Closure Assumptions in the cumulus parameterization problem. In *The representation of cumulus convection in numerical models*, K. A. Emanuel and D. J. Raymond, eds., *Meteorological Monographs*, Vol. 24, No 46, American Meteorological Society, Boston, MA, USA, 1–15.

Arakawa, A., 2004: The cumulus parameterization problem: Past, present, and future. *J. Climate*, 13, 2493–2525.

Arnold, S. R., Chipperfield, M. P., Blitz, M. A., Heard, D. E., and Pilling, M. J., 2004: Photodissociation of acetone: Atmospheric implications of temperature-dependent quantum yields. *Geophys. Res. Lett.*, 31, L07110, doi:10.1029/2003GL019099.

Asman, W. A. H., Lawrence, M. G., Brenninkmejer, C. A. M., Crutzen, P. J., Cuijpers, J. W. M., and Nédélec, P., 2003: Rarity of upper-tropospheric low O_3 mixing ratio events during MOZAIC flights. *Atmos. Chem. Phys.*, 3, 1541–1549.

Atkinson, R., Baulch, D. L., Cox, R. A., Hampson, Jr, R. F., Kerr, J. A., Rossi, M. J., and Troe, J., 1997: Evaluated kinetic and heterogeneous data for atmospheric chemistry: Supplement V. *J. Phys. Chem. Ref. Data*, 26, 521–1011.

Atkinson, R., Baulch, D. L., Cox, R. A., R. F. Hampson, Jr, Kerr, J. A., Rossi, M. J., and Troe, J., 1999: Evaluated kinetic and photochemical data for atmospheric chemistry, Organic species: Supplement VII. *J. Phys. Chem. Ref. Data*, 28, 191–393, `http://www.iupac--kinetic.ch.cm.ac.uk/`.

Baker, M. B., Christian, H. J., and Latham, J., 1995: A computational study of the relationships linking lightning frequency and other parameters. *Q. J. R. Meteorol. Soc.*, 121, 1525–1548.

Bartels-Rausch, T., Eichler, B., Zimmermann, P., Gäggeler, H. W., and Ammann, M., 2002: The adsorption enthalpy nitrogen oxides on crystalline ice. *Atmos. Chem. Phys.*, 2, 235–247.

Barth, M. C., Stuart, A. L., and Skamarock, W. C., 2001: Numerical simulations of the July 10, 1996, Stratospheric-Tropospheric Experiment: Radiation, Aerosols, and Ozone (STERAO)-Deep Convection Experiment storm: Redistribution of soluble tracers. *J. Geophys. Res.*, 106, 12381–12400.

Barth, M. C., Hess, P. G., and Madronich, S., 2002: Effect of marine boundary layer clouds on tropospheric chemistry as analyzed in a regional chemistry transport model. *J. Geophys. Res.*, 107, 4126, 10.1029/2001JD000468.

Barth, M. C., S.-W, Kim, Wang, C., Fridlind, A., Ackerman, A., Pinty, J.-P., Mari, C., Leriche, M., Cautenet, S., Spiridonov, V., Pickering, K., Ott, L., and Stenchikov, G., 2005: Summary of the chemistry transport in deep convection cloud modeling workshop intercomparison. *Geophys. Res. Abstr.*, 7, SRef–ID: 1607–7962/gta/EGU05–A–05419.

Battisti, D. S., and Sarachik, E. S., 1995: Understanding and predicting ENSO. *Rev. Geoph.*, 33, 1367–1376, doi:10.1029/95RG00933.

Bechtold, P., Redelsperger, J.-L., Beau, I., Blackburn, M., Brinkop, S., Grandpeix, J.-Y., Grant, A., Gregory, D., Guichard, F., Hofff, C., and Ioannidou, E., 2000: A GCSS model intercomparison for a tropical squall line observed during TOGA-COARE. II: Intercomparison of single-column models and a cloud-resolving model. *Q. J. R. Meteorol. Soc.*, 126, 865–888.

Bechtold, P., Chaboureau, J.-P., and Gonard, L., 2005: Present and projects in convection and tracer transport at ECMWF. *Geophys. Res. Abstr.*, 7, 02012, Sref–ID: 1607–7962/gra/EGU05–A–02012.

Beirle, S., Platt, U., Wenig, W., and Wagner, T., 2004: NO_x production by lightning estimated with GOME. *Adv. Space Res.*, 34, 793–797.

Benkovitz, C. M., Scholtz, M. T. Tevor, Pacyna, J., Tarrasón, L., Dignon, J., Voldner, E. C., Spiro, P. A., Logan, J. A., and Graedel, T. E., 1996: Global gridded inventories of anthropogenic emissions of sulfur and nitrogen. *J. Geophys. Res.*, 101, 29239–29253.

Berntsen, T. K., Isaksen, I. S. A., Wang, W. C., and Liang, X. Z., 1996: Impacts of increased anthropogenic emissions in Asia on tropospheric ozone and climate. *Tellus*, 48, 13–32.

Betts, A. K., Gatti, L. V., Cordova, A. M., and anf J. D. Fuentes, M. A. F. Silva-Dias., 2002: Transport of ozone to the surface by convective downdrafts at night. *J. Geophys. Res.*, 107, 8046, doi:10.1029/2000JD000158.

Bey, I., Jacob, D. J., Logan, J. A., and Yantosca, R. M., 2001a: Asian chemical outflow to the Pacific in spring: Origins, pathways, and budgets. *J. Geophys. Res.*, 106, 23097–23113.

Bey, I., Jacob, D. J., Yantosca, R. M., Logan, J. A., Field, B., Fiore, A. M., Li, Q., Liu, H., Mickley, L. J., and Schultz, M., 2001b: Global modeling of tropospheric chemistry with assimilated meteorology: Model description and evaluation. *J. Geophys. Res.*, 106, 23073–23096.

Biazar, A. P., and McNider, R. T., 1993: Regional estimates of lightning production of nitrogen oxides. *J. Geophys. Res.*, 100, 22861–22874.

Bjerknes, J., 1969: Atmospheric teleconnections from the equatorial Pacific. *Mon. Weather Rev.*, 97, 27–50.

Blitz, M. A., Heard, D. E., Pilling, M. J., Arnold, S. R., and Chipperfield, M. P., 2004: Pressure and temperature-dependent quantum yields for the photodissociation of acetone between 279 and 327.5 nm. *Geophys. Res. Lett.*, 31, L06111, doi:10.1028/2003GL018793.

Boersma, K. F., Eskes, H. J., and Kelder, H. M., 2005: Estimates of lightning NO_x production from GOME satellite observations. *Atmos. Chem. Phys. Discuss.*, 5, 3047–3104.

Bradshaw, J., Newell, R., Sandholm, S., and Liu, S., 2000: Observed distributions of nitrogen oxides in the remote free troposphere from the NASA Global Tropospheric Experiment programs. *Rev. Geoph.*, 38, 61–116.

Brasseur, G. P., Kiehl, J. T., Müller, J-F., Schneider, T., Garnier, C., Tie, X., and Hauglustaine, D., 1998: Past and future changes in global tropospheric ozone: Impact on radiative forcing. *Geophys. Res. Lett.*, 25, 3807–3810.

Brasseur, G. P., Orlando, J. J., and Tyndall, eds., G. S., 1999: *Atmospheric Chemistry and Global Change.* New York: Oxford University Press, 784pp.

Bretherton, C. S., and Smolarkiewicz, P. K., 1989: Gravity waves, compensating subsi-

dence and detrainment around cumulus clouds. *J. Atmos. Sci.*, 46, 740–759.

Carey, L. D., Murphy, M. J., Martin, J., McCormick, T. L., and Demetriades, N. W. S., 2005: Lightning location relative to storm structure in a leading-line, trailing-stratiform mesoscale convective system. *J. Geophys. Res.*, 110, D03105, doi:10.1029/2003JD004371.

Chameides, W. L., 1979: Effect of variable energy input on nitrogen fixation in instantaneous linear discharges. *Nature*, 277, 123–125.

Chameides, W. L., and Walker, J. C. G., 1973: A photochemical theory of tropospheric ozone. *J. Geophys. Res.*, 78, 8751–8760.

Chameides, W. L., Stedman, D. H., Dickerson, R. R., Rusch, D. W., and Cicerone, R. J., 1977: NO_x production in lightning. *J. Atmos. Sci.*, 34, 143–149.

Chameides, W. L., Davis, D. D., Bradshaw, J., Rodgers, M., Sandholm, S., and Bai, D. B., 1987a: An estimate of the NO_x production rate in electrified clouds based on NO observations from the GTE/CITE 1 fall 1983 field operation. *J. Geophys. Res.*, 92, 2153–2156.

Chameides, W. L., Davis, D. D., Rodgers, M., Bradshaw, J., and Sandholm, S., 1987b: Net ozone photochemical production over the Eastern and central North Pacific as inferred from GTE/CITE 1 observations during fall 1983. *J. Geophys. Res.*, 92, 2131–2152.

Chatfield, R. B., and Crutzen, P. J., 1984: Sulfur dioxide in remote oceanic air: Cloud transport of reactive precursors. *J. Geophys. Res.*, 89, 7111–7132.

Chatfield, R. B., and Delany, A. C., 1990: Convection links biomass burning to increased tropical ozone: However, models will tend to overpredict O_3. *J. Geophys. Res.*, 85, 18473–18488.

Chen, G., Huey, L. G., Trainer, M., Nicks, D., Corbett, J., Ryerson, T., Parrish, D., Neuman, J. A., Nowak, J., Tanner, D., Holloway, J., Brock, C., Crawford, J., Olson, J. R., Sullivan, A., Weber, R., Schauffler, S., Donelly, S., Atlas, E., Roberts, J., Flocke, F., Hübler, G., and Fehsenfeld, F., 2005: An investigation of the chemistry of ship emission plumes during ITCT 2002. *J. Geophys. Res.*, 110, D10S90, doi:10.1029/2004JD005236.

Chen, S. S., and Houze, R. A., 1997: Interannual variability of deep convection over the tropical warm pool. *J. Geophys. Res.*, 102, 25783–25795.

Chou, M.-D., Suarez, M. J., Ho, C.-H., Yan, M. M.-H., and Lee, K.-T., 1998: Parameterizations for cloud overlapping and shortwave single-scattering properties for use in general circulation and cloud ensemble models. *J. Climate*, 11, 202–21 4.

Christian, H. J., Blakeslee, R. J., Boccippio, D. J., Boeck, W. L., Buechler, D. E., Driscoll, K. T., Goodman, S. J., Hall, J. M., Koshak, W. J., Mach, D. M., and Stewart, M. F., 2003: Global frequency and distribution of lightning as observed from space by the Optical Transient Detector. *J. Geophys. Res.*, 108, 4005, doi:10.1029/2002JD002347.

Ciesielski, P. E., Johnson, R. H., Haertel, P. T., and Wang, J., 2003: Corrected TOGA COARE sounding humidity data: Impact on diagnosed properties of convection and climate over the warm pool. *J. Climate*, 16, 2370–2384.

Clegg, S. M., and Abatt, J. P. D., 2001: Uptake of gas-phase SO_2 and H_2O_2 by ice surfaces: dependence on partial pressure, temperature, and surface acidity. *J. Phys. Chem. A*, 105, 6630–6636.

Conklin, M. H., Sigg, A., and Neftel, A., 1993: Atmosphere-snow transfer function for H_2O_2: Microphysical considerations. *J. Geophys. Res.*, 98, 18367–18376.

Cooray, V., 1997: Energy dissipation in lightning flashes. *J. Geophys. Res.*, 102, 21401–21410.

Corbett, J. J., Fischbeck, J. J., and Pandis, S. N., 1999: Global nitrogen and sulfur inventories for oceangoing ships. *J. Geophys. Res.*, 104, 3457–3470.

Corti, T., Luo, B. P., and Peter, T., 2005: Mean radiative energy balance and vertical mass fluxes in the equatorial upper troposphere and lower stratosphere. *J. Geophys. Res.*, 32, L06802, doi:10.1029/2004GL021889.

Costa, A. A., Cotton, W. R., Walko, R. L., Pielke Sr., R. A., and Jiang, H., 2001: SST sensitivities in multiday TOGA COARE cloud-resolving simulations. *J. Atmos. Sci.*, 58, 253–268.

Crawford, J., Davis, D., Olson, J., Chen, G., Liu, S., Gregory, G., Barrick, J., Sachse, G., Sandholm, S., Heikes, B., Singh, H., and Blake, D., 1999: Assessment of upper tropospheric HO_x sources over the tropical Pacific based on NASA GTE/PEM data: Net effect on HO_x and other photochemical parameters. *J. Geophys. Res.*, 104, 16255–16273.

Crawford, J. H., Davis, D., Chen, G., Bradshaw, J., Sandholm, S., Gregory, G., Sachse, G., Anderson, B., Collins, J., Blake, D., Singh, H., Heikes, B., Talbot, R., and Rodriguez, J., 1996: Photostationary state analysis of the NO_2–NO system based on airborne observations from the western and central North Pacific. *J. Geophys. Res.*, 101, 2053–2072.

Crawford, J. H., Davis, D. D., Chen, G., Bradshaw, J., Sandholm, S., Kondo, Y., Liu, S., Browell, E., Gregory, G., Anderson, B., Sachse, G., Collins, J., Barrick, J., Blake, D., Talbot, R., and Singh, H., 1997a: An assessment of ozone photochemistry in the extratropical western North Pacific: Impact of continental outflow during the late winter/early spring. *J. Geophys. Res.*, 102, 28469–28487.

Crawford, J. H., Davis, D. D., Chen, G., Bradshaw, J., Sandholm, S., Kondo, Y., Merill, J., Liu, S., Browell, E., Gregory, G., Anderson, B., Sachse, G., Barrick, J., Blake, D., Talbot, R., and Pueschel, R., 1997b: Implications of large shifts in tropospheric NO_x levels in the remote tropical Pacific. *J. Geophys. Res.*, 102, 28447–28468.

Crosley, D. R., 1996: NO_y Blue Ribbon panel. *J. Geophys. Res.*, 101, 2049–2052.

Crutzen, P. J., 1972: *Gas-phase nitrogen and methane chemistry in the atmosphere.* Tech. rept. AP-10. Institute of Meteorology, University of Stockholm, International Meteorological Institute in Stockholm, Arrhenius Laboratory, S-10691 Stockholm, Sweden.

Crutzen, P. J., 1973: *A discussion of the chemistry of some minor constituents in the stratosphere and troposphere.* Tech. rept. AP-12. Institute of Meteorology, University of Stockholm, International Meteorological Institute in Stockholm, Arrhenius Laboratory, S-10691 Stockholm, Sweden.

Crutzen, P. J., 1974: Photochemical reactions initiated by and influencing ozone in unpolluted tropospheric air. *Tellus*, 26, 49–57.

Crutzen, P. J., and Lawrence, M. G., 2000: The impact of precipitation scavenging on the transport of trace gases: A 3-dimensional model sensitivity study. *J. Atmos. Chem.*, 37, 81–112.

Crutzen, P. J., Lawrence, M. G., and Pöschl, U., 1999: On the background photochemistry of tropospheric ozone. *Tellus*, 51 A-B, 123–146.

Damian, V., Sandu, A., Damian, M., Potra, F., and Carmichael, G. R., 2002: The kinetic preprocessor KPP - a software environment for solving chemical kinetics. *Computers and Chemical Engineering*, 26, 1567 – 1579.

Damian-Iordache, V., 1996: *KPP – Chemistry simulation development environment.* Master's thesis, University of Iowa, Iowa City, Iowa.

Davis, D., Grodzinsky, G., Chen, G., Crawford, J., Eisele, F., Mauldin, L., Tanner, D., Cantrell, C., Burne, W., Tan, D., Faloona, I., Ridley, B., Montzka, D., Walega, J., Grahek, F., Sandholm, S., Sachse, G., Vay, S., Anderson, B., Avery, M., Heikes, B., Snow, J., O'Sullivan, D., Shetter, R., Lefer, B., Blake, D., Blake, N., Carroll, M., and Wang, Y., 2001a: Marine latitude/altitude OH distributions: Comparison of Pacific Ocean observations with models. *J. Geophys. Res.*, 106, 32691–32707.

Davis, D., Crawford, G. Chen J. H., Liu, S., Tan, D., sanholm, S. T., Jing, P., Cunnold, D. M., DiNunno, B., Browell, E. V., Grant, W. B., Fenn, M. A., Anderson, B. E., Barrick, J. D., Sachse, G. W., Vay, S. A., Hudgins, C. H., Avery, M. A., Lefer, B., Shetter, R. E., Heikes, B. G., Blake, D. R., Blake, N., Kondo, Y., and Oltmans, S.,

2003: An assessment of western North Pacific ozone photochemistry based on springtime observations from NASA's PEM-West B (1994) and TRACE-P (2001) field studies. *J. Geophys. Res.*, 108, 8829, doi:10.1029/2002JD003232.

Davis, D. D., Grodzinsky, G., Kasibhatla, P., Crawford, J., Chen, G., Liu, S., Bandy, A., Thornton, D., Guan, H., and Sandholm, S., 2001b: Impact of ship emissions on marine boundary layer NO_x and SO_2 distributions over the Pacific Basin. *Geophys. Res. Lett.*, 28, 235–238.

Dawson, G. A., 1980: Nitrogen-fixation by lightning. *J. Atmos. Sci.*, 37(1), 174–178.

DeCaria, A. J., Pickering, K. E., Stenchikov, G. L., Scala, J. R., Stith, J. L., Dye, J. E., Ridley, B. A., and Laroche, P., 2000: A cloud-scale model study of lightning-generated NO_x in an individual thunderstorm during STERAO-A. *J. Geophys. Res.*, 105, 11601–11616.

DeCaria, A. J., Pickering, K. E., Stenchikov, G. L., and Ott, L. E., 2005: Lightning generated NO_x and its impact on tropospheric ozone production: A 3-D modeling study of a STERAO-A thunderstorm. *J. Geophys. Res.*, 110, D14303, doi:10.1029/2004JD005556.

DeMore, W. B., Sander, S. P., Howard, C. J., Ravishankara, A. R., Golden, D. M., Kolb, C. E., Hampson, R. F., Kurylo, M. J., and Molina, M. J., 1997: *Chemical Kinetics and Photochemical Data for Use in Stratospheric Modeling.* Evaluation 12, 97-4. Jet Propulsion Laboratory, Pasadena, California.

Dentener, F. J., and Crutzen, P. J., 1993: Reaction of N_2O_5 on tropospheric aerosols: Impact on the global distributions of NO_x, O_3, and OH. *J. Geophys. Res.*, 98, 7149–7163.

Dickerson, R. R., Huffman, G. J., Luke, W. T., Nunnermacker, L. J., Pickering, K. E., Leslie, A. C. D., Lindsey, C. G., Slinn, W. G. N., Kelly, T. J., Daum, P. H., Delaney, A. C., Greenberg, J. P., Zimmerman, P. R., Boatman, J. F., Ray, J. D., and Stedman, D. H., 1987: Thunderstorms: An important mechanism in the transport of air pollutants. *Science*, 235, 460–465.

Diehl, K., Mitra, S. K., and Pruppacher, H. R., 1995: A laboratory study of the uptake of HNO_3 and HCl vapor by snow crystals and ice spheres at temperatures between 0 and -40C. *Atmos. Environ.*, 29, 975–981.

DiNunno, B., Davis, D., Chen, G., Crawford, J., Olson, J., and Liu, S., 2003: An assessment of ozone photochemistry in the central/eastern North Pacific as determined from multilayer airborne field studies. *J. Geophys. Res.*, 108, 8237, doi:10.1029/2001JD001468.

Doherty, R. M., Stevenson, D. S., and Sanderson, M. G., 2005: Influence of convective transport on tropospheric ozone and its precursors in a chemistry-climate model. *Atmos. Chem. Phys. Discuss.*, 5, 3747–3771.

Dominé, F., and Thibert, E., 1996: Mechanism of incorporation of trace gases in ice grown from the gas phase. *J. Geophys. Res.*, 23, 3627–3630.

Dominé, F., and Thibert, E., 1998: Comment on "Diffusion of HNO_3 in ice". *Geophys. Res. Lett.*, 25, 4389–4390.

Doswell III, C. A., and Markowski, P. M., 2004: Is buoyancy a relative quantity? *Mon. Weather Rev.*, 132, 853–863.

Dransfield, T. J., Perkins, K. K., Donahue, N. M., Anderson, J. G., Sprengnether, M. M., and Demerjian, K. L., 1999: Temperature and pressure dependent kinetics of the gas-phase reaction of the hydroxy radicals with nitrogen dioxide. *Geophys. Res. Lett.*, 26, 687–690.

Drapcho, D. L., Sisterson, D., and Kumar, R., 1983: Nitrogen fixation by lightning activity in a thunderstorm. *J. Geophys. Res.*, 19(4), 729–734.

Ekman, A. M. L., Wang, C., and Ström, J., 2004: Explicit simulation of aerosol physics in a cloud-resolving model. *Atmos. Chem. Phys.*, 4, 773–791.

Emmons, L. K., Hauglustaine, D. H., Müller, J.-F., Carroll, M. A., Brasseur, G. P.,

Brunner, D., Staehelin, J., Thouret, V., and Marenco, A., 2000: Data composites of airborne observations of tropospheric ozone and its precursors. *J. Geophys. Res.*, 105, 20497–20538.

Esler, J. G., Roelofs, G. J., and O'Connor, F. M., 2004: A quantitative analysis of grid-related systematic errors in oxidising capacity and ozone production rates in chemistry transport models. *Atmos. Chem. Phys.*, 4, 1781–1795.

Fehr, T., Höller, H., and Huntrieser, H., 2004: Model study on production of lightning-produced NO_x in a EULINOX supercell storm. *J. Geophys. Res.*, 109, D09102, doi:10.1029/2003JD003935.

Fishman, J., Ramanathan, V., Crutzen, P. J., and Liu, S. C., 1979: Tropospheric ozone and climate. *Nature*, 282, 818–820.

Folkins, I., Chatfield, R., Singh, H., Chen, Y., and Heikes, B., 1998: Ozone production efficiencies of acetone and peroxides in the upper troposphere. *J. Geophys. Res.*, 25, 1305–1308.

Folkins, I., Baum, C., Thompson, A. M., and Witte, J., 2002: Tropical ozone as an indicator of deep convection. *J. Geophys. Res.*, 107, doi: 10.129/2001JD001178.

Franzblau, E., and Popp, C. J., 1989: Nitrogen oxides produced from lightning. *J. Geophys. Res.*, 94, 11089–11104.

Fu, Q., Krueger, S. K., and Liou, K. N., 1995: Interactions of radiation and convection in simulated tropical cloud clusters. *J. Atmos. Sci.*, 52, 1310–1328.

Gallardo, L., and Cooray, V., 1996: Could cloud-to-cloud discharges be as effective as cloud-to-ground discharges in producing NO_x? *Tellus*, 48B, 641–651.

Ganzeveld, L., and Lelieveld, J., 1995: Dry deposition parameterization in a chemistry general circulation model and its influence on the distribution of reactive trace gases. *J. Geophys. Res.*, 100, 20999–21012.

Gao, R. S., Popp, P. J., Fahey, D. W., Marcy, T. P., Herman, R. L., Weinstock, E. M., Baumgardner, D. G., Garrett, T. J., Rosenlof, K. H., Thompson, T. L., Bui, P. J., Ridley, B. A., Wofsy, S. C., Toon, O. B., Tolbert, M. A., Kärcher, B., Peter, Th., Hudson, P. K., Weinheimer, A. J., and Heymsfield, A. J., 2004: Evidence that nitric acid increases relative humidity in low-temperature cirrus clouds. *Science*, 303, 516–520.

GCSS Science Team., 1993: The GEWEX Cloud System Study (GCSS). *Bull. Am. Met. Soc.*, 74, 387–399.

Gidel, L. T., 1983: Cumulus cloud transport of transient tracers. *J. Geophys. Res.*, 88, 6587–6599.

Gill, A. E., 1982: *Atmosphere-Ocean Dynamics.* San Diego: Academic Press, 662pp.

Gregory, D., and Guichard, F., 2002: Aspects of the parameterization of organized convection: Contrasting cloud resolving model and single-column model realizations. *Q. J. R. Meteorol. Soc.*, 128, 625–646.

Grell, G. A., Peckham, S. E., McKeen, S. A., Wilczak, J., and Eder, B., 2005: Fully coupled online chemistry within the WRF model. *Atmos. Environ.*, 39, accepted.

Gutzler, D. S., Kiladis, G. N., Meehl, G. A., Weickmann, K. M., and Wheeler, M., 1994: The global climate of December 1992– February 1993. Part II: Large-scale variability across the tropical western Pacific during TOGA COARE. *J. Climate*, 7, 1606–1622.

Hairer, E., and Wanner, G., 1996: *Solving ordinary differential equations II.* Berlin: Springer, 614pp.

Hauglustaine, D. A., Ridley, B. A., Solomon, S., Hess, P. G., and Madronich, S., 1996: HNO_3/NO_x ratio in the remote troposphere during MLOPEX 2: Evidence for nitric acid reduction on carbonaceous aerosols? *Geophys. Res. Lett.*, 23, 2609–2612.

Hegglin, M. I., Brunner, D., Wernli, H., Schwierz, C., Martius, O., Hoor, P., Fischer, H., Parchatka, U., Spelten, N., Schiller, C., Krebsbach, M., Weers, U., Staehlin, J., and Peter, T., 2004: Tracing troposphere-to-stratosphere transport above a mid-latitude deep convective system. *Atmos. Chem. Phys.*, 4, 741–756.

Helsdon, Jr., J. H., 2004: Comment on "On the roles of deep convective clouds in tropospheric chemistry" by Chien Wang and R. G. Prinn. *J. Geophys. Res.*, 109, 143–146.

Heymsfield, A. J., and McFarquhar, G. M., 1996: High albedos of cirrus in the tropical Pacific warm pool: Microphysical interpretations from CEPEX and from Kwajalein, Marshall Islands. *J. Atmos. Sci.*, 53, 2424–2451.

Hill, R. D., Rinker, R. G., and Wilson, H. D., 1980: Atmospheric nitrogen-fixation by lightning. *J. Atmos. Sci.*, 37(1), 179–192.

Hoell, J. M., Davis, D. D., Liu, S. C., Newell, R., Shipman, M., , Akimoto, H., McNeal, R. J., Bendura, R. J., and Drewry, J. C., 1996: The Pacific Exploratory Mission-West A (PEM-West A): September–October 1991. *J. Geophys. Res.*, 101, 1641–1653.

Hoell, J. M., Davis, D. D., Liu, S. C., Newell, R. E., Akimoto, H., McNeal, R. J., and Bendura, R. J., 1997: The Pacific Exploratory Mission-West Phase B: February–March, 1994. *J. Geophys. Res.*, 102, 28223–28239.

Hoell, J. M., Davis, D. D., Jacobs, D. J., Rogers, M. O., Newell, R. E., Fuelberg, H. E., McNeal, R. J., Raper, J. L., and Bendura, R. J., 1999: The Pacific Exploratory Mission in the tropical Pacific: PEM-Tropics A, August–September 1996. *J. Geophys. Res.*, 104, 5567–5584.

Holton, J. R., Haynes, P. H., McIntyre, M. E., Douglass, A. R., Rood, R. B., and Pfister, L., 1995: Stratosphere-troposphere exchange. *Rev. Geoph.*, 33, 403–439.

Hong, S.-Y., and Pan, H.-L., 1996: Nonlocal boundary layer vertical diffusion in a medium range forecast model. *Mon. Weather Rev.*, 124, 2322–2339.

Horowitz, L. W., Walters, S., Mauzerall, D. L., Emmons, L. K., Rasch, P. J., Garnier, C., Tie, X., Lamarque, J.-F., Schultz, M. G., Tyndall, G. S., Orlando, J. J., and Brasseur, G. P., 2003: A global simulation of tropospheric ozone and related tracers: Description and evaluation of MOZART, version 2. *J. Geophys. Res.*, 108, 4728, doi:10.1029/2002JD002853.

Houze, Jr., R. A., 1993: *Cloud dynamics.* San Diego: Academic Press, Inc, 573pp.

Houze, Jr., R. A., 2004: Mesoscale convective systems. *Rev. Geoph.*, 42, RG4003, doi:10.1029/2004RG000150.

Hudson, P. K., Shilling, J. E., Tolbert, M. A., and Toon, O. B., 2002: Uptake of nitric acid on ice at tropospheric temperatures: Implications for cirrus clouds. *J. Phys. Chem. A*, 106, 9874–9882.

Huntrieser, H., Schlager, H., Feigl, C., and Höller, H., 1998: Transport and production of NO_x in electrified thunderstorms: Survey of previous studies and new observations at midlatitudes. *J. Geophys. Res.*, 103, 28,247–28,264.

Huntrieser, H., Feigl, C., Schlager, H., Schröder, F., Gerbig, C., van Velthoven, P., Flatøy, F., Thery, C., Petzold, A., Höller, H., and Schumann, U., 2002: Airborne measurements of NO_x, tracer species, and small particles during the European Lightning Nitrogen Oxides Experiment. *J. Geophys. Res.*, 107(D11), 4113 doi: 10.1029/2000JD000209.

Hynes, R., Fernandez, M. A., and Anthony Cox, R., 2002: Uptake of HNO_3 on water-ice and coadsorption of HNO_3 and HCl in the temperature range 210–235K. *J. Geophys. Res.*, 107, 4797, doi: 10.1029/2001JD001557.

IPCC., 2001: *Climate change 2001: The Scientific basis. Contribution of Working Group I to the Third Assessment Report of the Intergovernmental Panel on Climate Change.* J. T. Houghton, Y. Ding, D. J. Griggs, M. Nouger, P. J. van der Linden, X. Dai, K. Maskell, and C. A. Johnson, eds., Cambridge University Press, Cambridge, United Kingdom and New York, NY, USA, 881pp.

Iribarne, J. V., and Psyhnov, T., 1990: The effect of freezing on the composition of supercooled droplets - I. Retention of HCl, HNO_3, NH_3, and H_2O_2. *Atmos. Environ.*, 24A, 383–387.

Isaac, G. A., and Joe, P. I., 1983: The vertical transport and redistribution of pollutants by clouds. In *The Meteorology of Acid Deposition*, P. J. Samson, ed., Air Pollution

Control Association, Pittsburg, PA, USA, 496–512.

Jacob, D. J., Logan, J. A., and Murti, P. P., 1999: Effect of rising Asian emissions on surface ozone in the United States. *J. Geophys. Res.*, 26, 2175–2178.

Jacob, D. J., Field, B. D., Jin, E. M., Bey, I., Li, Q., Logan, J. A., and Yantosca, R. M., 2002: Atmospheric budget of acetone. *J. Geophys. Res.*, 107, 4100,doi:10.1029/2001JD000694.

Jacob, D. J., Crawford, J. H., Kleb, M. M., Connors, V. S., Bendura, R. J., Raper, J. L., Sachse, G. W., Gille, J. C., Emmons, L., and Heald, C. L., 2003: Transport and chemical evolution over the Pacific (TRACE-P) aircraft mission; Design, execution and first results. *J. Geophys. Res.*, 108, 9000,doi:10.1029/2002JD003276.

Jaeglé, L., Jacob, D. J., Wennberg, P. O., Spivakovsky, C. M., Hanisco, T. F., Lanzendorf, E. J., Hinsta, E. J., Fahey, D. W., Keim, E. R., Proffit, E. R., Atlas, M. H., Flocke, E. L., Schauffer, S., McElroy, C. T., Midwinter, C., Pfister, L., and Wilson, J. C., 1997: Observed OH and HO_2 in the upper troposphere suggest a major source from convective injection of peroxides. *Geophys. Res. Lett.*, 24, 3181–.

Jaeglé, L., Jacob, D. J., Brune, W. H., Faloona, I., Tan, D., Heikes, B. G., Kondo, Y., Sachse, G. W., Anderson, B., Greogory, G. L., Singh, H. B., Pueschel, R., Ferry, G., Blake, D. R., and Shetter, R. E., 2000: Photochemistry of HO_x in the upper troposphere at northern midlatitudes. *J. Geophys. Res.*, 105, 3877–3892.

Jaeglé, L., Jacob, D. J., Brune, W. H., and Wennberg, P. O., 2001: Chemistry of HO_x radicals in the upper troposphere. *Atmos. Environ.*, 35, 469–489.

Jayne, J. T., Duan, S. X., Davidovits, P., Worsnop, D. R., Zahniser, M. S., and Colb, C. E., 1991: Uptake of gas-phase alcohol and organic acid molecules by water surfaces. *J. Phys. Chem.*, 95, 6329–6336.

Jöckel, P., von Kuhlmann, R., Lawrence, M. G., Steil, B., Brenninkmeijer, C. A. M., Crutzen, P. J., Rasch, P. J., and Eaton, B., 2001: On a fundamental problem in implementing flux-form advection schemes for tracer transport in 3-dimensional general circulation and chemical transport models. *Q. J. R. Meteorol. Soc.*, 127, 1035–1052.

Johnson, D. E., Gammon, R. H., Larsen, J., Bates, T. S., Oltmans, S. J., and Farmer, J. C., 1990: Ozone in the marine boundary layer over the Pacific and Indian Oceans: Latitudinal gradients and diurnal cycles. *J. Geophys. Res.*, 95, 11847–11856.

Johnson, D. E., Tao, W.-K., Simpson, J., and Sui, C.-H., 2002: A study of the response of deep tropical clouds to large-scale thermodynamic forcings. Part I: Modeling strategies and simulations of TOGA COARE convective systems. *J. Atmos. Sci.*, 59, 3492–3518.

Jonquieres, I., and Marenco, A., 1998: Redistribution by deep convection and long-range transport of CO and CH_4 emissions from the Amazon basin, as observed by the airborne campaign TROPOZ II during the wet season. *J. Geophys. Res.*, 103, 19075–19091.

Jonson, and Isaksen., 1993: Tropospheric ozone chemistry. The impact of cloud chemistry. *J. Atmos. Chem.*, 16, 99–122.

Jorgensen, D. P., LeMone, M. A., and Trier, S. B., 1997: Structure and evolution of the 22 February 1993 TOGA COARE squall line: Aircraft observations of precipitation, circulation and surface energy fluxes. *J. Atmos. Sci.*, 54, 1961–1985.

Kalnay, E., Kanamitsu, M., Kistler, R., Collins, W., Deaven, D., Gandin, L., Iredell, M., Saha, S., White, G., Woollen, J., Zhu, Y., Chelliah, M., Ebisuzaki, W., Higgins, W., Janowiak, J., Mo, K. C., Ropelewski, C., Wang, J., Leetmaa, A., Reynolds, R., Jenne, R., and Joseph, D., 1996: The NCEP/NCAR 40-year reanalysis project. *Bull. Am. Met. Soc.*, 77, 437–471.

Kanakidou, M., and Crutzen, P. J., 1999: The photochemical source of carbon monoxide: Importance, uncertainties and feedbacks. *Chemosphere – Global Change Science*, 1, 91–109.

Kasibhatla, P., Levy II, H., Moxim, W. J., Pandis, S. N., Corbett, J. J., Peterson, M. C., Honrath, R. E., Frost, G. J., Knapp, K., Parrish, D. D., and Ryerson, T. B., 2000: Do

emissions from ships have a significant impact on concentrations of nitrogen oxides in the marine boundary layer? *Geophys. Res. Lett.*, 27, 2229–2232.

Kasting, J. F., and Singh, H. B., 1986: Nonmethane hydrocarbons in the troposphere: Impact on the odd hydrogen and odd nitrogen chemistry. *J. Geophys. Res.*, 91, 13239–13256.

Kawakami, S., Kondo, Y., Koike, M., Nakajima, H., Gregory, G. L., Sachse, G. W., Newell, R. E., Browell, E. W., Blake, D. R., Rodriguez, J. M., and Merrill, J. T., 1997: Impact of lightning and convection on reactive nitrogen in the tropical free troposphere. *Geophys. Res. Lett.*, 102, 28367–28384.

Kiladis, G. N., von Storch, H., and van Loon, H., 1989: Origin of the South Pacific Convergence Zone. *J. Climate*, 2, 1185–1195.

Kiladis, G. N., Meehl, G. A., and Weickmann, K. M., 1994: Large-scale circulation with westerly wind bursts and deep convection over the equatorial Pacific. *J. Geophys. Res.*, 99, 18527–18544.

Kley, D., Crutzen, P. J., Smith, H. G. J., Vömel, H., Oltmans, S. J., Grassl, H., and Ramanathan, V., 1996: Observations of near-zero ozone concentrations over the convective Pacific: Effects on air chemistry. *Science*, 274, 230–233.

Kley, D., Smit, H. G. J., Vömel, H., Grassl, H., Ramanathan, V., Crutzen, P. J., Williams, S., Meyerwerk, J., and Oltmans, S. J., 1997: Tropospheric water-vapour and ozone cross-sections in a zonal plane over the central equatorial Pacific Ocean. *Q. J. R. Meteorol. Soc.*, 123, 2009–2040.

Ko, M., Hu, W., Rodrìguez, J. M., Kondo, Y., Koike, M., nad S. Kawakami, K. Kita, Blake, D., Liu, S., and Ogawa, T., 2003: Photochemical ozone budget during the BIBLE A and B campaigns. *J. Geophys. Res.*, 108, doi:10.1029/2001JD000800.

Kondo, Y., Ziereis, H., Koike, M., Gregory, G. L., Sachse, G. W., Singh, H. B., Davis, D. D., and Merrill, J. T., 1996: Reactive nitrogen over the Pacific Ocean during PEM-West A. *J. Geophys. Res.*, 101, 1809–1828.

Kondo, Y., Koike, M., Kawakami, S., Singh, H.B., Nakajima, H., Gregory, G. L., Blake, D. R., Sachse, G. W., Merrill, J. T., and Newell, R. E., 1997: Profiles and partitioning of reactive nitrogen over the Pacific Ocean in winter and early spring. *J. Geophys. Res.*, 102, 28405–28424.

Kondo, Y., Toon, O. B., Irie, H., Gamblin, B., Koike, M., Takegawa, N., Tolbert, M. A., Hudson, P. K., Viggiano, A. A., Avallone, L. M., Hallar, A. G., Anderson, B. E., Sachse, G. W., Vay, S. A., Hunton, D. E., Ballenthin, J. O., and Miller, T. M., 2003: Uptake of reactive nitrogen on cirrus cloud particles in the upper troposphere and lowermost stratosphere. *Geophys. Res. Lett.*, 30, 1154, doi:10.1029/2002GL016539.

Kondo, Y., Morino, Y., Takegawa, N., Koike, M., Kita, K., Miyazaki, Y., Sachse, G. W., Vay, S. A., Avery, M. A., Flocke, F., Weinheimer, A. J., Eisele, F. L., Zondlo, M. A., Weber, R. J., Singh, H. B., Chen, G., Crawford, J., Blake, D. R., Fuelberg, H. E., Clarke, A. D., Talbot, R. W., Sandholm, S. T., Browell, E. V., Streets, D. G., and Liley, B., 2004a: Impacts of biomass burning in Southeast Asia on ozone and reactive nitrogen over the western Pacific in spring. *J. Geophys. Res.*, 109, D15S12, doi:10.1029/2003JD004203.

Kondo, Y., Nakamura, K., Chen, G., Takegawa, N., Koike, M., Miyazaki, Y., Kita, K., Crawford, J., Ko, M., Blake, D. R., Kawakami, S., Shirai, T., Liley, B., Wang, Y., and Ogawa, T., 2004b: Photochemistry of ozone over the western Pacific from winter to spring. *J. Geophys. Res.*, 109, doi:10.1029/2004JD004871.

Kowalczyk, M., and Bauer, E., 1982 (December). *Lightning as a source of NO_x in the troposphere.* Technical Memorandum ORNL/TM-2001/268. Federal Aviation Administration, Oak Ridge, Tenn.

Krishnamurti, T. N., 1971: Tropical east-west circulations during northern summer. *J. Atmos. Sci.*, 28, 1342–1347.

Krishnamurti, T. N., Kanamitsu, M., Koss, W. J., and Lee, J. D., 1973: Tropical east-west circulations during northern winter. *J. Atmos. Sci.*, 30, 780–787.

Krueger, S. K., and Lazarus, S. M., 1999 (Jan). Intercomparison of multi-day simulations of convection during TOGA COARE with several cloud-resolving and single-column models. *In: Preprints, 23rd Conf. on Hurricanes and Tropical Meteorology* Amer. Meteor. Soc., Dallas, TX.

Krueger, S. K., Fu, Q., Liou, K. N., and Chin, H.-N. S., 1995: Improvements of an ice-phase microphysics parameterization for use in numerical simulations of tropical convection. *J. Appl. Met.*, 34, 281–287.

Labrador, L. J., von Kuhlmann, R., and Lawrence, M. G., 2004: Strong sensitivity of the global mean OH concentration and the tropospheric oxidizing efficiency to the source of NO_x from lightning. *Geophys. Res. Lett.*, 31, L06102, doi:10.1029/2003GL019229.

Labrador, L. J., von Kuhlmann, R., and Lawrence, M. G., 2005: The effects of lightning-produced NO_x and its vertical distribution on atmospheric chemistry: sensitivity simulations with MATCH-MPIC. *Atmos. Chem. Phys.*, 5, 1815–1834.

Lac, C., Lafore, J. P., and Redelsperger, J. L., 2002: Role of gravity waves in triggering deep convection during TOGA COARE. *J. Geophys. Res.*, 59, 1293–1316.

Laidler, K. J., Glasstone, S., and Eyring, H., 1940: Application of the theory of absolute reaction rates to heterogeneous processes. *J. Chem. Phys.*, 8, 659–667.

Landgraf, J., and Crutzen, P. J., 1998: An efficient method for online calculations of photolysis and heating rates. *J. Atmos. Sci.*, 55, 863–878.

Lane, T. P., and Reeder, M. J., 2001: Convectively generated gravity waves and their effect on the cloud environment. *J. Atmos. Sci.*, 58, 2427–2440.

Lawrence, M. G., 1996: *Photochemistry in the Tropical Pacific Troposphere: Studies with a Global 3D Chemistry-Meteorology Model.* Ph.D. thesis, Georgia Institute of Technology, 520pp.

Lawrence, M. G., 2005: The relationship between relative humidity and the dewpoint temperature in moist air: A simple conversion and applications. *Bull. Am. Met. Soc.*, 86, 225–233.

Lawrence, M. G., and Crutzen, P. J., 1999: Influence of NO_x emission from ships on tropospheric photochemistry and climate. *Nature*, 402, 167–170.

Lawrence, M. G., and Rasch, P. J., 2005: Tracer transport in deep convective updrafts: plume ensemble versus bulk formulation. *J. Atmos. Sci.*, *in press.*

Lawrence, M. G., and Salzmann, M., 2005: Deep convection, subsidence, and large-scale circulations in Eulerian and Lagrangian models. *Geophys. Res. Abstr.*, 7, 05805, Sref–ID: 1607–7962/gra/EGU05–A–05805.

Lawrence, M. G., Chameides, W. L., Kasibhatla, P. S., Levy II, H., and Moxim, W., 1995: Lightning and atmospheric chemistry: The rate of atmospheric NO production. In *Handbook of Atmospheric Electrodynamics*, H. Volland, ed., CRC Press, Inc., 189–202.

Lawrence, M. G., Crutzen, P. J., and Rasch, P. J., 1999a: Analysis of the CEPEX ozone data using a 3D chemistry-meteorology model. *Q. J. R. Meteorol. Soc.*, 125, 2987–3009.

Lawrence, M. G., Crutzen, P. J., Rasch, P. J., Eaton, B. E., and Mahowald, N. M., 1999b: A model for studies of tropospheric photochemistry: Description, global distributions, and evaluation. *J. Geophys. Res.*, 104, 26245–26277.

Lawrence, M. G., von Kuhlmann, R., Salzmann, M., and Rasch, P. J., 2003a: The balance of effects of deep convective mixing on tropospheric ozone. *Geophys. Res. Lett.*, 30, 1940, doi:10.1029/2003GL017644.

Lawrence, M. G., Rasch, P. J., von Kuhlmann, R., Williams, J., Fischer, H., de Reus, M., Lelieveld, J., Crutzen, P. J., Schultz, M., Stier, P., Huntrieser, H., Heland, J., Stohl, A., Forster, C., Elbern, H., Jakobs, H., and Dickerson, R. R., 2003b: Global chemical weather forecasts for field campaign planning: predictions and observations of large-scale features during MINOS, CONTRACE, and INDOEX. *Atmos. Chem. Phys.*, 3,

267–289.

Lee, W.-C., and Hildbrand, P. H., 1995: Kinematic and thermodynamic structure of a TOGA COARE squall line retrieved from the ELDORA data. *Pages 811–813 of: Preprints, 27th Conf. on Radar Meteorology* Amer. Meteor. Soc., Vail, CO.

Lelieveld, J., and Crutzen, P. J., 1991: The role of clouds in tropospheric photochemistry. *J. Atmos. Chem.*, 12, 229–267.

Lelieveld, J., and Crutzen, P. J., 1992: Indirect chemical effects of methane on climate warming. *Nature*, 355, 339–342.

Lelieveld, J., and Crutzen, P. J., 1994: Role of deep cloud convection in the ozone budget of the troposphere. *Science*, 264, 1759–1761.

Lelieveld, J., and Crutzen, P. J., 1995: Influences of cloud photochemical processes on tropospheric ozone. *Nature*, 343, 227–233.

Lelieveld, J., and Dentener, F., 2000: What controls tropospheric ozone? *J. Geophys. Res.*, 105, 3531–3551.

Lelieveld, J., van Aardenne, J., Fischer, H., de Reus, M., Williams, J., and Winkler, P., 2004: Increasing ozone over the Atlantic Ocean. *Science*, 304, 1483–1487.

Levine, J. S., Rogowski, R. S., Gregory, G. L., Howell, W. E., and Fishman, J., 1981: Simultaneous measurements of NO_x, NO, and O_3 production in a laboratory discharge: Atmospheric implications. *Geophys. Res. Lett.*, 8(4), 357–360.

Levy II, H., 1971: Normal atmosphere: Large radical and formaldehyde concentrations predicted. *Science*, 173, 141–143.

Levy II, H., 1972: Photochemistry of the lower troposphere. *Planet. Space. Sci.*, 19, 919–935.

Levy II, H., Moxim, W. J., and Kasibhatla, P. S., 1996: A global 3-dimensional time-dependent lightning source of tropospheric NO_x. *J. Geophys. Res.*, 101, 22911–22922.

Liang, J., and Jacob, D. J., 1997: Effect of aqueous phase cloud chemistry on tropospheric ozone. *J. Geophys. Res.*, 102, 5993–6001.

Liaw, Y. P., Sisterson, D. L., and Miller, N. L., 1990: Comparison of field, laboratory, and theoretical estimates of global nitrogen-fixation by lightning. *J. Geophys. Res.*, 22(D13), 22489–22494.

Liberti, G. L., Cheruy, F., and Desbois, M., 2001: Land effect on the diurnal cycle of clouds over the TOGA COARE area, as observed from GMS IR radar. *Mon. Weather Rev.*, 129, 1500–1517.

Lin, X., and Johnson, R. H., 1996: Kinematic and thermodynamic characteristics of the flow over the western Pacific warm pool during TOGA-COARE. *J. Atmos. Sci.*, 53, 695–715.

Lin, Y.-L., Farley, R. D., and Orville, H. D., 1983: Bulk parameterization of the snow field in a cloud model. *J. Climate Appl. Meteor.*, 2, 1065–1092.

Lind, J. A., and Kok, G. L., 1986: Henry's Law determinations for aqueous solutions of hydrogen peroxide, methylhydroperoxide, and peroxyacetic acid. *J. Geophys. Res.*, 91D, 7889–7895.

Liu, H., Jacob, D. J., Bey, I., Yantosca, R. M., and Duncan, B. N., 2003: Transport pathways for Asian pollution over the Pacific: Interannual and seasonal variations. *J. Geophys. Res.*, 108, 8786, doi:10.1029/2002JD003102.

Liu, S. C., McFarland, M., Kley, D., Zafiriou, O., and Huebert, B., 1983: Tropospheric NO_x and O_3 budgets in the equatorial Pacific. *J. Geophys. Res.*, 88, 1360–1368.

Liu, S. C., Trainer, M., Fehsenfeld, F. C., Parrish, D. D., Williams, E. J., Fahey, D. W., Hübler, G., and Murphy, P. C., 1987: Ozone production in the rural troposphere and the implications for regional and global ozone distributions. *J. Geophys. Res.*, 92, 4191–4207.

Liu, S. C., Trainer, M., Carroll, M. A., Hübler, G., Montzka, D. D., Norton, R. B., Ridley,

B. A., Walega, J. G., Atlas, E. L., Heikes, B. G., Huebert, B. J., and Warren, W., 1992: A study of the photochemistry and ozone budget during the Manua Loa Observatory Photochemistry Experiment. *J. Geophys. Res.*, 7, 10463–10471.

Logan, J. A., Prather, M. J., Wofsy, S. C., and McElroy, M. B., 1981: Tropospheric chemistry: A global perspective. *J. Geophys. Res.*, 86, 7210–7254.

Logan, J. A., Megretskaia, I. A., Miller, A. J., Tiao, G. C., Choi, D., Zhang, L., Stolarski, R. S., Labow, G. J., Hollandsworth, S. M., Bodeker, G. E., Claude, H., De Muer, D., Kerr, J. B., Tarasick, D. W., Oltmans, S. J., Johnson, B., Schmidlin, F., Staehelin, J., Viatte, P., and Uchino, O., 1999: Trends in the vertical distribution of ozone: A comparison of two analysis of ozonesonde data. *J. Geophys. Res.*, 104, 26373–26399.

Lord, S. J., Willoughby, H. E., and Piotrowicz, J. M., 1984: Role of a parameterized ice-phase microphysics in an axisymmetric, nonhydrostatic tropical cyclone model. *J. Atmos. Sci.*, 42, 2836–2848.

Lu, R., Lin, C., Turco, R., and Arakawa, A., 2000: Cumulus transport of chemical tracers. 1. Cloud-resolving model simulations. *J. Geophys. Res.*, 105, 10001–10221.

Lucas, C., and Orville, R. E., 1996: TOGA COARE: Oceanic lightning. *Mon. Weather Rev.*, 114, 2077–2082.

Mackerras, D., Darveniza, M., Orville, R. E., Williams, E. R., and Goodmann, S. J., 1998: Global lightning: Total, cloud and ground flash estimates. *J. Geophys. Res.*, 103, 19791–19809.

Madden, R. A., and Julian, P. R., 1972: Detection of global scale circulation cells in the tropics with a 40–50 day period. *J. Atmos. Sci.*, 29, 1109–1123.

Madden, R. A., and Julian, P. R., 1994: Observations of the 40–50 day tropical oscillation – A review. *Mon. Weather Rev.*, 122, 814–836.

Magi, L., Schweitzer, F., Pallares, C., Cherif, S., Mirabel, P., and George, C., 1997: Investigation of the uptake rate of ozone and methyl hydroperoxide by water surfaces. *J. Phys. Chem.*, 101, 4943–4949.

Mahowald, N. M., Rasch, P. J., and Prinn, R. G., 1995: Cumulus parameterizations in chemical transport models. *J. Geophys. Res.*, 100, 26173–26189.

Manabe, S., and Strickler, R. F., 1964: Thermal Equilibrium of the Atmosphere with a Convective Adjustment. *J. Atmos. Sci.*, 21, 361–385.

Mapes, B. E., 1993: Gregarious tropical convection. *J. Atmos. Sci.*, 50, 2026–2037.

Mapes, B. E., Warner, T. T., Xu, M., and Gochis, D. J., 2004: Comparisons of cumulus parameterization and entrainment using domain-mean wind divergence in a regional model. *J. Atmos. Sci.*, 61, 1284–1295.

Mari, C., Jacob, D. J., and Bechtold, P., 2000: Transport and scavenging of soluble gases in a deep convective cloud. *J. Geophys. Res.*, 105, 22255–22267.

Mari, C., Saüt, C., Jacob, D. J., Ravetta, F., Anderson, B., Avery, M. A., D, R. Blake, Brune, W. H., Faloona, I., Gregory, G. L., Heikes, B. H., Sachse, G. W., Sandholm, S. T., Singh, H. B., Talbot, R. W., Tan, D., and Vay, S., 2003: Sources of upper tropospheric HO_x over the South Pacific Convergence Zone: A case study. *J. Geophys. Res.*, 108, 8229, doi:10.1029/2000JD000304.

Martinez, M., Harder, H., Kovacs, T. A., Simpas, J. B., Bassis, J., Lesher, R., Brune, W. H., Frost, G. J., Williams, E. J., Stroud, C. A., Jacobson, B. T., Roberts, J. M., Hall, S. R., Shetter, R. E., b. Wert, Fried, A., Alicke, B., Stutz, J., Young, V. L., White, A. B., and Zamora, R. J., 2003: OH and HO_2 concentrations, sources, and loss rates during the Southern Oxidant Study in Nashville, Tennessee, summer 1999. *J. Geophys. Res.*, 108, 4617, doi:10.1029/2003JD003551.

Massman, W. J., 1998: A review of the molecular diffusivities of H_2O, CO_2, CH_4, SO_2, NH_3, N_2O, NO, and NO_2 in air, O_2 and N_2 near STP. *Atmos. Environ.*, 32, 1111–1127.

Massman, W. J., and Meehl, G. A., 1987: The annual cycle and interannual variability in the tropical Pacific and Indian Ocean regions. *Mon. Weather Rev.*, 27, 27–50.

McBride, J. L., Davidson, N. E., and Tyrell, G. C., 1995: The flow during TOGA COARE as diagnosed by the BMRC tropical analysis and prediction system. *Mon. Weather Rev.*, 123, 717–736.

McPhaden, M. J., 2004: Evolution of the 2002/03 El Niño. *Bull. Am. Met. Soc.*, 85, 677–695.

Meier, A., and Hendricks, J., 2002: Model studies on the sensitivity of upper tropospheric chemistry to heterogeneous uptake of HNO_3 on cirrus ice particles. *J. Geophys. Res.*, 107, 10.1029/2001JD000735.

Meilinger, S. K., Tsias, A., Dreiling, V., Kuhn, M., Feigl, Ch., Ziereis, H., Schlager, H., Curtius, J., Sireau, B., Arnold, F., Zöger, M., Schiller, C., and Peter, Th., 1999: HNO_3 partitioning in cirrus clouds. *Geophys. Res. Lett.*, 26, 2207–2210.

Merrill, J. T., Newell, R. E., and Bachmeier, A. S., 1997: A meteorological overview for the Pacific Exploratory Mission-West phase B. *J. Geophys. Res.*, 102, 28241–28253.

Mlawer, E. J., Taubman, S. J., Brown, P. D., Iacono, M. J., and Clough, S. A., 1997: Radiative transfer for inhomogeneous atmosphere: RRTM a validated correlated-k model for the longwave. *J. Geophys. Res.*, 102, 16663–16682.

Monks, P. S., 2000: A review of observations and origins of the spring ozone maximum. *Atmos. Environ.*, 34, 3545–3561.

Mühle, J., Brenninkmeijer, C. A. M., Rhee, T. S., Slemr, F., Oram, D. E., Penkett, S. A., and Zahn, A., 2002: Biomass burning and fossil fuel signatures in the upper troposphere observed during a CARIBIC flight from Namibia to Germany. *Geophys. Res. Lett.*, 29, doi: 10.1029/2002GL015764.

National Research Council., 2001: Global Air Quality: An imperative for long-term observational strategies. Committee on Atmospheric Chemistry (M. M. Molina, Chair, J. H. Seinfeld, Vice-Chair), Board on Atmospheric Sciences and Climate, Division of Earth and Life Studies, National Research Council. National Academy of Sciences, National Academy Press, Washington, D.C.

Nesbitt, S. W., Zhang, R., and Orville, R. E., 2000: Seasonal and global NO_x production by lightning estimated from the Optical Transient Detector (OTD). *Tellus*, 52B, 1206–1215.

Newell, R. E., Wu, Z.-X., Zhu, Y., Hu, W., Browell, E. V., Gregory, G. L., Sachse, G. W., Collins Jr., J. E., Kelly, K. K., and Liu, S. C., 1996: Vertical fine-scale atmospheric structure measured from NASA DC-8 during PEM-West A. *J. Geophys. Res.*, 101, 1943–1960.

Newell, R. E., Thouret, V., Cho, J. Y. N., Stoller, P., Marenco, A., and Smit, H. G., 1999: Ubiquity of quasi-horizontal layers in the troposphere. *Nature*, 398, 316–319.

Nicholls, M. E., Pielke, R. A., and Cotton, W. R., 1991: Thermally forced gravity waves in an atmosphere at rest. *J. Atmos. Sci.*, 48, 1869–1884.

Noxon, J. F., 1976: Atmospheric nitrogen-fixation by lightning. *Geophys. Res. Lett.*, 3(8), 463–465.

Olson, J. R., Crawford, J. H., Davis, D. D., Chen, G., Avery, M. A., Barrick, J. D. W., Sachse, G. W., Vay, S. A., Sanholm, S. T., Tan, D., Brune, W. H., Faloona, I. C., Heikes, B. G., Shetter, R. E., Leffer, B. L., Singh, H. B., Talbot, R. W., and Blake, D. R., 2001: Seasonal differences in the photochemistry of the South Pacific: A comparison of observations and model results from PEM-Tropics A and B. *J. Geophys. Res.*, 106, 32749–32766.

Oltmans, S. J., Lefohn, A. S., Scheel, H. E., Harris, J. M., Levy II, H., Galbally, I. E., Brunke, E.-G., Meyer, C. P., Lathrop, J. A., Johnson, B. J., Shadwick, D. S., Cuevas, E., Schmidlin, F. J., Tarasick, D. W., Claude, H., Kerr, J. B., Uchino, O., and Mohen, V., 1998: Trends of ozone in the troposphere. *Geophys. Res. Lett.*, 25, 139–142.

Orville, R. E., Zisper, E. J., Brook, M., Weidman, C., Aulich, G., Krider, E. P., Christian, H., Goodman, S., Blakeslee, R., and Cummins, K., 1997: Lightning in the region of the

TOGA COARE. *Bull. Am. Met. Soc.*, 78, 1055–1067.

O'Sullivan, D. W., Lee, M., Noone, B. C., and Heikes, B. G., 1996: Henry's Law constant determinations for hydrogen peroxide, methyl hydroperoxide, hydroxymethyl hydroperoxide, ethyl hydroperoxide, and peroxyacetic acid. *J. Phys. Chem.*, 100, 3241–3247.

Petch, J. C., and Gray, M. E.B., 2001: Sensitivity studies using a cloud resolving model simulation of the tropical west Pacific. *Q. J. R. Meteorol. Soc.*, 127, 2287–2306.

Petersen, W. A., and Rutledge, S. A., 1996: Cloud-to-ground lightning observations from TOGA COARE: Selected results and lightning location algorithms. *Mon. Weather Rev.*, 124, 602–620.

Petersen, W. A., Cifelli, R. C., Rutledge, S. A., Ferrier, B. S., and Smull, B. F., 1999: Shipborne dual-Doppler operations during TOGA COARE: Integrated observations of storm kinematics and electrification. *Bull. Am. Met. Soc.*, 80, 81–97.

Petersen, W. A., Christian, H. J., and Rutledge, S. A., 2005: TRIMM observations of the global relationship between ice water content and lightning. *Geophys. Res. Lett.*, 32, L14819, doi:10.1029/2005GL023236.

Peyrous, R., and Lapyere, R. M., 1982: Gaseous products created by electrical discharges in the atmosphere and condensation nuclei resulting from gaseous-phase reactions. *Atmos. Environ.*, 6(5), 959–968.

Philander, G. S., 1990: *El Niño, La Niña, and the Southern Oscillation.* San Diego: Academic Press, 293pp.

Pickering, K. E., Thompson, A. M., Dickerson, R. R., Luke, W. T., McNamara, D. P., Greenberg, J. P., and Zimmerman, P. R., 1990: Model calculations of tropospheric ozone production potential following observed convective events. *J. Geophys. Res.*, 95, 14049–14062.

Pickering, K. E., Thompson, A. M., Tao, W.-K., and Kucsera, T. L., 1993: Upper tropospheric ozone production following mesoscale convection during STEP/EMEX. *J. Geophys. Res.*, 98, 8737–8749.

Pickering, K. E., Thompson, A. M., Wang, Y., Tao, W.-K., McNamara, D. P., Kirchhoff, V. W. J. H., Heikes, B. G., Sachse, G. W., Bradshaw, J. D., Gregory, G. L., and Blake, D. R., 1996: Convective transport of biomass burning emissions over Brazil during TRACE A. *J. Geophys. Res.*, 101, 23993–24012.

Pickering, K. E., Wang, Y., Tao, W.-K., Price, C., and Müller, J.-F., 1998: Vertical distributions of lightning NO_x for use in regional and global chemical transport models. *J. Geophys. Res.*, 103, 31203–31216.

Pickering, K. E., Thompson, A. M., Kim, H., DeCaria, A. J., Pfister, L., Kucsera, T. L., Witte, J. C., Avery, M. A., Blake, D. R., Crawford, J. H., Heikes, B. G., Sachse, G. W., Sandholm, S. T., and Talbot, R. W., 2001: Trace gas transport and scavenging in PEM-Tropics B South Pacific Convergence Zone convection. *J. Geophys. Res.*, 106, 32591–32602.

Pierce, E. T., 1970: Latitudinal variation of lightning parameters. *J. Appl. Met.*, 9, 194–195.

Popp, P. J., Gao, R. S., Marcy, T. P., Fahey, D. W., Hudson, P. K., Thompson, T. L., Kärcher, B., Ridley, B. A., Weinheimer, A. J., Knapp, D. J., Montzka, D. D., Baumgardner, D., Garrett, T. J., Weinstock, E. M., Smith, J. B., Sayres, D. S., Pittman, J. V., Dhaniyala, S., Bui, T. P., and Mahoney, M. J., 2004: Nitric acid uptake on subtropical cirrus cloud particles. *J. Geophys. Res.*, 109, doi: 10.1029/2003JD004255.

Prather, M. J., and Jacob, D. J., 1997: A persistent imbalance in HO_x and NO_x photochemistry of the upper troposphere driven by deep tropical convection. *Geophys. Res. Lett.*, 24, 3189–3192.

Prentice, S. A., and Mackerras, D., 1977: The ratio of cloud to cloud-ground lightning flashes in thunderstorms. *J. Appl. Met.*, 16, 545–550.

Price, C., and Rind, D., 1992: A simple lightning parameterization for calculating global

lightning distributions. *J. Geophys. Res.*, 97, 9919–9933.

Price, C., and Rind, D., 1993: What determines the cloud-to-ground lightning fraction in thunderstorms? *Geophys. Res. Lett.*, 20, 463–466.

Price, C., Penner, J., and Prather, M., 1997a: NO_x from lightning: 1. Global distribution based on lightning physics. *J. Geophys. Res.*, 102, 5929–5941.

Price, C., Penner, J., and Prather, M., 1997b: NO_x from lightning: 2. Constraints from the global atmospheric electric circuit. *J. Geophys. Res.*, 102, 5942–5951.

Pruppacher, H. R., and Klett, J. D., 1997: *Microphysics of clouds and precipitation.* Dordrecht: Kluwer, 954pp.

Raper, J. L., Kleb, M. M., Jacob, D. J., Douglas, D. D., Newell, R. E., Fuelberg, H. E., Bendura, R. J., Hoell, J. M., and Neal, R. J. Mc., 2001: Pacific Exploratory Mission in the tropical Pacific: PEM-Tropics B, March–April 1999. *J. Geophys. Res.*, 106, 132401–32425.

Rasch, P., Zurovac-Jevtic, D., Emanuel, K., and Lawrence, M., 2003: Consistent representation of convective processes for chemistry and climate models. *Geophys. Res. Abstr.*, 5, 12440.

Ridley, B., Ott, L., Pickering, K., Emmons, L., Montzka, D., Weinheimer, A., Knapp, D., Grahek, F., Li, L., Heymsfield, G., McGill, M, Kucera, P., Mahoney, M. J., Baumgardner, D., Schultz, M., and Brasseur, G., 2004: Florida thunderstorms: A faucet of reactive nitrogen to the upper troposphere. *J. Geophys. Res.*, 109, D17305,doi:10.1029/2004JD004769.

Ridley, B. A., Dye, J. E., Walega, J. G., Zheng, J., Grahek, F. E., and Rison, W., 1996: On the production of active nitrogen by thunderstorms over New Mexico. *J. Geophys. Res.*, 101, 20985–21005.

Riehl, H., and Malkus, J. S., 1958: On the heat balance in the equatorial trough zone. *Geophysica (Helsinki)*, 6, 503–538.

Rodhe, H., 1983: Precipitation scavenging and tropospheric mixing. In *Precipitation scavenging, dry deposition, and resuspension*, Pruppacher et al., eds, Elsevier Science Publishing Co., Inc., 719–729.

Roehl, C. M, Nizkorodov, S. A., Zhang, H., Blake, G. A., and Wennberg, P. O., 2002: Photodissociation of peroxynitric acid in the near-IR. *J. Phys. Chem.*, 106, 3766–3772.

Rossow, W. B., and Schiffer, R. B., 1999: Advances in understanding clouds from ISCCP. *Bull. Am. Met. Soc.*, 80, 2261–2287.

Rui, H., and Wang, B., 1990: Development characteristics and dynamical structure of tropical intraseasonal convection anomalies. *J. Atmos. Sci.*, 47, 357–379.

Rutledge, S. A., Williams, E. R., and Keenan, T. D., 1992: The Down Under Doppler and Electricity Experiment (DUNDEE): Overview and preliminary results. *Bull. Am. Met. Soc.*, 73, 3–16.

Ryerson, T. B., Trainer, M., Holloway, J. S., Parish, D. D., Huey, L. G., Sueper, D. T., Frost, G. J., Donelly, S. G., s. Schauffler, Atlas, E. L., Kuster, W. C., Goldan, P. D., Hübler, G., Meagher, J. F., and Fehsenfeld, F. C., 2001: Observations of ozone formation in power plant plumes and implications for ozone control strategies. *Science*, 292, 719–723.

Saito, K., Keenan, T., Holland, G., and Puri, K., 2001: Numerical simulation of the diurnal evolution of tropical island convection over the Maritime Continent. *Mon. Weather Rev.*, 129, 378–400.

Salzmann, M., Lawrence, M. G., Phillips, V. T. J., and Donner, L. J., 2004: Modelling tracer transport by a cumulus ensemble: Lateral boundary conditions and large-scale ascent. *Atmos. Chem. Phys.*, 4, 1797–1811.

Sander, R., Keene, W. C., Pszenny, A. A. P., Arimoto, R., Ayers, G. P., Baboukas, E., Cainey, J. M., Crutzen, P. J., Duce, R. A., Hönninger, G., Huebert, B. J., W, Maenhaut, Mihalopoulos, N., Turekian, V. C., and Van Dingenen, R., 2003: Inorganic bromine in

the marine boundary layer: A critical review. *Atmos. Chem. Phys.*, 3, 1301–1336.

Sander, R., Kerkweg, A., Jöckel, P., and Lelieveld, J., 2005: Technical note: The new comprehensive atmospheric chemistry module MECCA. *Atmos. Chem. Phys.*, 5, 445–450.

Sander, S. P., Friedl, R. R., DeMore, W. B., Ravishankara, A. R., Golden, D. M., Kolb, C. E., Kurylo, M. J., Hampson, R. F., Huie, R. E., Molina, M. J., and Moortgat, G. K., 2000: *Chemical Kinetics and Photochemical Data for Use in Stratospheric Modeling — Supplement to Evaluation 12: Update of Key Reactions.* Evaluation 13, 00-3. Jet Propulsion Laboratory, Pasadena, California.

Scala, J. R., Garstang, M., Tao, W.-K., Pickering, K. E., Thompson, A. M., Simpson, J., Kirchhoff, V. W. J. H., Browell, E. V., Sachse, G. W., Torres, A. L., Gregory, G. L., Rasmussen, R. ., and Khalil, M. A. K., 1990: Cloud draft structures and trace gas transport. *J. Geophys. Res.*, 95, 17015–17030.

Schultz, M. G., Jacob, D. J., Wang, Y., Logan, J. A., Atlas, E. L., Blake, D. R., Blake, N. J., Bradshaw, J. D., Browell, E. V., Fenn, M. A., Flocke, F., Gregory, G. L., Heikes, B. G., Sachse, G. W., Sandholm, S. T., Shetter, R. E., Singh, H. B., and Talbot, R. W., 1999: On the origin of tropospheric ozone and NO_x over the tropical South Pacific. *J. Geophys. Res.*, 104, 5829–5843.

Schwartz, S. E., 1986: Mass-transport considerations pertinent to aqueous phase reactions of gases in liquid-water clouds. *Pages 415–471 of:* Jaeschke, W. (ed.), *Chemistry of Multiphase Atmospheric Systems*, Springer-Verlag, Berlin and Heidelberg, Germany.

Schwartz, S. E., and White, W. H., 1981: Solubility equilibria of the nitrogen oxides and oxyacids in dilute aqueous solution. *Pages 1–45 of:* Pfafflin, J. R., and Ziegler, E. N. (eds), *Advances in Environmental Science and Engineering*, vol. 4 Gordon and Breach Science Publishers, NY.

Seinfeld, J. H., and Pandis, S. N., 1998: *Atmospheric Chemistry and Physics.* New York: Wiley and Sons, 1326pp.

Sillman, S., Logan, J. A., and Wofsy, S. C., 1990: A regional model for ozone in the United States with subgrid representation of urban and power plant plumes. *J. Geophys. Res.*, 95, 5731–5748.

Singh, H., Chen, Y., Staudt, A., Blake, D., Heikes, B., and Snow, J., 2001: Evidence from the Pacific troposphere for large global sources of oxygenated organic compounds. *Nature*, 401, 1078–1081.

Singh, H. B., and Hanst, P. L., 1981: Peroxyacetyl nitrate (PAN) in the unpolluted atmosphere - an important reservoir for nitrogen oxides. *Geophys. Res. Lett.*, 8, 941–944.

Singh, H. B., Kanakidou, M., Crutzen, P. J., and Jacob, D. J., 1995: High concentrations and photochemical fate of oxygenated hydrocarbons in the global troposphere. *Nature*, 378, 50–54.

Singh, H. B., Gregory, G. L., Anderson, B., Browell, E., Sachse, G. W., Davis, D. D., Crawford, J., Bradshaw, J. D., Talbot, R., Blake, D. R., Thornton, D., Newell, R., and Merrill, J., 1996: Low ozone in the marine boundary layer of the tropical Pacific Ocean: Photochemical loss, chlorine atoms, and entrainment. *J. Geophys. Res.*, 101, 1907–1917.

Singh, H. B., Viezee, W., Chen, Y., Thakur, A. N., Kondo, Y., Talbot, R. W., Gregory, G. L., Sachse, G. W., Blake, D. R., Bradshaw, J. D., Wang, Y., and Jacob, D. J., 1998: Latitudinal distribution of reactive nitrogen in the free troposphere over the Pacific Ocean in late winter/early spring. *J. Geophys. Res.*, 103, 28237–28246.

Sisterson, D. L., and Liaw, Y. P., 1990: An evaluation of lightning and corona discharge on thunderstorm air and precipitation chemistry. *J. Atmos. Chem.*, 10(1), 83–96.

Skamaraock, W. C., Klemp, J. B., and Dudhia, J., 2001 (30 Jul-2 Aug). Prototypes for the WRF (Weather Research and Forecasting) model. *Pages J11–J15 of: Preprints,*

Ninth Conf. Mesoscale Processes Amer. Meteor. Soc., Fort Lauderdale, FL.

Skamarock, W. C., Powers, J. G., Barth, M., Dye, J. E., Matejka, T., Bartels, D., Baumann, K., Stith, J., Parrish, D. D., and Hubler, G., 2000: Numerical simulations of the July 10 Stratospheric-Tropospheric Experiment: Radiation, Aerosols, and Ozone/Deep Convection Experiment convective system: Kinematics and transport. *J. Geophys. Res.*, 105, 19973–19990.

Skamarock, W. C., Dye, J. E., Barth, M. C., Stith, J. L., Ridley, B. A., and Baumann, K., 2003: Observational- and modeling-based budget of lightning-produced NO_x in a continental thunderstorm. *J. Geophys. Res.*, 108, 4035, doi:10.1029/2002JD002163.

Skamarock, W. C., Byran, G., Rotunno, R., and Barth, M., 2005: The resolution dependence of explicitly modeled convection. *Geophys. Res. Abstr.*, 7, Sref–ID: 05266, 1607–7962/gra/EGU05–A–05266.

Snider, J. R., and Dawson, G. A., 1985: Tropospheric light alcohols, carbonyls, and acetonitrile: Concentrations in the southwestern United States and Henry's law data. *J. Geophys. Res.*, 90D, 3797–3805.

Snider, J. R., and Huang, J., 1998: Factors influencing the retention of hydrogen peroxide and molecular oxygen in rime ice. *J. Geophys. Res.*, 103, 1405–1415.

Snider, J. R., Montague, D. C., and Vali, G., 1992: Hydrogen peroxide retention in rime ice. *J. Geophys. Res.*, 97, 7569–7578.

Solomon, R., and Baker, M., 1998: Lightning flash rate and type in convective storms. *J. Geophys. Res.*, 103, 14041–14057.

Sommerfeld, R. A., Knight, C. A., and Kay Laird, S., 1998: Diffusion of HNO_3 in ice. *J. Geophys. Res.*, 25, 935–938.

Soong, S.-T., and Ogura, Y., 1980: Response of tradewind cumuli to large-scale processes. *J. Atmos. Sci.*, 37, 2035–2050.

Staudinger, J., and Roberts, P. V., 1996: A critical review of Henry's law constants for environmental applications. *Crit. Rev. Environ. Sci. Technol.*, 26, 205–297.

Staudt, A. C., Jacob, D. J., Logan, J. A., Biachiochi, D., Krishnamurti, T. N., and Sachse, G. W., 2001: Continental sources, transoceanic transport, and interhemispheric exchange of carbon monoxide over the Pacific. *J. Geophys. Res.*, 106, 32571–32590.

Staudt, A. C., Jacob, D. J., Ravetta, F., Logan, J. A., Biachiochi, D., Krishnamurti, T. N., Sandholm, S., Ridley, B., Singh, H. B., and Talbot, B., 2003: Sources and chemistry of nitrogen oxides over the tropical Pacific. *J. Geophys. Res.*, 108, 8239, doi:10.1029/2002JD002139.

Stuart, A. L., and Jacobson, M. Z., 2003: A timescale investigation of volatile chemical retention during hydrometeor freezing: Nonrime freezing and dry growth riming without spreading. *J. Geophys. Res.*, 108, doi: 10.1029/2001JD001408.

Stuart, A. L., and Jacobson, M. Z., 2004: Chemical retention during dry growth riming. *J. Geophys. Res.*, 109, doi: 10.1029/2003JD004197.

Stull, Roland B., 1988: *An Introduction to Boundary Layer Meteorology.* Dordrecht: Kluwer Academic Press.

Su, H., Chen, S. S., and Bretherton, C. S., 1999: Three-dimensional week-long simulations of TOGA COARE convective systems using the MM5 mesoscale model. *J. Atmos. Sci.*, 56, 2326–2344.

Tabazadeh, A., and Turco, R. P., 1993: A model for heterogeneous chemical processes on the surfaces of ice and nitric acid trihydrate particles. *Geophys. Res. Lett.*, 98, 12727–12740.

Tabazadeh, A., Toon, O. B., and Jensen, E. J., 1999: A surface chemistry model for nonreactive trace gas adsorption on ice: Implications for nitric acid scavenging by cirrus. *Geophys. Res. Lett.*, 26, 2211–2214.

Takemi, T., and Rotunno, R., 2003: The effects of subgrid model mixing and numerical filtering in simulations of mesoscale cloud systems. *Mon. Weather Rev.*, 131, 2085–2191.

Tan, D., I, Faloona, J, B. Simpas, Olson, J., Crawford, J., Avery, M., Sachse, G., Vay, S., Sandholm, S., Guan, H.-W., Vaughan, T., Mastromarinao, J., Heikes, B., Snow, J., Podolske, J., and Singh, H., 2001: OH and HO_2 in the tropical Pacific: Results from PEM-Tropics B. *J. Geophys. Res.*, 106, 32667–32682.

Thompson, A. M., Johnson, J. E., Torres, A. L., Bates, T. S., Kelly, K. C., Atlas, A., Greenberg, J. P., Donahue, N. M., Yvon, S. A., abd B. G. Heikes, E. S. Saltzman, Mosher, B. W., Shashkov, A. A., and Yegorov, V. I., 1993: Ozone observations and a model of marine boundary layer photochemistry during SAGA 3. *J. Geophys. Res.*, 98, 16955–16968.

Thompson, A. M., Witte, J. C., McPeters, R. D., Oltmans, S. J., Schmidlin, F. J., Logan, J. A., Fujiwara, M., Kirchhoff, V. W. J. H., Posny, F., Coetzee, G. J. R., Hoegger, B., Kawakami, S., T. Ogawa, B J. Johnson, Vömel, H., and Labow, G., 2003: Southern Hemisphere Additional Ozonesondes (SHADOZ) 1998-2000 tropical ozone climatology 1. Comparison with Total Ozone Mapping Spectrometer (TOMS) and ground-based measurements. *J. Geophys. Res.*, 108, doi: 10.1029/2001JD000967.

Trembley, A., 1987: A three-dimensional cloud chemistry model. *Atmos. Environ.*, 21, 2345–2364.

Trembley, A., and Leighton, H., 1986: A three-dimensional cloud chemistry model. *Journal of the ACM*, 25, 652–671.

Trenberth, K. E., and Stepaniak, D. P., 2003: Seamless poleward atmospheric energy transport and implications for the Hadley circulation. *J. Climate*, 16, 3706–3722.

Trentmann, J., Andreae, M. O., Graf, H.-F., Hobbs, P. V., Ottmar, R. D., and Trautmann, T., 2002: Simulation of a biomass-burning plume: Comparison of model results with observations. *J. Geophys. Res.*, 107, 10.1029/2001JD000410.

Trentmann, J., Luderer, G., Fromm, M. D., Servranckx, R., Rosenfeld, D., Diner, D., Winterrath, T., Textor, C., Andreae, M. O., and Hobbs, P. V., 2005: Formation of a fire-induced convective cloud: Observations and simulations of the Chrisholm fire, 2001. *Geophys. Res. Abstr.*, 7, 05550, Sref–ID: 1607–7962/gra/EGU05–A–05550.

Trier, S. T., Skamarock, W. C., and LeMone, M. A., 1997: Structure and evolution of the 22 February 1993 TOGA COARE squall line: Organization mechanisms inferred from numerical simulation. *J. Atmos. Sci.*, 54, 386–407.

Tsutsumi, Y., Makino, Y., and Jensen, J. B., 2003: Vertical and horizontal distributions of tropospheric ozone over the western Pacific: Case studies from the PACE aircraft missions. *J. Geophys. Res.*, 108, 4251, doi:1029/2001JD001374.

Tuck, A. F., 1976: Production of nitrogen-oxides by lightning discharges. *Q. J. R. Meteorol. Soc.*, 102(434), 749–755.

Tyndall, G. S., Cox, R. A., Garnier, C., Lesclaux, R., Moortgat, G. K., Pilling, M. J., Ravishankara, A. R., and Wallington, T. J., 2001: The atmospheric chemistry of small organic peroxy radicals. *J. Geophys. Res.*, 106, 12157–12182.

U. S. Environmental Protection Agency., 1996: Air quality criteria for ozone and related photochemical oxidants. EPA/600/P-93/004a-cF. Research Triangle Park, NC: U.S. Environmental Protection Agency.

von Glasow, R., Lawrence, M. G., Sander, R., and Crutzen, P. J., 2003: Modelling the chemical effects of ship exhaust in the cloud-free marine boundary layer. *Atmos. Chem. Phys.*, 3, 233–250.

von Kuhlmann, R., Lawrence, M. G., Crutzen, P. J., and Rasch, P. J., 2003a: A model for studies of tropospheric ozone and nonmethane hydrocarbons: Model description and ozone results. *J. Geophys. Res.*, 108, doi: 10.1029/2002JD002893.

von Kuhlmann, R., Lawrence, M. G., Crutzen, P. J., and Rasch, P. J., 2003b: A model for studies of tropospheric ozone and nonmethane hydrocarbons: Model evaluation and ozone-related species. *J. Geophys. Res.*, 108, 4729, doi: 10.1029/2002JD003348.

von Kuhlmann, R., Lawrence, M. G., Pöschl, U., and Crutzen, P. J., 2004: Sensitivities

in global scale modeling of isoprene. *Atmos. Chem. Phys.*, 4, 1–17.

von Kuhlmann, Rolf., 2001: *Photochemistry of Tropospheric Ozone, its Precursors and the Hydroxyl Radical: A 3D-Modeling Study Considering Non-Methane Hydrocarbons.* Ph.D. thesis, Johannes Gutenberg-Universität Mainz, Mainz, Germany, 220pp.

Wahner, A., Mentel, T. F., and Sohn, M., 1998: Gas-phase reaction of N_2O_5 with water vapor: Importance of heterogeneous hydrolysis of N_2O_5 and surface desorption of HNO_3 in a large teflon chamber. *Geophys. Res. Lett.*, 25, 2169–2172.

Walcek, C. J., 2000: Minor flux adjustment near mixing ratio extremes for simplified yet highly accurate monotonic calculation of tracer advection. *J. Geophys. Res.*, 105, 9335–9348.

Walcek, C. J., Yuan, H.-H., and Stockwell, W. R., 1997: The influences of aqueous-phase chemical reactions on ozone formation in polluted and nonpolluted clouds. *J. Geophys. Res.*, 31, 1221–1237.

Wang, C., and Chang, J. S., 1993a: A three-dimensional numerical model of cloud dynamics, microphysics, and chemistry: 3. Redistribution of pollutants. *J. Geophys. Res.*, 98, 16787–16798.

Wang, C., and Chang, J. S., 1993b: A three-dimensional numerical model of cloud dynamics, microphysics, and chemistry: 4. Cloud chemistry and precipitation chemistry. *J. Geophys. Res.*, 98, 16799–16808.

Wang, C., and Crutzen, P. J., 1995: Impact of a simulated severe local storm on the redistribution of sulfur dioxide. *J. Geophys. Res.*, 100, 11357–11367.

Wang, C., and Prinn, R. G., 2000: On the roles of deep convective clouds in tropospheric chemistry. *J. Geophys. Res.*, 105, 22269–22297.

Wang, C., and Prinn, R. G., 2004: Reply to comment by John H. Helsdon Jr on "On the roles of deep convective clouds in tropospheric chemistry". *J. Geophys. Res.*, 109, D10205, doi:10.1029/2002JD002399.

Wang, C., Crutzen, P. J., Ramanathan, V., and F.Williams, S., 1995: The role of a deep convective storm over the tropical Pacific Ocean in the redistribution of atmospheric chemical species. *J. Geophys. Res.*, 100, 11509–11516.

Wang, P. K., 2003: Moisture plumes above thunderstorm anvils and their contributions to cross-tropopause transport of water vapor in midlatitudes. *J. Geophys. Res.*, 108, doi: 10.1029/2002JD002581.

Wang, Y., DeSilva, A. W., Goldenbaum, G. C., and Dickerson, R. R., 1998: Nitric oxide production by simulated lightning: dependence on current, energy, and pressure. *J. Geophys. Res.*, 103, 19149–19159.

Wang, Y., Liu, S. C., Yu, H., Sandholm, S. T., Chen, T.-Y., and Blake, D. R., 2000: Influence of convection and biomass burning outflow on tropospheric chemistry over the tropical Pacific. *J. Geophys. Res.*, 105, 9321–9333.

Wang, Y., Liu, S. C., Wine, P. H., Davis, D. D., Sandholm, S. T., Atlas, E. L., Avery, M. A., Blake, D. R., Burne, W. H., Heikes, B. G., Sachse, G. W., Shetter, R. E., Singh, H. B., Talbot, R. W., and Tan, D., 2001: Factors controlling tropospheric O_3, OH, NO_x, and SO_2 over the tropical Pacific during PEM-Tropics B. *J. Geophys. Res.*, 106, 32733–32747.

Warner, J., 1970: On steady-state one-dimensional models of cumulus convection. *J. Atmos. Sci.*, 27, 1035–1040.

Webster, P. J., and Lukas, R., 1992: TOGA COARE: The Coupled Ocean-Atmosphere Response Experiment. *Bull. Am. Met. Soc.*, 73, 1377–1416.

Wesely, M. L., 1989: Parameterization of surface resistance to gaseous dry deposition in regional-scale numerical models. *Atmos. Environ.*, 23, 1293–1304.

WHO., 2000: Air quality guidelines for Europe. Second edition, WHO Regional Publication Series, no. 91, WHO Regional Office for Europe, Copenhagen, Denmark.

Wicker, L. J., and Skamarock, W. C., 2002: Time-splitting methods for elastic models

using forward time schemes. *Mon. Weather Rev.*, 130, 2088–2097.

Wild, O., Prather, M. J., Akimoto, H., Sundet, J. K., Isaksen, I. S. A., Crawford, J. H., Davis, D. D., Avery, M. A., Kondo, Y., Sachse, G. W., and Sandholm, S. T., 2004: Chemical transport model ozone simulations for spring 2001 over the western Pacific: Regional ozone production and its global impacts. *J. Geophys. Res.*, 109, D15S02, doi:10.1029/2003JD004041.

WMO., 1995: World Meteorological Organization, Scientific assessment of ozone depletion: 1994, Report. No. 37, Global Ozone Res. and Monit. Proj., Geneva.

Wollenhaupt, M., and Crowley, J. N., 2000: Kinetic studies of the reactions $CH_3 + NO_2 \rightarrow$ products, $CH_3 + NO_2 \rightarrow$ products, and $OH + CH_3C(O)CH_3 \rightarrow CH_3C(O)OH + CH_3$, over a range of temperature and pressure. *J. Phys. Chem.*, 104, 6429–6438.

Wollenhaupt, M., Carl, S. A., Horowitz, A., and Crowley, J. N., 2000: Rate coefficients for reaction of OH with Acetone between 202 and 395K. *J. Phys. Chem.*, 104, 2695–2705.

Wurzler, S., 1995: *The Scavenging and Wet Deposition of Nitrogen Compounds by a Warm Convective Cloud Using Two Cloud Dynamic Models.* Ph.D. thesis, Universität Mainz, 160pp.

Wurzler, S., 1997: The scavenging of nitrogen compounds by clouds and precipitation: Part II. The effects of cloud microphysical parameterization on model predictions of nitric acid scavenging by clouds. *Atmos. Ocean*, 47-48, 219–233.

Xie, S., and Cederwall, R. T., 2004: Developing long-term single-column model/cloud system-resolving model forcing data using numerical prediction products constrained by surface and top of the atmosphere observations. *J. Geophys. Res.*, 109, D01104, doi:10.1029/2003JD004045.

Xie, S., Xu, K.-M., Cederwall, R. T., Bechthold, P., Genio, A. D. Del, Klein, S. A., Cripe, D. G., Ghan, S. J., Gregory, D., Iacobellis, S. I., Krueger, S. K., Lohmann, U., Petch, J. C., Randall, D. A., Rotstayn, L. D., Somerville, R. C. J., Sud, Y. C., von Salzena, K., Walker, G. K., Wolf, A., Yio, J. J., Zhang, G. J, and Zhang, M., 2002: Intercomparison and evaluation of cumulus parameterizations under summertime midlatitude continental conditions. *Q. J. R. Meteorol. Soc.*, 128, 1095–1135.

Xu, K.-M., and Krueger, S. K., 1991: Evaluation of cloudiness parameterizations using a cumulus ensemble model. *Mon. Weather Rev.*, 119, 342–367.

Xu, K.-M., and Randall, D., 1996: Explicit simulation of cumulus ensembles with GATE phase III data: Comparison with observations. *J. Atmos. Sci.*, 53, 3710–3736.

Xu, K.-M., Arakawa, A., and Krueger, S. K., 1992: The macroscopic behaviour of cumulus ensembles simulated by a cumulus ensemble model. *J. Atmos. Sci.*, 49, 2402–2420.

Xu, K.-M., Cederwall, R. T., Donner, L. J., Grabowski, W. W., Guichard, F., Johnson, D. E., Khairoudtdinov, M., Krueger, S. K., Petch, J. C., Randall, D. R., Seman, C. J., Tao, W.-K, Wang, D., Xie, S. C., Yio, J. J., and Zhang, M.-H., 2002: An intercomparison of cloud-resolving models with the Atmospheric Radiation Measurement summer 1997 Intensive Observation Period data. *Q. J. R. Meteorol. Soc.*, 128, 593–624.

Yanai, M., Esbensen, S., , and Chu, J., 1973: Determination of bulk properties of tropical cloud clusters from large-scale heat and moisture budgets. *J. Atmos. Sci.*, 30, 611–627.

Yanai, M., Chen, B., and Tung, W.-W., 2000: The Madden-Julian Oscillation observed during the TOGA COARE IOP: Global View. *J. Atmos. Sci.*, 57, 2374–2396.

Yano, J.-I., Guichard, F., Lafore, J.-P., and Redelsperger, J.-L., 2004: Estimations of mass fluxes for cumulus parameterizations from high-resolution spatial data. *J. Atmos. Sci.*, 61, 829–842.

Yienger, J.J., Galanter, M., Holloway, T.A., Phadnis, M.J., Guttikunda, S.K., Carmichael, G.R., Moxim, W.J., and Levy, H., 2000: The episodic nature of air pollution transport from Asia to North America. *J. Geophys. Res.*, 105, 26931–26945.

Yin, Y., Parker, D. J., and Carslaw, K. A., 2001: Simulation of trace gas redistribution

by convective clouds - Liquid phase processes. *Atmos. Chem. Phys.*, 1, 19–36.

Yin, Y., Carslaw, K. S., and Parker, D. J., 2002: Redistribution of trace gases by convective clouds - mixed phase processes. *Atmos. Chem. Phys.*, 2, 293–306.

Yin, Y., Carslaw, K. S., and Feingold, G., 2005: Vertical transport and processing of aerosols in a mixed-phase convective cloud and the feedback on cloud development. *Q. J. R. Meteorol. Soc.*, 131, 221–245.

Yuter, S. E., and Houze Jr, R. A., 1998: The natural variability of precipitating clouds over the western Pacific warm pool. *Q. J. R. Meteorol. Soc.*, 124, 53–100.

Zdunkowski, W. G., Panhans, W. G., Welch, R. M., and Korb, G. J., 1982: A radiation scheme for circulation and climate models. *Contributions to Atmospheric Physics*, 55, 215–238.

Zhang, C., 2005: Madden–Julian Oscillation. *Rev. Geoph.*, 43, doi:10.1029/2004RG000158.

Zhang, X., Heldson, J. H., and Farley, R. D., 2003: Numerical modeling of lightening-produced NO_x using an explicit lightning scheme: 1. Two-dimensional simulation as a "proof of concept". *J. Geophys. Res.*, 108, 4579, doi:10.1029/2002JD003224.

Ziereis, H., Minikin, A., Schlager, H., Gayet, J. F., Auriol, F., Stock, P., Baehr, J., Petzold, A., Schumann, U., Weinheimer, A., Ridley, B., and Ström, J., 2004: Uptake of reactive nitrogen on cirrus cloud particles during INCA. *Geophys. Res. Lett.*, 31, L05115, doi:10.1029/2003GL018794.

Zisper, E. J., 1994: Deep cumuloninmbus cloud systems in the Tropics with and without lightning. *Mon. Weather Rev.*, 122, 1837–1851.

Zondlo, M. A., Barone, S. B., and Tolbert, M. A., 1997: Uptake of HNO_3 on ice under upper tropospheric conditions. *Geophys. Res. Lett.*, 24, 1391–1394.

Acknowledgments

PLEASE NOTE THAT FOR PRIVACY REASONS THE UNIVERSITY LIBRARY DOES NOT ALLOW THE AUTHOR TO MENTION THE NAMES OF THOSE WHO HE WOULD LIKE TO ACKNOWLEDGE. PLEASE CONTACT THE AUTHOR (salzmann@mpch-mainz.mpg.de) FOR A COMPLETE VERSION OF THE DISSERTATION INCLUDING THE ACKNOWLEDGMENTS.